

UNIVERSIDADE FEDERAL DO RIO GRANDE DO SUL
PROGRAMA DE PÓS-GRADUAÇÃO EM FÍSICA
PhD Thesis

Eduardo Osório Rizzatti

Thermodynamic Anomalies in
Ultracold Quantum Gases

Porto Alegre
2021

Eduardo Osório Rizzatti

Thermodynamic Anomalies in Ultracold Quantum Gases

Tese submetida ao Programa de Pós-
Graduação em Física do Instituto de
Física da UFRGS

Advisor: Prof. Dr. Marcia Cristina
Bernardes Barbosa

Co-Advisor: Prof. Dr. Marco Au-
rílio Alves Barbosa

Porto Alegre

2021

A Deus e minha família

Abstract

Although well-researched as a prototype Hamiltonian for strongly interacting quantum systems, the Bose-Hubbard model has not so far been explored as a fluid system with waterlike anomalies. Water, the substance of life, is known for its myriad of anomalous properties, whose origins are still subject of intense debates. In order to provide a different insight into this problem, we show how its density anomaly can be reproduced using a quantum simulator. In particular, we demonstrate that the Bose-Hubbard model, such paradigm system in quantum mechanics, exhibits an increase in density with temperature at fixed pressure in the regular fluid regime and in the superfluid phase. We propose that the mechanism underlying the anomalies is related to zero point entropies and ground state phase transitions. A connection with the typical experimental scales and setups including confinement effects is also addressed. In this scenario, such finding opens a new pathway for theoretical and experimental studies of waterlike anomalies in the area of ultracold quantum gases.

We also discuss in detail the occurrence of anomalous double peaks in their specific heat dependence on temperature. This feature, usually associated with a high geometrical frustration, can also be a consequence of a purely energetic competition. By employing self-energy functional calculations combined to finite-temperature perturbation theory, we propose a mechanism based on ground-state degeneracies expressed as residual entropies. A general decomposition of the specific heat in terms of all possible transitions between the system's eigenvalues provides an insight on the nature of each maximum. Furthermore, we address how the model parameters modify the structure of these peaks based on its spectral properties and atom-atom correlation function.

Regarding the theoretical foundations of the methods employed, we address a deep analysis of the Legendre transformation, and how it can be conceived as extremum principle. We discuss the geometrical implications in a general framework, which includes the techniques explored throughout this thesis.

Keywords: quantum many-body systems. thermodynamics. statistical mechanics.

thermodynamic anomalies. Bose-Hubbard model. water. Legendre transformation.

Publications and Submissions

This work is based on the following publications and preprints which are partially reprinted.

Core-softened potentials, multiple liquid–liquid critical points, and density anomaly regions: An exact solution

Eduardo Osório Rizzatti, Marco Aurélio A. Barbosa, Marcia C. Barbosa

Frontiers of Physics volume 13, Article number: 136102 (2018)

The pressure versus temperature phase diagram of a system of particles interacting through a multiscale shoulder-like potential is exactly computed in one dimension. The N-shoulder potential exhibits N density anomaly regions in the phase diagram if the length scales can be connected by a convex curve. The result is analyzed in terms of the convexity of the Gibbs free energy.

Waterlike anomalies in the Bose–Hubbard model

Eduardo Osório Rizzatti, Márcio Sampaio Gomes Filho, Mariana Malard, Marco

Aurélio A. Barbosa

Physica A: Statistical Mechanics and its Applications

Volume 518, 15 March 2019, Pages 323-330

Although well-researched as a prototype Hamiltonian for strongly interacting quantum systems, the Bose–Hubbard model has not so far been explored as a fluid system with waterlike anomalies. In this work we show that this model supports, in the limit of a strongly localizing confining potential, density anomalies which can be traced back to ground state (zero-temperature) phase transitions between different Mott insulators.

Quantum density anomaly in optically trapped ultracold gases

Eduardo O. Rizzatti, Marco Aurelio A. Barbosa, Marcia C. Barbosa

Phys. Rev. A 102, 033331 – Published 22 September 2020

Water, the substance of life, is known for its myriad of anomalous properties, whose origins are still the subject of intense debates. In order to provide a different insight into this problem, we show how its density anomaly can be reproduced using a quantum simulator. In particular, we demonstrate that the Bose-Hubbard model, a paradigm system in quantum mechanics, exhibits an increase in density with temperature at fixed pressure in the regular fluid regime and in the superfluid phase. We propose that the mechanism underlying the anomalies is related to zero-point entropies and ground-state phase transitions. A connection with the typical experimental scales and setups including confinement effects is also addressed. In this scenario, such finding opens a pathway for theoretical and experimental studies of waterlike anomalies in the area of ultracold quantum gases.

Double-peak specific heat anomaly and correlations in the Bose-Hubbard model

Eduardo O. Rizzatti, Marco Aurelio A. Barbosa, Marcia C. Barbosa
arXiv:2010.06560v1, Submitted to Phys. Rev. B

Considering the thermodynamics of bosons in a lattice described by the Bose-Hubbard Hamiltonian, we report the occurrence of anomalous double peaks in their specific heat dependence on temperature. This feature, usually associated with a high geometrical frustration, can also be a consequence of a purely energetic competition. By employing self-energy functional calculations combined with finite-temperature perturbation theory, we propose a mechanism based on ground-state degeneracies expressed as residual entropies. A general decomposition of the specific heat regarding all possible transitions between the system's eigenvalues provides an insight into the nature of each maximum. Furthermore, we address how the model parameters modify the structure of these peaks based on its spectral properties and atom-atom correlation function.

Geometric Aspects of Thermodynamics and Legendre Transformations

Eduardo O. Rizzatti, Marcia C. Barbosa

In this paper we show the geometrical realization of the Legendre transformation as an extremum principle, connecting it to the foundations of the equilibrium Thermodynamics. In this formulation, the equation of state can be regarded as a path in the Gibbs manifold, which arises naturally as a test of thermodynamic stability. Particularly, we explore how these transformations codify a test for thermodynamic stability locally with response functions, and globally with the well known Maxwell construction.

List of Figures

1-1	Density of Water and Ice	19
1-2	Anomalous Thermodynamic Properties of Water: Response Functions	20
1-3	Water density and TMD line entering the supercooled domain.	21
1-4	Water Response functions entering the supercooled domain	21
1-5	Simplified water's temperature-pressure phase diagram and the domains of stability and metastability for liquid and glassy water.	22
2-1	Bose-Einstein Condensate	28
2-2	Quantum Simulation	29
2-3	Magneto-Optical Trap	31
2-4	Evaporative Cooling	33
2-5	Gaussian laser beams and intensity profile	37
2-6	Optical Lattices	38
3-1	Superfluid ground state and Poissonian atom number statistics.	45
3-2	Mott insulator ground state and the atom number statistics.	45
3-3	Ground state phase diagram of the Bose-Hubbard model	47
3-4	Time of flight image of the SF/MI phase transition	48
3-5	Density, entropy, and thermal expansion coefficient as a function of the chemical potential at fixed temperatures.	50
3-6	Pressure vs. temperature phase diagram	53
3-7	Density as a function of temperature for fixed pressures.	53
3-8	Thermal expansion coefficients at fixed pressure and chemical potential	55

3-9	The density ρ as a function of the temperature T for a simple cubic lattice.	61
3-10	The density ρ as a function of the temperature T for a square lattice.	61
3-11	The entropy and thermal expansion coefficient as functions of the chemical potential.	64
3-12	The density distribution in the normal phase, considering harmonic confinement effects.	67
3-13	Analysis of the set up presented describing the harmonic confinement.	68
4-1	Finite-temperature analysis of the specific heat and entropy in the atomic limit $J = 0$	74
4-2	The specific heat decomposition and its temperature behavior is exhibited considering four fixed values of chemical potential: (a) $\mu = 0.9U$, (b) $\mu = 1.1U$, (c) $\mu = 1.3U$ and (d) $\mu = 1.6U$	75
4-3	The specific heat c_μ is shown as a function of the temperature T at fixed $\mu = 0.9U$ for simple cubic (a)-(d) and square lattices (e)-(h) considering four different hopping amplitudes.	78
4-4	The spectral function A dependence on the real frequency ω at fixed $J = 0.006U$ and $\mu = 0.9U$, considering a simple cubic (a) and a square lattice (b).	81
4-5	The specific heat c_μ (a), free energy variation $\Delta\Omega$ (b) and atom-atom correlation \mathcal{C} (c) are shown as functions of temperature at $J = 0.006U$	84
4-6	Integration of the correlation functions $\mathcal{C}^{(\lambda)}$ and the free energy	85
5-1	Legendre transformation as a constrained optimization	94
5-2	The geometrical construction of the potential $\tilde{\Phi}^{(1)}(P^R X) = \Phi(X) - P^R X$, involved in the reformulation of the extremal principle.	95
5-3	Schematic representation of a thermodynamic system $\tilde{\sigma}$ and the mental experimental which enables the analysis of the fluxes δX_i	100
5-4	The Legendre transformation and the Maxwell Construction.	114

5-5	The equation of state, obtained as the solution of the extremization procedure.	117
6-1	Strange Metals	121

Nomenclature

α	Isobaric Thermal Expansion Coefficient
α_μ	Thermal Expansion Coefficient at fixed μ
λ	Laser Wavelength
Φ	One-Point (Condensate) Green's Function
Σ	Two-Point Self-Energy
$\Sigma_{1/2}$	One-Point Self-Energy
\mathbf{G}_0	Non-interacting Green's Function
\mathbf{G}	Two-Point Green's Function
μ	Chemical Potential
Ω	Equilibrium Free Energy
Ω_{BK}	Baym-Kadanoff Functional
Ω_{SE}	Self-energy Free energy
Φ_{LW}	Luttinger-Ward Functional
ρ	Density
a	Lattice cell size
c_P	Isobaric Specific Heat Capacity

c_μ Specific Heat Capacity at constant chemical potential

E_r Recoil Energy

J Hopping Amplitude

K_T Isothermal Compressibility

P Pressure

s Entropy per volume

T Temperature

U Interaction Energy

V Volume

v_0 Lattice cell volume

GSPT Ground State Phase Transition

PT Perturbation Theory

SFT Self-energy Functional Theory

Contents

1	Introduction	19
2	Quantum Simulators and Atoms in Optical Lattices	27
2.1	Cooling and Trapping Neutral Atoms	29
2.2	Optical Lattices in a Nutshell	35
2.3	Optical Lattices and the Bose-Hubbard model	39
3	The Bose-Hubbard Model and the Density Anomaly	43
3.1	Overview	44
	Superfluid Phase	44
	Mott Insulator Phase	46
3.2	Atomic Limit: where the anomaly is born	46
	The Ground State Phase Transitions	49
	Thermodynamics	49
	Results and discussions	51
3.3	Complete Scenario	55
	The Self-energy Functional Theory	55
3.4	Density anomaly	60
3.5	Residual entropy mechanism	65
3.6	2D in situ observation including confinement effects	66
4	Specific heat anomaly and correlations in the Bose-Hubbard model	71
4.1	The Atomic Limit ($J = 0$)	73

Contents	16
<hr/>	
4.2 Finite Hopping ($J \neq 0$)	78
Spectral Functions	80
Correlations and the Double Peaks	83
5 Geometry, Thermodynamics and Legendre Transformations	89
5.1 Basic Definitions and the Variational Principle	90
5.2 Legendre Transformations	93
5.3 Thermodynamic Stability	100
Local Stability	100
Global Stability and the Maxwell Construction	113
6 Conclusions and Perspectives	119
A Two-states approximation and the critical densities	123
B Self-energy Functional Theory	125
B.1 General Aspects	125
B.2 Tensor Products	130
B.3 Traces	132
General Definitions	132
High Frequency Expansion	132
Trace of Logarithm	135
B.4 Reference System	136
B.5 Lattice System	137
B.6 High Frequency Expansion of the Green's Function	138
Reference System	138
Lattice System	140
C The SFA3 code	143
D Equation of State and Pressure for the Harmonic Confinement	147

E	Perturbation Theory	149
E.1	General Aspects	149
E.2	Moments and Cumulants	151
E.3	Diagrammatic Expansion of the Partition Function	157
E.4	Diagrammatic Expansion of the free energy	162
E.5	Diagrammatic Expansion of the Green's Function	164
E.6	Evaluation of the Free energy and Green's Function	169
E.7	The Free Energy	171
E.8	The Green's Function and the atom-atom Correlation Funcion	173
F	Decomposition of the Specific Heat, Spectral Functions and Corre-	
	lations	175
F.1	Decomposition of the Specific Heat	175
F.2	Spectral Function in the Atomic Limit	177
F.3	Correlations and free energy	178
G	Publications and Submissions	181

Chapter 1

Introduction

“The scariest moment is always just before you start.”

– Stephen King

Water, the most abundant substance on Earth and the second most common molecule in the Universe, plays a fundamental role mediating the physicochemical processes of life, structuring biomolecules, as a valuable human resource and even as an essential ingredient to star formation [1–3]. Despite its simple molecular structure, the strength and directionality of hydrogen bonds in water induces rather anomalous and complex behaviors [4, 5]. High surface tension, specific heat and decreasing viscosity with pressure are among its 74 anomalies [6] cataloged up to now. Another striking property of water is its increase of density with temperature in the range

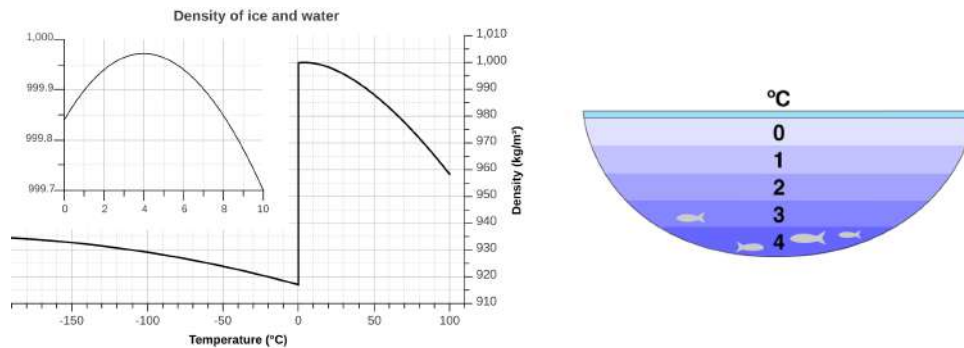


Figure 1-1: (a) Density of water and ice at 1 atm, with its maximum value around 4°C detailed by the inset. (b) This anomalous property enables maintenance of complex life even in wintry frozen lakes, due to its freezing from the top down [1].

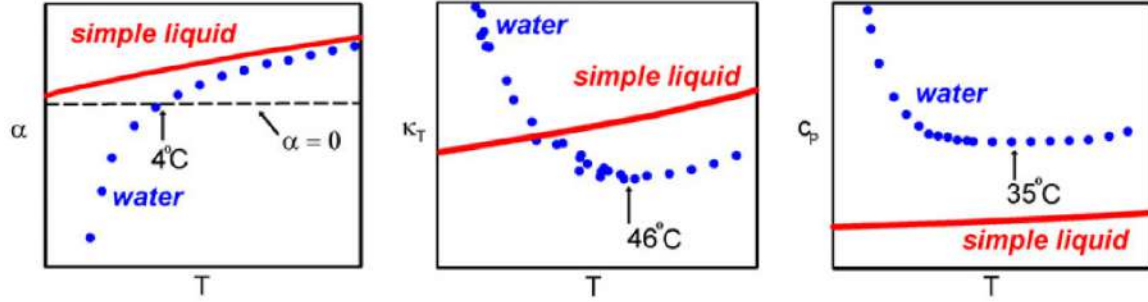


Figure 1-2: Representative comparison between a simple liquid and the anomalous behavior of H_2O water. (a) The isobaric thermal expansion α , (b) isothermal compressibility K_T and (c) the isobaric heat capacity C_P are portrayed as functions of temperature T . Extracted from Ref. [8]

from 0°C to 4°C , setting it apart from regular liquids [7]. Indeed, this feature enables the maintenance of aquatic life in lakes during winter since the bottom can reach higher temperatures while ice is formed on surface, freezing from the top down [1] as depicted in Fig. 1-1. In addition, thermodynamic response functions (related to fluctuations in volume and energy, such as heat capacity, isothermal compressibility and isobaric thermal expansion) also present anomalous behavior [8,9] as illustrated in Fig. 1-2. Water also exhibits anomalies in its structure which are connected to density and diffusion anomalies through the so-called hierarchy of anomalies [10–13].

This myriad of anomalies makes water a great puzzle in regards to the mechanism underlying its weirdness. Interestingly, these anomalous properties become more prominent in its supercooled state, the metastable liquid phase below the melting point [8,9,14]. In this region, it is still possible to perform measurements in the liquid state until about 232 K, where eventually homogeneous nucleation of ice takes place [15]. In Fig. 1-3, we exhibit experimental data regarding density in the supercooled domain as well as the temperature of maximum density (TMD) line entering the metastable regime above 40 MPa [16], which is associated to the zeroes of the thermal expansion coefficient.

On the other side of its phase diagram, through compression of hexagonal ice at 77 K and beyond 1.1 GPa, its amorphous was obtained and a first-order-like phase transition from a high-density amorphous ice (HDA) to low-density amorphous ice (LDA) by heating the sample at ambient pressure [17,18]. The melting of such glassy

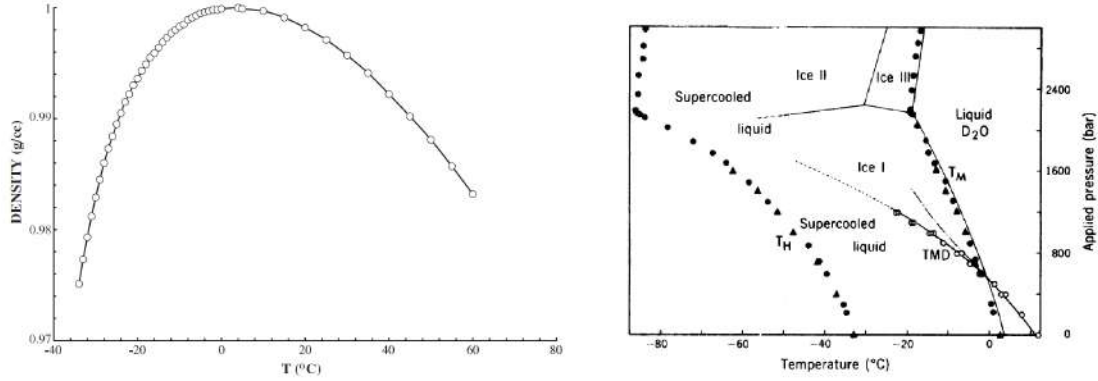


Figure 1-3: (a) Liquid water’s density at atmospheric pressure varying with temperature, from Ref. [8]. (b) The TMD line for D₂O as a function of pressure: T_M is the melting temperature and T_H is the homogeneous nucleation locus. Reprinted from Ref. [16].

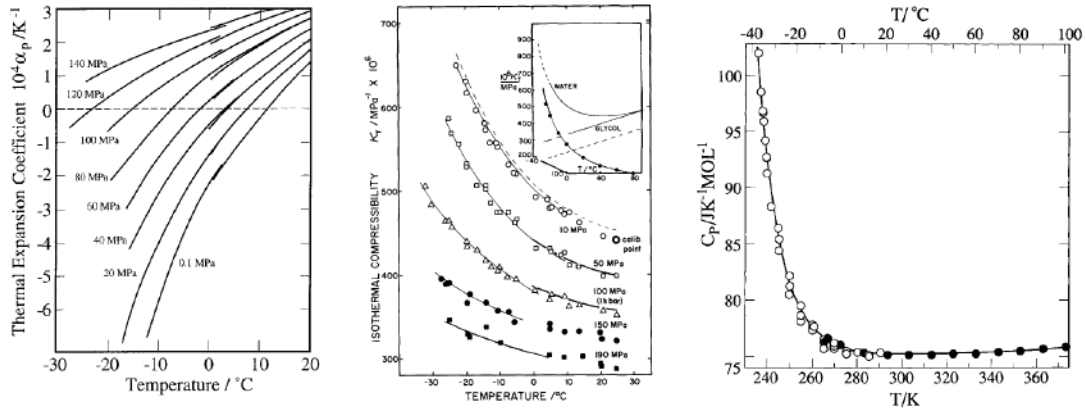


Figure 1-4: Temperature dependence of supercooled water’s (a) isobaric thermal expansion α , (b) isothermal compressibility K_T and (c) isobaric heat capacity C_P . Extracted from Ref. [19].

phases into its possible corresponding liquid phases, a high-density liquid (HDL) and a low-density liquid (LDL), is prevented once crystallization prevails around 160 K. The window between 232 K and 160 K constitutes the so called no man’s land, since experimental techniques can’t avoid the ice nucleation in this domain. These observations motivated great scientific interest¹ towards its metastable liquid state as well as its amorphous solid glassy forms. The current explanations are based on the possible extrapolations of the thermodynamic response functions into the no-man’s land.

¹Supercooled water impacts on certain technologies including pharmaceutical, food industries and cryopreservation, the technique of preserving organs and other biomaterials in low temperature. Supercooled water also appears in clouds resulting in the problematic formation of large ice crystals over the surface of aircrafts [4].

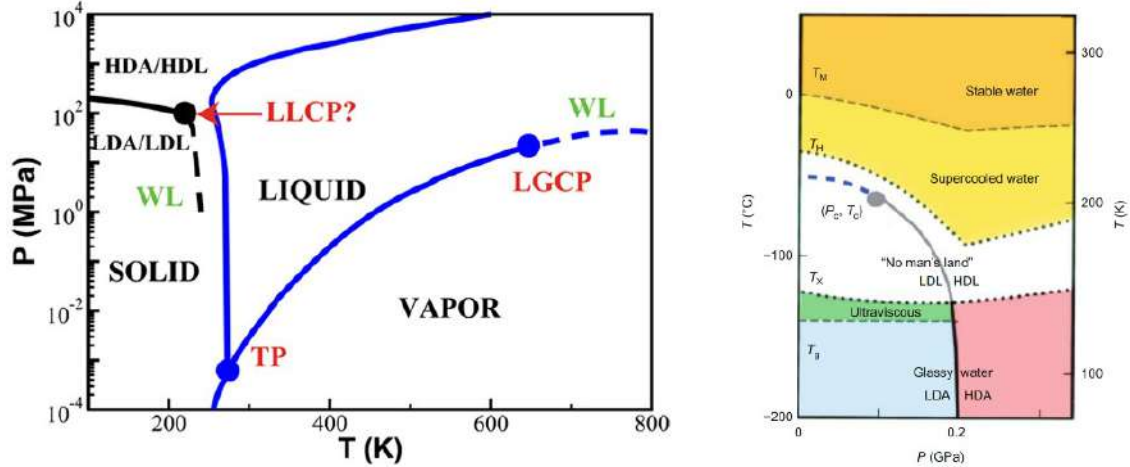


Figure 1-5: (a) Simplified water's temperature-pressure phase diagram portraying its solid, liquid and gaseous phases as well as the hypothetical liquid-liquid coexistence line ending in a critical point, printed from Ref. [9]. (b) A detailed picture regarding the domains of stability and metastability for liquid and glassy water. A first order LLPT line separates HDL and LDL. The LLPT ends with a LLCP at P_c , T_c . T_m , T_g and T_H represent the melting temperature, glass transition temperature, and homogeneous nucleation temperature, respectively. Extracted from Ref. [31].

The origins for the thermodynamic and dynamic anomalous behavior of liquid water has been disputed through different thermodynamic scenarios. The most influential, supported and even contested one is the "second critical point hypothesis" (SCP) of Poole, Sciortino, Essmann and Stanley [20]. This conjecture, based on computer simulations of the ST2 atomically detailed model of water, attests that the apparent divergence of thermodynamic response functions in the metastable supercooled region is a consequence of a metastable liquid-liquid phase transition (LLPT) ending in a liquid-liquid critical point (LLCP) [20, 21]. Nevertheless, this behavior in the case of water was never observed experimentally. The liquid-liquid transitions were reported in models for carbon [22], silicon [23], silica [24], and experimentally observed in phosphorus [25], triphenyl phosphite, and n-butanol [26]. More recently, experiments with mixtures of water and glycerol [27] and measurements of correlations functions using time-resolved optical Kerr effect (OKE) of supercooled water [28] favor the SCP hypothesis, despite debates in literature [29, 30].

This hypothesis is consistent with the mentioned anomalous and pronounced increase in magnitude of the response functions upon cooling and the existence of two forms of amorphous solids at low temperatures. In other words, it connects the anoma-

lies of stable and supercooled water to the transition between HDA and LDA. The experimentally observed transition between these amorphous phases can be thought as a prelude of a phase transition between two form of liquid water. This polyarmorphism of supercooled and glassy water also reinforces its interpretations as a mixture of two states, the arrangements of hydrogen bonds accommodated by thermodynamic parameters as temperature and pressure. In the same direction, simulations of fluids, whose interactions are parametrized by intermolecular potentials with two length and energy scales, can reproduce liquid-liquid phase separation. Indeed the competition between configurations seems to constitute an important ingredient generating anomalies if both structures are thermodynamically accessible. Water and its anomalies were investigated by various models, from which we mention the simplified lattice and the core softened models. Among lattice models for water, it should be relevant to mention that waterlike anomalies were found for models of orientational bonding fluids in the triangular lattice, and on 3D simple cubic lattice, through a variety of techniques, varying from Bethe lattice [32], cluster variational method [33] and Monte Carlo simulations [34]. Core softened were investigated using molecular dynamics [35–37] and analytically through integral equations [38], being found that pair potentials with competing two scale can reproduce various anomalies including those on density, structure and diffusion.

The suggested connection between thermodynamic anomalies and criticality is indeed difficult to be tested experimentally since the system freezes before reaching the critical temperature. In addition, the complexity of the water structure makes difficult to unveil the connection between the microscopic interactions, thermodynamic anomalies and criticality.

A possible route to overcome such challenges is to look for the anomalies in other contexts and models, which could provide a clearer visualization of the reported phenomena. In particular, the recent advances in the manipulation of atoms cooled to extremely low temperatures (below nanoKelvins) have produced extremely controllable and rich environments. Quantum particles imprisoned by electromagnetic fields can emulate Hamiltonians with precise control of geometry and interactions, making

a solid bridge between experiments and theory. These experimental setups gather qualities rising them as precursors of the so called quantum simulators: the notion of creating a quantum system to simulate properties of another one, originally formulated by Feynman [39, 40]. Following these ideas we propose to study waterlike anomalies using the Bose-Hubbard model, a widely known Hamiltonian simulated in laboratory by Greiner et al. [41], with Rubidium atoms trapped in a optical lattice.

We begin providing some general definitions and concepts regarding quantum gases in optical lattices, our new arena to test anomalies. Then we analyze the Bose-Hubbard model, starting from the atomic limit. We focus our attention on the density anomaly in two (square lattices) and three dimensions (simple cubic lattices). Here we find some basic ingredients already familiar from our present discussion: phase transitions, the competing interaction scales and the two-states mixing process. We also show how a residual entropy mechanism ties them together. We extended the analysis to the complete parameter space, mapping the evolution of the density anomaly as the free parameters of the model are changed.

We also discuss in detail the occurrence of anomalous double peaks in the specific heat dependence on temperature. This feature, usually associated with a high geometrical frustration, can also be a consequence of a purely energetic competition. By employing self-energy functional calculations combined to finite-temperature perturbation theory, we propose a mechanism based on ground-state degeneracies expressed as residual entropies. A general decomposition of the specific heat in terms of all possible transitions between the system's eigenvalues provides an insight on the nature of each maximum. Furthermore, we address how the model parameters modify the structure of these peaks based on its spectral properties and atom-atom correlation function.

Finally, this text explores the theoretical foundations of the methods employed. We address a deep analysis of the Legendre transformation, and how it can be conceived as extremum principle. We discuss the geometrical implications in a general framework, which includes the techniques explored throughout this thesis. All details of our methodologies can be found in the Appendix sections, where the computational

codes are included. We conclude our work showing the perspectives of our research, which includes fermionic models and transport quantities, specially relevant due their technological applications.

Chapter 2

Quantum Simulators and Atoms in Optical Lattices

“Nature isn’t classical, dammit, and if you want to make a simulation of nature, you’d better make it quantum mechanical, and by golly it’s a wonderful problem, because it doesn’t look so easy.”

– Richard Feynman

The challenges posed in treating and decomposing fundamental mechanisms of complex systems turned the scientific community’s attention towards systems which could emulate them in clear and controllable fashions. In this context, the so called quantum simulators stand as a possible alternative, designing the quantum computation envisioned by Feynman towards the creation of a quantum system to simulate another [39, 40].

The first step forward in creating such highly controllable systems was the experimental realization of the Bose-Einstein condensate (BEC) [42–44], firstly predicted by Bose and Einstein in 1924. Bose-Einstein condensation is the effect in which particles with bosonic statistics can macroscopically occupy a single mode at low enough temperature, even in the absence of interactions. However, its experimental achievement was inaccessible until the recent days, due to the extremely low temperature needed to produce a condensate in a weakly interacting gas, which is in the microKelvin

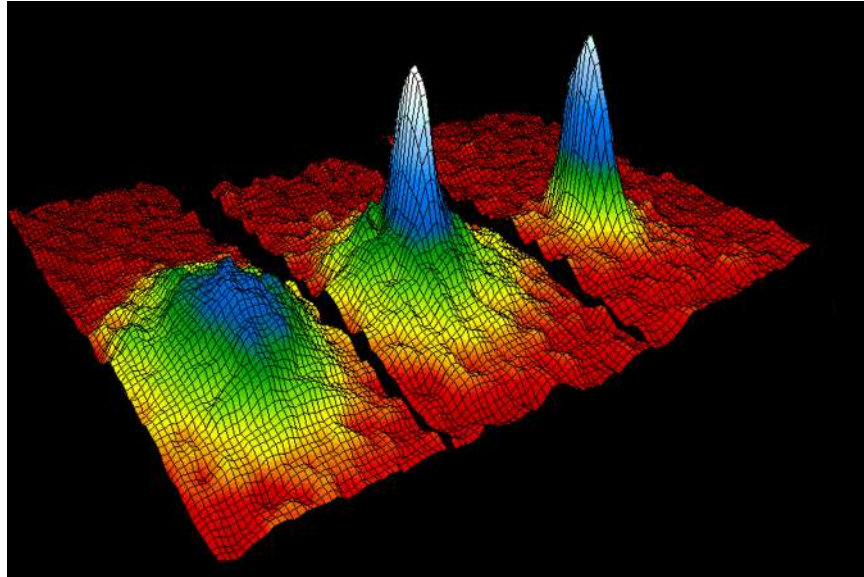


Figure 2-1: The momentum distribution for a gas of rubidium-87 atoms, attesting the discovery of a new phase of matter, the Bose–Einstein condensate. From the left to the right: (left) the system just before the appearance of a Bose–Einstein condensate; (center) just after the appearance of the condensate; (right) after further evaporation, leaving a sample of nearly pure condensate. Image from [42].

range. Combining laser cooling [45] and evaporative cooling techniques [46], different groups were able to experimentally create BEC (see Fig. 2-1) in dilute atomic vapors of rubidium [42], sodium [43], and lithium [44], respectively. For this achievement, Ketterle, Wieman and Cornell were awarded the Nobel prize in 2001.

The next decisive landmark towards simulating complex systems was the realization of ultracold atoms imprisoned in optical lattices by Greiner et. al [41]. In these optical lattices, counter propagating laser beams form a periodic potential generating literal crystal arrays of light trapping neutral cold atoms [47]. Due to the coupling of light and matter, the particles can be trapped in the potential wells. Depending on the intensity of the laser beams the particles can tunnel through the potential barrier to the neighboring lattice site whereas the interaction between the atoms can be controlled with Feshbach resonances [48]. Therefore, this system serves as a suitable arena to simulate physics of real materials [49–51]. However, compared to real materials, cold atom systems are much more flexible since many parameters can be finely tuned in a wide range. Since both the interaction and the mobility of the particles can be accurately controlled, this allows to go from a regime with weak to strong

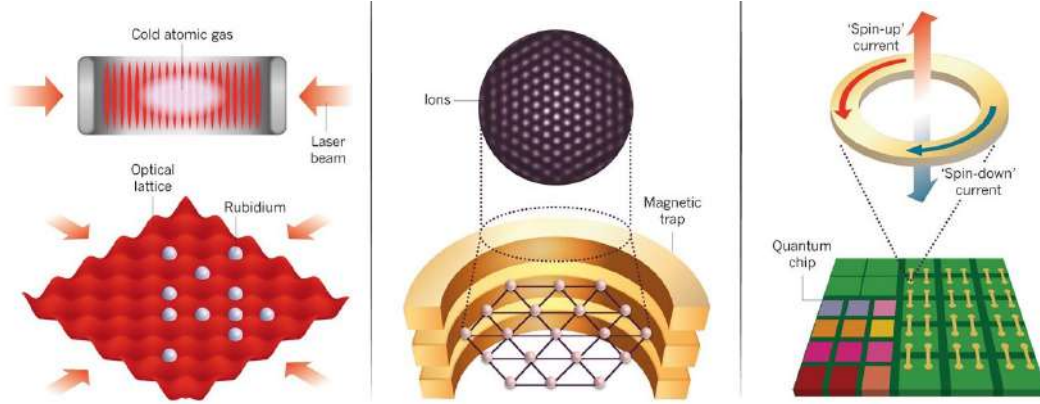


Figure 2-2: Different quantum simulator setups: optical lattices, trapped ions and superconducting loops. Extracted from Ref. [52].

interactions, therefore exploring possible phase transitions.

In recent years, several experimental setups have been proposed to simulate specific models, as illustrated in Fig. 2-2: the universe of quantum simulators is quite rich, ranging from neutral atoms in optical lattices to electrons in superconducting circuits and arrays of quantum dots to trapped ions [52, 53]. In particular, cold atomic gases confined into optical lattices have already proved to be a faithful simulator of typical condensed matter problems in a series of notable experiments which describe at different levels the Mott Insulator-superfluid transition of the Bose-Hubbard model [41, 54, 55]. Our idea is to use this experimental and theoretical accessibility, which is a problem in the case of water previously analyzed, to investigate the possible origins of its reported thermodynamic anomalies.

2.1 Cooling and Trapping Neutral Atoms

The ultracold atomic physics takes place at the lowest temperatures scales in the universe, which are achieved only by means of sophisticated cooling and trapping experimental techniques. Next we discuss briefly the methods employed in order to control and bring the atoms to such extreme conditions [56–62].

Laser cooling methods encompass several optical procedures used to slow the motion small particles, such as atoms or ions, in low-density gases. They have been

used to cool particles into the milliKelvin, microKelvin, and nanoKelvin ranges, depending on the applied procedure. The simplest method of laser cooling is known as *Doppler Cooling* and it was first suggested in 1975 by Theodor Hänsch and Arthur Schawlow [45] for free atoms and by David Wineland and Hans Dehmelt [63] for trapped ions.

If laser beam photons are emitted in the right frequency, compatible with the atomic energy levels, the particles in a gas of atoms will absorb photons, reaching an excited state. However, each atom will emit a photon with the same frequency in an arbitrary direction after a brief period of time, returning to a less excited state. Since photons also carry momentum, the atoms experience a recoil when they absorb and emit photons. Note that there is an imbalance in the process: the photons that are absorbed by the atoms and emitted by the laser all travel in the same direction, while the photons that the atoms emit travel in any arbitrary direction. This implies that, on average, the atoms feel a force in the direction away from the laser. Actually, naively hitting the particles with laser light is not the way to efficiently cool the particles. For example, if the particles are already moving slowly, then the average force from photon collisions would cause them to move more again, increasing the temperature of the sample. This is a step backwards as far as cooling the gas particles.

In order to avoid these effects, the laser is tuned to a frequency slightly lower than the resonant frequency of the atoms. This simple but clever idea takes advantage of the Doppler effect. Indeed, particles moving slowly or away from the laser beam will not absorb photons. In contrast, particles moving towards the laser will observe a Doppler shift in the frequency of the laser light; this effect enables these particles to absorb photons. As a result, such particles experience a force backwards away from the laser.

By arranging counter-propagating laser beams for each orthogonal direction, the atoms will experience a net force away from each laser. This limitation of three degrees of freedom reduces the particles' kinetic energy and thus cools the gas. During this process, the frequency of the laser light needs to be periodically reduced: as the atoms cool they will reach the point where not even those that are travelling towards a laser

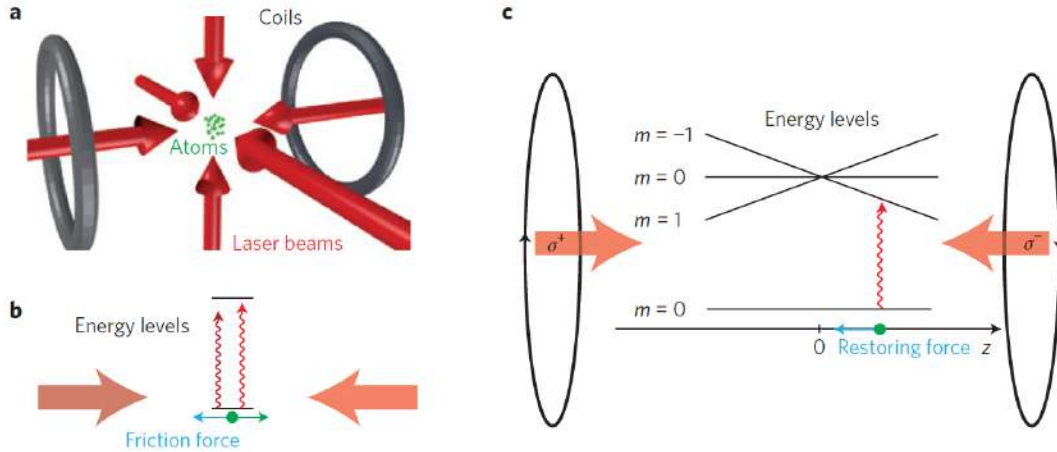


Figure 2-3: Principle of laser cooling and magneto-optical trapping. (a) Six-beam configuration for an optical molasses. Introducing a magnetic field gradient, using two coils in an anti-Helmholtz configuration, a restoring force appears that gathers the atoms around the zero of the magnetic field, creating a magneto-optical trap. (b) Basic principle of laser cooling along one direction of an optical molasses. The two beams are slightly red detuned from the atomic transition: then the atom scatters more photons from the right beam, which results in a friction force slowing down the atom. (c) Exploring the internal energy level structure of the atom, the radiation pressure force of the beams in the molasses can be spatially modulated by using circularly polarized light and the magnetic field gradient. Extracted from Ref. [65].

can readily absorb a photon. Because of this frictional force effect that dissipates the energy of the atom to the electromagnetic field, the configuration of oppositely directed laser beams is referred to as optical molasses [64].

An alternative to sweeping the laser frequency is sweeping the atomic resonances using a spatially varying magnetic field, through the *Zeeman slowing* process [66]. In the Zeeman slower, a laser beam propagates in the direction opposite that of the atomic beam, and the kinetic energy of the atoms is reduced by the radiation force produced by absorption of photons. As a result of the Doppler effect, the frequency of the atomic transition in the laboratory frame is not constant along its path, since the atomic velocity varies. However, by applying an inhomogeneous magnetic field tuned in order that the Doppler and Zeeman effects cancel, the frequency of the transition in the rest frame of the atom maybe held fixed.

The Doppler friction effect described previously is necessarily accompanied by fluctuations due to the fluorescence photons which are spontaneously emitted in random directions. Each emission process transfer to the atom a random recoil momentum

$\hbar k_L$, responsible for a momentum diffusion parametrized by a diffusion coefficient. As in ordinary Brownian motion, competition between friction and diffusion leads to a steady-state. A detailed analysis [56] shows that the temperature obtained with such a scheme is always larger than a certain limit T_D , called the Doppler limit. This limit is given by $k_B T_D = \hbar \frac{\Gamma}{2}$, where Γ is the natural width of the excited state. It is reached for a detuning $\delta = \omega_L - \omega_A = -\frac{\Gamma}{2}$, and its value is on the order of 100 μK for alkali atoms. Actually, the precision of experiments indicated that the temperature in optical molasses was much lower than expected [67]. This suggested that other laser cooling mechanisms, more powerful than Doppler cooling, are operating. One of these sub-Doppler techniques is known as *Sisyphus cooling*. It involves a polarization gradient, as generated by two counterpropagating linearly polarized laser beams with perpendicular polarization directions, and is therefore sometimes called polarization gradient cooling. This efficiently transfers kinetic energy into photon energy, and can cool atoms into the microKelvin range, a few times the recoil energy gained by the scattering of a single photon.

The temperatures reached by laser cooling are remarkably low, but they are not low enough to produce Bose–Einstein condensation in gases at the densities that are realizable experimentally. In the experiments performed to date, Bose–Einstein condensation of alkali gases is achieved by using the so-called *evaporative cooling* [46] after laser cooling. Such a technique was first proposed by Hess [68] in 1986 and its general physical effect is that, if particles escaping from a system have an energy higher than the average energy of particles in the system, the remaining particles are cooled. The process is analogous to the way a cup of hot coffee cools down by giving off the most energetic molecules as steam. As the energetic atoms are removed from the trap, collisions readjust the remaining atoms into a lower temperature thermal distribution as shown in Fig. 2-6. In some versions, atoms are “evaporated” via a forced spin-flip and their subsequent repulsion from the trapping region. In a magnetic trap, the most energetic atoms sample the largest magnetic fields and thereby experience the largest Zeeman shifts. By tuning an radio frequency (RF) field to be resonant with atoms at relatively large fields, it is possible to remove a specific high-energy portion

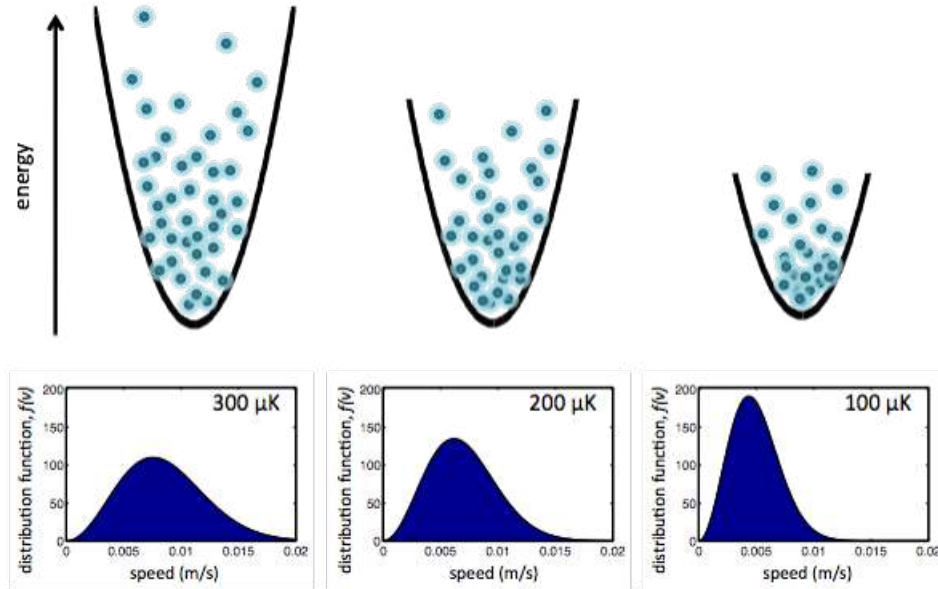


Figure 2-4: Schematic image of evaporative cooling extracted from Ref. [69]. Evaporative cooling is performed in a magnetic trap where the height of the trapping potential is reduced in order to let the hottest atoms escape. The remaining atoms then thermalize at a lower temperature.

of the trapped atoms and leave the low-energy portion unaltered. As a result of this coupling, the height of the top of the trapping potential becomes a function of the RF frequency. After the remaining atoms rethermalize to a lower temperature, the RF frequency can be decreased and the process repeated. Trapped atoms have been evaporatively cooled to the nanoKelvin scale by precisely controlling the removal of the energetic atoms and making traps with very good thermal isolation.

As already mentioned, the reported cooling techniques are also associated to specific and appropriate trapping methods. The most common classes of traps for neutral atoms comprehends magnetic, radiation pressure, and optical dipole traps. *Magnetic traps* explore the state-dependent force on the magnetic dipole moment in an inhomogeneous field. An atom with magnetic moment $\boldsymbol{\mu}$ can be confined by an inhomogeneous magnetic field \mathbf{B} because of the interaction between the moment and the field, according to $-\boldsymbol{\mu} \cdot \mathbf{B}$. This yields a force expressed by $\mathbf{F} = \nabla(\boldsymbol{\mu} \cdot \mathbf{B})$, capable of trapping the atoms. The general features of the magnetic fields of a large class of possible traps has been presented in the literature [70]. Indeed, such traps represent excellent tools for evaporative cooling and Bose-Einstein condensation. In the context

of neutral atoms they were firstly reported in 1985 [71] using a magnetic quadrupole magnetic field formed by two opposed, separated, coaxial current loops.

The most widely used trap for neutral atoms is a hybrid, employing both optical and magnetic fields, to make a *magneto-optical trap* (MOT) first demonstrated in 1987 [72]. They use an inhomogeneous magnetic field to produce a position-dependent scattering force. The magnetic field Zeeman-shifts transitions towards or away from resonance with red-detuned, counter-propagating, oppositely circularly polarised laser beams. The presence of the quadrupole magnetic field causes a Zeeman shift in the atomic internal magnetic levels, which increases with the radial distance from the centre of the trap. Hence, as an atom moves away from the centre of the trap, the atomic resonance is shifted closer to the frequency of the laser light, and the atom becomes more likely to scatter a photon, being impulsed towards the centre of the trap. The direction of the impulse is given by the polarization of the light, either left or right handed circular, providing different interactions with the different shifted levels. The magnetic field and laser polarisations are such that atoms are pushed back to the centre after displacement in any direction. The nonzero value of the detuning provides cooling of the trapped atoms, according to the mechanisms outlined previously.

The radiation-pressure and the optical dipole traps exploit the fact that light can exert a radiative force on an atom because photons carry momentum. Such mechanism happens either incoherently by absorption and emission of photons as in radiation-pressure traps or coherently as in optical dipole ones. Incoherent interaction exerts the scattering force. In *radiation-pressure traps* [73, 74] one uses three orthogonal standing wave laser beams to create an optical molasses, which is used to cool down the atoms. The narrower the atomic resonance the better the red detuned standing laser beam can cool the atoms. These traps cause naturally very strong dissipation, thus cool quite effectively, but lead to unstable trap dynamics. On the other hand, the *optical dipole traps* [75, 76] use coherent interactions of the atoms with far detuned laser light. The laser field polarizes the atom and the polarized atom experiences a force in the inhomogeneous electromagnetic field of the incident light

field. In these traps the potential is nearly conservative with only very weak influence from spontaneous photon scattering. Based on such properties, optical lattices can be formed by the periodic modulation of the light intensity in a laser standing wave. In the following we dedicate a brief time to discuss such optical dipolar interactions which are protagonists of the systems we investigate.

2.2 Optical Lattices in a Nutshell

Neutral atoms interact with light in both conservative and dissipative ways. The dissipative portion of the interaction arises due to the absorption of photons followed by spontaneous emission. It implies a dissipative force on the atoms caused by the momentum transfer of the absorbed and spontaneously emitted photons. As seen, this mechanism is widely used for laser cooling and magneto optical traps. Alternatively, the conservative component results from the interaction of the light field with the induced dipole moment of the atom. This interaction causes a shift in the potential energy, called the ac-Stark shift. For large detunings of the light compared to the atomic resonances, spontaneous emission processes can be neglected and the energy shift can be used to create a conservative trapping potential for neutral atoms. By shining a spatially modulated light field onto a cloud of atoms an energy landscape can be formed, where the local potential energy is proportional to the local light intensity.

In order to examine the ac-Stark effect of an oscillating electric field on an atom we employ a semiclassical treatment of the radiation field and assume the atom presents only two relevant energy levels, an excited state and a ground state. This approach comprehends the combined system "atom plus photons", known as the dressed state picture [77, 78]. The unperturbed Hamiltonian of the atom may be expressed simply as $H_A = \hbar\omega_A |e\rangle \langle e|$, where ω_A is the atomic transition frequency. Assuming the wavelength of the light is large compared to the atomic dimensions (the dipole approximation), the interaction Hamiltonian reads as $H_I = -\mathbf{d} \cdot \mathbf{E}$, where \mathbf{d} is the dipole operator and $\mathbf{E}(\mathbf{x}, t) = \mathbf{E}(\mathbf{x}) \cos(\omega_L t)$ is the electric field oscillating with frequency

ω_L . Hence, the total Hamiltonian $H = H_A + H_I$ can be written as

$$H = \hbar\omega_A |e\rangle \langle e| - \hbar\Omega(\mathbf{x}) \cos(\omega_L t) (|g\rangle \langle e| + |e\rangle \langle g|) \quad (2.1)$$

where $\Omega(\mathbf{x}) = \langle e| \mathbf{d} |g\rangle \cdot \mathbf{E}(\mathbf{x})/\hbar$ is the Rabi frequency. In a far detuned situation, we can simplify it even further according to the rotating wave approximation

$$H = -\hbar\delta |e\rangle \langle e| - \frac{\hbar\Omega(\mathbf{x})}{2} (|g\rangle \langle e| + |e\rangle \langle g|) \quad (2.2)$$

with $\delta = \omega_L - \omega_A$. Since we assume the laser to be far detuned from the atomic transition, the population of the ground state is not significantly reduced through optical excitations. Therefore, for large detunings ($|\delta| \gg \Omega$), the corresponding ground state energy shift reads as

$$\Delta E_g = \frac{\hbar\Omega^2(\mathbf{x})}{4\delta}. \quad (2.3)$$

As the atom is practically always in the ground state, the potential energy is nothing but the shift of the relevant atomic internal state induced by the electric field

$$\mathcal{V}_{dip}(\mathbf{x}) = \frac{\hbar\Omega^2(\mathbf{x})}{4\delta} \propto \frac{I(\mathbf{x})}{\delta}, \quad (2.4)$$

where I is the intensity of the electric field. From this result, the energy shift is positive for blue-detuned laser light $\delta > 0$ ($\omega_L > \omega_A$) and the atoms are repelled in the regions of maximal field intensity. On the other hand, for red detuned laser light $\delta < 0$ ($\omega_L < \omega_A$) the atoms are attracted toward the points of maximal light intensity. The force originated from this potential is simply $\mathbf{F}_{dip} = -\nabla\mathcal{V}_{dip}$, proportional to the gradient of the intensity.

Until now we did not include the possibility of spontaneous emission of photons. The atomic excited state can get a natural width Γ , which is also the rate at which a photon is spontaneously emitted from such state. Mathematically, this is described by an imaginary part, $-i\hbar\frac{\Gamma}{2}$, added to the energy level. Within our two level approach

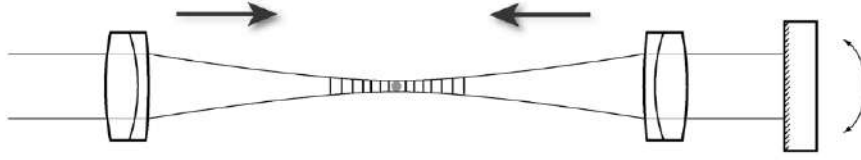


Figure 2-5: Two counter-propagating Gaussian laser beams, forming a periodic intensity profile due to the interference of the two laser field [47].

we obtain the correction

$$\Delta E_g = \frac{\hbar\Omega^2(\mathbf{x})}{4\delta} - i\hbar\frac{\Gamma}{8}\left(\frac{\Omega(\mathbf{x})}{\delta}\right)^2, \quad (2.5)$$

Hence, not only the sign of the detuning is relevant but also its magnitude. Indeed, the scattering rate becomes

$$\Gamma_{sc}(\mathbf{x}) = \frac{\Gamma}{4}\left(\frac{\Omega(\mathbf{x})}{\delta}\right)^2. \quad (2.6)$$

This last result shows that incoherent light-atom interactions which lead to dissipation are negligible when the detuning is large. In order to create a conservative potential during the lifetime of the experiment the laser detuning for a dipolar trap should be chosen as large as possible, within the available laser power in order to minimize inelastic scattering processes.

The presented analysis shows that spatial variations of light intensity provide spatial potential energy variations for the atoms. Therefore, one can create various potential energy surfaces. For example, in order to form a periodic potential one can use counter-propagating laser beams. A simple cubic lattice can be formed by superimposing three standing waves orthogonal to each other, with mutually orthogonal polarisations. The beam pairs creating the standing wave in the x , y and z directions have typically a Gaussian shape with waists w_x, w_y and w_z . Then the trapping potential for a red detuned lattice can be expressed as

$$\mathcal{V}(\mathbf{x}) = -V_x \sin^2(kx) e^{-2\frac{y^2+z^2}{w_x^2}} - V_y \sin^2(ky) e^{-2\frac{x^2+z^2}{w_y^2}} - V_z \sin^2(kz) e^{-2\frac{x^2+y^2}{w_z^2}}, \quad (2.7)$$

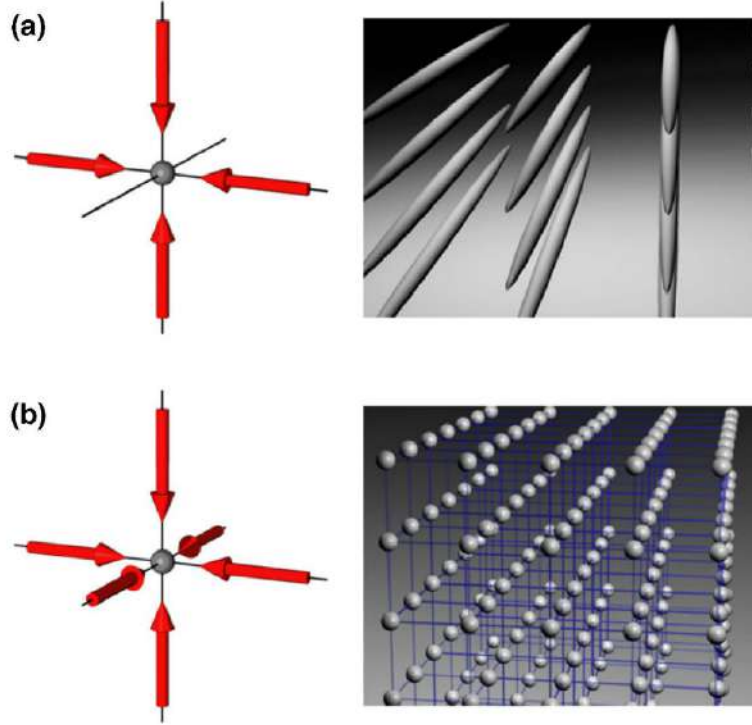


Figure 2-6: Two-dimensional (a) and three-dimensional (b) optical lattice potentials formed by superimposing two or three orthogonal standing waves [47].

where V_x , V_y and V_z are the potential depths. Around the center of the trap, for distances much smaller than the beam waist, such potential can be regarded as the sum of a periodic part and an external harmonic confinement

$$\mathcal{V}(\mathbf{x}) = -V_x \sin^2(kx) - V_y \sin^2(ky) - V_z \sin^2(kz) + \frac{m}{2}(\omega_x^2 x^2 + \omega_y^2 y^2 + \omega_z^2 z^2), \quad (2.8)$$

with ω_x , ω_y and ω_z the effective trapping frequencies. If we neglect the effects of the harmonic confinement, the standing wave interference pattern yields a periodic sinusoidal lattice potential

$$\mathcal{V}(\mathbf{x}) = -V_0 (\sin^2(kx) + \sin^2(ky) + \sin^2(kz)) , \quad (2.9)$$

in a homogeneous setup with V_0 the corresponding potential depth. This particular three dimensional configuration will be considered in our analysis of the thermodynamics of the Bose-Hubbard model. The confinement effects will be introduced via

local density approximation.

So far we have reviewed some basic aspects in the area of ultracold atomic physics, comprehending cooling and trapping methods, the formation of a BEC and the creation of optical lattices. Our next step is to outline how we can theoretically describe the physics of bosons in these environments. Here we introduce the famous Bose-Hubbard.

2.3 Optical Lattices and the Bose-Hubbard model

The Bose-Hubbard model is a quantum many-particle lattice model. It was first introduced by Gersch and Knollman [79] as a simple model to study the competition between thermal and quantum fluctuations with the localization of particles due to their high density and interaction strength. The model was recovered in 1989 by Fisher et al. [80] and its relevance as a theoretical model suitable to describe real systems was shown by Jaksch et al. [81]. It turns out that it is particularly well suited model for describing experiments with cold atomic gases in optical lattices. Below we sketch how to represent a general, many-body problem in periodic potential in a basis of localized states.

We consider a second-quantized form of the Hamiltonian of a many-particle system in a periodic potential according to Eq.(2.9)

$$\mathcal{V}(\mathbf{x}) = -\mathcal{V}_0 \sum_{i=1}^d \sin^2(k_i x_i), \quad (2.10)$$

with \mathcal{V}_0 the amplitude, related to the light intensity, d is the dimensionality of the system ¹, and $k = \frac{2\pi}{\lambda}$ are wave-vectors of the light along different directions. Explicitly, we have

$$\begin{aligned} H = & \int d^d \mathbf{x} \psi^\dagger(\mathbf{x}) \left(-\frac{\hbar^2}{2m} \nabla^2 + \mathcal{V}(\mathbf{x}) \right) \psi(\mathbf{x}) + \\ & + \frac{1}{2} \int d^d \mathbf{x} d^d \mathbf{x}' U(|\mathbf{x}' - \mathbf{x}|) \psi^\dagger(\mathbf{x}) \psi^\dagger(\mathbf{x}') \psi(\mathbf{x}') \psi(\mathbf{x}), \end{aligned} \quad (2.11)$$

¹our analysis employs $d = 3$, a simple cubic lattice.

where m is the mass of the particle and U is the two-particle interaction potential, considered to be spherically symmetric. Furthermore, $\psi(\mathbf{x})$ is a bosonic operator field satisfying the commutation relations

$$[\psi(\mathbf{x}), \psi^\dagger(\mathbf{x}')] = \delta(\mathbf{x} - \mathbf{x}') \quad (2.12)$$

and

$$[\psi(\mathbf{x}), \psi(\mathbf{x})] = 0 . \quad (2.13)$$

The eigenfunctions of the non-interacting problem are in the form of Bloch waves $\phi_{\nu,\mathbf{k}}(\mathbf{x})$, with ν the corresponding band. Turning attention towards the interaction, the Wannier basis functions, orthogonal and centered at the lattice sites, are suitable to describe the real space according to

$$\chi_{\nu,i}(\mathbf{x}) = \frac{1}{2\pi} \int_{BZ} d^d \mathbf{k} e^{i\mathbf{k} \cdot \mathbf{R}_i} \phi_{\nu,\mathbf{k}}(\mathbf{x}) , \quad (2.14)$$

where \mathbf{R}_i are lattice coordinates and the integration is performed over the first Brillouin zone (BZ). Expressing the bosonic field in such basis, we obtain

$$\psi(\mathbf{x}) = \sum_{\nu,i} \chi_{\nu,i}(\mathbf{x}) b_{\nu,i} ; \quad (2.15)$$

with $b_{\nu,i}$ representing the annihilation operator of a particle from the band ν at the site R_i . Both operators $b_{\nu,i}$ and $b_{\nu,i}^\dagger$ satisfy the canonical commutation relations as follows

$$[b_{\nu,i}, b_{\nu',i'}] = \delta_{i,i'} \delta_{\nu,\nu'} . \quad (2.16)$$

Substituting this representation for the bosonic field in Eq. (2.15), the Hamiltonian

takes the form

$$H = - \sum_{\substack{i,j \\ \mu,\nu}} J_{ij}^{\mu,\nu} b_{\nu,i}^\dagger b_{\mu,j} + \frac{1}{2} \sum_{\substack{i,j,k,l \\ \nu_1,\nu_2,\nu_3,\nu_4}} U_{ijkl}^{\nu_1\nu_2\nu_3\nu_4} b_{\nu_1,i}^\dagger b_{\nu_2,j}^\dagger b_{\nu_3,k} b_{\nu_4,l}, \quad (2.17)$$

where

$$J_{ij}^{\mu,\nu} = \int d^d \mathbf{x} \chi_{\mu,i}^*(\mathbf{x}) \left(-\frac{\hbar^2}{2m} \nabla + \mathcal{V}(\mathbf{x}) \right) \chi_{\nu,j}(\mathbf{x}) \quad (2.18)$$

is the hopping matrix element and

$$U_{ijkl}^{\nu_1\nu_2\nu_3\nu_4} = \int d^d \mathbf{x} U(|\mathbf{x}' - \mathbf{x}|) \chi_{\nu_1,i}^*(\mathbf{x}) \chi_{\nu_2,j}^*(\mathbf{x}') \chi_{\nu_3,k}(\mathbf{x}') \chi_{\nu_4,l}(\mathbf{x}) \quad (2.19)$$

is the interaction energy matrix element. Indeed, this is a quite general Hamiltonian. Due to the typical low temperatures considered, only the lowest energy states are populated by bosons and, therefore, one can disregard all but one Bloch band, accordingly. For deep lattices, the overlap of the Wannier functions is only relevant between first neighbors; hence, $J_{ij} \neq 0$ only in such cases. Furthermore, for a short ranged potential, one can discard all non-local interaction terms. These considerations combined lead to a much simpler yet complex Hamiltonian:

$$H = -J \sum_{\langle i,j \rangle} b_i^\dagger b_j + \frac{U}{2} \sum_i b_i^\dagger b_i^\dagger b_i b_i. \quad (2.20)$$

The parameter U represents the (typically repulsive) interaction of bosons on the same lattice site. More precisely, it corresponds to the atom-atom s-wave scattering process, which can be regarded as an effective contact interaction of the form $U(\mathbf{r}) = g\delta(\mathbf{r})$, with a coupling constant $g = 4\pi\hbar^2 a_s/m$ depending on the s-wave scattering length a_s and mass m of the atoms. By employing the local Wannier states $w(\mathbf{r})$, the term U is expressed through the matrix element

$$U = g \int d\mathbf{r} |w(\mathbf{r})|^4. \quad (2.21)$$

On the other hand, the parameter J indicates the hopping amplitude, a kinetic term involving the probability of tunneling between first neighbor sites. Explicitly, it is quantified as the following overlapping integral over adjacent Wannier functions

$$J = - \int d\mathbf{r} w(\mathbf{r} - \mathbf{r}_i) \left(-\hbar^2 \frac{\nabla^2}{2m} + V_L(\mathbf{r}) \right) w(\mathbf{r} - \mathbf{r}_j). \quad (2.22)$$

Therefore, the Bose-Hubbard model terms U and J can be related to the experimental parameters λ , a_s and V_0 through Eqs. (2.21) and (2.22) [47, 82], numerically calculating the band structure and obtaining the Wannier states [83, 84]. These prescriptions allow us to express temperatures in kelvin units and the lattice depth in terms of the recoil energy $E_r = \hbar^2 \pi^2 / 2ma^2$, according to the values of U and J chosen. It is thus possible to consider our theoretical results within the context of a specific optical trap implementation, from which we select a gas of rubidium-87 atoms in simple cubic [41, 54] and square optical lattices [85, 86]. This is our starting point for the next chapter.

Chapter 3

The Bose-Hubbard Model and the Density Anomaly

“Not only is the Universe stranger than we think, it is stranger than we can think.”

– Werner Heisenberg

Our investigation of the thermodynamics concerning the Bose-Hubbard model starts from the atomic limit. In this case, waterlike anomalies arise in a quite natural fashion, generated by a clear mechanism merging phase transitions and zero point entropies. Later, we include the hopping parameter in order to provide a complete analysis of the model.

As derived in the previous chapter, the dynamics of itinerant bosons in a lattice is governed by the Bose-Hubbard Hamiltonian¹

$$H = -J \sum_{\langle i,j \rangle} b_i^\dagger b_j + \frac{U}{2} \sum_i n_i(n_i - 1) - \mu \sum_i n_i, \quad (3.1)$$

where b_i^\dagger , b_i , n_i designates the bosonic creation, annihilation and number operators at site i , respectively; μ is the chemical potential. The parameter U represents the on site interaction (typically repulsive, taking positive values) and J accounts for the

¹We include the chemical potential as a part of the Hamiltonian in order to simplify the notation.

hopping amplitude, a kinetic term involving the probability of tunneling between first neighbor sites.

3.1 Overview

The Bose-Hubbard model Hamiltonian as presented has two distinct ground states depending on the strength of the interaction U compared to the hopping term J : a *superfluid* and a *Mott insulator* phase (which gives rise to a normal phase for finite temperatures).

Superfluid Phase

If the tunneling matrix element is much larger than the onsite interaction, each atom is delocalized over the lattice and the many-body ground state can be expressed as a product state of zero quasi-momentum Bloch waves as follows

$$|\Psi_{SF}\rangle \propto \left(\sum_{i=1}^L b_i \right)^N |0\rangle, \quad (3.2)$$

considering N bosons and L lattice sites. The system can be described by a macroscopic wave function. Hence a macroscopic phase is well defined on each lattice site and the system is superfluid. This gives rise to a non zero expectation value of the field operator $\phi = \langle b \rangle$, the condensed order parameter. In the limit $N, L \rightarrow \infty$ at fixed density N/L , the state (3.2) becomes indistinguishable in a local measurement from a coherent state which factorizes into a product of local Poissonian states. Therefore the many-body state on a lattice site is a superposition of different atom numbers, following a Poissonian atom number distribution, as illustrated in Fig. 3.1. Despite the certainty in momentum space, the atom number per site is uncertain.

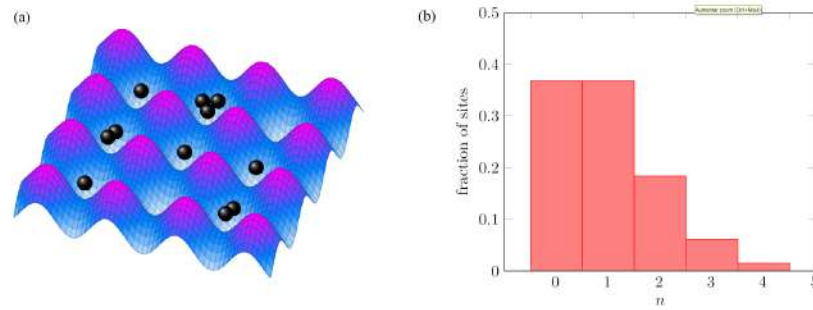


Figure 3-1: (a) Representation of the superfluid ground state ($U = 0$), with a Poissonian atom number statistics described in (b).

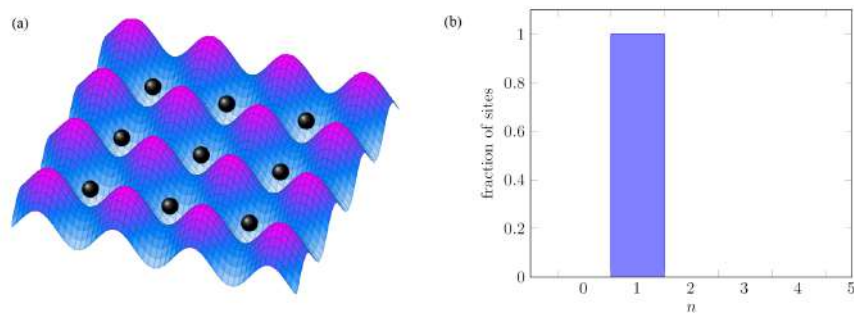


Figure 3-2: (a) Representation of the Mott insulator ground state ($J = 0$) with commensurate filling of the lattice, and Fock states in the atom number on each site (b).

Mott Insulator Phase

On the other side, if the interaction is dominant over the hopping, then fluctuations in the number of atoms on a single site become energetically costly. The many-body ground state is then a product of local Fock states in the atom number for each lattice. In this so called *atomic limit*, the ground state for a commensurate filling of n atoms per lattice site is simply given by

$$|\Psi_{MI}\rangle \propto \prod_{i=1}^L (b_i^\dagger)^n |0\rangle, \quad (3.3)$$

Each atom is localized to a lattice site and the number density is determined by the total number of particles or the chemical potential, see Fig. 3.1. In contrast to the certainty in the position space, no macroscopic phase coherence is prevalent in the system, with zero expectation value $\phi = \langle b \rangle = 0$.

The competition between such terms generates a ground state phase diagram as exhibited in Fig. 3.1, which shows the boundary between the Mott insulating phase and the superfluid in terms of the tunneling coupling J and the chemical potential μ , in units of the onsite interaction U . When the strength of the interaction relative to the tunnelling is modified, the system may undergo a quantum phase transition [87] from the superfluid ground state to the Mott insulator ground state. Experimentally, such transitions were firstly observed by Greiner et al. [41], using rubidium-87 atoms trapped in a simple cubic optical lattice. Fig. 3.1 represents the time of flight images taken from these experiments. The sequence presents the collapse of the Bose-Einstein as the lattice depth is increased until the Mott insulator phase is reached.

Once we know the basic ingredients of this model, we are ready to explore its thermodynamics in the following sections.

3.2 Atomic Limit: where the anomaly is born

Here we analyze the thermodynamics of the atomic limit by setting $J = 0$. With this choice, tunneling between different sites is forbidden and the superfluid phase,

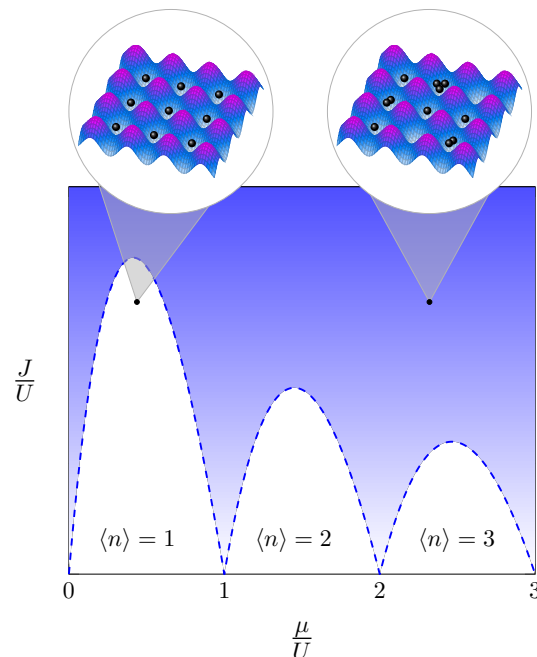


Figure 3-3: Schematic representation of the Bose-Hubbard model ground state phase diagram, for bosons in a simple cubic lattice. The continuous superfluid/Mott insulator phase transition is shown as the blue dashed line.

which is composed by particles in a delocalized state, does not exist. Even in this limit, the model presents regions of waterlike anomalous density behavior, as we will be shown. In the context of quantum gases on optical traps this limit correspond to a strong trapping field. Noting that in this regime the Hamiltonian is becomes composed by single-site hamiltonians, \hat{H}_i , which are diagonalized with number operators eigenvectors $\hat{n}_i |n_i\rangle = n_i |n_i\rangle$. Hence the energy eigenvalue of a single site with occupation $n_i = n$ becomes

$$\epsilon_n = \frac{U}{2}n(n-1) - \mu n, \quad (3.4)$$

and since lattice sites are *distinguishable*, quantum statistics end up identical to Boltzmann statistics [88].

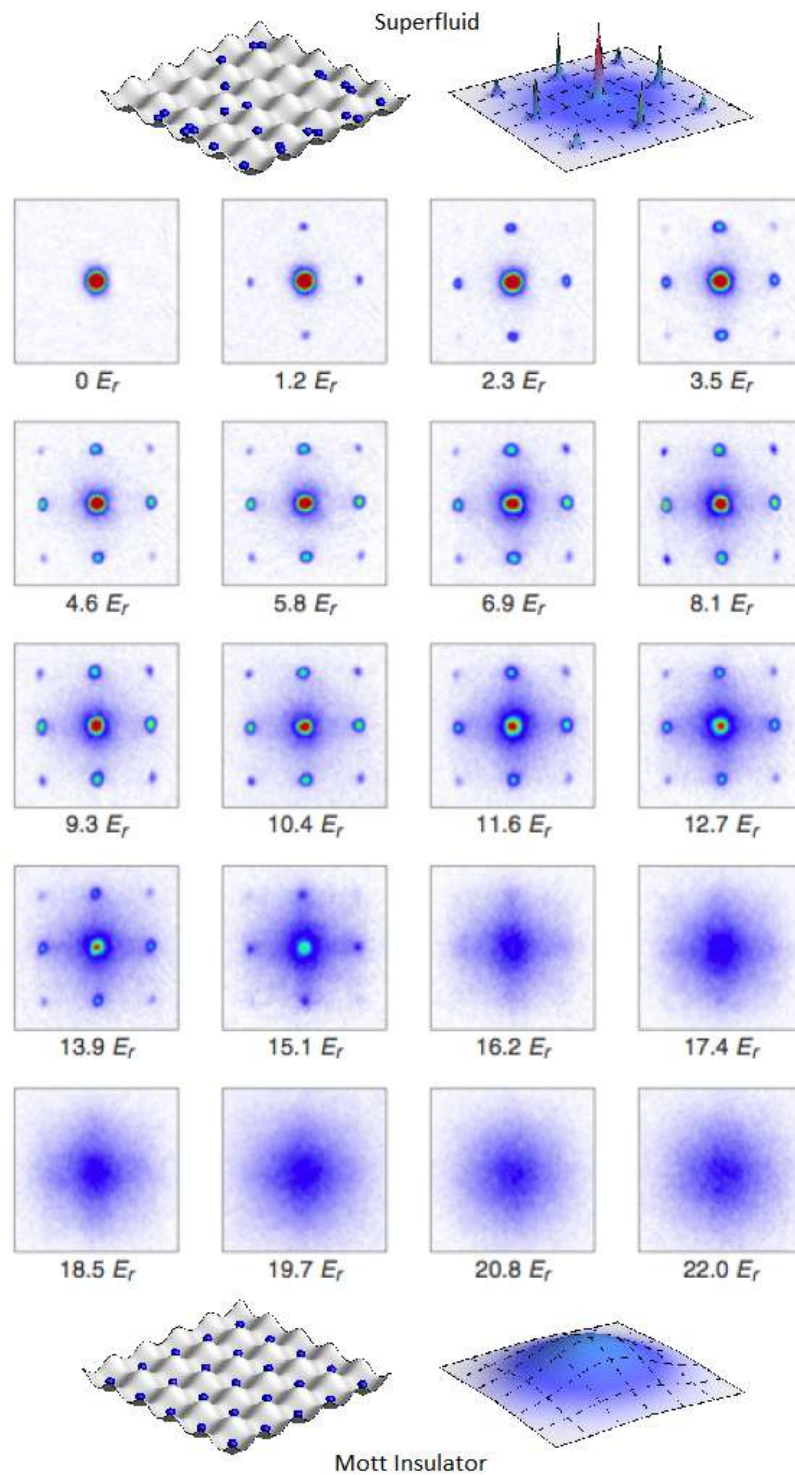


Figure 3-4: Time of flight absorption images of multiple matter wave interference patterns adapted from Greiner's experiment [41]. These were obtained after suddenly releasing the atoms from an optical lattice potential with different potential depths V_0 after a time of flight of 15 ms.

The Ground State Phase Transitions

We proceed by investigating the ground state phase transitions (GSPT). At $T = 0$ and a given μ , the grand canonical free energy $\Omega = V\omega$ (volume $V = v_0L$, with v_0 defining the lattice cell volume) is simply the result of the minimization procedure $\omega(T = 0, \mu) = \min_n \epsilon_n$. Therefore $\omega(T = 0, \mu) = \epsilon_n$ for n satisfying $(n-1)U < \mu < nU$. This implies that GSPT occur whenever the chemical potential hits an integer value of the on site interaction, where a coexistence between successive occupation states n and $n+1$, called Mott Insulators, takes place. This analysis yields the critical chemical potentials $\mu_n = nU$ and the corresponding critical pressures $P_n v_0 = n(n+1)\frac{U}{2}$.

Calculating the densities that are observed in the GSPT at fixed chemical potential in the μVT ensemble is simple and requires assuming that states n and $n+1$ are equal *a priori*. The result is $v_0\rho_n = n+1/2$ and will not be the same observed at fixed pressures in the NPT ensemble, since the pressure is a non differentiable function of μ at the GSPT. These numbers can be obtained exactly within a two states description as will be explained in the Appendix A.

Thermodynamics

The grand canonical partition function of the system can be expressed as:

$$Z(T, V, \mu) = \left(\sum_{n=0}^{\infty} e^{-\beta\epsilon_n} \right)^L, \quad (3.5)$$

where $\beta = 1/k_B T$, with T being the temperature and k_B the Boltzmann constant. Considering that $Z = e^{-\beta\Omega}$, the fundamental relation for the grand thermodynamic potential Ω becomes: The grand canonical partition function of the system can be expressed as:

$$\Omega(T, V, \mu) = -k_B T V \ln \left[\sum_{n=0}^{\infty} e^{-\beta\epsilon_n} \right]. \quad (3.6)$$

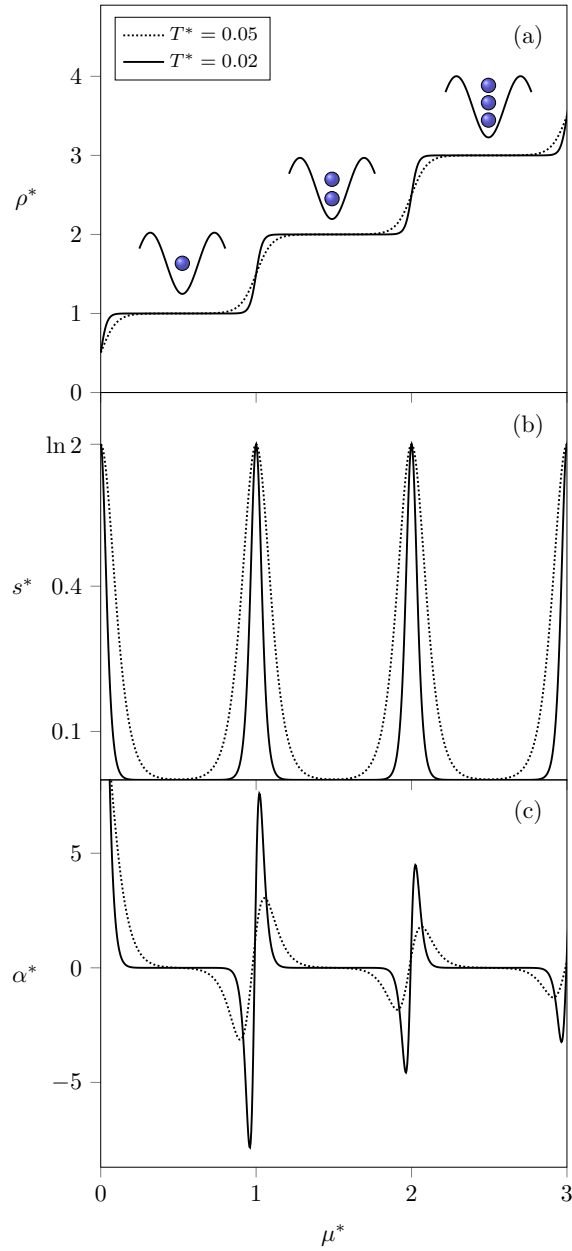


Figure 3-5: (a) Density, (b) entropy, and (c) thermal expansion coefficient as a function of the chemical potential at fixed temperatures.

Pressure can be obtained using $\Omega = -PV$ and one can calculate density and entropy per site, employing the standard expressions:

$$\rho(T, \mu) = \frac{N}{V} = -\frac{1}{V} \left(\frac{\partial \Omega}{\partial \mu} \right)_T, \quad (3.7)$$

and

$$s(T, \mu) = \frac{S}{V} = -\frac{1}{V} \left(\frac{\partial \Omega}{\partial T} \right)_\mu. \quad (3.8)$$

For the purpose of comparing our results with other works on the literature of the Bose-Hubbard model, it will be important to write the thermal expansion coefficient in terms of appropriate variables. Through a Jacobian transformation [89, p. 364] one obtains:

$$\begin{aligned} \alpha &= \frac{1}{V} \left(\frac{\partial V}{\partial T} \right)_{P,N} = -\frac{1}{\rho} \left(\frac{\partial \rho}{\partial T} \right)_P \\ &= \alpha_\mu + \frac{1}{\rho} \left(\frac{\partial \rho}{\partial \mu} \right)_T \frac{\left(\frac{\partial \Omega}{\partial T} \right)_\mu}{\left(\frac{\partial \Omega}{\partial \mu} \right)_T}, \end{aligned} \quad (3.9)$$

where α_μ was defined as:

$$\alpha_\mu(T, \mu) = -\frac{1}{\rho} \left(\frac{\partial \rho}{\partial T} \right)_\mu. \quad (3.10)$$

Expressions (3.7)-(3.10) will be calculated in the μVT ensemble and converted to the NPT ensemble whenever necessary.

Results and discussions

Before proceeding let us note that variables are reduced in terms of U , v_0 and k_B , as $T^* = k_B T/U$, $\mu^* = \mu/U$ and $P^* = P v_0/U$. Our analysis starts by comparing density, entropy and thermal expansion α as a function of chemical potential at fixed temperature (Fig. 3.2). Also note that α is the same used in the fluid literature and was calculated from (3.9). Fig. 3.2 (a) shows that the density is highly sensitive

to changes in the chemical potential around $\mu_n^* = n$, for integer n , and that this response becomes sharper at lower temperatures, approaching true phase transition discontinuities in the $T \rightarrow 0$ limit. This confirms that μ_n^* are indeed the critical values of the zero-temperature GSPT.

On Fig. 3.2 (b) entropy is shown to develop maximum values exactly at the critical chemical potentials μ_n^* . As temperature decreases entropy goes to zero except at the transition points, where it becomes sharper and turn into a residual entropy in the limit $T \rightarrow 0$. Note that the maximum equals $s_n^* = \ln 2$ which is expected for a two state mixture. From the Maxwell relation

$$\left(\frac{\partial S}{\partial P}\right)_T = -\left(\frac{\partial V}{\partial T}\right)_P = -V\alpha, \quad (3.11)$$

it follows that α is negative (positive) whenever entropy increases (decreases) with pressure². Thus, an entropy maximum introduces an oscillation in thermal expansion α , with its amplitude increasing as temperature is lowered according to Fig. 3.2 (c). The oscillations evolve to a peculiar double divergence with $\alpha \rightarrow -\infty (+\infty)$ as $\mu \rightarrow \mu_n^- (\mu_n^+)$. Indeed, such mechanism establishes a quite general connection between GSPT, residual entropy and density anomaly. The multiple configurations remaining from each critical point produce a macroscopic zero point entropy. When temperature is raised, the possibility of the system accessing these states can induce an anomalous behavior depending on the chosen external fields.

Next we discuss the emergence of TMD lines in the phase diagram of the model. On Fig. 3.2 their *loci*, corresponding to $\alpha = 0$, are shown in a range of pressures covering two regions where density increases with temperature ($\alpha < 0$). As in our previous studies [90, 91], TMD lines are emanating from GSPT (filled circles) and draws a curve enclosing a region of the phase diagram starting and ending at $T = 0$. The endpoint of these lines can be obtained by analyzing enthalpy variations for adding or excluding a particle in the system. Even though we have chosen to show two TMD lines starting from transitions at $P_1^* = 1$ and 3, the model exhibits an

²The chemical potential monotonically increases with pressure.

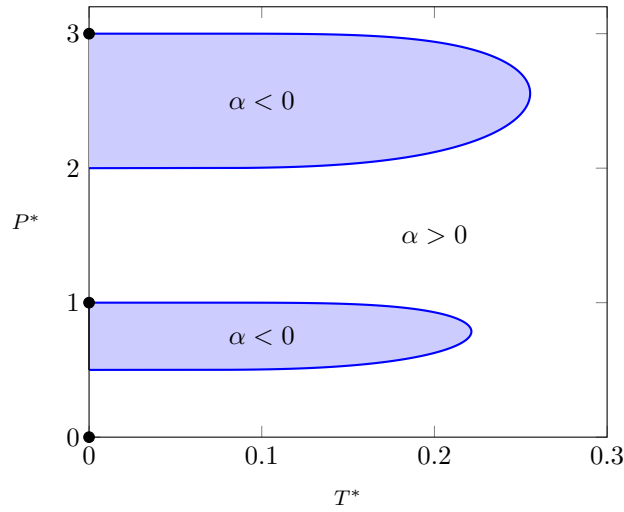


Figure 3-6: Pressure vs. temperature phase diagram with GSPT marked with filled circles and continuous lines representing the TMD. The anomalous states are represented by the filled areas.

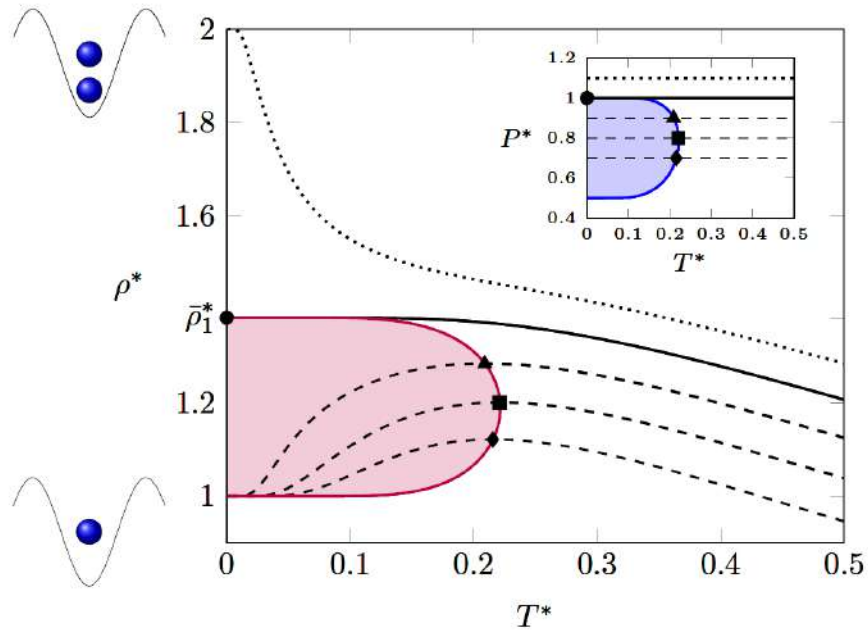


Figure 3-7: Density as a function of temperature for fixed pressures. Density increases with temperature (region filled in purple) and presents a maximum (highlighted points over the continuous purple curve) for pressures slightly below (dashed lines) the critical pressure $P_1^* = 1$ (continuous black line). Density decreases monotonically with temperature for pressures above (dotted line) the critical value. The inset contains the $P \times T$ phase diagram featuring a TMD line and the pressures chosen.

infinite number of GSPT and also an infinite number of regions in the $P \times T$ phase diagram where $\alpha < 0$.

A more detailed view on the density behavior is presented in Fig. 3.2, where it is plotted against temperature at pressures slightly above, below and equal to the critical value $P_1^* = 1$. It is interesting to observe that density increases with temperature below P_1^* , reaching a maximum value and then decreasing again, while above P_1^* density decreases, as in a normal fluid. Exactly at P_1^* density reaches a fixed value at about the same temperature where the TMD line becomes horizontal in the $P \times T$ phase diagram (see the inset of Fig. 3.2). It is possible to calculate this value within a low temperature, two-states expansion (see Appendix A), resulting in the polynomial:

$$(1 - 2\delta_n)^{n+1} = 2(1 + 2\delta_n)^n \quad (3.12)$$

where $\delta_n = \bar{\rho}_n^* - \rho_n^*$, with $\bar{\rho}_n^*$ ($\rho_n^* = n + 1/2$) being the critical density at fixed pressure (fixed chemical potential) for the n -th transition. From this it is possible to find $\bar{\rho}_1^*$, the critical density at constant pressure for $n = 1$, as

$$\bar{\rho}_1^* = \frac{5 - \sqrt{5}}{2} \approx 1.381966. \quad (3.13)$$

Accordingly, the critical densities obtained from Eq.(3.12) are indeed relevant as they *predict the maximum densities found along the TMD lines* emanating from GSPT at critical pressures $P_n^* = n(n + 1)/2$. Next, let us compare the low temperature aspects of α and α_μ by rewriting Eq. (3.9) as:

$$\rho(\alpha - \alpha_\mu) = \frac{s}{\rho} \left(\frac{\partial \rho}{\partial \mu} \right)_T.$$

At small temperatures, it follows from the r.h.s. of this expression that $\alpha \approx \alpha_\mu$ for $\mu \neq \mu_n$ since $\lim_{T \rightarrow 0} s \rightarrow 0$. Consequently, α and α_μ are resembling functions at low temperatures, and $\alpha_\mu < 0$ can be used to infer a waterlike behavior in the NPT . As shown in Fig. 3.2, near the ground state phase transition between fluid phases with $n = 1$ and $n = 2$ particles at $\mu_1^* = 1$, α_μ presents an oscillation similar to α , this

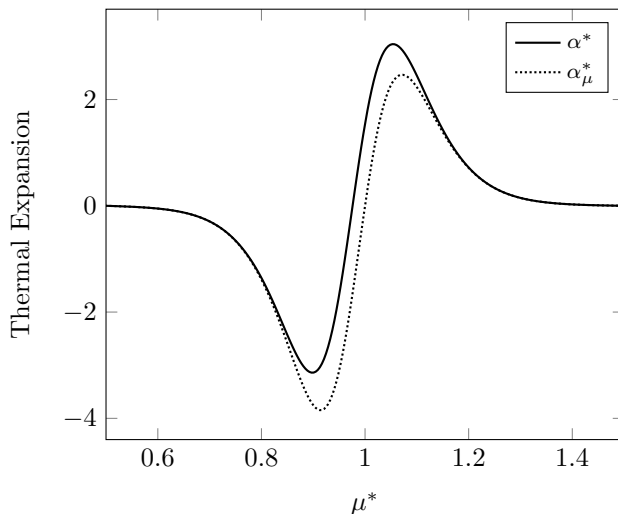


Figure 3-8: Thermal expansion coefficients at fixed pressure and chemical potential, α^* and α_{μ}^* , as a function of chemical potential at temperature $T^* = 0.05$. At low temperature the behavior of both coefficients are similar (see text).

being a signature of the proximity to the GSPT and waterlike behavior [90].

3.3 Complete Scenario

The difficulty in solving the Bose–Hubbard Hamiltonian comes from the distinct role played by its two characteristic parameters: its non interacting limit is diagonal in the momentum space whereas its atomic limit is diagonal in position space. Several treatments to model the thermodynamics were developed during the past decades [92]. They comprehend mean field approaches [93,94], Bogoliubov approximation for weak interactions [95], perturbative methods using Green’s functions, exact diagonalization procedures, path integral quantum Monte Carlo (QMC) using the worm algorithm [96], bosonic dynamical mean field theory (BDMFT) [97,98], just to name a few.

The Self-energy Functional Theory

In order to map the thermodynamics of the bosons we employ a variational and non-perturbative self-consistent approach, the self-energy functional theory derived by

Hügel *et al.* [99], inspired in the original works for fermions by Potthoff [100]. The formalism, which includes $U(1)$ symmetry breaking and comprehends previous BDMFT approaches [97, 98, 101–103], is based on successive Legendre transformations of the free energy functional Ω leading to a new functional Ω_{SE} of the self-energies. The approximation scheme to the many-body problem constricts the variational space: the self-energy domain is restricted to a subspace of self-energies of a simpler reference system. Then, the original problem is transformed into determining stationary solutions of this new functional in terms of the reference system's free propagators. This section is devoted to provide an overview of the method, following the references [99, 104, 105].

First, we write the Hamiltonian of Eq. (3.1) in a more concise and general form

$$H = \frac{1}{2} \mathbf{b}_\alpha^\dagger \mathbf{t}_\beta^\alpha \mathbf{b}^\beta + \mathcal{V} + \mathbf{F}_\alpha^\dagger \mathbf{b}^\alpha, \quad (3.14)$$

including an explicit symmetry breaking field \mathbf{F} which couples to the bosonic operators. In this notation, we use the Einstein summation convention and the superindex α spans the site index i as well as the Nambu index ν . Explicitly, the bosonic operator reads as $\mathbf{b}_\alpha^\dagger \equiv \mathbf{b}_{i\nu}^\dagger = (b_i^\dagger, b_i)_\nu$, with commutation relations $[\mathbf{b}_\alpha, \mathbf{b}_\beta^\dagger] = (\mathbf{1} \otimes \sigma_z)_\beta^\alpha$. Also, we have the generalized hopping $\mathbf{t}_\beta^\alpha = \mathbf{t}_{j\nu}^{i\eta} = t_{ij} \otimes \mathbf{1}_{\eta\nu}$ and interaction of the form $\mathcal{V} = U_{\alpha\beta\gamma\delta} \mathbf{b}^\alpha \mathbf{b}^\beta \mathbf{b}^\gamma \mathbf{b}^\delta$.

Including finite temperature effects (with $k_B T = 1/\beta$), the partition function $\mathcal{Z} = \text{Tr}[\mathcal{T}e^{-\mathcal{S}}]$ follows as a trace comprising the imaginary time ordered exponential of the action \mathcal{S} [106–108],

$$\begin{aligned} \mathcal{S}[\mathbf{F}, \mathbf{G}_0^{-1}] &= -\frac{1}{2} \int_0^\beta \int_0^\beta d\tau d\tau' \mathbf{b}^\dagger(\tau) \mathbf{G}_0^{-1}(\tau, \tau') \mathbf{b}(\tau') \\ &\quad + \int_0^\beta d\tau \mathcal{V}[\mathbf{b}(\tau)] + \int_0^\beta d\tau \mathbf{F}^\dagger \mathbf{b}(\tau), \end{aligned} \quad (3.15)$$

written according to its explicit dependence on \mathbf{F} and the non-interacting Green's function \mathbf{G}_0

$$\mathbf{G}_0^{-1} = \delta(\tau - \tau')(-[\mathbf{1} \otimes \sigma_z] \partial_{\tau'} - \mathbf{t}) . \quad (3.16)$$

From the partition function, averages can be defined as $\langle O(\tau) \rangle = \text{Tr}[\mathcal{T} e^{-S} O(\tau)] / \mathcal{Z}$. Also, its logarithm provides the free energy $\Omega[\mathbf{F}, \mathbf{G}_0^{-1}] = -\ln[\mathcal{Z}] / \beta$, which is a generating functional of the propagators: the condensate Green's function Φ

$$\beta \frac{\delta \Omega}{\delta \mathbf{F}^\dagger} = \langle \mathbf{b} \rangle \equiv \Phi , \quad (3.17)$$

and the connected interacting Green's function \mathbf{G}

$$2\beta \frac{\delta \Omega}{\delta \mathbf{G}_0^{-1}} = -\langle \mathbf{b}(\tau) \mathbf{b}^\dagger(\tau') \rangle \equiv \mathbf{G}(\tau, \tau') - \Phi^\dagger \Phi . \quad (3.18)$$

Further details regarding products and traces are addressed in the Appendix B.

Based on a Legendre transformation, the free energy functional dependence can be exchanged from \mathbf{F} and \mathbf{G}_0^{-1} to the dressed propagators Φ and \mathbf{G} , leading to the Baym-Kadanoff functional [109–112]

$$\begin{aligned} \beta \Omega_{BK}[\Phi, \mathbf{G}] &= \mathbf{F}^\dagger \Phi - \frac{1}{2} \Phi^\dagger \mathbf{G}_0^{-1} \Phi + \frac{1}{2} \text{Tr}[\mathbf{G}_0^{-1} \mathbf{G}] \\ &+ \frac{1}{2} \text{Tr} \ln[-\mathbf{G}^{-1}] + \Phi_{LW}[\Phi, \mathbf{G}] . \end{aligned} \quad (3.19)$$

In Eq. (3.19), $\Phi_{LW}[\Phi, \mathbf{G}]$ is the Luttinger-Ward functional [113, 114], a universal contribution which encompasses the complexity of the many-body system, containing all two-particle irreducible (2PI) diagrams [115, 116]. At the physical solution, the functional $\Omega_{BK}[\Phi, \mathbf{G}]$ is stationary

$$\frac{\delta \Omega_{BK}}{\delta \Phi^\dagger} = 0 , \quad \frac{\delta \Omega_{BK}}{\delta \mathbf{G}} = 0 , \quad (3.20)$$

and it is equal to the equilibrium free energy $\Omega_{BK} = \Omega$. The variations

$$\beta \frac{\delta \Omega_{BK}}{\delta \Phi^\dagger} = \mathbf{F} - \mathbf{G}_0^{-1} \Phi + \frac{\delta \Phi_{LW}}{\delta \Phi^\dagger} \quad (3.21)$$

and

$$2\beta \frac{\delta \Omega_{BK}}{\delta \mathbf{G}} = \mathbf{G}_0^{-1} - \mathbf{G}^{-1} + 2 \frac{\delta \Phi_{LW}}{\delta \mathbf{G}}, \quad (3.22)$$

associated to the conditions of Eq. (3.20) lead to the following identification

$$\Sigma_{1/2} = -\frac{\delta \Phi_{LW}}{\delta \Phi^\dagger}, \quad \Sigma = -2 \frac{\delta \Phi_{LW}}{\delta \mathbf{G}}, \quad (3.23)$$

where $\Sigma_{1/2}$ and Σ are the one and two-point self-energies, respectively. Therefore, the propagators obey the Dyson's equations

$$\mathbf{G}_0^{-1} \Phi = \mathbf{F} - \Sigma_{1/2} \quad (3.24)$$

and

$$\mathbf{G}^{-1} = \mathbf{G}_0^{-1} - \Sigma. \quad (3.25)$$

With another Legendre transform, the Baym-Kadanoff functional dependence can be exchanged from the one and two-point propagators Φ and \mathbf{G} to their respective self-energies $\Sigma_{1/2}$ and Σ , yielding the self-energy functional

$$\begin{aligned} \beta \Omega_{SE}[\Sigma_{1/2}, \Sigma] &= \frac{1}{2} (\mathbf{F} - \Sigma_{1/2})^\dagger \mathbf{G}_0 (\mathbf{F} - \Sigma_{1/2}) \\ &+ \frac{1}{2} \text{Tr} \ln [-(\mathbf{G}_0^{-1} - \Sigma)] + \mathcal{F}[\Sigma_{1/2}, \Sigma]. \end{aligned} \quad (3.26)$$

The universal functional $\mathcal{F}[\Sigma_{1/2}, \Sigma] = \Phi_{LW}[\Phi, \mathbf{G}] + \Sigma_{1/2}^\dagger \Phi + \frac{1}{2} \text{Tr}[\Sigma \mathbf{G}]$ is simply the Legendre transform of the Luttinger-Ward functional $\Phi_{LW}[\Phi, \mathbf{G}]$, with the following

variations

$$\frac{\delta \mathcal{F}}{\delta \Sigma_{1/2}^\dagger} = \Phi, \quad 2 \frac{\delta \mathcal{F}}{\delta \Sigma} = \mathbf{G}. \quad (3.27)$$

At the physical solution, Ω_{SE} is stationary and equal to the free energy $\Omega_{SE} = \Omega_{BK} = \Omega$ (as a result of Ω , Ω_{BK} and Ω_{SE} being connected by successive Legendre transforms), yielding once again the Dyson's equations

$$0 = \beta \frac{\delta \Omega_{SE}}{\delta \Sigma_{1/2}^\dagger} = -\mathbf{G}_0(\mathbf{F} - \Sigma_{1/2}) + \Phi \quad (3.28)$$

and

$$0 = 2\beta \frac{\Omega_{SE}}{\delta \Sigma} = -(\mathbf{G}_0^{-1} - \Sigma)^{-1} + \mathbf{G}. \quad (3.29)$$

The mentioned universality of the functional \mathcal{F} enables us to overcome its complexity with the introduction of an exactly solvable reference system (denoted by primed quantities) exhibiting the same symmetry and interactions as the original one. According to Eq. (3.26), the reference system's self-energy functional

$$\begin{aligned} \beta \Omega'_{SE}[\Sigma_{1/2}, \Sigma] &= \frac{1}{2}(\mathbf{F}' - \Sigma_{1/2})^\dagger \mathbf{G}'_0(\mathbf{F}' - \Sigma_{1/2}) \\ &+ \frac{1}{2} \text{Tr} \ln[-(\mathbf{G}'_0^{-1} - \Sigma)] + \mathcal{F}[\Sigma_{1/2}, \Sigma] \end{aligned} \quad (3.30)$$

evaluated at the physical solutions $\Sigma_{1/2} = \Sigma'_{1/2}$ and $\Sigma = \Sigma'$ is equal to the reference system's free energy $\Omega'_{SE}[\Sigma'_{1/2}, \Sigma'] = \Omega'[\mathbf{F}', \mathbf{G}'_0^{-1}]$. Subtracting Eq. (3.30) from Eq. (3.26), Ω_{SE} evaluated at $\Sigma_{1/2} = \Sigma'_{1/2}$ and $\Sigma = \Sigma'$ becomes

$$\begin{aligned} \beta \Omega_{SE}[\Sigma'_{1/2}, \Sigma'] &= \beta \Omega' + \frac{1}{2}(\mathbf{F} - \Sigma'_{1/2})^\dagger \mathbf{G}_0(\mathbf{F} - \Sigma'_{1/2}) \\ &- \frac{1}{2}(\mathbf{F}' - \Sigma'_{1/2})^\dagger \mathbf{G}'_0(\mathbf{F}' - \Sigma'_{1/2}) + \frac{1}{2} \text{Tr} \ln \left[\frac{\mathbf{G}_0^{-1} - \Sigma'}{\mathbf{G}'_0^{-1} - \Sigma'} \right]. \end{aligned} \quad (3.31)$$

Therefore, the solution of the reference system provides a parametrization of the self-energies in terms of \mathbf{F}' and \mathbf{G}'_0 , which allows the construction of the self-energy functional theory approximation Ω_{SFT} to the self-energy functional Ω_{SE} according to

$$\Omega_{SFT}[\mathbf{F}', \mathbf{G}'_0] = \Omega_{SE}[\Sigma'_{1/2}[\mathbf{F}', \mathbf{G}'_0], \Sigma'[\mathbf{F}', \mathbf{G}'_0]] . \quad (3.32)$$

The approximation consists in constraining the variational principle to the subspace of self-energies of the reference system; this procedure applied to the variations of Eqs. (3.28) and (3.29) yields the Euler equations $\delta_{\mathbf{F}'}\Omega_{SFT} = 0$ and $\delta_{\mathbf{G}'_0}\Omega_{SFT} = 0$.

In particular, we choose a local reference system, the SFA3 minimal construction [99], comprehending three variational parameters: the $U(1)$ symmetry-breaking linear field F' conjugated to the creation b^\dagger and annihilation b operators; the two fields Δ_{00} , coupled with the density $b^\dagger b$, and Δ_{01} , conjugated to pair creation $b^\dagger b^\dagger$ and pair annihilation bb operators. The Hamiltonian describing the bosonic state is given by

$$H'[\mathbf{F}', \mathbf{\Delta}] = \frac{1}{2}\mathbf{b}^\dagger \mathbf{\Delta} \mathbf{b} + \frac{U}{2}n(n-1) - \mu n + \mathbf{F}'^\dagger \mathbf{b} , \quad (3.33)$$

where $\mathbf{b} = (b, b^\dagger)$, $\mathbf{F}' = (F', F'^*)$ and $\mathbf{\Delta} = \Delta_{00}\mathbf{1} + \Delta_{01}\sigma_x$.

Therefore, the states of thermodynamic equilibrium are determined by the stationary points of Ω_{SFT} , given by $\nabla\Omega_{SFT}[F, \Delta_{00}, \Delta_{01}] = 0$ (or $\delta_{\mathbf{F}'}\Omega_{SFT} = 0$ and $\delta_{\mathbf{\Delta}}\Omega_{SFT} = 0$). The functional can be evaluated according to the steps developed throughout the Appendix B. The code employed in our calculations is also available in Appendix C.

3.4 Density anomaly

From the equilibrium free energy $\Omega = \Omega_{SFT}$ calculated previously, the density is given by

$$\rho = -\frac{1}{V} \left(\frac{\partial \Omega}{\partial \mu} \right)_T , \quad (3.34)$$

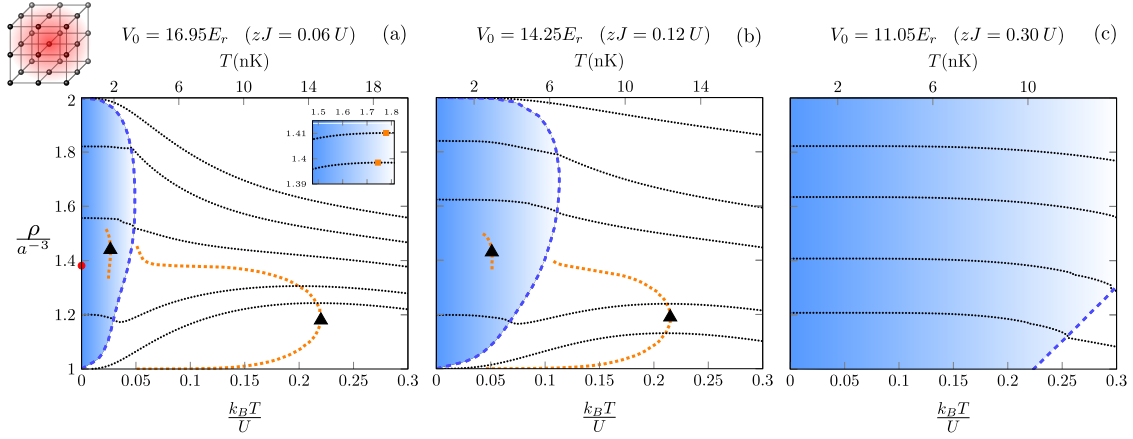


Figure 3-9: The density ρ as a function of the reduced temperature $k_B T/U$ (bottom) and the temperature T in nanokelvin units (top) at fixed pressures for hopping amplitudes: (a) $zJ = 0.06U$, (b) $zJ = 0.12U$, and (c) $zJ = 0.30U$, considering a simple cubic lattice ($z = 6$). The superfluid phase is highlighted in blue while the normal phase is portrayed in white. Blue dashed lines denote the boundaries between superfluid and normal phases, while orange dotted lines represent the TMD curves. In (a), the inset exhibits a zoom of isobaric curves in the superfluid phase, while the red point signals the atomic limit critical point at $T = 0$. The triangular points denote the maximum temperatures reached by each TMD curve.

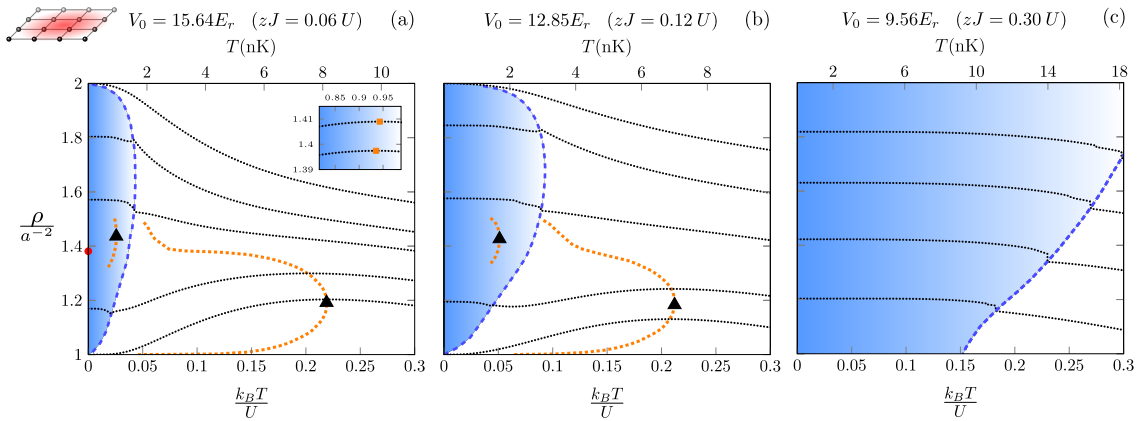


Figure 3-10: The density ρ as a function of the reduced temperature $k_B T/U$ (bottom) and the temperature T in nanokelvin units (top) at fixed pressures for hopping amplitudes: (a) $zJ = 0.06U$, (b) $zJ = 0.12U$, and (c) $zJ = 0.30U$, considering a square lattice ($z = 4$).

Table 3.1: Experimental parameters regarding potential depths V_0 , scattering length a_s , and laser wavelengths λ of optical lattices implemented using different alkali metal elements, for the hopping amplitudes $zJ = 0.06 U$ and $zJ = 0.12 U$. The maximum temperatures in which density anomalies are observed in superfluid T_{SF} and normal phases T_{NA} (the highlighted triangular points in Fig. ?? and Fig. ??) are also addressed. In the 2D scenarios, the vertical confinement is achieved by an optical potential along the z axis. For rubidium-87 [86] the lattice depth is $V_{0,z} = 26 E_r$ while the cesium-133 [117] atoms are confined in a Gaussian wavepacket of width $a_z = 0.30 \mu\text{m}$.

Element	Geometry	λ (nm)	a_s (a_0)	$zJ = 0.06 U$			$zJ = 0.12 U$		
				V_0/E_r	T_{NA} (nK)	T_{SA} (nK)	V_0/E_r	T_{NA} (nK)	T_{SA} (nK)
²³ Na [118]	Simple Cubic ($z = 6$)	595	52	18.30	88.35	10.68	15.49	74.67	17.82
⁸⁷ Rb [41]	Simple Cubic ($z = 6$)	852	103	16.95	14.76	1.78	14.25	12.39	2.95
⁸⁷ Rb [86]	Square ($z = 4$)	1064	103	15.64	8.13	0.95	12.85	7.00	1.69
¹³³ Cs [117]	Square ($z = 4$)	1064	310	16.65	4.36	0.51	13.77	3.77	0.91

where $V = N_s a^d$ is the volume and N_s is the number of lattice sites. Its temperature dependence at fixed pressure P is determined by the isobaric thermal expansion coefficient

$$\alpha = -\frac{1}{\rho} \left(\frac{\partial \rho}{\partial T} \right)_P. \quad (3.35)$$

For $\alpha < 0$, density increases with temperature and a region of anomalous density behavior is identified by a temperature of maximum density (TMD) line defined as $\alpha = 0$. The pressure is fixed employing the Gibbs-Duhem relation $dP = \rho d\mu + s dT = 0$, where $s = -\frac{1}{V} \left(\frac{\partial \Omega}{\partial T} \right)_\mu$ is the entropy density and P is related to the grand-canonical potential according to $-PV = \Omega = \Omega_{SFT}$.

Considering a simple cubic lattice, with $z = 6$, Figs. 3-9(a)-(c) illustrate the density ρ versus the reduced temperature $k_B T/U$ at fixed pressures (represented as black lines) for increasing hopping amplitudes: (a) $zJ = 0.06 U$, (b) $zJ = 0.12 U$ and (c) $zJ = 0.30 U$. The corresponding potential depths, which decrease from (a) to (c), and temperature scales in nanokelvin units are calculated considering atoms of rubidium-87, with realistic values based on the experiments performed by Greiner *et al.* [41]. The superfluid to normal phase boundary is illustrated as a reentrant dashed blue line and the blue filled area represents the superfluid phase. Figs. 3-9(a)-(b) show that at sufficient high values of V_0 (low values of zJ/U) there are two regions in which density presents a local maximum, the TMD curves represented as orange dots: one at the normal phase (normal phase anomaly, NA) and another at the superfluid

phase (superfluid phase anomaly, SA). The maximum temperature values reached by the TMD curves are highlighted as triangular black points.

Fig. 3-9(a) portrays a large area in the density versus temperature phase diagrams where the NA is present. However, as the hopping increases, according to Fig. 3-9(b), the anomaly occupies a smaller region in temperatures. In addition to the normal phase TMD, the superfluid phase also exhibits a density anomalous behavior illustrated in Fig. 3-9(a), with a few superfluid isobaric densities drawn in the inset. When the hopping becomes larger it dominates the free energy, leading the superfluid to occupy a bigger region in the phase diagram and suppressing both superfluid and normal anomalies, as presented Fig. 3-9(c).

Analogously, Fig. 3-10 displays the two dimensional results considering a square lattice geometry, with $z = 4$. For comparison reasons, we chose the same ratios zJ/U as shown in Fig. 3-9. The superfluid domain exhibits a small retraction when compared to the simple cubic case. In spite of this, the same general behavior is observed. Specifically, Fig. 3-10(a) presents the density anomaly in both phases; the anomaly is reduced for a larger hopping amplitude as illustrated in Fig. 3-10(b), and finally it vanishes completely as shown in Fig. 3-10(c). For this two dimensional system, the respective potential depths and temperature scales in nanokelvin units are calculated also considering atoms of rubidium-87, with parameters according to the experiments performed by Sherson *et al.* [86].

Although the upper temperature scales and potential depths addressed in Figs. 3-9 and 3-10 refer to specific setups using rubidium-87, they can be adapted to other elements. Indeed, we collect in Table 3.1 the temperatures, T_{SA} and T_{NA} , that must be achieved for experimentally detecting SA and NA not only for the previous cases of rubidium-87 but also for sodium-23 [118] (in a simple cubic lattice) and cesium-133 [117, 119, 120] (in a square lattice). These points are marked as the triangular symbols over the TMD curves.

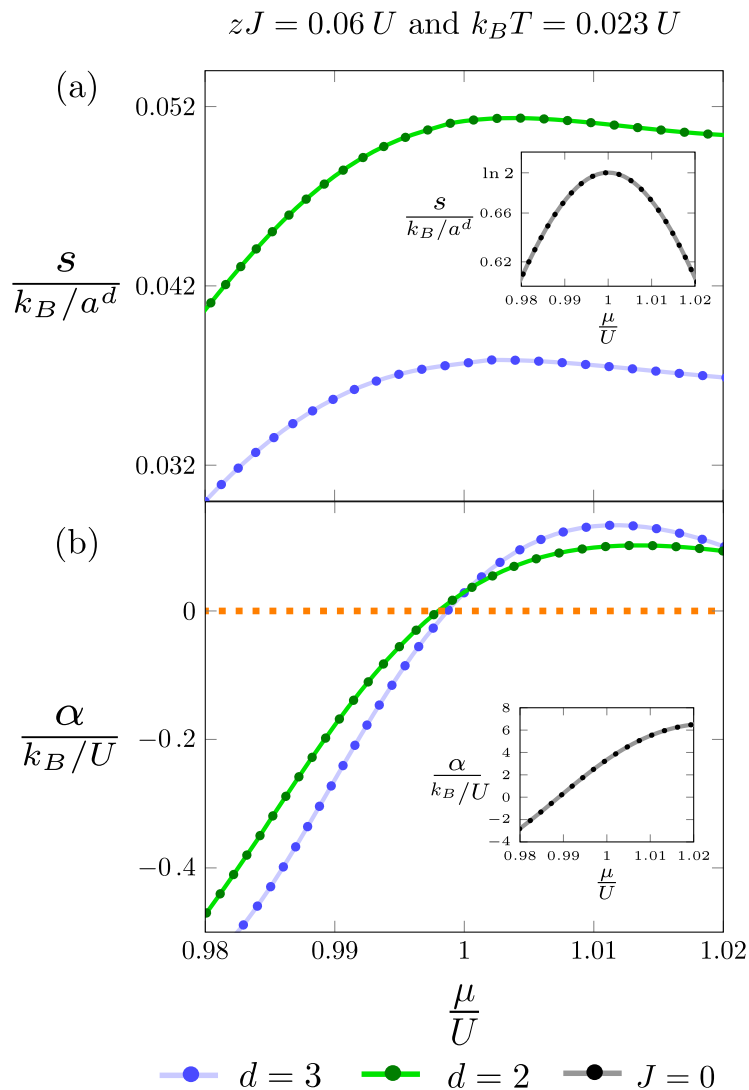


Figure 3-11: Considering square ($d = 2$) and simple cubic ($d = 3$) lattices, the entropy (a) and thermal expansion coefficient (b) are exhibited as functions of the chemical potential μ for $zJ = 0.06 U$ at $k_B T = 0.023 U$ deep in the superfluid regime. The respective insets depict the atomic limit ($J = 0$) scenario.

3.5 Residual entropy mechanism

The density anomalies in the normal fluid can be traced back to the ground state phase transitions between Mott Insulators of successive occupation numbers [121]. This anomalous behavior, present even in the absence of hopping, arises from the competition between the chemical potential, which promotes the boson occupation in the lattice, with the on site repulsion interaction U , which favors the boson removal. As the temperature increases, entropy first favors filling up the sites but, for high enough temperatures, entropy increases by removing particles from the system to increase the mobility of the particles left. This is a classical behavior similar to that of liquid water, where bonding and non-bonding structures compete: at lower temperatures density increases by disrupting hydrogen bonds while at higher temperatures enhanced particles' velocities increase the available volume, decreasing density. The novelty here is that this phase is not completely destroyed by the hopping, persisting for values of the J possible to be observed experimentally.

Indeed, the hopping brings a new phenomenon not observed for $J = 0$: the SA, a quantum density anomaly. The physical origin of this behavior is also the competition between chemical potential and the repulsion U . But for the SA the TMD line appears at lower temperatures and higher densities when compared with the NA, because in this case the hopping contributes to the temperature effects, favouring the movement and the spread of particle over the lattice.

Such competition of interaction scales can also be translated in terms of degeneracies and residual entropies. Inhibiting the hopping, a ground state degeneracy, related to a phase transition in number occupation between Mott Insulators, is settled whenever the chemical potential μ reaches an integer value of the interaction U . At such transition points, two states are equally accessible and this degeneracy accounts for an observed macroscopic residual entropy of $k_B \ln 2$ per site. For finite temperatures, zero point entropies produce peaks near those points as the chemical potential is varied, see the inset of Fig. 3-11(a). By turning on the tunneling probability adiabatically the superfluid phase emerges exactly from Mott Insulator transition

points, mitigating residual entropies, since the previous degeneracy gets lifted. Thus, by turning on the hopping transition the previously mentioned entropy peaks remain deep in the superfluid phase but are less prominent, as shown in Fig. 3-11(a) for $zJ = 0.06 U$ and $k_B T = 0.023 U$. Formally, the entropy peaks mark a change in the behavior of density with temperature according to the Maxwell relation

$$\left(\frac{\partial s}{\partial \mu}\right)_T = \left(\frac{\partial \rho}{\partial T}\right)_\mu = -\rho \alpha_\mu, \quad (3.36)$$

which results in the sign flip of thermal expansion in the superfluid phase illustrated in Fig. 3-11(b).

3.6 2D in situ observation including confinement effects

On the basis of the recently developed in situ measurements of ultracold gases in optical lattices [122], we discuss a physical realization of the reported phenomenon considering rubidium-87 atoms disposed in a square lattice, as Fig. 3-12(a) depicts. These modern tools encompass high resolution absorption [117, 120], fluorescence imaging [85, 86] and even scanning electron microscopy [123], each technique with its specific applications. Considering the range of density and fluctuations presented here, our theoretical proposal appears better suited to the absorption imaging realized by Chin *et al.* [117, 120], complementing the well known time-of-flight methods which probe the system in momentum space. In such experimental framework, in situ density distributions $\rho(x, y)$ of 2D gases can be determined by performing absorption imaging perpendicular to the horizontal plane xy . This technique allows mapping the occupation number at a single site resolution, providing direct access to density fluctuations, which is our ultimate goal in the analysis of the anomaly.

In our discussion, the confinement effects of the harmonic trapping field, represented in Fig. 3-12(b), are considered using a local density approximation (LDA). The harmonic confinement potential is given by $V_h(r) = \frac{1}{2}m\omega^2 r^2$, where $r = \sqrt{x^2 + y^2}$ is

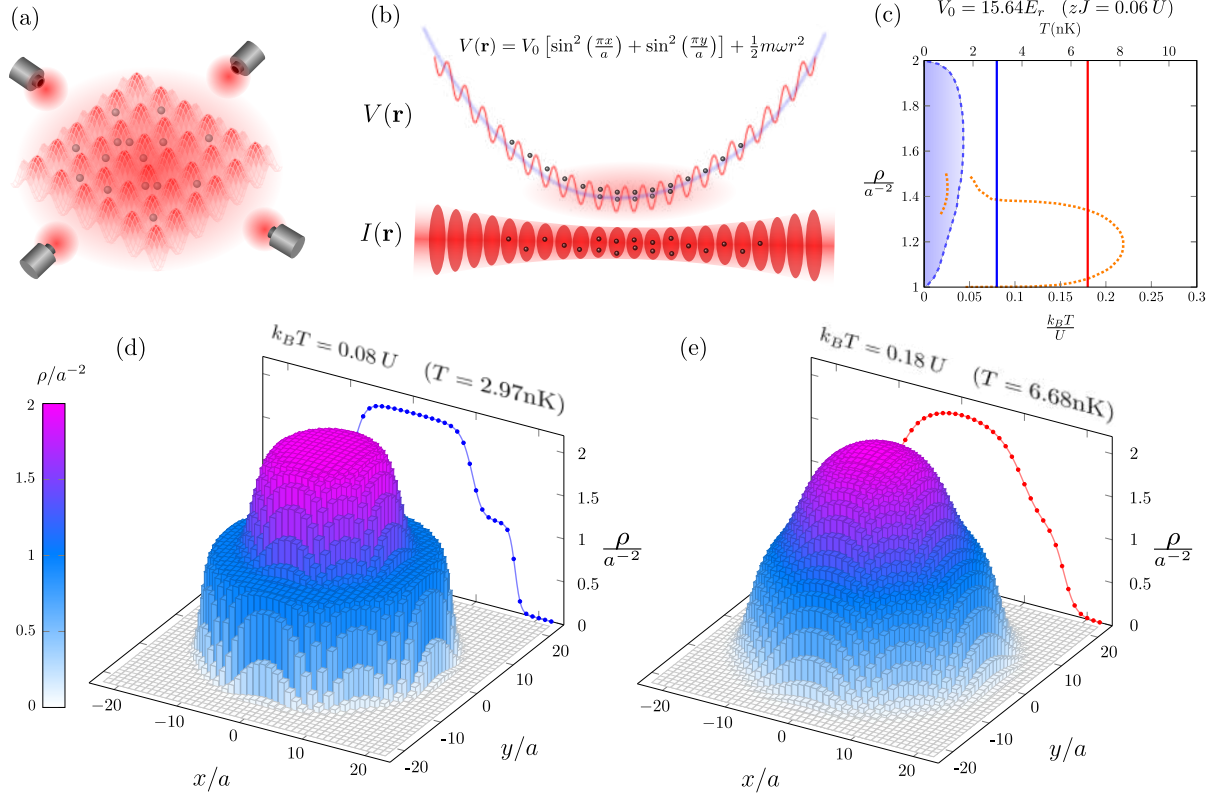


Figure 3-12: The density distribution in the normal phase, considering harmonic confinement effects. (a) The two dimensional configuration of a square optical lattice is created by counter propagating red detuned laser beams. The additional harmonic effects are represented in (b) where the optical potential $V(\mathbf{r})$ and the intensity profile $I(\mathbf{r})$ are schematically shown. (c) The phase diagram ρ versus T for the configuration $V_0 = 15.64 E_r$ ($zJ = 0.06 U$) highlights two chosen temperatures $k_B T = 0.08 U$ (blue) and $k_B T = 0.18 U$ (red). Considering the LDA scenario, the density ρ is mapped in the xy plane for the respective temperatures in (d) and (e).

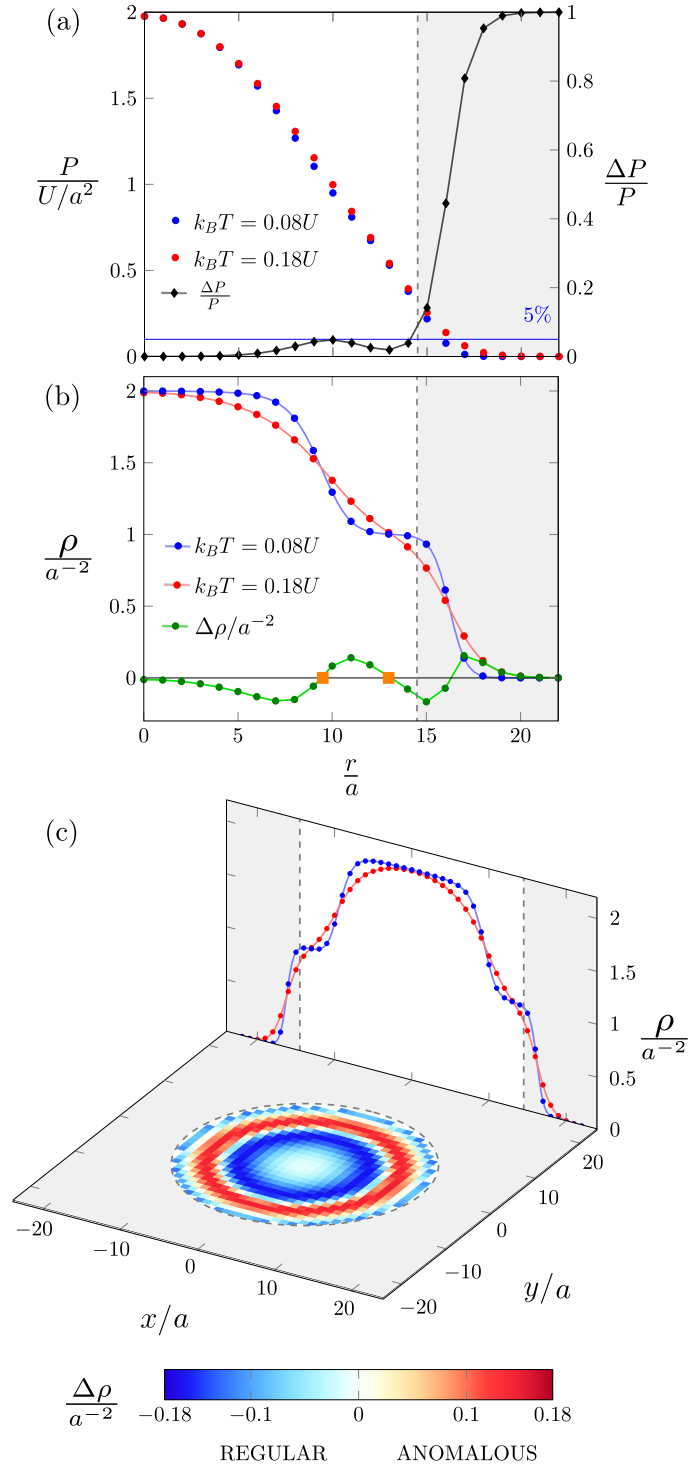


Figure 3-13: Analysis of the set up presented in Fig. 3-12. Panel (a) shows the pressure P for two different temperatures ($k_B T = 0.08 U$ and $k_B T = 0.18 U$) and their relative differences $\Delta P/P$ as a function of the radial distance r . The gray area signals the distances where such pressure deviation becomes greater than 5%. (b) The density profiles for these temperatures are exhibited as functions of distances as well as their difference $\Delta \rho$, with the anomalous region ($9 a \leq r \leq 14 a$) delimited by two TMD points (orange squares). (c) $\Delta \rho$ is represented as a color map in the xy plane.

the radial distance from the center of the trap and the associated oscillation frequency ω is fixed at $\omega/2\pi = 60$ Hz, as typically chosen. Consequently, in the LDA framework the chemical potential across the lattice takes the form $\mu(r) = \mu_0 - V_h(r)$. The lattice depth is held at $V_0 = 15.64 E_r$ ($zJ = 0.06 U$) as already discussed in Fig. 3-10(a). Furthermore, the total number of particles is kept constant $N_{total} = 1096$ as well as the total pressure $P_{total} = 1.9765 U/a^2$. Under these described conditions, such quantities satisfy the equation of state [124, 125]

$$P_{total} = \frac{m\omega^2}{2\pi} N_{total} , \quad (3.37)$$

as demonstrated in Appendix D. This simple relation implies that if N_{total} is fixed, then P_{total} is naturally held constant. Given all these parameters, we restrict our analysis to the normal phase anomaly since the variations in density with temperature are more prominent.

Since we want to investigate how the density behaves when temperature is changed at fixed pressure, Figs. 3-12(d) and (e) exhibit the density ρ on each lattice site of the xy plane for temperatures $k_B T = 0.08 U$ ($T = 2.97$ nK) and $k_B T = 0.18 U$ ($T = 6.68$ nK), respectively. These two temperatures are also marked as blue and red straight lines in the phase diagram of Fig. 3-12(c), showing that only the normal phase is present. In a qualitative perspective, it is observed a melting of the steps as temperature is raised and a larger number fluctuation between the steps of integer density. Quantitatively, a closer look at how the local pressure P varies across the radial direction is discussed in Fig. 3-13(a). Due to the finite difference between such temperatures $k_B \Delta T = 0.1 U$, there are differences in pressure ΔP compared to their respective values at each site which are less than 5% until $r = 14 a$. Larger distances are filled in gray, comprehending an area where the relative difference $\Delta P/P$ grows towards the boundaries of the lattice. Hence, the pressure is kept approximately constant at each site except inside the gray area, where $r > 14 a$. Fig. 3-13(b) shows the radial density profiles in greater detail, with their difference $\Delta \rho$ in green. This curve shows oscillations, taking on positive values. These positive values indicates

the density anomaly and are limited by two TMD points, shown as orange square points. Finally, Fig. 3-13(c) summarizes our analysis where the difference in density $\Delta\rho$ is represented through a color map in the xy plane. The anomalous region $\Delta\rho > 0$ denotes an increase in density with temperature at fixed pressure, while the regular behavior corresponds to $\Delta\rho < 0$. As previously, the gray area excludes the regions where the local pressure does not remain fixed. Under these circumstances, we have shown a signature of the density anomaly in this 2D configuration, illustrated as the red circular ring of Fig. 3-13(c).

Chapter 4

Specific heat anomaly and correlations in the Bose-Hubbard model

“O ser humano normal acredita no que vê, no que experimenta e no que sabe. O fingidor histérico, naquilo que aprendeu a dizer.”

– Olavo de Carvalho

In the field of condensed matter physics, the specific heat is a valuable physical observable that provides general information regarding the energy spectrum of a system, a key to its microscopic details [126, 127]. It encodes information on the entropy, a useful thermodynamic quantity directly connected to such microscopic degrees of freedom, which is in general inaccessible by direct measurements. Among interesting anomalous properties, the appearance of a second peak in the specific heat at low temperatures, known as the Schottky-type anomaly, is experimentally and theoretically observed in several frustrated systems. Typical examples are the magnetic systems on geometrically frustrated lattices with kagome, triangular, or pyrochlore structures. Experimentally, the double-peak anomaly is measured in magnetic pyrochlore oxides [128], the canonical spin-ice material $\text{Dy}_2\text{Ti}_2\text{O}_7$ [129–131] and $\text{Tb}_2\text{Ti}_2\text{O}_7$ [132], their mixtures $\text{Dy}_{2-x}\text{Tb}_x\text{Ti}_2\text{O}_7$ [133], lead-based pyrochlores [134],

and spin-glasses like $R_2Mo_2O_7$ ($R=Y, Sm, \text{ or } Gd$) [135]. Other examples include heavy-fermion compounds [136, 137], bosonic superfluids in spin-dimer networks [138], CO_2N_2 plasma [139], lipid bilayers containing cholesterol [140], as well as mixtures of liquid crystal and nanoparticles [141]. In a theoretical framework, the anomaly was verified for spin models with antiferromagnetic Heisenberg interactions [142–147], Ising pyrochlore magnets using Monte Carlo simulations [148, 149], Ising models [150–153] in distinct geometries, and quantum ferrimagnets [154].

Since the entropy dependence on temperature determines the specific heat of a given system, this thermodynamic quantity is a relevant ingredient in the presented anomaly. Fundamentally, the geometrical frustration arises from a conflict between the interaction degrees of freedom and the underlying crystal geometry [155]. The described frustration leads to a macroscopic degeneracy which is computed as a ground-state finite entropy, the so-called residual entropy. One of the first examples of geometrical frustration was given by Linus Pauling, when describing the low-temperature ordering of protons in water ice I_h [156]. The many ways of satisfying the lowest-energy state which reconcile the crystal structure of ice with the known bond lengths were given by the Bernal-Fowler rules [157]. Based on their prescription, Pauling calculated the residual “macroscopic” ground-state entropy per hydrogen atom of $(1/2)R \ln(3/2) \approx 1.68 \text{ mol}^{-1}\text{K}^{-1}$. Interestingly, a similar physical mechanism is verified for the already mentioned high degeneracy observed in pyrochlore magnets, constituting the named spin-ice materials [129, 158]. The particular ways these systems can fluctuate between such multiple ground-state configurations can be responsible not only for the anomalies addressed but also for emergence all sorts of novel behaviors in fluid and solid phases, including even an artificial edition of electromagnetism [159].

In this chapter we report the occurrence of the double-peak specific heat anomaly in the Bose-Hubbard model based on theoretical calculations. Here we present an alternative mechanism of frustration observed in this model, devoting some attention to the influence of correlations created by a finite tunneling amplitude. In the previously mentioned systems the frustration was essentially derived from incompatibilities

between geometry and interactions; in the Bose-Hubbard model the frustration is a consequence of the competition of lattice occupation and the local interactions. The essential ingredient, a ground-state residual entropy, is also present. When appropriate, we also complement our SFT results with finite-temperature perturbation theory around the atomic limit.

Given the equilibrium free energy Ω obtained from the previously cited techniques, the specific heat is explicitly given by

$$c_\mu = -\frac{T}{N_s} \left(\frac{\partial^2 \Omega}{\partial T^2} \right)_\mu = T \left(\frac{\partial s}{\partial T} \right)_\mu, \quad (4.1)$$

where T is the temperature and s is the thermodynamic entropy per site

$$s = -\frac{1}{N_s} \left(\frac{\partial \Omega}{\partial T} \right)_\mu, \quad (4.2)$$

considering N_s sites at a fixed chemical potential μ .

4.1 The Atomic Limit ($J = 0$)

In the following, we show that the specific heat c_μ presents a double-peak structure as a function of the temperature whose origin can be traced back to the atomic limit. Since the hopping amplitude is absent in the atomic limit ($J = 0$), there is no superfluid phase and the bosons are found in a normal fluid state. The Hamiltonian described by Eq. (3.1) becomes

$$H^{(0)} = \frac{U}{2} \sum_i n_i(n_i - 1) - \mu \sum_i n_i, \quad (4.3)$$

a sum of single-site Hamiltonians $H_i^{(0)}$ which can be diagonalized by the number operators eigenvectors $|n_i\rangle$. Thus, the energy eigenvalue of a single site with occupation n is expressed by

$$E_n = \frac{U}{2} n(n - 1) - \mu n. \quad (4.4)$$

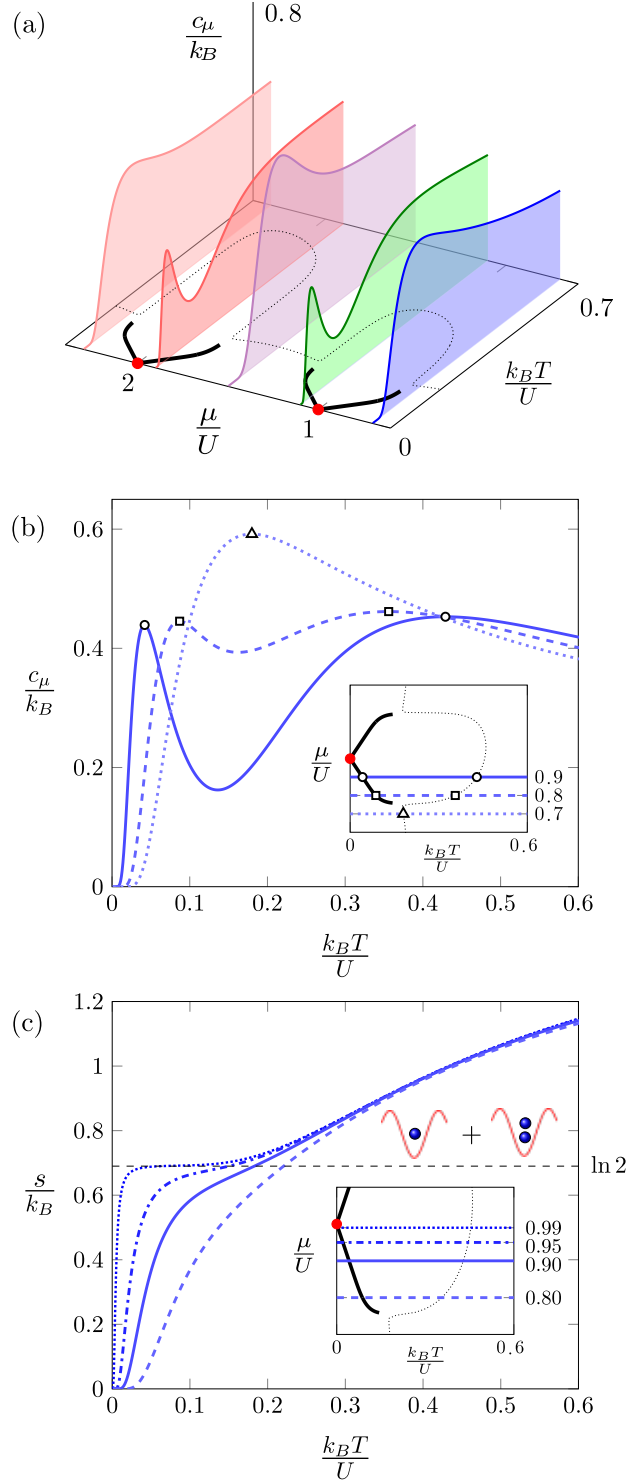


Figure 4-1: Finite-temperature analysis of the specific heat and entropy in the atomic limit $J = 0$. (a) The 3D diagram portrays the specific heat c_μ as a function of the temperature T in a wide range of chemical potential μ values. The continuous and dotted black curves in the μT plane represent the loci of the maximum values attained by c_μ . Red dots denote ground-state phase transitions between Mott insulators. In (b) is shown a detailed vision on the temperature dependence of c_μ considering the values $\mu = 0.7U, 0.8U$ and $0.9U$, portrayed by the inset. Panel (c) contains the entropy per site s as temperature varies for $\mu = 0.8U, 0.9U, 0.95U$ and $0.99U$.

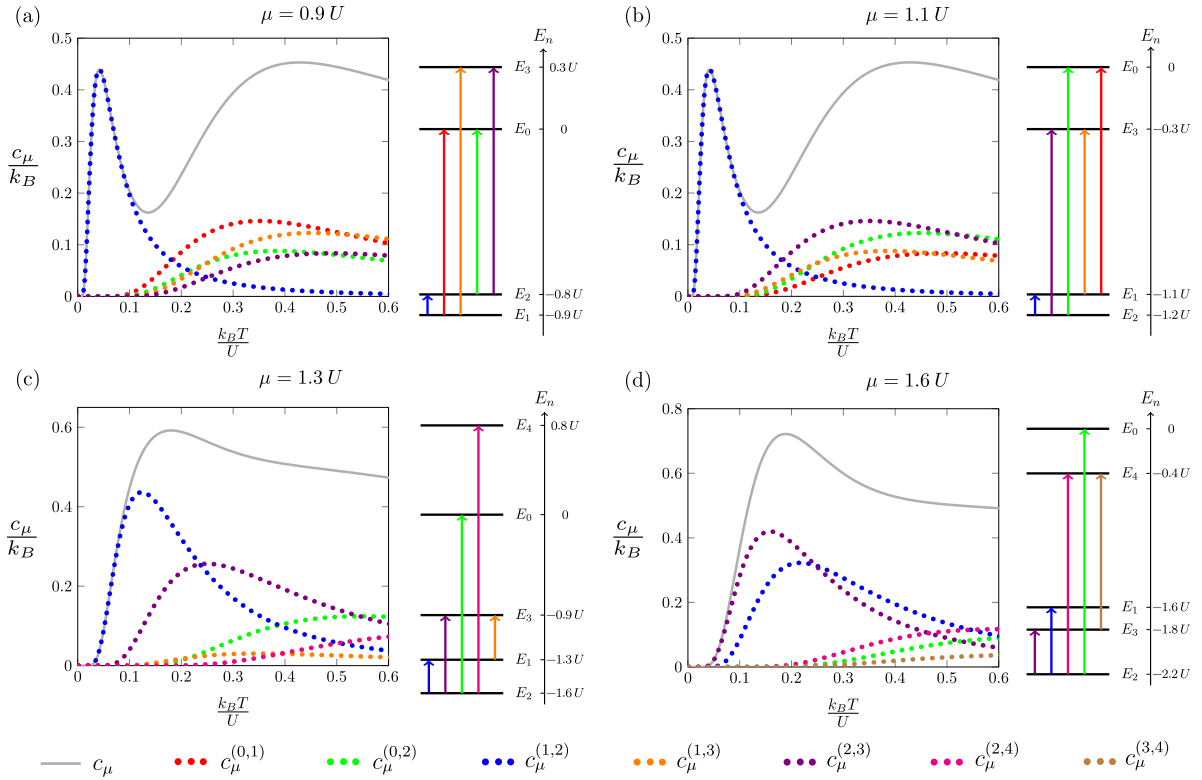


Figure 4-2: The specific heat decomposition and its temperature behavior is exhibited considering four fixed values of chemical potential: (a) $\mu = 0.9U$, (b) $\mu = 1.1U$, (c) $\mu = 1.3U$ and (d) $\mu = 1.6U$. The dotted curves represent the contributions $c_\mu^{(n,m)}$ to the total specific heat c_μ , which is shown as the continuous curve. Each panel contains a diagram of energy levels assigning a different color to each transition $|n\rangle \rightarrow |m\rangle$ (with energies $E_n \rightarrow E_m$), referring to the respective term $c_\mu^{(n,m)}$.

In this limit the grand-canonical partition function

$$\mathcal{Z}^{(0)}(T, \mu) = \text{Tr} \left[e^{-\beta H^{(0)}} \right] = \prod_{i=1}^{N_s} \mathcal{Z}_i^{(0)} = \left[\mathcal{Z}_1^{(0)} \right]^{N_s} \quad (4.5)$$

becomes simply a product of single-site partition functions

$$\mathcal{Z}_1^{(0)}(T, \mu) = \sum_{n=0}^{\infty} e^{-\beta E_n} , \quad (4.6)$$

where $\beta = 1/k_B T$ and k_B is the Boltzmann constant. The free-energy potential $\Omega^{(0)}$ follows directly from Eqs. (4.5) and (4.6) according to

$$\Omega^{(0)}(T, \mu) = -\frac{1}{\beta} \ln \mathcal{Z}^{(0)} = -\frac{N_s}{\beta} \ln \mathcal{Z}_1^{(0)} . \quad (4.7)$$

Fig. 4-1(a) portrays the specific heat c_μ as a function of the temperature T in a three-dimensional diagram including a wide range of chemical potential values (in different colors), with the loci of maxima represented as dotted and continuous black lines in the μT plane. At zero temperature, there are ground-state phase transitions (GSPT) between Mott insulators of successive occupation numbers whenever the chemical potential μ takes on integer values of the local interaction U [160,161], shown as red dots. At higher temperatures, it is observed a maximum at any value of fixed μ , symbolized by dotted lines. However, as the chemical potential approaches integer values of the interaction, the specific heat develops another peak at low temperatures (the continuous black lines), which is connected to its corresponding GSPT. The low- and high-temperature maxima start to merge together as the chemical potential values move away from the integers values of U , finally coalescing in a single peak according to Fig. 4-1(b).

The entropy dependence on temperature illustrated in Fig. 4-1(c) suggests that the low-temperature maxima are related to a residual entropy per site of $k_B \ln 2$. This zero-point entropy is due to the degeneracy established at the GSPT between states with different occupations. As the chemical potential approaches the integer multiples

of the local interaction, the entropy curves develop a sharp step towards the residual value $k_B \ln 2$ which induces a change in their concavities. This behavior leads to a Schottky-like peak at low temperatures close to the critical points.

A deeper understanding on the evolution of the reported double-peak structure can be attained by decomposing the specific heat in terms of contributions regarding all possible transitions between the different eigenvalues E_n . Indeed, we show in Appendix F.1 that c_μ can be expressed as

$$c_\mu = \sum_{n < m} c_\mu^{(n,m)}, \quad (4.8)$$

where the defined partial specific heat describes the fluctuations between the energy levels m and n according to

$$c_\mu^{(n,m)} = k_B \frac{\beta^2}{\left[\mathcal{Z}_1^{(0)} \right]^2} (E_n - E_m)^2 e^{-\beta(E_n + E_m)}. \quad (4.9)$$

Since the specific heat accounts for fluctuations in energy with respect to its mean value, the intuitive idea brought by this decomposition is to visualize the fluctuations in energy as a result of transitions between all possible energy levels. This outcome allows us to understand how these peaks behave and influence each other, isolating the relevance of each transition.

In Fig. 4-2 we present the specific heat as a function of temperature as continuous lines including four different values of chemical potential: (a) $\mu = 0.9U$, (b) $\mu = 1.1U$, (c) $\mu = 1.3U$ and (d) $\mu = 1.6U$. For each case, the most relevant partial contributions $c_\mu^{(n,m)}$ are addressed as the colored dotted lines, with the respective level transitions depicted accordingly. Figure 4-2(a) shows the $\mu = 0.9U$ case. The low-temperature peak appears due to the $|1\rangle \rightarrow |2\rangle$ transition. Other contributions add up to form the second maximum at a higher temperature; among them, the most relevant terms in this temperature range arise from the transitions $|1\rangle \rightarrow |0\rangle$ (red) and $|1\rangle \rightarrow |3\rangle$ (orange) which connect the states $|0\rangle$ and $|3\rangle$ to the ground state $|1\rangle$, respectively. In Fig. 4-2(b), for $\mu = 1.1U$, the ket $|2\rangle$ becomes the new ground state and the first

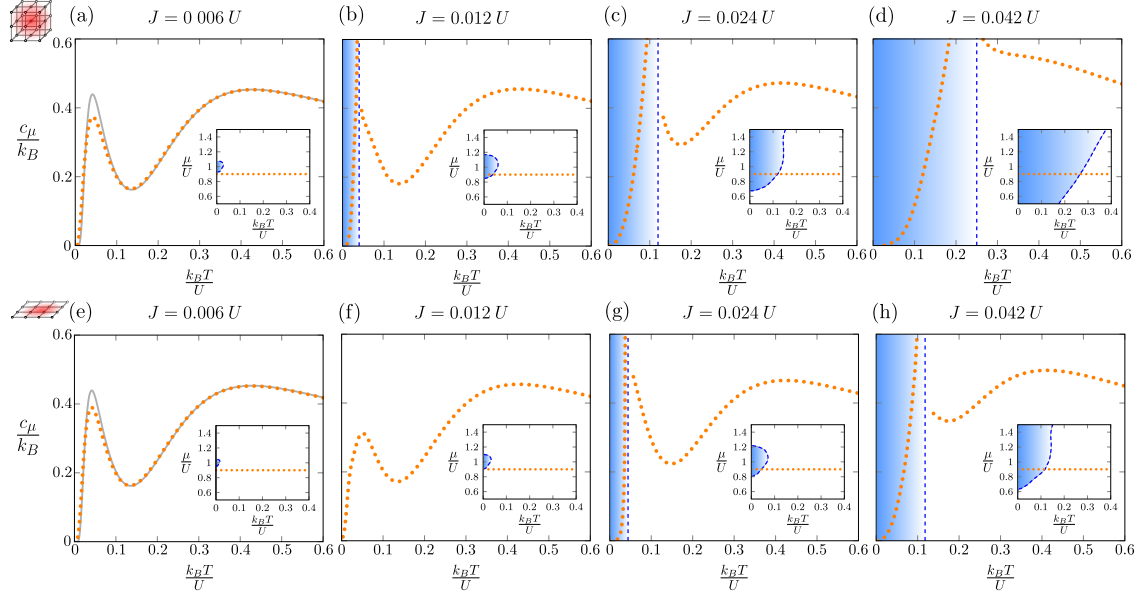


Figure 4-3: The specific heat c_μ is shown as a function of the temperature T at fixed $\mu = 0.9U$ for simple cubic (a)-(d) and square lattices (e)-(h) considering four different hopping amplitudes: (a) and (e) $J = 0.006U$ (the gray continuous lines are the corresponding atomic limits), (b) and (f) $J = 0.012U$, (c) and (g) $J = 0.024U$, (d) and (h) $J = 0.042U$. The superfluid domain is represented by the blue area, with the phase boundaries symbolized by the blue dashed lines. The insets exhibit the respective μT phase diagrams.

peak persists due to the available transition $|2\rangle \rightarrow |1\rangle$. As a result of this new ground state, the contributions for the second maximum from $|2\rangle \rightarrow |0\rangle$ (green) and $|2\rangle \rightarrow |3\rangle$ (purple) become more prominent than the previous transitions $|1\rangle \rightarrow |0\rangle$ (red) and $|1\rangle \rightarrow |3\rangle$ (orange). In Fig. 4-2(c), where $\mu = 1.3U$, the transition $|2\rangle \rightarrow |3\rangle$ (purple) starts to gain relevance since the energy level E_3 approaches E_1 . As a consequence of these two competing contributions, the specific heat develops only one maximum. Figure 4-2(d), which displays $\mu = 1.6U$, finally shows E_3 becoming the first excited state, with $c^{(2,3)}$ the most relevant term at low temperatures. By increasing the chemical potential another analogous cycle starts, presenting the same fundamental mechanisms already explored.

4.2 Finite Hopping ($J \neq 0$)

Including finite-hopping effects, the specific heat behavior with temperature for simple-cubic and square lattices is illustrated in Figs. 4-3(a)-(d) and Figs. 4-3(e)-(h),

respectively. The observables were evaluated using the previously described SFT formalism. In this framework, we considered four values of tunneling: $J = 0.006U$, $J = 0.012U$, $J = 0.024U$ and $J = 0.042U$, for a fixed chemical potential $\mu = 0.9U$. Physically, such increasing tunneling amplitudes correspond to decreasing lattice potential depths, going from very deep lattices to shallower ones. The introduction of the kinetic term J gives rise to a superfluid phase which grows from the GSPT points [162]. The superfluid phase is represented in the blue area, with the superfluid to normal phase boundaries shown as dashed blue lines. The respective insets portray the μT phase diagrams.

First we analyze the three-dimensional case, exhibited in Figs. 4-3(a)-(d). Considering the chosen value $J = 0.006U$ in Figs. 4-3(a), the system is found in the normal phase and the two-peak structure of the specific heat remains present. For comparison reasons, we also indicate the corresponding atomic limit result as the gray continuous line. It is observed a clear reduction of the first peak when the hopping is slightly turned on; the second one, however, does not exhibit relevant quantitative differences. Intuitively, since the low-temperature maximum is a result of the energetic competition between two states, the introduction of the hopping breaks this degeneracy, mitigating its magnitude. A detailed analysis regarding such behavior is also developed in Subsecs. 4.2 and 4.2, involving the analysis of spectral properties and correlation functions. By increasing the hopping to $J = 0.0012U$, Fig. 4-3(b) shows the appearance of the superfluid phase. Since the response functions tend to grow in magnitude near continuous phase transitions, we observe an increasing of c_μ in the neighborhood of the phase transition. As a consequence the first peak turns into a critical divergence, while the second one is still observed. Figure 4-3(c) portrays the $J = 0.024U$ scenario, where c_μ increases monotonically in the superfluid, while the second maximum remains to be seen in the normal phase. For a larger hopping term $J = 0.042U$ in Fig. 4-3(d), the superfluid domain increases to the point that the high-temperature peak disappears. Thus the two original maxima, born in the the atomic limit, are only verified in a perturbative regime.

Considering the same hopping values and $\mu = 0.9U$, Figs. 4-3(e)-(h) depict the

specific heat dependence on temperature for the square lattice configuration. The superfluid domain for each tunneling amplitude is smaller when compared to the three-dimensional picture. Indeed, since there is a reduction on the number of available directions for a particle to hop in a square lattice, the superfluid region shrinks. Therefore, it takes larger values of J to observe in a square lattice the same effects seen in a simple cubic one. For $J = 0.006U$, Fig. 4-3(e) shows two peaks in the normal phase, with the low-temperature one appearing reduced in comparison to the atomic limit (continuous line). Increasing J , Fig. 4-3(f) shows that such peak is diminished even further for $J = 0.012U$. Finally, Figs. 4-3(g) and 4-3(h) demonstrate that the rise of the superfluid phase starts to destroy the developed peaks.

In the next Subsections we analyze the two peaks of c_μ in the presence of hopping in greater detail. The $J = 0.006U$ case, which preserves such property in two and three dimensions, is explored inside the normal phase.

Spectral Functions

Since spectral functions reveal how states occupy a given energy interval, they also provide useful information on the specific heat behavior. The spectral function, a generalized density of states in frequency ω and momentum space \mathbf{k} , is defined by the imaginary part of the retarded Green's function [114] according to

$$A(\mathbf{k}, \omega) = -\frac{1}{\pi} \Im[G^R(\mathbf{k}, \omega)]. \quad (4.10)$$

This follows from the Matsubara Green's function by analytic continuation, applying the prescription $i\omega_n \rightarrow \omega + i0^+$, where $\omega_n = 2\pi n/\beta$. Its integration over the momentum yields the local spectral function

$$A(\omega) = \frac{1}{N_s} \sum_{\mathbf{k}} A(\mathbf{k}, \omega). \quad (4.11)$$

Concerning other range of parameters, the spectral properties of the Bose-Hubbard were also discussed using SFT [99], as well as employing QMC and BDMFT meth-

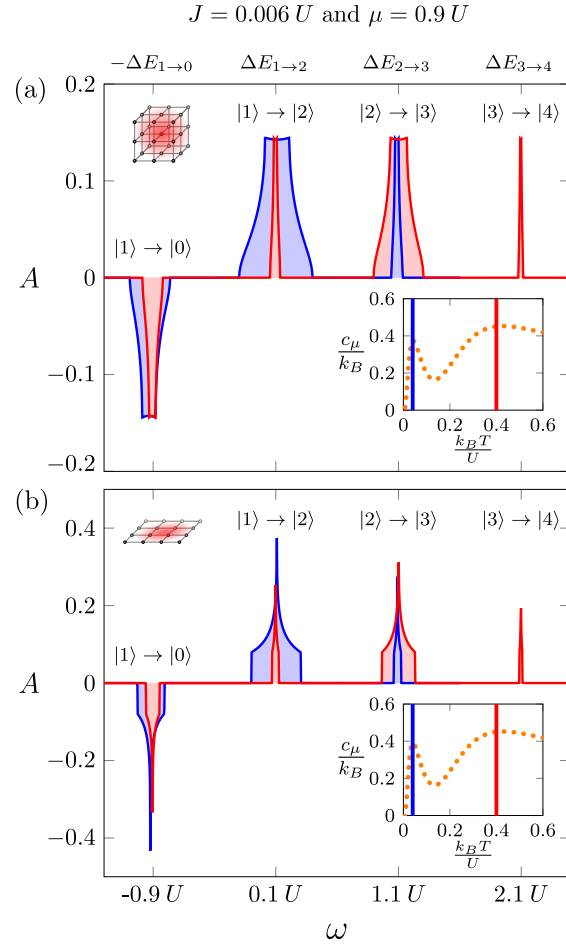


Figure 4-4: The spectral function A dependence on the real frequency ω at fixed $J = 0.006U$ and $\mu = 0.9U$, considering a simple cubic (a) and a square lattice (b). The two temperatures addressed $k_B T = 0.08U$ (blue) and $k_B T = 0.4U$ (red), located around each maximum of the specific heat, are marked in the inset panel. Above each resonance, the most significant transitions $|n\rangle \rightarrow |m\rangle$ are identified.

ods [163, 164]. In Figs. 4-4(a) and 4-4(b), we show the behavior of A as ω is varied considering $\mu = 0.9U$ and $J = 0.006U$ in the SFT framework for simple cubic and square lattices, respectively. These are the same scenarios reported by Figs. 4-3(a) and 4-3(e). The temperatures addressed in our analysis, $k_B T = 0.04U$ (blue) and $k_B T = 0.4U$ (red), are located near each maximum of c_μ as the inset panel illustrates. The noticed resonances can be thought in terms of transitions between local occupation number states, which are eigenvectors of the atomic limit Hamiltonian explored in Sec. 4.1. As demonstrated in Appendix F.2, the local spectral function in the atomic limit reads as

$$\begin{aligned} A^{(0)}(\omega) &= \frac{1}{\mathcal{Z}^{(0)}} \sum_n \delta(\omega - \Delta E_{n \rightarrow n+1}) (n+1) e^{-\beta E_n} \\ &- \frac{1}{\mathcal{Z}^{(0)}} \sum_n \delta(\omega - \Delta E_{n-1 \rightarrow n}) n e^{-\beta E_n}, \end{aligned} \quad (4.12)$$

a collection of delta functions centered around the energy level transitions $E_{n \rightarrow m} = E_m - E_n$. With the perturbative inclusion of hopping, the relevant observed Hubbard bands emerge from such values, with a particular shape reflecting the dimensionality of each case.

Regarding the low-temperature regime (blue curve), there are contributions from only three transitions: singlon-holon $|1\rangle \rightarrow |0\rangle$, singlon-doublon $|1\rangle \rightarrow |2\rangle$ and doublon-triplon $|2\rangle \rightarrow |3\rangle$. Given its larger width, the most relevant of them is the portion $|1\rangle \rightarrow |2\rangle$, because the chosen μ value is close to the transition between states of occupation number 1 and 2. These states at low temperatures produce the Schottky peak as explained in the $J = 0$ scenario. Regarding the second maximum (red curve), other states of higher energy start to become available such as the transition triplon-quadruplon $|3\rangle \rightarrow |4\rangle$, while the transition singlon-doublon $|1\rangle \rightarrow |2\rangle$ becomes less probable to happen. Therefore, the spectral distribution suggests that the second specific heat peak contains contributions from the thermal mixing of states as already indicated in Sec. 4.1.

Correlations and the Double Peaks

As pointed out by Figs. 4-3(a) and 4-3(e), the first maximum appearing in the specific heat versus temperature plot presents a reduction when compared to the atomic limit case. In Fig. 4-5, we address a detailed view on this subject considering the simple cubic setup for deep lattices $J = 0.006U$ (the results for the square lattice are quantitatively similar in such regime) for three values of chemical potential $\mu = 0.7U$ (purple), $\mu = 0.8U$ (green) and $\mu = 0.9U$ (orange). Colored dots symbolize SFT calculations while the respective continuous lines represent the results obtained via perturbation theory until second order on J/U . Figure 4-5(a) exhibits c_μ as T varies in the described scenario, including the atomic limit results as continuous gray lines. We observe that the deviations from the $J = 0$ situation become more prominent as the chemical potential approaches $\mu = 1.0U$. Since the specific heat is essentially a second derivative of the free energy with respect to the temperature, we show in Fig. 4-5(b) the difference $\Delta\Omega = \Omega - \Omega^{(0)}$ of the system's free energy Ω in the presence of hopping, $J = 0.006U$, relative to its atomic limit $\Omega^{(0)}$, $J = 0$. For $\mu = 0.7U$ the contribution introduced by the hopping term to the free energy is relatively small. However, for $\mu = 0.8U$ and $\mu = 0.9U$, we verify more important deviations in a low-temperature regime. Such prominent curvature in the free energy implies a relevant second derivative. This gets translated into a contribution to c_μ , which becomes the mentioned reduction of the first maximum.

The question remaining is what physical mechanism is generating such curvature in the free energy. Since the inclusion of the tunneling term induces correlations among particles located at different sites, we analyze the atom-atom correlation function [165, 166] defined by

$$\mathcal{C}_{j'j} = \langle b_{j'}^\dagger b_j \rangle, \quad (4.13)$$

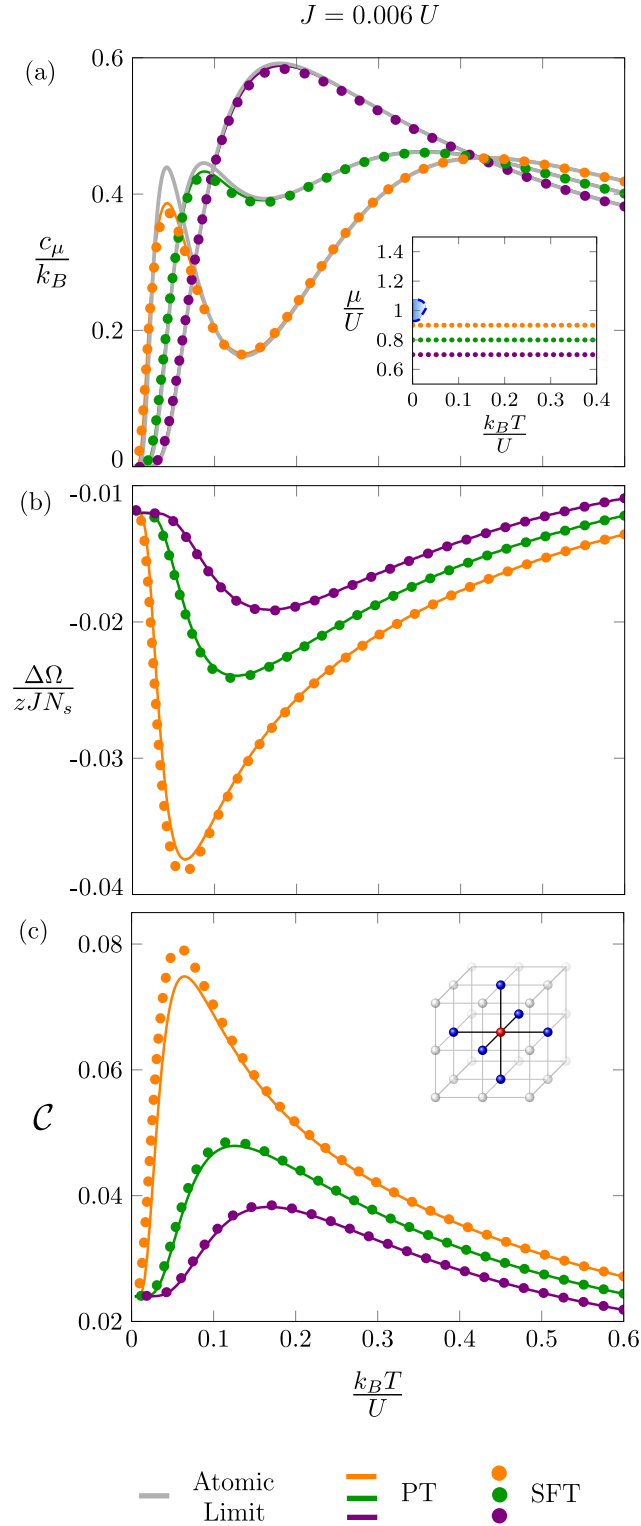


Figure 4-5: The specific heat c_μ (a), free energy variation $\Delta\Omega$ (b) and atom-atom correlation \mathcal{C} (c) are shown as functions of temperature at $J = 0.006U$. Three values of chemical potential are considered $\mu = 0.7U$ (purple), $\mu = 0.8U$ (green) and $\mu = 0.9U$ (orange) as the inset phase diagram μT reveals. The dots represent SFT calculations while the respective colored continuous lines symbolize results from perturbation theory. The atomic limit results of c_μ in (a) are shown as gray continuous curves.

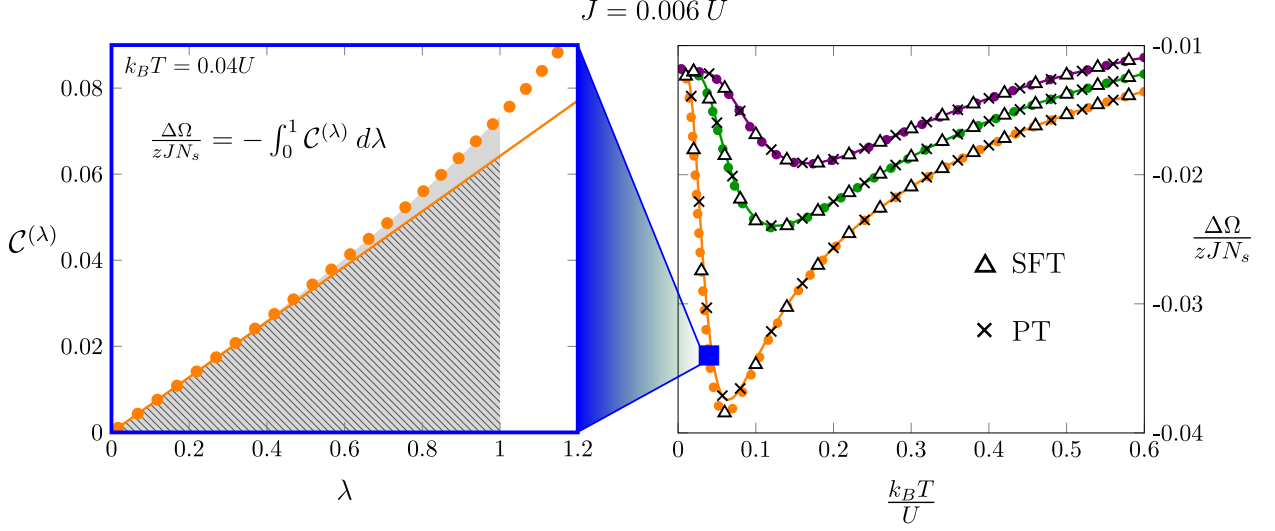


Figure 4-6: In the right panel, $\Delta\Omega$ is plotted against temperature T showing the agreement between points (crosses and triangles) evaluated through Eq. (??) and the curves from Fig. ??(b). Crosses and triangles correspond to perturbation theory and SFT calculations, respectively. For $k_B T = 0.04U$ and $\mu = 0.9U$, the left panel illustrates how these points are determined by integration of the correlation functions $\mathcal{C}(\lambda)$.

for atoms at sites j' and j . The atom-atom correlation is directly related to the imaginary-time Green's function

$$\mathcal{G}_{jj'}(\tau, \tau') = -\langle \mathcal{T}[b_j(\tau)b_{j'}^\dagger(\tau')] \rangle, \quad (4.14)$$

according to $\mathcal{C}_{j'j} = -G_{jj'}(0, 0^+)$. Also, the atom-atom correlation function can be indirectly probed experimentally since it is related to the Fourier transform of the momentum distribution function

$$n(\mathbf{k}) = \frac{|w(\mathbf{k})|^2}{N_s} \sum_{j,j'} \mathcal{C}_{j'j} e^{-i\mathbf{k}(\mathbf{r}_{j'} - \mathbf{r}_j)}, \quad (4.15)$$

where $w(\mathbf{k})$ is the Fourier transform of the Wannier function. This quantity is measured by the time-of-flight absorption experiments, in which the trapping field is turned off enabling the cloud of atoms to expand during a certain amount of time [167, 168]. More specifically, we focus our attention to the atom-atom correlation function between first neighbors (since the particles of the model are able to hop to first-neighbor sites), denoted simply as \mathcal{C} , because the system is homogeneous. In

Fig. 4-5(c) we show \mathcal{C} as a function of the temperature, mirroring the parameters of Figs. 4-5(a) and 4-5(b). Similarly to the corrections in free energy $\Delta\Omega$, the correlations become important as we increase the chemical potential towards the integer values of U , developing a sharp peak at low temperatures $k_B T \approx 0.1U$.

The impact of the correlations on the free energy can be examined in an analytical perspective. Indeed, it is possible to exactly determine the free energy from the atom-atom correlation function based on the introduction of a continuous coupling parameter, following Refs. [106, 107]. First, we parametrize the Hamiltonian of Eq. (3.1) in the form

$$H^{(\lambda)} = H^{(0)} + \lambda \mathcal{H} , \quad (4.16)$$

where $H^{(0)}$ corresponds to the atomic limit defined in Eq. (4.3) and \mathcal{H} is the kinetic term

$$\mathcal{H} = -J \sum_{\langle i,j \rangle} b_i^\dagger b_j . \quad (4.17)$$

Note that the value $\lambda = 0$ correspond to the atomic limit, while $\lambda = 1$ recovers the original model considered, with $H^{(1)} = H$. As demonstrated in Appendix F.3, the change in free energy caused by the hopping reads as

$$\Delta\Omega = \int_0^1 \langle \mathcal{H} \rangle_\lambda d\lambda , \quad (4.18)$$

where the thermal averages $\langle \dots \rangle_\lambda$ are taken with respect to the Hamiltonian of Eq. (4.16). The definitions from Eqs. (4.17) and (4.13) substituted into Eq. (4.18) lead to the exact expression

$$\Delta\Omega = -z J N_s \int_0^1 \mathcal{C}^{(\lambda)} d\lambda , \quad (4.19)$$

with $\mathcal{C}^{(\lambda)} = \langle b_{j'}^\dagger b_j \rangle_\lambda$ for first neighbors j and j' thermally averaged at a hopping value of λJ . This expression relates the theoretical free energy to the atom-atom correlation,

an indirect measurable quantity, by a process of charging up the tunneling amplitude until the desired value. Through Fig. 4-6, we verify the agreement between both sides of Eq. (4.19) considering SFT and perturbative methods. In particular, perturbation theory up to second order yields the direct relation

$$\Delta\Omega = -\frac{zJN_s}{2} \mathcal{C} + \mathcal{O}(J^4) . \quad (4.20)$$

Therefore, the low-temperature correlations, which grow near integers multiples of the interaction, generate an important curvature change to the free energy, whose impact is revealed in the reduction of the first maximum of the specific heat.

Chapter 5

Geometry, Thermodynamics and Legendre Transformations

“There are far, far better things ahead than any we leave behind.”

– C. S. Lewis

Our analysis of the Bose Hubbard model thermodynamics was based on the Self-Energy Functional Theory, which is essentially a composition of Legendre transformations. We devote this chapter to discuss more deeply the Legendre transformations (one of the basis of our work) in a general and conceptual framework. The most important point addressed is the visualization of the Legendre Transformation as an extremum principle. Here we explore the physical content regarding the Gibbs space geometry, its direct and natural relation to Legendre transformations and stability conditions about the equilibrium states.

Thermodynamics present in modern applications. Concerning the classical aspects of its logical construction (formulation), two schemes stand out: the thermodynamics of Clausius and Kelvin, with axiomatic foundations formulated by Carathéodory; and the Gibbs approach, with precise postulational basis given by Tisza [169, 170].

Thermodynamic systems or subsystems are treated as spatially disjoint volume elements, whose states are determined by a set of extensive quantities (variables proportional to the overall scale of the system) like energy/entropy, volume and number

of particles. In this framework, the complete information about each subsystem is contained in the so-called fundamental equation, formulated in entropy/energy representations. The phase space spanned by these extensive variables is designated as *Gibbs space* and it plays an important role in the mathematical development of the theory. When the flux of such parameters between subsystems is allowed through the manipulation of appropriate walls, thermodynamic processes are said to occur. The new equilibrium state achieved is postulated to be the one which maximizes/minimizes the total entropy/energy restricted to manifold of the constrained variables. The essence of the theory relies on an extremum principle, just as seen in different context of physics. The application of the variational principle to the system coupled to reservoirs of extensive quantities leads naturally to the Legendre transformations. The procedure generates equations of states as solutions and also provide a test for the thermodynamic stability for local and global fluctuations about the obtained equilibrium states. Here we focus on the physical interpretation of some properties and elements regarding the geometry of the Gibbs space and Legendre transformations. Particularly, how these transformations naturally codify a test for thermodynamic stability with the compliance coefficients (or response functions) and the well known Maxwell construction.

5.1 Basic Definitions and the Variational Principle

We consider a composite thermodynamic system $\tilde{\sigma}$, constituted by a collection of simple subsystems $\{\sigma^{(\alpha)}\}$. Its equilibrium states are parametrized by a set of coordinates comprising $m + 1$ extensive variables $\mathbf{X}^{(\alpha)} = \left(X_1^{(\alpha)}, \dots, X_{m+1}^{(\alpha)}\right)$, which can encompass energy/entropy, volume, and number of particles. The subsystem's boundaries may be permeable or not to the flux of such quantities, according to the appropriate collection of thermodynamic walls. The set of parameters $\{\mathbf{X}^{(\alpha)}\}$ specifies the state of the composite system; each quantity is considered additive over its subsystems, as well as conserved if the total system is isolated. Hence, the composite

system variables satisfy

$$\tilde{\mathbf{X}} = \sum_{\alpha} \mathbf{X}^{(\alpha)}, \quad (5.1)$$

summed over all the subsystems. The referred thermodynamic walls constitute the internal constraints for the composite system, represented by relations $\omega_i(\{\mathbf{X}^{(\alpha)}\}) = 0$. For simplicity, we symbolize this set of equations by ω . These relations determine a new set of free variables usually called virtual states: states that are consistent with the imposed constraints. In this sense, virtual processes or displacements correspond to variations from one virtual state to another.

Based on these definitions, the classical thermodynamics is essentially developed from a variational principle, as usually seen in other areas of physics. In the present context, this idea is constructed by assigning to each subsystem an entropy function (also called fundamental equation or thermodynamic potential) $\Psi^{(\alpha)} = \Psi^{(\alpha)}(\mathbf{X}^{(\alpha)})$, first-order homogeneous, continuous, with piecewise continuous higher-order derivatives. The total entropy $\tilde{\Psi}$ of the composite system is introduced as an additive function over its components

$$\tilde{\Psi}(\{\mathbf{X}^{(\alpha)}\}) = \sum_{\alpha} \Psi^{(\alpha)}(\mathbf{X}^{(\alpha)}). \quad (5.2)$$

since the interactions among them are considered short ranged. The occurrence of thermodynamic processes, defined as the transfer of extensive quantities between the subsystems, is mediated by the modification of internal constraints, symbolized by the transformation $\omega \mapsto \theta$. In such scenario, the extremal principle is structured as follows: the new state of equilibrium achieved $\{\mathbf{X}_0^{(\alpha)}\}$ is such that it maximizes the total entropy restricted to the manifold of new internal constraints. In other terms, from all possible states obeying the restrictions $\theta_i(\{\mathbf{X}^{(\alpha)}\}) = 0$, the state of thermodynamic equilibrium $\{\mathbf{X}_0^{(\alpha)}\}$ corresponds to the largest value of total entropy:

$$\tilde{\Psi}(\{\mathbf{X}_0^{(\alpha)}\}) = \max \left\{ \sum_{\alpha} \Psi^{(\alpha)}(\mathbf{X}^{(\alpha)}) \right\}. \quad (5.3)$$

Therefore, the description of a thermodynamic system relies not only on defining its subsystems, through the corresponding fundamental equations, but also on the identification of its internal constraints.

The entropy maximum principle can be reformulated in terms of the internal energy $\Phi^{(\alpha)}$, represented by one of the variables $X_1^{(\alpha)}, \dots, X_{m+1}^{(\alpha)}$. The postulate of Eq. (5.3) becomes equivalent to the minimization of the total internal energy

$$\tilde{\Phi}(\{\mathbf{X}_0^{(\alpha)}\}) = \min \left\{ \sum_{\alpha} \Phi^{(\alpha)}(\mathbf{X}^{(\alpha)}) \right\}, \quad (5.4)$$

respecting the analogous constraints. The inversion of Eq. (5.2) is allowed locally since the derivative $\frac{\partial \Psi^{(\alpha)}}{\partial \Phi^{(\alpha)}} = \frac{1}{T^{(\alpha)}}$ is the inverse temperature, a quantity regarded as positive. These representations correspond to different physical configurations and setups. In the entropy scheme, the total system is considered in isolation with constant total energy while the entropy is permitted to vary. The energy scheme allows for fluctuations in energy at fixed total entropy by the coupling of an external working source.

First we analyze the variational principle in a local perspective, studying infinitesimal virtual displacements around the equilibrium state. For a local extremum, the condition

$$\delta \tilde{\Phi} = 0 \quad (5.5)$$

implies the equality of the thermodynamic potential's first derivatives

$$P_j^{(\alpha)} = \frac{\partial \Phi^{(\alpha)}}{\partial X_j^{(\alpha)}}, \quad (5.6)$$

with

$$P_j^{(\alpha)} = P_j^{(\beta)} \quad (5.7)$$

for all $j = 1, \dots, m$ and α, β coupled through the exchange of X_j . These intensive quantities are named as the fields $P_j^{(\alpha)}$ conjugated to $X_j^{(\alpha)}$ and they act like passive generalized forces induced by the corresponding permeable walls. The relations brought by Eqs. (5.6) determine the so-called equations of state in a local scope. The entropic representation receives the notation

$$H_j^{(\alpha)} = \frac{\partial \Psi^{(\alpha)}}{\partial X_j^{(\alpha)}}. \quad (5.8)$$

The fundamental equation lacks direct physical appeal, sometimes distant from the experimental reality. Indeed, the connection between the formalism and the laboratory environment is established more properly by the already mentioned equations of state. As discussed in the Sec. 5.2, they are naturally generated by Legendre transformations, arising from an adaptation of the extremum principle considering interactions between the system and proper reservoirs. In spite of being an extensively discussed subject, its possible to connect the Legendre transformations and the geometry of the Gibbs space through an unified view encompassing the obtaining of equations of state, and the analysis of local and global stability criteria.

5.2 Legendre Transformations

The Legendre transformations are commonly associated to the convex envelope or supporting hyperplanes of sufficient regular functions [171, 172], connected to the duality between points and lines [173]. Indeed, they preserve the information content of the original function by relating an element of the Gibbs manifold to its respective tangent space as illustrated in Fig. 5-1(a). This association is actually a consequence of the ideas brought by the extremal principle, subjecting it to adequate constraints. To explore this latent meaning in a geometrical perspective, we generalize the mental experiment from the previous section.

We consider a composite system $\tilde{\sigma}$ constituted by the studied system σ and a reservoir σ^R . The later is characterized by the intensive parameter P^R conjugated

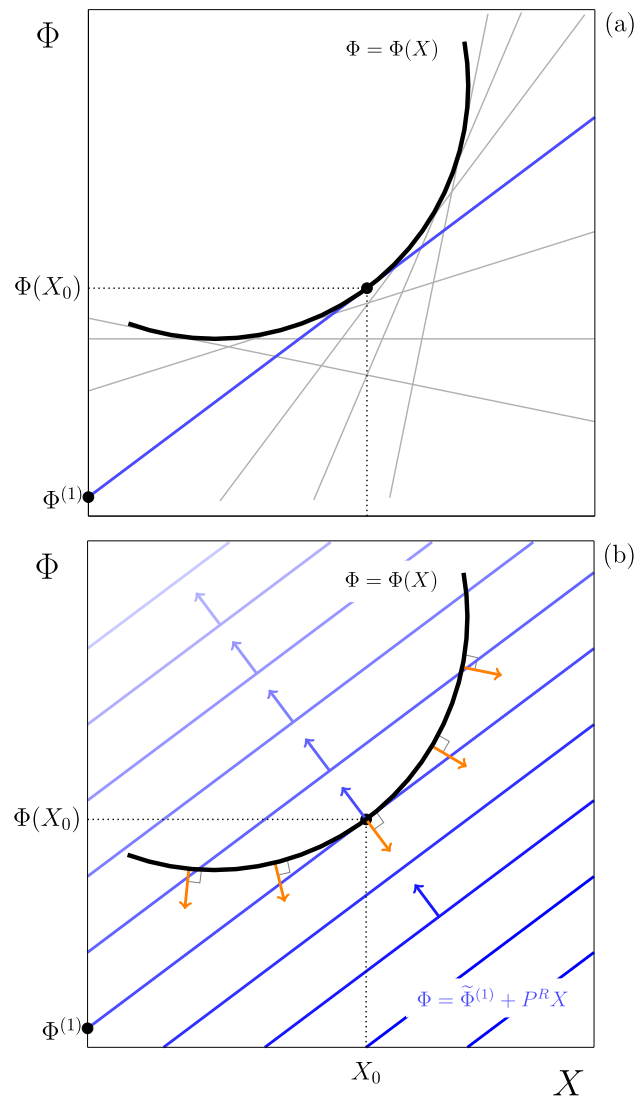


Figure 5-1: Panel (a) depicts the fundamental equation as a function of the extensive variable X , with some of its tangent lines. Their intercepts with the Φ axis determine the Legendre transform $\Phi^{(1)}$. An equivalent construction is shown in (b), considering the intrinsic variational character of the discussed problem. The contour curves of $\tilde{\Phi}^{(1)} = \Phi - P^R X$ are shown as the blue lines with constant slope P^R , concerning the reservoir σ^R . This function is explicitly minimized subjected to the constraint $\Phi = \Phi(X)$, regarding the system σ originally studied. Arrows symbolize the gradient vectors of the corresponding curves. At the extremum solution X_0 , the gradient vectors become parallel, with $P^R = P$. The minimum value reached by the intercepts is $\Phi^{(1)} = \Phi^{(1)}(P^R)$, the Legendre transform of Φ at the value P^R . The extremization procedure yields also the equation of state $X_0 = X_0(P^R)$.

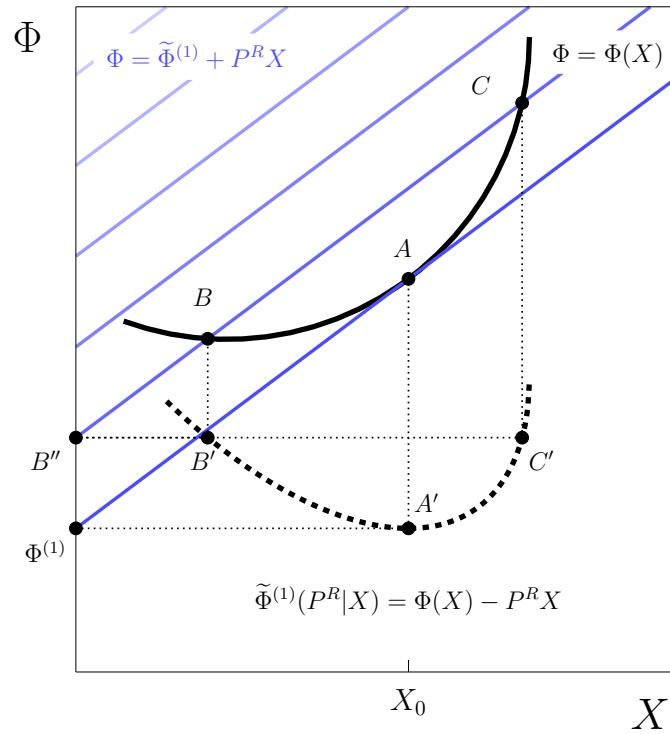


Figure 5-2: The geometrical construction of the potential $\tilde{\Phi}^{(1)}(P^R|X) = \Phi(X) - P^R X$, involved in the reformulation of the extremal principle. The points A , B and C correspond to the intersection of $\Phi = \Phi(X)$ and the level curves $\Phi = \tilde{\Phi}^{(1)} + P^R X$. The intercepts A' , B' and C' projected into the X axis yields A'' , B'' and C'' , composing the function $\tilde{\Phi}^{(1)}(P^R|X)$ (dotted curve). Its minimum value is the Legendre transform $\Phi^{(1)}$ of Φ at fixed P^R .

to the extensive variable X . Both system are allowed to exchange X through a corresponding permeable wall. The total energy is additive over its subsystems with

$$\tilde{\Phi}(X, X^R) = \Phi(X) + \Phi^R(X^R) . \quad (5.9)$$

As Eq. (5.4) postulates, the equilibrium state (X_0, X_0^R) reached by the transfer of X is such that $\tilde{\Phi}(X_0, X_0^R) \leq \tilde{\Phi}(X, X^R)$, for any state (X, X^R) satisfying the imposed constraint

$$\tilde{X} = X + X^R , \quad (5.10)$$

with \tilde{X} constant. This implies that the deviation from equilibrium

$$\Delta\tilde{\Phi} \equiv \tilde{\Phi}(X, X^R) - \tilde{\Phi}(X_0, X_0^R) \geq 0 \quad (5.11)$$

must be positive-definite. We decompose this variation through Eq. (5.9), following the contribution of the two subsystems

$$\Delta\tilde{\Phi} = \Delta\Phi + \Delta\Phi^R . \quad (5.12)$$

According to Eq. (5.10), the fluxes of the analysed quantities vary in the opposite sense

$$\Delta X^R = -\Delta X \quad (5.13)$$

in order to ensure the conservation of \tilde{X} . The choice of a reservoir σ^R mediating the interactions with σ provides a particularly simple variation for the total thermodynamic potential. Since the higher order derivatives of P^R are negligible for a reservoir, $\Delta\Phi^R$ becomes simply

$$\Delta\Phi^R = P^R \Delta X^R . \quad (5.14)$$

Indeed, using Eqs. (5.13) and (5.14), we rewrite Eq. (5.12) as

$$\begin{aligned}\Delta\tilde{\Phi} &= \Delta\Phi - P^R\Delta X \\ &= \Delta(\Phi - P^RX) ,\end{aligned}\tag{5.15}$$

since P^R is fixed. The energy minimum postulate brought by Eq. (5.11) and the deviation expressed in Eq. (5.15) imply that the equilibrium state achieved minimizes the function

$$\tilde{\Phi}^{(1)}(P^R|X) \equiv \Phi(X) - P^RX .\tag{5.16}$$

Consequently, the Legendre transform $\Phi^{(1)}(P^R)$ is defined by the solution of the variational procedure

$$\begin{aligned}\Phi^{(1)}(P^R) &= \min_X\{\Phi(X) - P^RX\} \\ &= \min_X\tilde{\Phi}^{(1)}(P^R|X) \\ &= \tilde{\Phi}^{(1)}(P^R|X_0) ,\end{aligned}\tag{5.17}$$

for each value of P^R as the reservoirs are varied. The solution obtained develops into an equation of state, with

$$X_0 = X_0(P^R) .\tag{5.18}$$

These steps reformulate the extremal principle, allowing for fluctuations in the studied system. They reveal the essential ingredient composing the Legendre transformations: the maintenance of the variational principle adapted to a set of new constraints.

As typically done under these circumstances, the optimization problem in the presence of constraints is treated employing Lagrange multipliers, as Fig. 5-1(b) depicts. In the $X\Phi$ plane, the minimization of $\tilde{\Phi}^{(1)}(P^R|X)$ is equivalent to finding the

minimum value of the function

$$\tilde{\Phi}^{(1)}(P^R|X) = \Phi - P^R X , \quad (5.19)$$

for a constant value of P^R and restricted to the manifold

$$\Phi = \Phi(X) . \quad (5.20)$$

The level curves of $\tilde{\Phi}^{(1)}$ correspond to a family of lines with slope P^R ; their values constitute the intercepts of the Φ axis ($X = 0$). By defining the function $h(\Phi, X) = \Phi(X) - \Phi$, which is identically zero, the solution to the posed problem satisfies

$$\nabla \tilde{\Phi}^{(1)} = \lambda \nabla h , \quad (5.21)$$

corresponding to the equilibrium state X_0 . Geometrically, this codifies the parallelism of the gradient vectors regarding the considered curves. In other terms, the minimum value assumed by the intercepts of the refereed lines, restricted to $\Phi = \Phi(X)$, occurs for the line tangent to the system's fundamental relation curve. Precisely, the components of Eq. (5.21) yield

$$\frac{\partial \tilde{\Phi}^{(1)}}{\partial \Phi} = \lambda \frac{\partial h}{\partial \Phi} \iff \lambda = -1 , \quad (5.22)$$

and

$$\frac{\partial \tilde{\Phi}^{(1)}}{\partial X} = \lambda \frac{\partial h}{\partial X} \iff -P^R = \lambda \frac{\partial \Phi}{\partial X} , \quad (5.23)$$

whose combination provides

$$P^R = \frac{\partial \Phi}{\partial X} . \quad (5.24)$$

This relation brings up the equilibrium condition

$$P = P^R , \quad (5.25)$$

corroborating the equivalence between the tangent planes construction and the extremal principle adapted to the interaction with the reservoir.

Going further in our analysis, Fig. 5-2 details the geometrical construction of the function $\tilde{\Phi}^{(1)}(P^R|X)$, which is set to be minimized. As an example, the points A , B and C signal the crossing of the fundamental equation $\Phi = \Phi(X)$ and the family of parallel lines $\Phi = \tilde{\Phi}^{(1)} + P^R X$. The intercepts of these lines with the Φ axis correspond to the values of $\tilde{\Phi}^{(1)}$, designated by A' , B' , and C' . These points projected into their respective X values determine A'' , B'' , and C'' , which compose the function $\tilde{\Phi}^{(1)}(P^R|X)$ illustrated as the dotted curve. Indeed, the lengths of the segments AA'' , BB'' , and CC'' are equal to $P^R X$; when the $\Phi(X)$ values (the points A , B , and C) are subtracted by $P^R X$ (the length of AA'' , BB'' , and CC''), we obtain $\tilde{\Phi}^{(1)}(P^R|X)$. This affine construction naturally produces the Legendre transform as the extremal solution to the posed variational procedure, yielding an equation of state. The fluctuations of the variable X between the system and the reservoir are such that they minimize this new function, combining elements from the system and the reservoir.

To generalize our discussion in the multivariable case, we define the successive Legendre transform of order k by

$$\Phi^{(k)}(P_k) = \min_{X_k} \tilde{\Phi}^{(k)}(P_k|X_k) , \quad (5.26)$$

following the extremization of

$$\tilde{\Phi}^{(k)}(P_k|X_k) \equiv \Phi^{(k-1)}(X_k) - P_k X_k . \quad (5.27)$$

Its solution, the equation of state

$$X_{k,0} = X_{k,0}(P_k) , \quad (5.28)$$

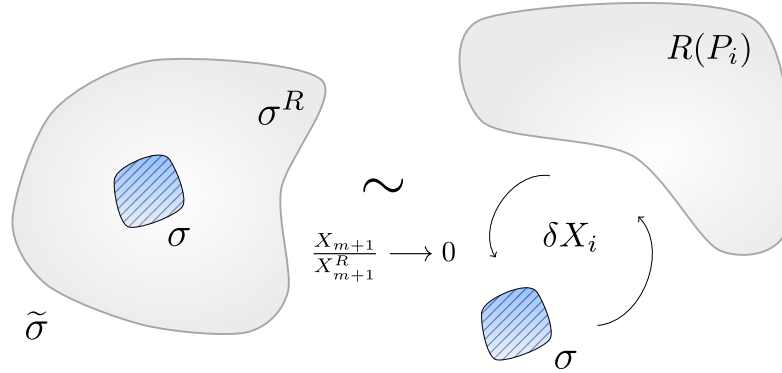


Figure 5-3: Schematic representation of a thermodynamic system $\tilde{\sigma}$ and the mental experimental system which enables the analysis of the fluxes δX_i , obeying the originally imposed constraints. In the left hand side, we highlight a subsystem σ , with a fixed scale parameter X_{m+1} . The right hand portion presents the limit $\frac{X_{m+1}}{X_{m+1}^R} \rightarrow 0$ leading to a replica of the studied system interacting with reservoirs $R(P_i)$ of extensive quantities X_i .

is such that

$$\Phi^{(k)}(P_k) = \tilde{\Phi}^{(k)}(P_k | X_{k,0}) . \quad (5.29)$$

Only the dependence on the transformed parameters is addressed; the complete notation reads as $\Phi^{(k)} = \Phi^{(k)}(P_1, \dots, P_k, X_{k+1}, \dots, X_{m+1})$.

5.3 Thermodynamic Stability

The variational procedure can be employed not only to obtain the equilibrium state \mathbf{X}_0 of a homogeneous system $\tilde{\sigma}$ but also to probe its thermodynamic stability. In order to do so, we analyze the system's response to global or local fluctuations starting from the attained equilibrium state. (define global and local variations).

Local Stability

The presented formulation imposes an inherent obstacle: the fluctuations from the equilibrium value as a test to the stability must not violate the originally imposed constraints. We overcome this difficulty by highlighting a subsystem σ , with a fictitious boundary with the complementary subsystem σ^R . In analogy to the set theory,

we write the described decomposition in the form $\tilde{\sigma} = \sigma \cup \sigma^R$. Such procedure enables the analysis of fluctuations about an equilibrium state obeying the system's constraints. If we assign to each subsystem its fundamental equation, the total energy becomes

$$\tilde{\Phi}(\mathbf{X}, \mathbf{X}^R) = \Phi(\mathbf{X}) + \Phi^R(\mathbf{X}^R), \quad (5.30)$$

with the enclosure relations

$$\tilde{\mathbf{X}} = \mathbf{X} + \mathbf{X}^R. \quad (5.31)$$

The subsystem σ can be regarded as a re-scaled replica of the original one due to its homogeneity.

We submit σ to a virtual process about the equilibrium state $(\mathbf{X}_0, \mathbf{X}_0^R)$. The minimum energy postulate states that $\Delta\tilde{\Phi} \equiv \tilde{\Phi}(\mathbf{X}, \mathbf{X}^R) - \tilde{\Phi}(\mathbf{X}_0, \mathbf{X}_0^R) \geq 0$, for any $(\mathbf{X}, \mathbf{X}^R)$ compatible with the constraints of Eq. (5.31). In terms of a Taylor expansion about $(\mathbf{X}_0, \mathbf{X}_0^R)$, this variation of the total energy corresponds to

$$\begin{aligned} \Delta\tilde{\Phi} &= \Delta\Phi + \Delta\Phi^R \\ &= (\delta\Phi + \delta^2\Phi + \dots) + (\delta\Phi^R + \delta^2\Phi^R + \dots). \end{aligned} \quad (5.32)$$

In a local neighborhood of the equilibrium state, the thermodynamic potential satisfies $\delta\tilde{\Phi} = \delta\Phi + \delta\Phi^R = 0$, according to Eq. (5.5). Hence, the remaining higher order terms provide

$$\Delta\tilde{\Phi} = (\delta^2\Phi + \delta^3\Phi + \dots) + (\delta^2\Phi^R + \delta^3\Phi^R + \dots). \quad (5.33)$$

Additionally, we can fix a scale parameter from the set of variables describing the system. Usually the number of particles or volume in a simple fluid; here we designate this variable as X_{m+1} . By employing the extensive property of the thermodynamic

potential, we define the following generalized densities for σ

$$\phi = \frac{\Phi}{X_{m+1}} \quad \text{and} \quad x_i = \frac{X_i}{X_{m+1}}, \quad (5.34)$$

and the subsystem σ^R

$$\phi^R = \frac{\Phi^R}{X_{m+1}^R} \quad \text{and} \quad x_i^R = \frac{X_i^R}{X_{m+1}^R}, \quad (5.35)$$

considering $i = 1, \dots, m$. As both subsystems are complementary parts of the total system, the homogeneity condition brings the equation

$$\frac{\partial^2 \phi}{\partial x_i \partial x_j} = \frac{\partial^2 \phi^R}{\partial x_i^R \partial x_j^R}, \quad (5.36)$$

which readily yields

$$\frac{\partial^2 \Phi^R}{\partial X_i^R \partial X_j^R} = \frac{X_{m+1}}{X_{m+1}^R} \frac{\partial^2 \Phi}{\partial X_i \partial X_j}. \quad (5.37)$$

Since \tilde{X}_i is fixed, the restrictions from Eq. (5.31) imply

$$\delta \tilde{X}_i = -\delta \tilde{X}_i^R, \quad (5.38)$$

for all $i = 1, \dots, m$. The combination of Eqs. (5.37) and (5.38) relates the second order variations for σ^R and σ to the scale factor previously chosen according to

$$\delta^2 \Phi^R = \frac{X_{m+1}}{X_{m+1}^R} \delta^2 \Phi. \quad (5.39)$$

Similarly, the higher order variations also obey analogous relations

$$\delta^k \Phi^R = (-1)^k \left(\frac{X_{m+1}}{X_{m+1}^R} \right)^{k-1} \delta^k \Phi. \quad (5.40)$$

Note that $k = 1$ recovers the condition regarding a local extremum, from which we extract the equality between the intensive fields or generalized forces. In the limit

$$\frac{X_{m+1}}{X_{m+1}^R} \rightarrow 0, \quad (5.41)$$

the complementary system σ^R can be regarded as a reservoir if compared to the selected subsystem σ , which plays the role of a replica in reduced scale of the total system $\tilde{\sigma}$. This mental experiment is represented schematically in Fig. 5-3.

Considering the described scenario, the variation of the thermodynamic potential given in Eq. (5.33) simplifies to

$$\Delta\tilde{\Phi} \rightarrow \delta^2\Phi + \delta^3\Phi + \dots \quad (5.42)$$

Therefore, the sign of the quadratic form $\delta^2\Phi$ determines the thermodynamic stability in a local scope. Explicitly, the second variation $\delta^2\phi = \delta^2\phi(\mathbf{x}_0; \mathbf{x})$ of $\phi = \phi(x_1, \dots, x_m)$ is expressed by

$$\delta^2\phi = \frac{1}{2} \sum_{i=1}^m \sum_{j=1}^m \phi_{ij} \delta x_i \delta x_j, \quad (5.43)$$

a second order degree polynomial in m variables whose coefficients ϕ_{ij}

$$\phi_{ij} = \frac{\partial^2\phi}{\partial x_i \partial x_j}(\mathbf{x}_0) \quad (5.44)$$

are elements of the hessian matrix of ϕ evaluated at the equilibrium state \mathbf{x}_0 . In matrix notation, Eq. (5.43) becomes

$$\delta^2\phi = \frac{1}{2} \delta\mathbf{x}^T Q \delta\mathbf{x}, \quad (5.45)$$

where $Q = Q(\mathbf{x}_0)$ is the Hessian matrix of ϕ calculated at \mathbf{x}_0 :

$$Q = \begin{bmatrix} \phi_{11} & \phi_{12} & \cdots & \phi_{1m} \\ \phi_{21} & \phi_{22} & \cdots & \phi_{2m} \\ \vdots & \vdots & \ddots & \vdots \\ \phi_{m1} & \phi_{m2} & \cdots & \phi_{mm} \end{bmatrix}. \quad (5.46)$$

We seek a diagonal representation for this bilinear form in order to clarify the conditions determining its positivity. Indeed, every symmetric quadratic form admits a diagonal representation through a linear transformation [174]. Precisely, it is possible to conceive an appropriate change of basis $L : \delta \mathbf{x} \mapsto \delta \mathbf{y}$ given by

$$\delta \mathbf{y} = L \delta \mathbf{x}, \quad (5.47)$$

such that the quadratic form is diagonal

$$\delta^2 \phi = \frac{1}{2} \sum_{i=1}^m \lambda_i \delta y_i^2. \quad (5.48)$$

In a matrix notation, Eq. (5.48) assumes the form

$$\delta^2 \phi = \frac{1}{2} \delta \mathbf{y}^T \Lambda \delta \mathbf{y}, \quad (5.49)$$

with Λ the diagonal matrix

$$\Lambda = \begin{bmatrix} \lambda_1 & 0 & \cdots & 0 \\ 0 & \lambda_2 & \cdots & 0 \\ \vdots & \vdots & \ddots & \vdots \\ 0 & 0 & \cdots & \lambda_m \end{bmatrix}. \quad (5.50)$$

Therefore, both transformation are connected by a conjugation relation

$$Q = L^T \Lambda L. \quad (5.51)$$

Consequently, our stability analysis relies on determining the sign of the coefficients $\{\lambda_i\}$. In general, the referred coordinate transformation is not unique [175]. Nevertheless, the number of positive, negative and null terms among the supra-cited coefficients is always the same. This statement is known as the Sylvester's law of inertia [176], whose name alludes to an intrinsic property of the quadratic form which resists the mentioned change of basis. In a geometrical scope, the dimensions of the maximal subspaces in which the quadratic form is positive or negatively defined are invariant under these circumstances.

Regarding the non uniqueness associated to Q , we seek the transformation carrying physical meaning in the explored context. For example, we can diagonalize the Hessian form through an orthogonal transformation. In the linear algebra scenario, the spectral theorem attests that every symmetric matrix is diagonalizable by an orthogonal transformation, which preserves the euclidean metric. However, such procedure does not exhibit any physical information and meaning for the manifold defined by the fundamental equation in the Gibbs space. On the other hand, the orthogonal transformation finds applications in the context of vibrations and stability of structures, once the physical space is naturally endowed with the euclidean metric. Alternatively, we show in the following that a deeper connection with the thermodynamic structure presented is established when the diagonalization is carried by completing squares, also known as the Lagrange method.

Diagonalization for a non-singular quadratic form

We treat initially a non-degenerate quadratic form, with $\det(Q) \neq 0$. For $\phi_{11} \neq 0$, we separate the terms containing δx_1 , completing the square according to

$$\delta^2\phi = \frac{1}{2} \left\{ \phi_{11} \left(\delta x_1 + \sum_{j=2}^m \frac{\phi_{1j}}{\phi_{11}} \delta x_j \right)^2 + \sum_{i,j=2}^m \left(\phi_{ij} - \frac{\phi_{1i} \phi_{1j}}{\phi_{11}} \right) \delta x_i \delta x_j \right\}. \quad (5.52)$$

Two new parameters naturally arise from this procedure: the coordinate system

$$\delta y_1 = \delta x_1 + \sum_{j=2}^m \frac{\phi_{1j}}{\phi_{11}} \delta x_j , \quad (5.53)$$

as well as the set of coefficients

$$\phi_{ij}^{(1)} = \phi_{ij} - \frac{\phi_{1i} \phi_{1j}}{\phi_{11}} , \quad (5.54)$$

for $i, j = 2, \dots, m$. Including these definitions, Eq. (5.52) becomes

$$\begin{aligned} \delta^2 \phi &= \frac{1}{2} \left\{ \phi_{11} \delta y_1^2 + \sum_{i,j=2}^m \phi_{ij}^{(1)} \delta x_i \delta x_j \right\} \\ &= \frac{1}{2} \phi_{11} \delta y_1^2 + \delta^2 \phi^{(1)} , \end{aligned} \quad (5.55)$$

where the remaining sum was redefined as

$$\delta^2 \phi^{(1)} = \sum_{i,j=2}^m \phi_{ij}^{(1)} \delta x_i \delta x_j . \quad (5.56)$$

As deduced in Eq. (5.55), the reduction process generates the first element in the diagonal representation, given simply by

$$\lambda_1 = \phi_{11} = \frac{\partial^2 \phi}{\partial x_1^2} . \quad (5.57)$$

The coefficients $\phi_{ij}^{(1)}$ defined through Eq. (5.54) receive this label because they are second derivatives of the Legendre transform $\phi^{(1)} = \phi^{(1)}(P_1, x_2, \dots, x_m)$ of ϕ with respect to x_1 ,

$$\phi_{ij}^{(1)} = \left(\frac{\partial^2 \phi^{(1)}}{\partial x_i \partial x_j} \right)_{P_1} , \quad (5.58)$$

evaluated in terms of the natural variables P_1, x_2, \dots, x_m . Also, from the change of coordinates carried by the Legendre transformation, the new coordinate δy_1 addressed

in Eq. (5.53) can be expressed as

$$\delta y_1 = \delta x_1 - \sum_{j=2}^m \left(\frac{\partial x_1}{\partial x_j} \right)_{P_1} \delta x_j . \quad (5.59)$$

Note that we are in the same position when we started the diagonalization process. Therefore, it is possible to develop the next steps by induction. For $\phi_{22}^{(1)} \neq 0$, we obtain the new basis

$$\delta y_2 = \delta x_2 - \sum_{j=3}^m \left(\frac{\partial x_2}{\partial x_j} \right)_{P_1, P_2} \delta x_j , \quad (5.60)$$

and the coefficients

$$\phi_{ij}^{(2)} = \phi_{ij}^{(1)} - \frac{\phi_{2i}^{(1)} \phi_{2j}^{(1)}}{\phi_{22}^{(1)}} . \quad (5.61)$$

The next diagonal element is

$$\lambda_2 = \phi_{22}^{(1)} = \left(\frac{\partial^2 \phi^{(1)}}{\partial x_2^2} \right)_{P_1} , \quad (5.62)$$

and the second order variation from Eq. (5.55) transforms into

$$\delta^2 \phi = \frac{1}{2} \phi_{11} \delta y_1^2 + \frac{1}{2} \phi_{22}^{(1)} \delta y_2^2 + \delta^2 \phi^{(2)} . \quad (5.63)$$

In such non-singular case, the complete process provides the following diagonal terms

$$\lambda_k = \phi_{kk}^{(k-1)} = \left(\frac{\partial^2 \phi^{(k-1)}}{\partial x_k^2} \right)_{P_1, \dots, P_{k-1}} , \quad (5.64)$$

obtained through the change of basis

$$\delta y_k = \delta x_k - \sum_{j=k+1}^m \left(\frac{\partial x_k}{\partial x_j} \right)_{P_1, \dots, P_k} \delta x_j , \quad (5.65)$$

for $k = 1, \dots, m - 1$ and

$$\delta y_m = \delta x_m . \quad (5.66)$$

In a matrix language, the transformation L which diagonalizes Q into Λ is given by

$$L = \begin{bmatrix} 1 & -\left(\frac{\partial x_1}{\partial x_2}\right)_{P_1} & \cdots & -\left(\frac{\partial x_1}{\partial x_m}\right)_{P_1} \\ 0 & 1 & \cdots & -\left(\frac{\partial x_2}{\partial x_m}\right)_{P_1, P_2} \\ \vdots & \vdots & \ddots & \vdots \\ 0 & 0 & \cdots & 1 \end{bmatrix} . \quad (5.67)$$

The exposed diagonalization procedure presents a clear physical interpretation based on the presented decomposition for the total system $\tilde{\sigma}$. The artificial partition involves its re-scaled copy σ coupled to the complementary part σ^R , regarded as a reservoir of extensive quantities. This mental construction allows for testing the stability of an equilibrium state through fluctuations which are naturally implemented by Legendre transformations due to their intrinsic variational character. We begin our analysis with the variable x_1 . By enabling fluctuations δx_1 with the remaining variables x_2, \dots, x_m fixed, the extremal principle

$$\Delta \tilde{\phi} > 0 \quad (5.68)$$

transforms into

$$\Delta \tilde{\phi}^{(1)} = \Delta(\phi - P_1 x_1) > 0 , \quad (5.69)$$

following . The local stability with respect to the induced variation requires that the function $\tilde{\phi}^{(1)}$ presents a local minimum at the studied equilibrium state. Precisely, the second fundamental form must be positive definite

$$\delta^2 \tilde{\phi}^{(1)} = \delta^2 \phi = \frac{\partial^2 \phi}{\partial x_1^2} (\delta x_1)^2 > 0 , \quad (5.70)$$

yielding the first diagonal element

$$\lambda_1 = \frac{\partial^2 \phi}{\partial x_1^2} = \frac{\partial P_1}{\partial x_1} > 0. \quad (5.71)$$

This condition permits the local realization of the Legendre transformation involving the conjugate variables x_1 and P_1 . We derive the equation of state

$$x_1 = x_1(P_1, x_2, \dots, x_m) \quad (5.72)$$

as a solution of the extremization problem. Since its infinitesimal deviation $(\delta x_1)_{P_1}$ of x_1 at fixed P_1 is

$$(\delta x_1)_{P_1} = \left(\frac{\partial x_1}{\partial x_2} \right)_{P_1} \delta x_2 + \dots + \left(\frac{\partial x_1}{\partial x_m} \right)_{P_1} \delta x_m, \quad (5.73)$$

the choice $\delta x_1 = (\delta x_1)_{P_1}$ implies $\delta y_1 = 0$, according to Eq. (5.59). This means that, once we perform the Legendre transformation, the analysis of sign regarding the direction δx_1 gets completed. Such procedure verifies automatically the local stability for the corresponding variations. After this, our attention turns towards the fluxes of the variable x_2 conjugated to P_2 . The corresponding successive Legendre transformation of $\phi^{(1)}$ satisfies the condition

$$\Delta \tilde{\phi}^{(2)} = \Delta(\phi^{(1)} - P_2 x_2) > 0, \quad (5.74)$$

which locally produces

$$\delta^2 \tilde{\phi}^{(2)} = \delta^2 \phi^{(1)} = \left(\frac{\partial^2 \phi^{(1)}}{\partial x_2^2} \right)_{P_1} (\delta x_2)^2 > 0, \quad (5.75)$$

where the quantities x_3, \dots, x_m are kept constant. Consequently, we deduce the second diagonal element

$$\lambda_2 = \left(\frac{\partial^2 \phi^{(1)}}{\partial x_2^2} \right)_{P_1} = \left(\frac{\partial P_2}{\partial x_2} \right)_{P_1} > 0. \quad (5.76)$$

The equation of state derived from the new extremal principle

$$x_2 = x_2(P_1, P_2, x_3, \dots, x_m) \quad (5.77)$$

exhibits the local variation

$$(\delta x_1)_{P_1, P_2} = \left(\frac{\partial x_2}{\partial x_3} \right)_{P_1, P_2} \delta x_3 + \dots + \left(\frac{\partial x_2}{\partial x_m} \right)_{P_1, P_2} \delta x_m, \quad (5.78)$$

at fixed P_1 and P_2 . The new basis, shown in (5.77), assumes the form $\delta y_2 = \delta x_2 - (\delta x_1)_{P_1, P_2}$. For infinitesimal deviations determined by the path describing the obtained equation of state, with $\delta x_2 = (\delta x_1)_{P_1, P_2}$, the new basis yields. The diagonalization procedure can be carried out inductively providing the same conclusions. The path or directions in the Gibbs space which test the local stability of a given state are brought by the Legendre transforms through the change of coordinates L . Therefore the algebraic and physical level by the natural structure of Thermodynamics equilibrium. From the positivity of the quadratic form in the energy representation, we extract the Le Chatelier principle

$$\frac{\partial P_k}{\partial x_k} > \left(\frac{\partial P_k}{\partial x_k} \right)_{P_1} > \dots > \left(\frac{\partial P_k}{\partial x_k} \right)_{P_1, \dots, P_{k-1}} > 0, \quad (5.79)$$

where the displacement δx_k corresponds to a gradient of the generalized force δP_k . Such response is larger if the extensive quantities are kept fixed, and progressively smaller if the flux is allowed at fixed fields. Similarly, the local stability requires negative diagonal elements in the entropy representation.

As an example, consider a binary mixture described by a fundamental equation $U = U(S, V, N_1, N_2)$, involving the internal energy as a function of the entropy, volume, and number of particles N_i . From the total number of particles $N = N_1 + N_2$, we define the generalized densities

$$u = \frac{U}{N}, \quad s = \frac{S}{N}, \quad v = \frac{V}{N} \quad \text{and} \quad x = \frac{N_1}{N}. \quad (5.80)$$

The diagonalization of the quadratic form $\delta^2 u$ represented by

$$Q = \begin{bmatrix} \frac{\partial^2 u}{\partial s^2} & \frac{\partial^2 u}{\partial s \partial v} & \frac{\partial^2 u}{\partial s \partial x} \\ \frac{\partial^2 u}{\partial v \partial s} & \frac{\partial^2 u}{\partial v^2} & \frac{\partial^2 u}{\partial v \partial x} \\ \frac{\partial^2 u}{\partial x \partial s} & \frac{\partial^2 u}{\partial x \partial v} & \frac{\partial^2 u}{\partial x^2} \end{bmatrix} \quad (5.81)$$

provides the stability criteria

$$\lambda_1 = \frac{\partial^2 u}{\partial s^2} > 0, \quad (5.82)$$

$$\lambda_2 = \left(\frac{\partial^2 f}{\partial v^2} \right)_T > 0, \quad (5.83)$$

$$\lambda_3 = \left(\frac{\partial^2 g}{\partial x^2} \right)_{T,P} > 0, \quad (5.84)$$

according to . Indeed, these diagonal elements encompass appropriate curvature conditions over the internal energy $u = u(s, v, x)$ and its successive Legendre transforms: the Helmholtz free energy $f = f(t, v, x)$ and Gibbs free energy $g = g(T, P, x)$.

Diagonalization for a singular quadratic form

The so called critical points are commonly considered as the boundary between stable and unstable states. In the explored context, the critical manifold can be defined by the semi definite character of the previously analyzed quadratic form. This condition is achieved whenever one of its diagonal elements, say λ_r , becomes zero; this readily implies $\det Q = 0$. Since the order of the variables is not unique, we choose r with the least value as possible. We discern two possibilities: $r = m$ and $r < m$. In the case $r = m$, with

$$\lambda_m = \phi_{mm}^{(m-1)} = 0, \quad (5.85)$$

the diagonalization procedure is concluded without problems. This is the most usual scenario. Since the quadratic form can assume the value zero, a positive free-energy

variation is guaranteed locally if

$$\frac{\partial^3 \phi^{(m-1)}}{\partial x_m^3} = 0 \quad (5.86)$$

and

$$\frac{\partial^4 \phi^{(m-1)}}{\partial x_m^4} > 0 . \quad (5.87)$$

For the remaining case (responsible for the critical azeotropy in binary mixtures), the diagonalization is interrupted when we arrive at the variable x_r according to

$$\delta^2 \phi = \frac{1}{2} \sum_{i=1}^{r-1} \lambda_i \delta y_i^2 + \delta^2 \phi^{(r-1)} , \quad (5.88)$$

with

$$\delta^2 \phi^{(r-1)} = \sum_{i,j=r}^m \phi_{ij}^{(r-1)} \delta x_i \delta x_j . \quad (5.89)$$

Considering

$$\lambda_r = \phi_{rr}^{(r-1)} = 0 , \quad (5.90)$$

the quadratic form of Eq. (5.89) is semi-definite if

$$\phi_{rj}^{(r-1)} = 0 , \quad (5.91)$$

for $j = r + 1, \dots, m$. Indeed, by choosing the displacements

$$\delta y_i = 0 \quad (5.92)$$

for $1 \leq i \leq r - 1$, as well as

$$\delta x_j = 0 \quad (5.93)$$

for $r + 1 \leq j \leq m$, the quadratic form

$$\delta^2\phi = \phi_{rk}^{(r-1)} \delta x_r \delta x_k + \phi_{kk}^{(r-1)} \delta x_k^2 \quad (5.94)$$

can take on positive and negative values according to the arbitrated values of δx_r and δx_k . Then, we continue the diagonalization process keeping fixed the coordinate x_r , without submitting it to the Legendre transformation. Consequently, there is a decoupling between the sets of variables $\{x_1, \dots, x_{r-1}\}$ and $\{x_{r+1}, \dots, x_m\}$. Collecting the previous results, the critical points are determined by the following conditions

$$\lambda_r = \frac{\partial^3 \phi^{(r-1)}}{\partial x_r^2} = 0, \quad \lambda_j > 0 \quad (j \neq r) \quad (5.95)$$

$$\frac{\partial^3 \phi^{(r-1)}}{\partial x_r^3} = 0, \quad \frac{\partial^4 \phi^{(r-1)}}{\partial x_r^4} > 0 \quad (5.96)$$

$$\frac{\partial^2 \phi^{(r-1)}}{\partial x_j \partial x_r} = 0, \quad (j = r + 1, \dots, m). \quad (5.97)$$

Global Stability and the Maxwell Construction

We extend our stability analysis to global variations, including the emergence of several local minimum states. The general idea is already contained in the extremal principle which can be extended to its Legendre transformations. We highlight the following possibilities: locally

$$\delta^2 \tilde{\Phi}^{(k)} > 0 \quad (5.98)$$

$$\delta^2 \tilde{\Phi}^{(k)} = 0 \quad (5.99)$$

$$\delta^2 \tilde{\Phi}^{(k)} < 0, \quad (5.100)$$

and globally

$$\Delta \tilde{\Phi}^{(k)} \geq 0, \quad (5.101)$$

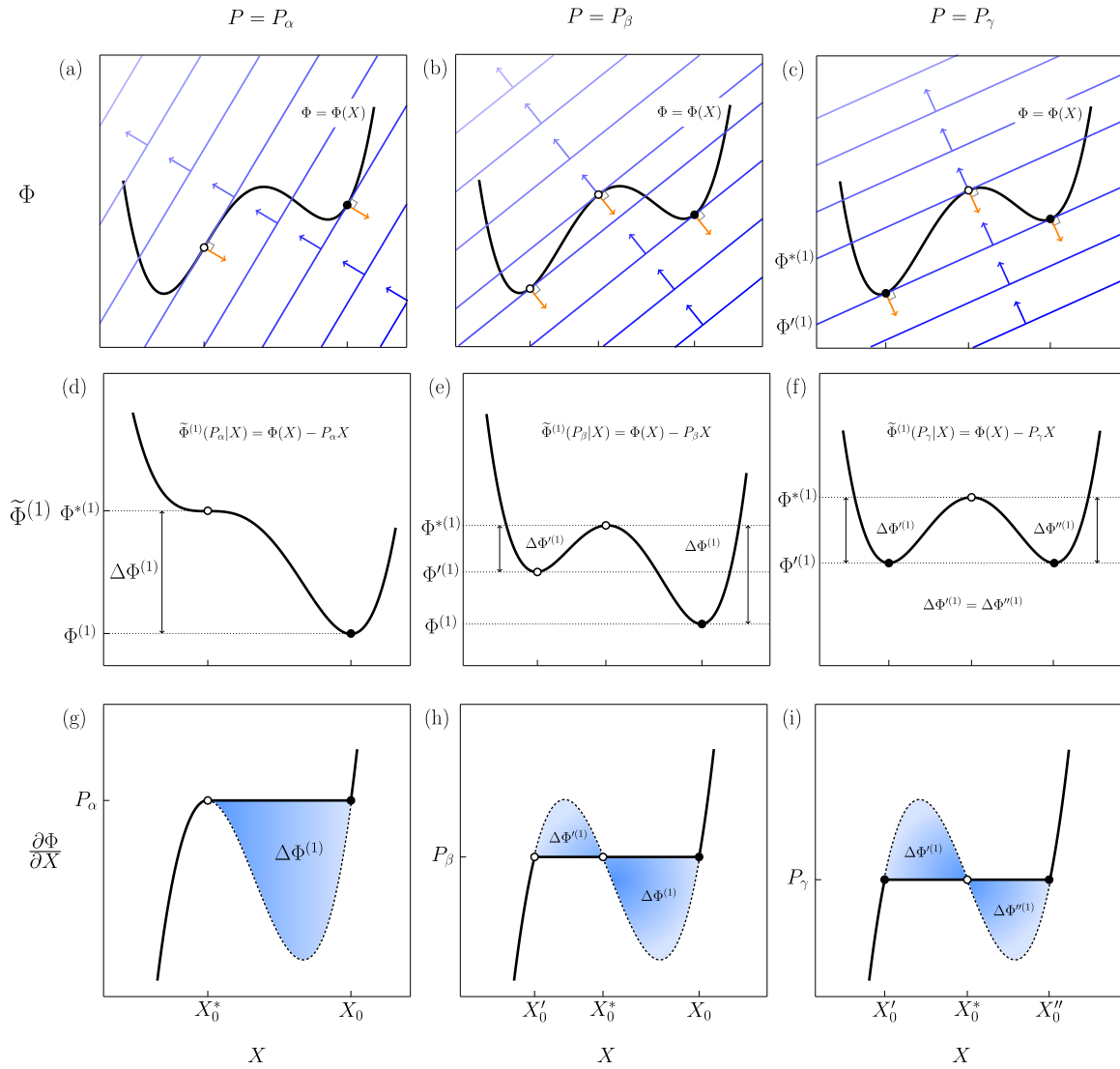


Figure 5-4: The Legendre transformation and the Maxwell Construction, considering three different values of the fixed field P .

for $k = 1, \dots, m$. The equilibrium is stable if the conditions of Eqs. (5.99) and (5.101) are satisfied; in the critical case, the local quadratic approximation for the thermodynamic potential becomes degenerated as stated by Eq. (5.100). Also, if Eq. (5.99) is fulfilled with violation of Eq. (5.101) for a certain displacement, such equilibrium state is designated as metastable. The equilibrium state is unstable if Eq. (5.100) is verified by some local displacement.

We explore these definitions by studying fluctuations of the quantity X (from a fundamental relation $\Phi = \Phi(X)$) obtained via interaction with reservoirs $R(P)$ through Legendre transformations. Figure 5-4 illustrates this procedure based on the described method of Lagrange multipliers, addressing three values of the conjugated field $P_\alpha > P_\beta > P_\gamma$. The respective thermodynamic potentials and families of lines of slope as functions of X are portrayed by Figs. 5-4(a)-(c); the construction of the corresponding potentials $\tilde{\Phi}^{(1)}$ is exhibited in Figs. 5-4(d)-(f) ; finally, Figs. 5-4(g)-(i) depict the equations of state resultant from the extremization procedure and locally symbolized by $\frac{\partial \Phi}{\partial X}$. In Figs., the case $P = P_\alpha$ points out the emergence of a local solution X_0^* to the extremization problem, besides the global minimum X_0 . The colored area in Fig. corresponds to the energetic barrier separating these equilibrium states. Precisely, this is verified because the highlighted region corresponds to the variation as follows

$$\begin{aligned}
 \int_{X_0}^{X_0^*} \left(P - \frac{\partial \Phi}{\partial X} \right) dX &= P(X_0 - X_0^*) - [\Phi(X_0) - \Phi(X_0^*)] \\
 &= [\Phi(X_0^*) - PX_0^*] - [\Phi(X_0) - PX_0] \\
 &= \Delta \tilde{\Phi}^{(1)}.
 \end{aligned} \tag{5.102}$$

For $P = P_\beta$, we observe a new metastable phase, the solution X_0' . The free energy available to reach the local maximum from this metastable state is not enough to accomplish the same process starting from the global minimum, since $\Delta \tilde{\Phi}''^{(1)} > \Delta \tilde{\Phi}'^{(1)}$. These variations are also represented by the areas in Fig. . When $P = P_\gamma$, two global minima occur, X_0' and X_0'' . Thus, the previous variations become equal, with $\Delta \tilde{\Phi}''^{(1)} = \Delta \tilde{\Phi}'^{(1)}$. This is equivalent to the Maxwell construction. Indeed,

the Maxwell construction is an artifice recovering a fundamental idea: the stable equilibrium states must be determined by the extremization of a thermodynamical potential. The variational procedure directly determines the equations of state, not the simple attribution

$$P \rightarrow \frac{\partial \Phi}{\partial X}, \quad (5.103)$$

which actually generates an imprecise equation of state that must be corrected by a Maxwell construction. The equilibrium points obtained in Figs. 5-4(g)-(i) are described in Fig 5-5. The stable presenting. Hence the adequate equation of state comes from the minimization of the potential

$$\Phi^{(1)} = \min_X \{ \Phi(X) + PX \} \quad (5.104)$$

providing the correct solution $X_0 = X_0(P)$, with $\Phi^{(1)}(P) = \tilde{\Phi}^{(1)}(P|X_0)$.

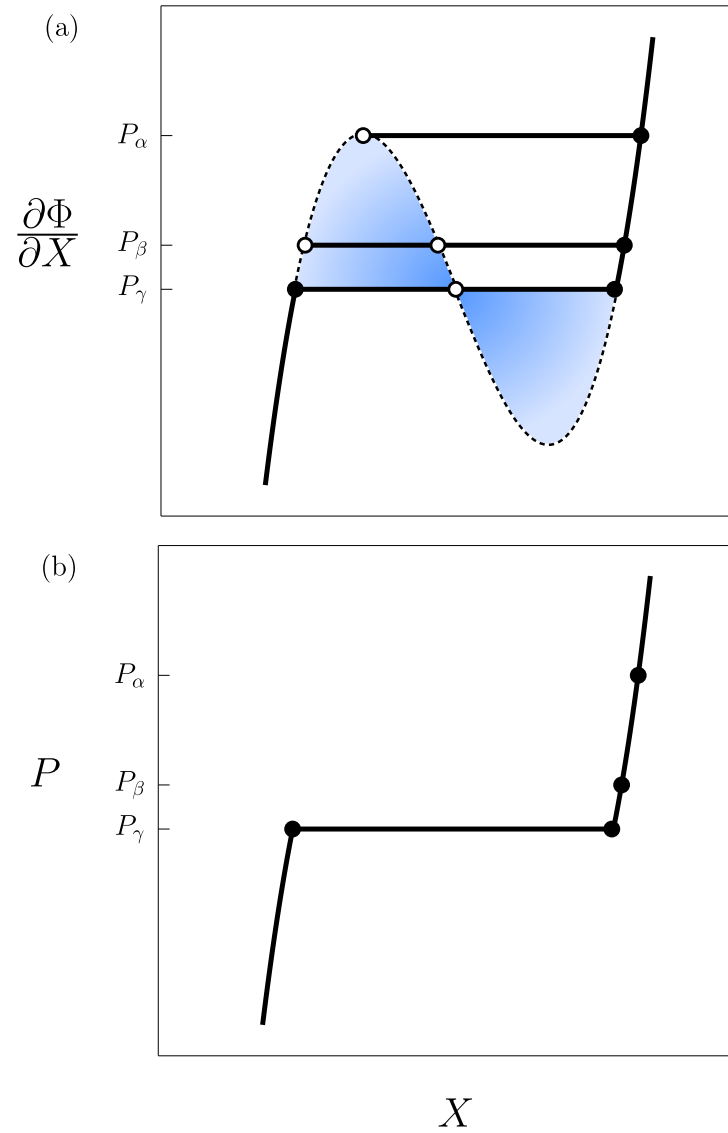


Figure 5-5: The equation of state, obtained as the solution of the extremization procedure.

Chapter 6

Conclusions and Perspectives

*“My words fly up, my thoughts remain below: Words without thoughts
never to heaven go.”*

– William Shakespeare, *Hamlet*

We have studied theoretically the occurrence of density anomaly in a quantum system considering parameters compatible with its experimental realization in optical lattices, within the framework described by the self-energy functional theory. It was also shown that the physical mechanism underlying normal density anomalies relies on the presence of a zero point entropy in the atomic limit, marking phase transitions between Mott Insulators with different occupation. The inclusion of the hopping amplitude (enabling the rise of a superfluid phase) lifts the ground state degeneracy, generates correlations among different sites and damps residual entropies and thermal expansion. Nevertheless, regions of anomalous density behavior can be found in a perturbative regime ($J \ll U$) corresponding to atomic recoil energy being much smaller than the intensities of the confining field $E_r \ll V_0$. For very intense confining fields waterlike anomalies are also found inside the superfluid regime, as was illustrated for the case of rubidium-87 in Figs. 3-9 and 3-10.

Our proposition is that by understanding the competition between different physical mechanisms contributing to free energy, usually manifested through interactions between particles (but here including chemical potential and hopping), and the re-

lation between residual entropy and ground state phase transitions, it is possible to design and predict the phenomenology of density anomaly in systems other than liquid water, as illustrated here with optical lattices of rubidium-87, sodium-23 and cesium-133 atoms.

We also studied in detail the specific heat capacity dependence on temperature of bosons described by the Bose-Hubbard model, considering simple cubic and square lattice geometries. Our theoretical analysis comprehended numerical methods, including the self-energy functional theory (a non-perturbative and self consistent approach, suitable for the description of both normal and superfluid phases) complemented by finite-temperature perturbation theory around the atomic limit. Our analysis revealed an anomalous double-peak behavior of the specific heat capacity as temperature is varied, connected to a residual entropy established in the atomic limit. Indeed, for $J = 0$, the anomaly is present for values of μ near ground-state phase transition between Mott insulators of successive occupation number. In this regime, such ground-state macroscopic degeneracy is originated from the energetic competition between the local interaction U and the chemical potential μ . While the local interaction is repulsive and tends to decrease the occupation of a single site, the chemical potential acts in the opposite direction, favoring occupation. Specifically, when μ takes on integer values of the on-site repulsion (which is exactly the energy required to add another particle at a given site), the system becomes frustrated energetically. This energetic frustration gets translated into an additional low-temperature maximum of c_μ as a function of T . In this scenario, we also demonstrated a general decomposition of the specific heat, based on all possible transitions realizable between the energy eigenvalues of the system's spectrum. This result enabled us to identify the relevant energy level transitions and how the noted peaks evolve as the chemical potential is varied.

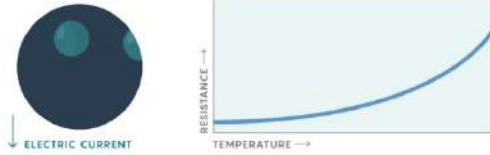
For finite hopping amplitudes, the superfluid phase tends to destroy the reported maxima. Indeed, the double-peak structure is only observed inside the normal phase and in a perturbative regime, corresponding to very deep optical lattices. Additionally, the low-temperature maximum presents a reduced magnitude when compared to

Strange Behaviors in Strange Metals

Exotic materials known as "strange metals" are bad at conducting electricity, yet they turn into powerful superconductors at low temperatures. What electrons are doing in both phases is a major mystery.

CONVENTIONAL METALS

In conventional metals like copper, an electric current can be thought of as a stream of individual electrons. Resistance to the current, caused by electrons scattering off each other, typically increases with the square of the temperature.



STRANGE METALS

Researchers theorize that electrons in strange metals are in a highly entangled quantum state. Their resistance depends on Planck's constant, the fundamental quantity of quantum mechanics, suggesting that the electrons are dissipating energy as fast as physics allows (B). When cooled to a critical temperature, strange metals become perfect conductors with zero resistance (A).

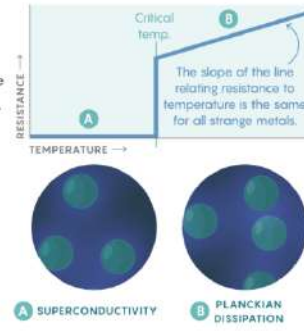


Figure 6-1: Schematically, the temperature dependence of resistance of usual and strange metals. Extracted from Ref. [177]

the atomic limit. This can be explained by the effects of correlations created between first neighbors (enabled by the hopping), producing a prominent change in the free energy's curvature. Such connection was established by an exact and general result relating the variation in free energy to the building up of correlations as the tunneling amplitude is turned on. Spectral functions were also used to illustrate the relevant excitations dominant at each maximum.

Taking into account the concepts demonstrated in this work, we intend to explore more deeply the capacity of these simulator in extracting fundamental mechanisms of complex systems. In our perspective, we aim to extended our analysis of anomalies to the domain of transport quantities. In particular, we envision to develop theoretical studies regarding the transport properties of strongly interacting systems. But why we consider this a relevant path? The conventional theories, which include the Fermi liquid theory associated to the Boltzmann kinetic equation [106, 178], applied to describe ordinary metals usually fail in this scenario. The consequent anomalous behaviors include a linear dependence of the resistivity with temperature at low temperatures and the absence of a saturation value in a high temperature range [179]. In special, such properties are exhibited by materials called *cuprates*, the first high temperature superconductors, which yielded the Nobel prize to their discoverers Bednorz and Müller in 1987 [180]. Since then, a myriad of cuprates were identified, attaining the superconductor state at temperatures around $-135\text{ }^{\circ}\text{C}$ or 138 K , compatible with

liquid nitrogen refrigeration [181]. Despite their simple structure and composition, the origins of the reported phenomena lack a full theoretical understanding, remaining one of the most challenging problems in the materials science.

In order to explore how resistivity and diffusion develops in such scenarios, we will use quantum gases trapped in optical lattices as a platform to emulate these systems in clear and controllable ways, following the recently studied quantum simulators. In this scenario, we aim to extract fundamental mechanisms underlying the behavior of *strange metals*, precursors of phenomena attaining great technological interest such as superconductivity at high temperatures.

Indeed, a recent work by Brown et al. [182, 183] (2019) announced a real breakthrough in the field. Manipulating atoms in an optical lattice, they observed the behavior of strange metals in a highly interacting fermionic system. Due to the absence of disorder and lattice phonons in the system, the observed effects are resultant of electronic correlations. Hence, the lithium atoms obey analogous physical effects compared to electrons in real metals.

Following this experimental evidence, we intend to investigate how resistivity and diffusion develops in the Fermi-Hubbard model [184], which theoretically describes the commented scenario. In particular, how and if the anomalies appear in a broader range of temperatures and coupling parameters, mapping the possible evolution of the system into a Fermi liquid by tuning the interaction among particles. With the considerations exposed, our goal is directed towards understanding how interactions lead to the breakdown of conventional theories describing the behavior of usual metals, generating collective and complex phenomena.

Appendix A

Two-states approximation and the critical densities

Near the GSPT between configurations of occupation numbers n and $n + 1$, the grand canonical free energy can be approximated by

$$\Omega \approx -\frac{1}{\beta} \ln (e^{-\beta\epsilon_n} + e^{-\beta\epsilon_{n+1}})^L, \quad (\text{A.1})$$

from which we calculate pressure as

$$Pv_0 \approx -\frac{\epsilon_n + \epsilon_{n+1}}{2} + \frac{1}{\beta} \ln \left\{ 2 \cosh \left[\frac{\beta(\epsilon_n - \epsilon_{n+1})}{2} \right] \right\}. \quad (\text{A.2})$$

Now we define $\Delta P = P - P_n$ and $\Delta\mu = \mu - \mu_n$ to rewrite

$$\Delta Pv_0 = \left(n + \frac{1}{2} \right) \Delta\mu + \frac{1}{\beta} \ln \left[2 \cosh \left(\frac{\beta\Delta\mu}{2} \right) \right], \quad (\text{A.3})$$

and calculate

$$\rho v_0 = \left(n + \frac{1}{2} \right) + \tanh \left(\frac{\beta\Delta\mu}{2} \right). \quad (\text{A.4})$$

By inverting Eq. (A.4) it is possible to obtain

$$e^{\beta\Delta P^*} (1 - 2\delta_n)^{n+1} = 2(1 + 2\delta_n)^n, \quad (\text{A.5})$$

with $\delta_n = \bar{\rho}_n^* - \rho_n^*$ as defined above. At the critical pressure, $\Delta P^* = 0$ and Eq. (3.12) is recovered. The case $n = 1$ leads to the second order polynomial

$$4\delta_1^2 - 8\delta_1 - 1 = 0, \quad (\text{A.6})$$

whose physically viable solution is $\delta_1 = (2 - \sqrt{5})/2$, resulting in $\bar{\rho}_1^* = (5 - \sqrt{5})/2$, as discussed in the Section 3.2. The values of the critical densities for arbitrary n can be calculated numerically from equation (3.12). These solutions have the property $\lim_{n \rightarrow \infty} \delta_n = 0$, meaning that in this limit critical densities become identical when calculated at fixed μ and fixed P .

Appendix B

Self-energy Functional Theory

B.1 General Aspects

In order to map the thermodynamics of the bosons we employ a variational and non-perturbative self-consistent approach, the self-energy functional theory derived by Hügel *et al.* [99, 161], inspired in the original works for fermions by Potthoff [100]. The formalism, which includes $U(1)$ symmetry breaking and comprehends previous BDMFT approaches [97, 98, 101, 102], is based on successive Legendre transformations of the free-energy functional Ω leading to a new functional Ω_{SE} of the self-energies. The approximation scheme to the many-body problem constricts the variational space: the self-energy domain is restricted to a subspace of self-energies of a simpler reference system. Then, the original problem is transformed into determining stationary solutions of this new functional in terms of the reference system's free propagators. This subsection is devoted to provide an overview of the method, following the references [99, 104, 105, 161].

First, we write the Bose-Hubbard Hamiltonian

$$H = -J \sum_{\langle i,j \rangle} b_i^\dagger b_j + \frac{U}{2} \sum_i n_i(n_i - 1) - \mu \sum_i n_i \quad (\text{B.1})$$

in a more concise and general form

$$H = \frac{1}{2} \mathbf{b}_\alpha^\dagger \mathbf{t}_\beta^\alpha \mathbf{b}^\beta + \mathcal{V} + \mathbf{F}_\alpha^\dagger \mathbf{b}^\alpha, \quad (\text{B.2})$$

including an explicit symmetry breaking field \mathbf{F} which couples to the bosonic operators. In this notation, we use the Einstein summation convention and the superindex α spans the site index i as well as the Nambu index ν . Explicitly, the bosonic operator reads as $\mathbf{b}_\alpha^\dagger \equiv \mathbf{b}_{i\nu}^\dagger = (b_i^\dagger, b_i)_\nu$, with commutation relations $[\mathbf{b}_\alpha, \mathbf{b}_\beta^\dagger] = (\mathbf{1} \otimes \sigma_z)_\beta^\alpha$. Also, we have the generalized hopping $\mathbf{t}_\beta^\alpha = \mathbf{t}_{j\nu}^{i\eta} = t_{ij} \otimes \mathbf{1}_{\eta\nu}$ and interaction of the form $\mathcal{V} = U_{\alpha\beta\gamma\delta} \mathbf{b}^\alpha \mathbf{b}^\beta \mathbf{b}^\gamma \mathbf{b}^\delta$.

Including finite-temperature effects (with $k_B T = 1/\beta$), the partition function $\mathcal{Z} = \text{Tr}[\mathcal{T}e^{-\mathcal{S}}]$ follows as a trace comprising the imaginary time ordered exponential of the action \mathcal{S} [106–108],

$$\begin{aligned} \mathcal{S}[\mathbf{F}, \mathbf{G}_0^{-1}] &= -\frac{1}{2} \int_0^\beta \int_0^\beta d\tau d\tau' \mathbf{b}^\dagger(\tau) \mathbf{G}_0^{-1}(\tau, \tau') \mathbf{b}(\tau') \\ &\quad + \int_0^\beta d\tau \mathcal{V}[\mathbf{b}(\tau)] + \int_0^\beta d\tau \mathbf{F}^\dagger \mathbf{b}(\tau), \end{aligned} \quad (\text{B.3})$$

written according to its explicit dependence on \mathbf{F} and the non-interacting Green's function \mathbf{G}_0

$$\mathbf{G}_0^{-1} = \delta(\tau - \tau')(-[\mathbf{1} \otimes \sigma_z] \partial_{\tau'} - \mathbf{t}). \quad (\text{B.4})$$

From the partition function, averages can be defined as $\langle O(\tau) \rangle = \text{Tr}[\mathcal{T}e^{-\mathcal{S}} O(\tau)]/\mathcal{Z}$. Also, its logarithm provides the free-energy $\Omega[\mathbf{F}, \mathbf{G}_0^{-1}] = -\ln[\mathcal{Z}]/\beta$, which is a generating functional of the propagators: the condensate Green's function Φ

$$\beta \frac{\delta \Omega}{\delta \mathbf{F}^\dagger} = \langle \mathbf{b} \rangle \equiv \Phi, \quad (\text{B.5})$$

and the connected interacting Green's function \mathbf{G}

$$2\beta \frac{\delta \Omega}{\delta \mathbf{G}_0^{-1}} = -\langle \mathbf{b}(\tau) \mathbf{b}^\dagger(\tau') \rangle \equiv \mathbf{G}(\tau, \tau') - \Phi \Phi^\dagger. \quad (\text{B.6})$$

Further details regarding products and traces are addressed in Subsections B.2 and B.3.

Based on a Legendre transformation, the free-energy functional dependence can be exchanged from \mathbf{F} and \mathbf{G}_0^{-1} to the dressed propagators Φ and \mathbf{G} , leading to the Baym-Kadanoff functional [109–112]

$$\begin{aligned} \beta\Omega_{BK}[\Phi, \mathbf{G}] &= \mathbf{F}^\dagger \Phi - \frac{1}{2} \Phi^\dagger \mathbf{G}_0^{-1} \Phi + \frac{1}{2} \text{Tr}[\mathbf{G}_0^{-1} \mathbf{G}] + \frac{1}{2} \text{Tr} \ln[-\mathbf{G}^{-1}] \\ &\quad + \Phi_{LW}[\Phi, \mathbf{G}]. \end{aligned} \quad (\text{B.7})$$

In Eq. (B.7), $\Phi_{LW}[\Phi, \mathbf{G}]$ is the Luttinger-Ward functional [113, 114], a universal contribution which encompasses the complexity of the many-body system, containing all two-particle irreducible (2PI) diagrams [115, 116]. At the physical solution, the functional $\Omega_{BK}[\Phi, \mathbf{G}]$ is stationary

$$\frac{\delta\Omega_{BK}}{\delta\Phi^\dagger} = 0, \quad \frac{\delta\Omega_{BK}}{\delta\mathbf{G}} = 0, \quad (\text{B.8})$$

and it is equal to the equilibrium free-energy $\Omega_{BK} = \Omega$. The variations

$$\beta \frac{\delta\Omega_{BK}}{\delta\Phi^\dagger} = \mathbf{F} - \mathbf{G}_0^{-1} \Phi + \frac{\delta\Phi_{LW}}{\delta\Phi^\dagger} \quad (\text{B.9})$$

and

$$2\beta \frac{\delta\Omega_{BK}}{\delta\mathbf{G}} = \mathbf{G}_0^{-1} - \mathbf{G}^{-1} + 2 \frac{\delta\Phi_{LW}}{\delta\mathbf{G}}, \quad (\text{B.10})$$

associated to the conditions of Eq. (B.8) lead to the following identification

$$\Sigma_{1/2} = -\frac{\delta\Phi_{LW}}{\delta\Phi^\dagger}, \quad \Sigma = -2 \frac{\delta\Phi_{LW}}{\delta\mathbf{G}}, \quad (\text{B.11})$$

where $\Sigma_{1/2}$ and Σ are the one and two-point self-energies, respectively. Therefore, the propagators obey the Dyson's equations

$$\mathbf{G}_0^{-1} \Phi = \mathbf{F} - \Sigma_{1/2} \quad (\text{B.12})$$

and

$$\mathbf{G}^{-1} = \mathbf{G}_0^{-1} - \boldsymbol{\Sigma}. \quad (\text{B.13})$$

With another Legendre transform, the Baym-Kadanoff functional dependence can be exchanged from the one and two-point propagators Φ and \mathbf{G} to their respective self-energies $\boldsymbol{\Sigma}_{1/2}$ and $\boldsymbol{\Sigma}$, yielding the self-energy functional

$$\begin{aligned} \beta\Omega_{SE}[\boldsymbol{\Sigma}_{1/2}, \boldsymbol{\Sigma}] &= \frac{1}{2}(\mathbf{F} - \boldsymbol{\Sigma}_{1/2})^\dagger \mathbf{G}_0(\mathbf{F} - \boldsymbol{\Sigma}_{1/2}) + \frac{1}{2} \text{Tr} \ln[-(\mathbf{G}_0^{-1} - \boldsymbol{\Sigma})] \\ &+ \mathcal{F}[\boldsymbol{\Sigma}_{1/2}, \boldsymbol{\Sigma}]. \end{aligned} \quad (\text{B.14})$$

The universal functional $\mathcal{F}[\boldsymbol{\Sigma}_{1/2}, \boldsymbol{\Sigma}] = \Phi_{LW}[\Phi, \mathbf{G}] + \boldsymbol{\Sigma}_{1/2}^\dagger \Phi + \frac{1}{2} \text{Tr}[\boldsymbol{\Sigma} \mathbf{G}]$ is simply the Legendre transform of the Luttinger-Ward functional $\Phi_{LW}[\Phi, \mathbf{G}]$, with the following variations

$$\frac{\delta \mathcal{F}}{\delta \boldsymbol{\Sigma}_{1/2}^\dagger} = \Phi, \quad 2 \frac{\delta \mathcal{F}}{\delta \boldsymbol{\Sigma}} = \mathbf{G}. \quad (\text{B.15})$$

At the physical solution, Ω_{SE} is stationary and equal to the free-energy $\Omega_{SE} = \Omega_{BK} = \Omega$ (as a result of Ω , Ω_{BK} and Ω_{SE} being connected by successive Legendre transforms), yielding once again the Dyson's equations

$$0 = \beta \frac{\delta \Omega_{SE}}{\delta \boldsymbol{\Sigma}_{1/2}^\dagger} = -\mathbf{G}_0(\mathbf{F} - \boldsymbol{\Sigma}_{1/2}) + \Phi \quad (\text{B.16})$$

and

$$0 = 2\beta \frac{\delta \Omega_{SE}}{\delta \boldsymbol{\Sigma}} = -(\mathbf{G}_0^{-1} - \boldsymbol{\Sigma})^{-1} + \mathbf{G}. \quad (\text{B.17})$$

The mentioned universality of the functional \mathcal{F} enables us to overcome its complexity with the introduction of an exactly solvable reference system (denoted by primed quantities) exhibiting the same symmetry and interactions as the original

one. According to Eq. (B.14), the reference system's self-energy functional

$$\begin{aligned} \beta\Omega'_{SE}[\boldsymbol{\Sigma}_{1/2}, \boldsymbol{\Sigma}] &= \frac{1}{2}(\mathbf{F}' - \boldsymbol{\Sigma}_{1/2})^\dagger \mathbf{G}'_0(\mathbf{F}' - \boldsymbol{\Sigma}_{1/2}) + \frac{1}{2} \text{Tr} \ln[-(\mathbf{G}'_0{}^{-1} - \boldsymbol{\Sigma})] \\ &\quad + \mathcal{F}[\boldsymbol{\Sigma}_{1/2}, \boldsymbol{\Sigma}] \end{aligned} \quad (\text{B.18})$$

evaluated at the physical solutions $\boldsymbol{\Sigma}_{1/2} = \boldsymbol{\Sigma}'_{1/2}$ and $\boldsymbol{\Sigma} = \boldsymbol{\Sigma}'$ is equal to the reference system's free-energy $\Omega'_{SE}[\boldsymbol{\Sigma}'_{1/2}, \boldsymbol{\Sigma}'] = \Omega'[\mathbf{F}', \mathbf{G}'_0{}^{-1}]$. Subtracting Eq. (B.18) from Eq. (B.14), Ω_{SE} evaluated at $\boldsymbol{\Sigma}_{1/2} = \boldsymbol{\Sigma}'_{1/2}$ and $\boldsymbol{\Sigma} = \boldsymbol{\Sigma}'$ becomes

$$\begin{aligned} \beta\Omega_{SE}[\boldsymbol{\Sigma}'_{1/2}, \boldsymbol{\Sigma}'] &= \beta\Omega' + \frac{1}{2}(\mathbf{F} - \boldsymbol{\Sigma}'_{1/2})^\dagger \mathbf{G}_0(\mathbf{F} - \boldsymbol{\Sigma}'_{1/2}) \\ &\quad - \frac{1}{2}(\mathbf{F}' - \boldsymbol{\Sigma}'_{1/2})^\dagger \mathbf{G}'_0(\mathbf{F}' - \boldsymbol{\Sigma}'_{1/2}) + \frac{1}{2} \text{Tr} \ln \left[\frac{\mathbf{G}_0{}^{-1} - \boldsymbol{\Sigma}'}{\mathbf{G}'_0{}^{-1} - \boldsymbol{\Sigma}'} \right] \end{aligned} \quad (\text{B.19})$$

Therefore, the solution of the reference system provides a parametrization of the self-energies in terms of \mathbf{F}' and $\mathbf{G}'_0{}^{-1}$, which allows the construction of the self-energy functional theory approximation Ω_{SFT} to the self-energy functional Ω_{SE} according to

$$\Omega_{SFT}[\mathbf{F}', \mathbf{G}'_0{}^{-1}] = \Omega_{SE}[\boldsymbol{\Sigma}'_{1/2}[\mathbf{F}', \mathbf{G}'_0{}^{-1}], \boldsymbol{\Sigma}'[\mathbf{F}', \mathbf{G}'_0{}^{-1}]] . \quad (\text{B.20})$$

The approximation consists in constraining the variational principle to the subspace of self-energies of the reference system; this procedure applied to the variations of Eqs. (B.16) and (B.17) yields the Euler equations $\delta_{\mathbf{F}'^\dagger} \Omega_{SFT} = 0$ and $\delta_{\mathbf{G}'_0{}^{-1}} \Omega_{SFT} = 0$.

In particular, we choose a local reference system, the SFA3 minimal construction [99, 161], comprehending three variational parameters: the $U(1)$ symmetry breaking linear field F' conjugated to the creation b^\dagger and annihilation b operators; the two fields Δ_{00} , coupled with the density $b^\dagger b$, and Δ_{01} , conjugated to pair creation $b^\dagger b^\dagger$ and pair annihilation bb operators. The Hamiltonian describing the bosonic state is given by

$$H'[\mathbf{F}', \boldsymbol{\Delta}] = \frac{1}{2} \mathbf{b}^\dagger \boldsymbol{\Delta} \mathbf{b} + \frac{U}{2} n(n-1) - \mu n + \mathbf{F}'^\dagger \mathbf{b} , \quad (\text{B.21})$$

where $\mathbf{b} = (b, b^\dagger)$, $\mathbf{F}' = (F', F'^*)$ and $\mathbf{\Delta} = \Delta_{00}\mathbf{1} + \Delta_{01}\sigma_x$.

Therefore, the states of thermodynamic equilibrium are determined by the stationary points of Ω_{SFT} , given by $\nabla\Omega_{SFT}[F, \Delta_{00}, \Delta_{01}] = 0$ (or $\delta_{\mathbf{F}^\dagger}\Omega_{SFT} = 0$ and $\delta_{\mathbf{\Delta}}\Omega_{SFT} = 0$). The functional can be evaluated according to the following steps, which are completely developed throughout the next Subsections. Given the parameters F' , Δ_{00} and Δ_{01} , the Hamiltonian of Eq. (B.21) is determined. From Subsection B.4, the reference system's partition function and free-energy are computed through Eqs. (B.55) and (B.56), followed by its one and two-point propagators of Eqs. (B.57) and (B.59), and the self-energies according to the Dyson's Eqs. (B.61) and (B.62). The next step is to calculate the lattice system's one and two-point propagators by using Eqs. (B.66) and (B.65), respectively. These products and the logarithmic trace $\text{Tr} \ln[\mathbf{G}'\mathbf{G}^{-1}]$ are determined following the prescriptions presented in Subsections B.2 and B.3, respectively. By collecting the required terms in Eq. (B.19), the desired self-energy functional is evaluated and its stationary points can be determined. The code employed in our calculations is also available in the Supplemental Material.

B.2 Tensor Products

The product $\mathbf{V}^\alpha(\tau)$ of a second order tensor $\mathbf{M}_\beta^\alpha(\tau, \tau')$ and a first order tensor $\mathbf{F}^\alpha(\tau)$ comprises the sum over the superindex and integration in imaginary time according to

$$\mathbf{V}^\alpha(\tau) = \sum_\gamma \int_0^\beta d\tilde{\tau} \mathbf{M}_\gamma^\alpha(\tau, \tilde{\tau}) \mathbf{F}^\gamma(\tilde{\tau}) . \quad (\text{B.22})$$

Similarly, the product $\mathbf{M}_\beta^\alpha(\tau, \tau')$ of two second-order tensors $\mathbf{A}_\beta^\alpha(\tau, \tau')$ and $\mathbf{B}_\beta^\alpha(\tau, \tau')$ is defined by

$$\mathbf{M}_\beta^\alpha(\tau, \tau') = \sum_\gamma \int_0^\beta d\tilde{\tau} \mathbf{A}_\gamma^\alpha(\tau, \tilde{\tau}) \mathbf{B}_\beta^\gamma(\tilde{\tau}, \tau') . \quad (\text{B.23})$$

As a consequence, a scalar $R = \mathbf{V}^\dagger \mathbf{M} \mathbf{F}$, given by the contraction of two first order tensors $\mathbf{V}^\alpha(\tau)$ and $\mathbf{F}^\alpha(\tau)$ with a second order tensor $\mathbf{M}_\beta^\alpha(\tau, \tau')$, can be expressed as

$$R = \sum_{\alpha\beta} \int_0^\beta \int_0^\beta d\tau d\tau' \mathbf{V}_\alpha^\dagger(\tau) \mathbf{M}_\beta^\alpha(\tau, \tau') \mathbf{F}^\beta(\tau'). \quad (\text{B.24})$$

Also, time and space translation invariances imply $\mathbf{M}_\beta^\alpha(\tau - \tau') = \mathbf{M}_{\mathbf{r}_j, \nu}^{\mathbf{r}_i, \eta}(\tau - \tau') = \mathbf{M}_\nu^\eta(\mathbf{r}_i - \mathbf{r}_j, \tau - \tau')$. The connection between the imaginary time domain and the Matsubara frequency space (with $\omega_n = \frac{2\pi}{\beta}n$) is established through the Fourier relations

$$\mathbf{M}_\beta^\alpha(i\omega_n) = \int_0^\beta d\tau e^{i\omega_n \tau} \mathbf{M}_\beta^\alpha(\tau), \quad (\text{B.25})$$

$$\mathbf{M}_\beta^\alpha(\tau) = \frac{1}{\beta} \sum_{n=-\infty}^{\infty} e^{-i\omega_n \tau} \mathbf{M}_\beta^\alpha(i\omega_n). \quad (\text{B.26})$$

Analogously, real and momentum spaces are related by

$$\mathbf{M}_\nu^\eta(\mathbf{k}, \tau) = \sum_{\mathbf{r}} e^{-i\mathbf{k}\cdot\mathbf{r}} \mathbf{M}_\nu^\eta(\mathbf{r}, \tau), \quad (\text{B.27})$$

$$\mathbf{M}_\nu^\eta(\mathbf{r}, \tau) = \frac{1}{N_s} \sum_{\mathbf{k}} e^{i\mathbf{k}\cdot\mathbf{r}} \mathbf{M}_\nu^\eta(\mathbf{k}, \tau). \quad (\text{B.28})$$

Similar conclusions also hold for first order tensors. Combining space and time translation invariances, in momentum and Matsubara frequency space the products exhibited by Eqs. (B.22), (B.23) and (B.24) simplify to

$$\mathbf{V}^\eta = \sum_{\nu} \mathbf{M}_\nu^\eta(\mathbf{k} = \mathbf{0}, i\omega_0) \mathbf{F}^\nu, \quad (\text{B.29})$$

$$\mathbf{M}_\nu^\eta(\mathbf{k}, i\omega_n) = \sum_{\mu} \mathbf{A}_\mu^\eta(\mathbf{k}, i\omega_n) \mathbf{B}_\nu^\mu(\mathbf{k}, i\omega_n), \quad (\text{B.30})$$

$$R = \beta N_s \sum_{\eta\nu} \mathbf{V}_\eta^\dagger \mathbf{M}_\nu^\eta(\mathbf{k} = \mathbf{0}, i\omega_0) \mathbf{F}^\nu. \quad (\text{B.31})$$

B.3 Traces

General Definitions

The traces presented in the functional formulations are defined as the complete contraction over superindices and a double integration in imaginary-time according to

$$\text{Tr}[\mathbf{M}] = \sum_{\gamma} \int_0^{\beta} \int_0^{\beta} d\tau d\tau' \delta_{\gamma}(\tau - \tau') \mathbf{M}_{\gamma}^{\gamma}(\tau, \tau'), \quad (\text{B.32})$$

where $\delta_{\gamma}(\tau) = \delta_{\mathbf{r}_i, \nu}(\tau) = \delta(\tau - (-1)^{\nu} 0^-)$ with $\nu = 0, 1$. The delta function is introduced in order to impose normal ordering of the diagonal Nambu components of \mathbf{M} . Considering time and space translation invariances, the trace defined by Eq. (B.32) becomes

$$\begin{aligned} \text{Tr}[\mathbf{M}] &= \beta N_s \sum_{\nu} \mathbf{M}_{\nu}^{\nu}(\mathbf{r}_i = \mathbf{0}, \tau = (-1)^{\nu} 0^-) \\ &= \sum_{\nu \mathbf{k} n} e^{i\omega_n (-1)^{\nu} 0^+} \mathbf{M}_{\nu}^{\nu}(\mathbf{k}, i\omega_n). \end{aligned} \quad (\text{B.33})$$

The summation over Matsubara frequencies within the described limit can impose difficulties depending on the asymptotic behavior of \mathbf{M} . In order to improve the convergence properties of such sums, we analyze explicitly its high frequency expansion in the following.

High Frequency Expansion

We define the high frequency expansion of

$$\mathbf{M}(\mathbf{k}, i\omega_n) = \mathcal{M}(\mathbf{k}, i\omega_n) + \mathcal{O}((i\omega_n)^{-(N_h+1)}) \quad (\text{B.34})$$

up to order N_h according to

$$\mathcal{M}(\mathbf{k}, i\omega_n) = \sum_{p=1}^{N_h} \mathbf{m}_p(\mathbf{k}) Q_p(i\omega_n), \quad (\text{B.35})$$

where

$$Q_p(i\omega_n) = \begin{cases} \frac{1}{(i\omega_n)^p}, & \omega_n \neq 0 \\ 0, & \omega_n = 0 \end{cases}. \quad (\text{B.36})$$

By adding and subtracting the term $\text{Tr}[\mathcal{M}]$ in Eq. (B.33), the corresponding trace can be expressed as

$$\text{Tr}[\mathbf{M}] = \sum_{\nu \mathbf{k}} \left(\sum_n [\mathbf{M}(\mathbf{k}, i\omega_n) - \mathcal{M}(\mathbf{k}, i\omega_n)]_{\nu}^{\nu} + \beta \mathcal{M}_{\nu}^{\nu}(\mathbf{k}, \tau = (-1)^{\nu} 0^-) \right), \quad (\text{B.37})$$

since the asymptotic behavior $[\mathbf{M} - \mathcal{M}]_{\nu}^{\nu} \sim (i\omega_n)^{-(N_h+1)}$ allows us to drop the exponent present in the trace definition. Considering a finite number N_{ω} of Matsubara frequencies and a high frequency expansion of order N_h , the trace approximation reads as

$$\begin{aligned} \text{Tr}[\mathbf{M}] \approx & \sum_{\nu \mathbf{k}} \left(\mathbf{M}_{\nu}^{\nu}(\mathbf{k}, i\omega_0) + \sum_{n=-N_{\omega}}^{N_{\omega}}{}' \left[\mathbf{M}(\mathbf{k}, i\omega_n) - \sum_{p=1}^{N_h} \frac{\mathbf{m}_p(\mathbf{k})}{(i\omega_n)^p} \right]_{\nu}^{\nu} \right. \\ & \left. + \beta \sum_{p=1}^{N_h} [\mathbf{m}_p(\mathbf{k})]_{\nu}^{\nu} Q_p(\mathbf{k}, \tau = (-1)^{\nu} 0^-) \right), \end{aligned} \quad (\text{B.38})$$

where the primed sum excludes $\omega_n = 0$. The calculations presented in this paper employ $N_{\omega} = 1000$ with a second order $N_h = 2$ tail expansion.

In order to compute the trace approximation of Eq. (B.38), the functions $Q_p(\tau)$, Fourier transforms of $Q_p(i\omega_n)$, need to be determined. The idea is to visualize them as sums of the residues [106] of a given complex function as follows

$$Q_p(\tau) = \frac{1}{\beta} \sum_{n=-\infty}^{\infty}{}' \frac{e^{-i\omega_n \tau}}{(i\omega_n)^p} = \sum_{n=-\infty}^{\infty}{}' \text{Res} \left[\frac{e^{-\tau z}}{z^p} h(z), i\omega_n \right], \quad (\text{B.39})$$

with $h(z) = (1 - e^{-\beta z})^{-1}$. The poles $z = i\omega_n$ are located along the imaginary axis; then, the residue theorem allows us to relate the result to a contour integral, comprehending the imaginary axis of the complex plane

$$\sum_{n=-\infty}^{\infty} \text{Res} \left[\frac{e^{-\tau z}}{z^p} h(z), i\omega_n \right] = \oint_C \frac{dz}{2\pi i} \frac{e^{-\tau z}}{z^p} h(z). \quad (\text{B.40})$$

By deforming the original contour C into two semi-circles of infinite radius this same integral becomes

$$\oint_{C'} \frac{dz}{2\pi i} \frac{e^{-\tau z}}{z^p} h(z) = 0, \quad (\text{B.41})$$

once this new path C' encloses regions free of poles. By inserting Eq. (B.41) into Eq. (B.40) and comparing to Eq. (B.39), $Q_p(\tau)$ is determined simply by $n = 0$

$$Q_p(\tau) = -\text{Res} \left[\frac{e^{-\tau z}}{z^p} h(z), 0 \right]. \quad (\text{B.42})$$

The relevant pole $z = 0$ is of order $p + 1$; hence, the corresponding residue is given by the formula

$$Q_p(\tau) = -\frac{1}{p!} \lim_{z \rightarrow 0} \left(\frac{d}{dz} \right)^p z e^{-\tau z} h(z), \quad (\text{B.43})$$

with the following first order terms

$$Q_1(\tau) = (2\tau - \beta)/(2\beta), \quad (\text{B.44})$$

$$Q_2(\tau) = (-6\tau^2 + 6\beta\tau - \beta^2)/(12\beta). \quad (\text{B.45})$$

Since the functions $Q_p(\tau)$ are periodic on the interval $\tau \in (0, \beta)$, the respective zero time limits are

$$Q_1(\tau = (-1)^\nu 0^-) = (-1)^\nu / 2, \quad (\text{B.46})$$

$$Q_2(\tau = (-1)^\nu 0^-) = -\beta / 12. \quad (\text{B.47})$$

Trace of Logarithm

Besides the already mentioned ordinary traces, the self-energy functionals also contain traces regarding the logarithm of the Green's Function \mathbf{G} . Actually, in order to guarantee the correct non-interacting limit, a regularization factor must be included. Therefore, we define the regularized Matsubara trace logarithm functional $\mathcal{L}[\mathbf{G}]$

$$\mathcal{L}[\mathbf{G}] = \frac{1}{2} \text{Tr} \ln[-\mathbf{G}^{-1}] - \frac{1}{2} \text{Tr} \ln[-\mathbf{G}_r^{-1}], \quad (\text{B.48})$$

with the regularization carried by the second order tensor

$$\mathbf{G}_r(i\omega_n) = \begin{cases} -\beta \mathbf{1}, & \omega_n = 0 \\ \frac{\sigma_z}{i\omega_n}, & \omega_n \neq 0 \end{cases}. \quad (\text{B.49})$$

According to Eq. (B.33), such trace is represented as

$$\mathcal{L}[\mathbf{G}] = -\frac{1}{2} \sum_{\nu \mathbf{k} n} e^{i\omega_n(-1)^{\nu}0^+} \left(\ln[\mathbf{G}_r^{-1} \mathbf{G}(\mathbf{k}, i\omega_n)] \right)_{\nu}^{\nu},$$

and the approximation described by Eq. (B.38) yields

$$\begin{aligned} \mathcal{L}[\mathbf{G}] \approx & -\frac{1}{2} \sum_{\nu \mathbf{k}} \left(\ln[-\mathbf{G}(\mathbf{k}, i\omega_0)/\beta]_{\nu}^{\nu} + \sum'_{n=-N_{\omega}}^{N_{\omega}} \left[\ln[(\sigma_z i\omega_n) \mathbf{G}(\mathbf{k}, i\omega_n)] - \sum_{p=1}^{N_h} \frac{\mathbf{q}_p(\mathbf{k})}{(i\omega_n)^p} \right]_{\nu}^{\nu} \right. \\ & \left. + \beta \sum_{p=1}^{N_h} [\mathbf{q}_p(\mathbf{k})]_{\nu}^{\nu} Q_p(\mathbf{k}, \tau = (-1)^{\nu}0^-) \right). \end{aligned} \quad (\text{B.50})$$

The terms $\mathbf{q}_p(\mathbf{k})$ are the coefficients from the high frequency expansion of $\ln[(\sigma_z i\omega_n) \mathbf{G}(\mathbf{k}, i\omega_n)] = \sum_{p=1}^{\infty} \frac{\mathbf{q}_p(\mathbf{k})}{(i\omega_n)^p}$ given explicitly by

$$\mathbf{q}_1(\mathbf{k}) = \sigma_z \mathbf{c}_2(\mathbf{k}), \quad (\text{B.51})$$

$$\mathbf{q}_2(\mathbf{k}) = \sigma_z \mathbf{c}_3(\mathbf{k}) - \frac{[\sigma_z \mathbf{c}_2(\mathbf{k})]^2}{2}, \quad (\text{B.52})$$

until second order, where $\mathbf{c}_p(\mathbf{k})$ are the coefficients in the high frequency expansion of the Green's function

$$\mathbf{G}(i\omega_n) = \sum_{p=1}^{\infty} \frac{\mathbf{c}_p(\mathbf{k})}{(i\omega_n)^p}. \quad (\text{B.53})$$

Hence, using second order tail corrections, the Matsubara trace logarithm exposed in Eq. (B.50) reads as

$$\begin{aligned} \mathcal{L}[\mathbf{G}] \approx & -\frac{1}{2} \sum_{\nu, \mathbf{k}} \left(\ln[-\mathbf{G}(\mathbf{k}, i\omega_0)/\beta] + \frac{\beta}{2} \mathbf{c}_2(\mathbf{k}) - \frac{\beta^2}{12} \mathbf{q}_2(\mathbf{k}) \right. \\ & \left. + \sum_{n=-N_\omega}^{N_\omega} \left[\ln[(\sigma_z i\omega_n) \mathbf{G}(\mathbf{k}, i\omega_n)] - \frac{\mathbf{q}_2(\mathbf{k})}{(i\omega_n)^2} \right] \right)_{\nu}. \end{aligned} \quad (\text{B.54})$$

B.4 Reference System

In the basis of local occupation number states, we generate matrix representations for the reference system Hamiltonian H' of Eq. (B.21) and the bosonic creation and annihilation operators b^\dagger and b . A cut-off $N_{max} = 10$ bounding the occupation number from above is introduced. The diagonalization of the Hamiltonian H' provides its eigenvalues E_n and eigenvectors $|n\rangle$. Given these procedures, the partition function is written as

$$\mathcal{Z}' = \sum_n e^{-\beta E_n}, \quad (\text{B.55})$$

from which we derive the reference system free-energy

$$\Omega' = -\frac{1}{\beta} \ln[\mathcal{Z}']. \quad (\text{B.56})$$

Regarding the propagators, the static expectation value of \mathbf{b} , defined in Eq. (B.5), is given by

$$\Phi' = \langle \mathbf{b} \rangle = \frac{1}{\mathcal{Z}'} \sum_n e^{-\beta E_n} \langle n | \mathbf{b} | n \rangle, \quad (\text{B.57})$$

and the connected Green's function of Eq. (B.6)

$$\mathbf{G}'(\tau) = -\langle \mathbf{b}(\tau) \mathbf{b}^\dagger \rangle + \mathbf{\Phi}' \mathbf{\Phi}'^\dagger \quad (\text{B.58})$$

expressed in the Matsubara frequency space yields

$$\begin{aligned} \mathbf{G}'(i\omega_n) &= \frac{1}{\mathcal{Z}'} \sum_{n,m} \frac{(e^{-\beta E_n} - e^{-\beta E_m})}{i\omega_n + E_n - E_m} \langle n | \mathbf{b} | m \rangle \langle m | \mathbf{b}^\dagger | n \rangle \\ &\quad - \delta_{\omega_n,0} \beta \frac{1}{\mathcal{Z}'} \sum_n e^{-\beta E_n} \langle n | \mathbf{b} | n \rangle \langle n | \mathbf{b}^\dagger | n \rangle + \delta_{\omega_n,0} \beta \mathbf{\Phi}' \mathbf{\Phi}'^\dagger . \end{aligned} \quad (\text{B.59})$$

The non-interacting Green's function is determined by setting $U = 0$ in Eq. (B.21)

$$\mathbf{G}'_0^{-1}(i\omega_n) = \sigma_z i\omega_n + \mathbf{1}\mu - \mathbf{\Delta} , \quad (\text{B.60})$$

while the self-energies follow from the Dyson's equations, Eqs. (B.16) and (B.17), as

$$\mathbf{\Sigma}'_{1/2} = \mathbf{F}' - \mathbf{G}'_0^{-1}(i\omega_0) \mathbf{\Phi}' , \quad (\text{B.61})$$

$$\mathbf{\Sigma}'(i\omega_n) = \mathbf{G}'_0^{-1}(i\omega_n) - \mathbf{G}'^{-1}(i\omega_n) . \quad (\text{B.62})$$

B.5 Lattice System

Considering the lattice system, the non-interacting Green's function satisfies

$$\mathbf{G}'_0^{-1}(\mathbf{k}, i\omega_n) = \sigma_z i\omega_n + \mathbf{1}(\mu - \epsilon_{\mathbf{k}}) , \quad (\text{B.63})$$

where $\epsilon_{\mathbf{k}}$ is the energy dispersion relation

$$\epsilon_{\mathbf{k}} = -2J \sum_{i=1}^d \cos(k_i a) \quad (\text{B.64})$$

for a hypercubic lattice in d dimensions. Also, the interacting lattice Green's function follows from Eq. (B.17) as

$$\mathbf{G}^{-1}(\mathbf{k}, i\omega_n) = \mathbf{G}_0^{-1}(\mathbf{k}, i\omega_n) - \boldsymbol{\Sigma}'(i\omega_n), \quad (\text{B.65})$$

evaluated at the reference system self-energy $\boldsymbol{\Sigma}'$. According to Eq. (B.16), the other Dyson's equation implies

$$\boldsymbol{\Phi} = -\mathbf{G}_0(i\omega_0)\boldsymbol{\Sigma}'_{1/2}, \quad (\text{B.66})$$

taking into account that $\mathbf{F} = \mathbf{0}$ since there is no symmetry breaking field on the complete lattice.

B.6 High Frequency Expansion of the Green's Function

To complete the evaluation of the trace log functional of Eq. (B.54), the coefficients \mathbf{c}_p , regarding the tail expansion of the Green's function in Eq. (B.53), remain to be determined for both reference and lattice systems.

Reference System

By expressing the Matsubara Green's function as a Fourier transform of the imaginary time Green's function, successive integration by parts yields

$$\begin{aligned} \mathbf{G}'(i\omega_n) &= \int_0^\beta d\tau e^{i\omega_n\tau} \mathbf{G}'(\tau) \\ &= \sum_{p=0}^{\infty} (-1)^p \frac{\partial_\tau^p \mathbf{G}'(\beta^-) - \partial_\tau^p \mathbf{G}'(0^+)}{(i\omega_n)^{p+1}}. \end{aligned} \quad (\text{B.67})$$

Therefore, the high frequency expansion coefficients take the form

$$\mathbf{c}'_{p+1} = (-1)^p [\partial_\tau^p \mathbf{G}'(\beta^-) - \partial_\tau^p \mathbf{G}'(0^+)]. \quad (\text{B.68})$$

From the definition of the Green's function as the time-ordered expectation value of Eq. (B.58) and the equation of motion satisfied by $\mathbf{b}(\tau)$

$$\partial_\tau \mathbf{b}(\tau) = [H', \mathbf{b}(\tau)] , \quad (\text{B.69})$$

we extract the imaginary time derivative of $\mathbf{G}'(\tau)$

$$\partial_\tau \mathbf{G}(\tau) = -\langle [H', \mathbf{b}(\tau)] \mathbf{b}^\dagger \rangle . \quad (\text{B.70})$$

By induction on Eq. (B.69) and Eq. (B.70), the derivative of order p reads as

$$\partial_\tau^p \mathbf{G}(\tau) = -\langle [[H', \mathbf{b}(\tau)]^{(p)} \mathbf{b}^\dagger] \rangle , \quad (\text{B.71})$$

with $[[H', \mathbf{b}(\tau)]^{(p)}] = [H, \dots, [H, [H, \mathbf{b}(\tau)]] \dots]$ the left side commutator of H' with $\mathbf{b}(\tau)$ applied p times. The evaluation of such derivatives at the imaginary times $\tau = 0^+$ and $\tau = \beta^-$ allows us to fix the time ordering

$$\partial_\tau^p \mathbf{G}'(0^+) = -\langle [[H', \mathbf{b}]]^{(p)} \mathbf{b}^\dagger \rangle , \quad (\text{B.72})$$

$$\partial_\tau^p \mathbf{G}'(\beta^-) = -\langle \mathbf{b}^\dagger [[H', \mathbf{b}]]^{(p)} \rangle . \quad (\text{B.73})$$

Inserting these results into Eq. (B.68), the desired coefficients simplify to

$$\mathbf{c}'_{p+1} = (-1)^p \langle [[H', \mathbf{b}]]^{(p)} \mathbf{b}^\dagger \rangle . \quad (\text{B.74})$$

Explicitly, the first order terms are

$$\mathbf{c}'_1 = \langle [\mathbf{b}, \mathbf{b}^\dagger] \rangle = \sigma_z , \quad (\text{B.75})$$

$$\mathbf{c}'_2 = -\langle [[H', \mathbf{b}], \mathbf{b}^\dagger] \rangle , \quad (\text{B.76})$$

$$\mathbf{c}'_3 = \langle [[H', [H', \mathbf{b}]], \mathbf{b}^\dagger] \rangle . \quad (\text{B.77})$$

Lattice System

According to Eqs. (B.63) and (B.65), the lattice Green's function $\mathbf{G}(\mathbf{k}, i\omega_n)$ presents a tail expansion of the form

$$\begin{aligned} \mathbf{G}(\mathbf{k}, i\omega_n) &= \frac{\sigma_z}{i\omega_n} + \frac{\sigma_z(\mathbf{1}(\epsilon_{\mathbf{k}} - \mu) + \mathbf{s}'_0)\sigma_z}{(i\omega_n)^2} + \frac{\sigma_z\mathbf{s}'_1\sigma_z + [\sigma_z(\mathbf{1}(\epsilon_{\mathbf{k}} - \mu) + \mathbf{s}'_0)]^2\sigma_z}{(i\omega_n)^3} \\ &+ \mathcal{O}\left(\frac{1}{(i\omega_n)^4}\right), \end{aligned}$$

where \mathbf{s}'_p are the high frequency expansion coefficients of the reference system's self-energy $\Sigma'(i\omega_n) = \sum_{p=1}^{\infty} \frac{\mathbf{s}'_p}{(i\omega_n)^p}$. Hence, the first order terms are

$$\mathbf{c}_1(\mathbf{k}) = \sigma_z, \quad (\text{B.78})$$

$$\mathbf{c}_2(\mathbf{k}) = \sigma_z(\mathbf{1}(\epsilon_{\mathbf{k}} - \mu) + \mathbf{s}'_0)\sigma_z, \quad (\text{B.79})$$

$$\mathbf{c}_3(\mathbf{k}) = \sigma_z\mathbf{s}'_1\sigma_z + [\sigma_z(\mathbf{1}(\epsilon_{\mathbf{k}} - \mu) + \mathbf{s}'_0)]^2\sigma_z. \quad (\text{B.80})$$

To determine the coefficients \mathbf{s}'_p of the self-energy $\Sigma'(i\omega_n) = \mathbf{G}'_0{}^{-1}(i\omega_n) - \mathbf{G}'^{-1}(i\omega_n)$, we need to compute the inverse of \mathbf{G}' , given by

$$\begin{aligned} \mathbf{G}'^{-1}(i\omega_n) &= \left[\frac{\sigma_z}{i\omega_n} + \sum_{p=2}^{\infty} \frac{\mathbf{c}'_p}{(i\omega_n)^p} \right]^{-1} \\ &= \sigma_z i\omega_n - \sigma_z \mathbf{c}'_2 \sigma_z + \frac{-\sigma_z \mathbf{c}'_3 \sigma_z + (\sigma_z \mathbf{c}'_2)^2 \sigma_z}{i\omega_n} + \mathcal{O}\left(\frac{1}{(i\omega_n)^2}\right). \end{aligned}$$

Then, the previous result combined to Eq. (B.60) implies

$$\begin{aligned} \Sigma'^{-1}(i\omega_n) &= \mathbf{G}'_0{}^{-1}(i\omega_n) - \mathbf{G}'^{-1}(i\omega_n) \\ &= \mathbf{1}\mu - \mathbf{\Delta} + \sigma_z \mathbf{c}'_2 \sigma_z - \frac{-\sigma_z \mathbf{c}'_3 \sigma_z + (\sigma_z \mathbf{c}'_2)^2 \sigma_z}{i\omega_n} + \mathcal{O}\left(\frac{1}{(i\omega_n)^2}\right). \end{aligned}$$

Consequently, the first order coefficients of the self-energy tail expansion can be written as

$$\mathbf{s}'_0 = \mathbf{1}\mu - \mathbf{\Delta} + \sigma_z \mathbf{c}'_2 \sigma_z, \quad (\text{B.81})$$

$$\mathbf{s}'_1 = \sigma_z \mathbf{c}'_3 \sigma_z - (\sigma_z \mathbf{c}'_2)^2 \sigma_z. \quad (\text{B.82})$$

From these terms, the desired lattice Green's function coefficients are evaluated according to Eqs. (B.78), (B.79) and (B.80).

Appendix C

The SFA3 code

```
SELF ENERGY FUNCTIONAL THEORY - SFA3 APPROXIMATION CODE (THE BOSE-HUBBARD MODEL)

(*
  This notebook file contains commented codes for the self-energy functional theory applied to the Bose-Hubbard model,
  considering the SFA3 approximation framework. Two codes regarding the functional (a detailed version and another more efficient) are provided.
  A routine that finds its stationary points is also included.
  At the end, we use the stationary points calculated in order to evaluate observables such as the total density and the kinetic energy of the bosons.

  Created by Eduardo Osório Rizzatti (Instituto de Física - Universidade Federal do Rio Grande do Sul)
*)

padIt[ v_? (Element[#, Reals]&), f_? List := OutputForm[AccountingForm[Chop[v, f, NumberSigns -> {"-", ""}, NumberPadding -> {"0", "0"}, SignPadding -> True]];

BASIC DEFINITIONS

Commutator[a_., b_.] := a.b - b.a (* Definition of the commutator between two operators *)
oz := {{1, 0}, {0, -1}} (* Pauli Matrix *)
e[h1_., h2_., h3_.] := -2.*Cos[h1] + Cos[h2] + Cos[h3] (* The dispersion relation in a simple cubic lattice *)

T : temperature;
μ : chemical potential;
J : hopping parameter;
U : local interaction;
z : coordination number (z = 6);
m : occupation number cutoff - off for the reference system;
nmax : number of Matsubara frequencies;

THE SELF - ENERGY FUNCTIONAL TSFT

TSFT[T_., μ_., f_., z00_., z01_., z1_., z2_., z3_., nmax_] := Module[ {},
  (* REFERENCE SYSTEM; *)
  Δ = {{z00, z01}, {Conjugate[z01], z00}};
  F = {f, Conjugate[f]};
  b = Table[Which[j == i + 1, Sqrt[i], True, 0], {i, 1, m}, {j, 1, m}]; (* Annihilation Operator b *)
  bd = Table[Which[i == j + 1, Sqrt[j], True, 0], {i, 1, m}, {j, 1, m}]; (* Creation Operator b† *)
  Href = U + bd.bd + b/2 - μ + bd.b + f + bd + Conjugate[f] + b + (z00 + (bd.b + bd.b) + Conjugate[z01] + b.b + Δ) + (bd.bd)/2; (* Reference System Hamiltonian *)
  λ = Eigenvalues[Href]; (* Eigenvalues of the Hamiltonian Href *)
  vλ = Eigenvectors[Href]; (* Eigenvectors of the Hamiltonian Href *)
  Zref = Sum[Exp[-λ[[i]]/T], {i, 1, m}]; (* Reference System Partition Function *)
  θref1 = Sum[Exp[-λ[[i]]/T] * (vλ[[i]].b.vλ[[i]]), {i, 1, m}]/Zref; (* Expectation Value of b *)
  θref2 = Sum[Exp[-λ[[i]]/T] * (vλ[[i]].bd.vλ[[i]]), {i, 1, m}]/Zref; (* Expectation Value of b† *)
  θref = {θref1, θref2}; (* Reference System Condensate; One-Point Green's Function *)
  Gref11[ω_] := Sum[If[i ≠ j, (Exp[-λ[[i]]/T] - Exp[-λ[[j]]/T]) * (vλ[[i]].b.vλ[[j]]) * (vλ[[j]].bd.vλ[[i]]) / (I*ω + λ[[i]] - λ[[j]]), 0], {i, 1, m}, {j, 1, m}]/(Zref)
  + If[ω == 0, -Sum[Exp[-λ[[i]]/T] * (vλ[[i]].b.vλ[[i]]) * (vλ[[i]].bd.vλ[[i]]), {i, 1, m}]/(7*Zref) + θref1 + θref1/T, 0];
  Gref12[ω_] := Sum[If[i ≠ j, (Exp[-λ[[i]]/T] - Exp[-λ[[j]]/T]) * (vλ[[i]].b.vλ[[j]]) * (vλ[[j]].b.vλ[[i]]) / (I*ω + λ[[i]] - λ[[j]]), 0], {i, 1, m}, {j, 1, m}]/(Zref)
  + If[ω == 0, -Sum[Exp[-λ[[i]]/T] * (vλ[[i]].b.vλ[[i]]) * (vλ[[i]].b.vλ[[i]]), {i, 1, m}]/(7*Zref) + θref1 + θref2/T, 0];
  Gref21[ω_] := Sum[If[i ≠ j, (Exp[-λ[[i]]/T] - Exp[-λ[[j]]/T]) * (vλ[[i]].bd.vλ[[j]]) * (vλ[[j]].bd.vλ[[i]]) / (I*ω + λ[[i]] - λ[[j]]), 0], {i, 1, m}, {j, 1, m}]/(Zref)
  + If[ω == 0, -Sum[Exp[-λ[[i]]/T] * (vλ[[i]].bd.vλ[[i]]) * (vλ[[i]].bd.vλ[[i]]), {i, 1, m}]/(7*Zref) + θref2 + θref1/T, 0];
  Gref22[ω_] := Sum[If[i ≠ j, (Exp[-λ[[i]]/T] - Exp[-λ[[j]]/T]) * (vλ[[i]].bd.vλ[[j]]) * (vλ[[j]].b.vλ[[i]]) / (I*ω + λ[[i]] - λ[[j]]), 0], {i, 1, m}, {j, 1, m}]/(Zref)
  + If[ω == 0, -Sum[Exp[-λ[[i]]/T] * (vλ[[i]].bd.vλ[[i]]) * (vλ[[i]].b.vλ[[i]]), {i, 1, m}]/(7*Zref) + θref2 + θref2/T, 0];
  Gref[ω_] := {{Gref11[ω], Gref12[ω]}, {Gref21[ω], Gref22[ω]}}; (* Reference System Connected Green's Function; Two-Point Green's Function *)
  IGref[ω_] := Inverse[Gref[ω]]; (* Inverse of the Reference System Connected Green's Function *)
  IGref0[ω_] := I + μ + z01 + IdentityMatrix[2] - Δ; (* Inverse of the Reference System Free Green's Function *)
  Gref0[ω_] := Inverse[IGref0[ω]]; (* Reference System Free Green's Function *)
  z1Zref = F - IGref0[0].θref; (* Reference System One-Point Self-energy *)
```

```

c2ref11= -Sum[Exp[-λ[[i]]/T]*(vλ[[i]].(Commutator[Commutator[Href,b],bd]).vλ[[i]],{i,1,m}]/Zref];
c2ref12= -Sum[Exp[-λ[[i]]/T]*(vλ[[i]].(Commutator[Commutator[Href,b],b]).vλ[[i]],{i,1,m}]/Zref];
c2ref21= -Sum[Exp[-λ[[i]]/T]*(vλ[[i]].(Commutator[Commutator[Href,bd],bd]).vλ[[i]],{i,1,m}]/Zref];
c2ref22= -Sum[Exp[-λ[[i]]/T]*(vλ[[i]].(Commutator[Commutator[Href,bd],b]).vλ[[i]],{i,1,m}]/Zref];
c2ref={c2ref11,c2ref12},{c2ref21,c2ref22};
c3ref11= Sum[Exp[-λ[[i]]/T]*(vλ[[i]].(Commutator[Commutator[Href,Commutator[Href,b],bd]).vλ[[i]],{i,1,m}]/Zref];
c3ref12= Sum[Exp[-λ[[i]]/T]*(vλ[[i]].(Commutator[Commutator[Href,Commutator[Href,b],b]).vλ[[i]],{i,1,m}]/Zref];
c3ref21= Sum[Exp[-λ[[i]]/T]*(vλ[[i]].(Commutator[Commutator[Href,Commutator[Href,bd],bd]).vλ[[i]],{i,1,m}]/Zref];
c3ref22= Sum[Exp[-λ[[i]]/T]*(vλ[[i]].(Commutator[Commutator[Href,Commutator[Href,bd],b]).vλ[[i]],{i,1,m}]/Zref];
c3ref={c3ref11,c3ref12},{c3ref21,c3ref22};
q2ref=oz.c2ref - MatrixPower[oz.c2ref,2]/2;
c2k=Tr[c2ref];
q2k = Tr[q2ref];
s0=IdentityMatrix[2]-Δ +oz.c2ref.oz;
s1=oz.c3ref.oz-oz.c2ref.oz.c2ref.oz;
(* TRACE LOG; (* Reference System Trace Log Functional *)
βref = -0.5*(Log[Det[-Gref[0]]]+Log[7^2]+c2k/(2*7)-q2k/(12*7^2)+2*Sum[Log[Det[I+oz.Gref[2*Pi+7*n]]]
+Log[(2*Pi+7*n)^2]-q2k/(I+2*Pi+7*n)^2,{n,1,mmax}]);
(* LATTICE SYSTEM;
IG0[h1,h2,h3,ω]=I+ω+oz+(μ-e[h1,h2,h3])*IdentityMatrix[2]; (* Inverse of the Free Green's Function *)
G0[h1,h2,h3,ω]=Inverse[IG0[h1,h2,h3,ω]]; (* Free Green's Function *)
IG[h1,h2,h3,ω]=IG0[h1,h2,h3,ω]-Zref[ω]; (* Inverse of the Interacting Lattice Green's Function *)
G[h1,h2,h3,ω]=Inverse[IG[h1,h2,h3,ω]]; (* Interacting Lattice Green's Function *)
$ = -G[0,0,0,0].I12ref; (* Condensate of the Lattice System *)
(* COEFFICIENTS; (* High-frequency tail coefficients of the Lattice System Green's Function and Self-Energies *)
c2t[h1,h2,h3,ω]=oz.(e[h1,h2,h3]-μ)*IdentityMatrix[2]+s0.oz;
c3t[h1,h2,h3,ω]=oz.s1.oz + MatrixPower[oz.(e[h1,h2,h3]-μ)*IdentityMatrix[2]+s0],2].oz;
q2t[h1,h2,h3,ω]=oz.c3t[h1,h2,h3,ω] - MatrixPower[oz.c2t[h1,h2,h3,ω],2]/2;
c2k=NIntegrate[Tr[c2t[k1,k2,k3]],{k1,0,2*Pi},{k2,0,2*Pi},{k3,0,2*Pi}]/(2*Pi)^3;
q2k=NIntegrate[Tr[q2t[k1,k2,k3]],{k1,0,2*Pi},{k2,0,2*Pi},{k3,0,2*Pi}]/(2*Pi)^3;
(* TRACE LOG; (* Matsubara Trace Log Functional *)
β = -0.5*(NIntegrate[Log[Det[-G[k1,k2,k3,0]]],{k1,0,2*Pi},{k2,0,2*Pi},{k3,0,2*Pi},Method->"LocalAdaptive"]/(2*Pi)^3
+Log[7^2]+c2tk/(2*7)-q2tk/(12*7^2)+2*Sum[NIntegrate[Log[Det[I+oz.G[k1,k2,k3,2*Pi+7*n]]],{k1,0,2*Pi},{k2,0,2*Pi},{k3,0,2*Pi}]/(2*Pi)^3
+Log[(2*Pi+7*n)^2]-q2tk/(I+2*Pi+7*n)^2,{n,1,mmax}]);
(* SELF-ENERGY FUNCTIONAL;
Γ = -Log[Zref] + (0.5*Conjugate[β].IG0[0,0,0,0].0)/T - (0.5*Conjugate[βref].IGref[0].βref)/T +βΔ-βAref; Γ]

```

THE SELF - ENERGY FUNCTIONAL 'ISFT' (ALTERNATIVE AND FASTER IMPLEMENTATION)

```

'ISFT2[T,μ,F,δ00,δ01,δ2,δ,ε,m,mmax]:=Module[{},
b=Table[Which[j==1,Sqrt[i],True,0],{i,1,m},{j,1,m}];
bd=Table[Which[i==j+1,Sqrt[j],True,0],{i,1,m},{j,1,m}];
Href=δ+bd.b.(bd.b-IdentityMatrix[m])/2 -μ+bd.b.F+(bd+b)+(δ00*(bd.b+bd.b)+δ01*(b.b+bd.bd))/2;
λ=Eigenvalues[Href];
vλ=Eigenvectors[Href];
Zref=Sum[Exp[-λ[[i]]/T],{i,1,m}];
βref= Sum[Exp[-λ[[i]]/T]*(vλ[[i]].b.vλ[[i]]),{i,1,m}]/Zref;
c2ref11= -Sum[Exp[-λ[[i]]/T]*(vλ[[i]].(Commutator[Commutator[Href,b],bd]).vλ[[i]],{i,1,m}]/Zref];
c2ref12= -Sum[Exp[-λ[[i]]/T]*(vλ[[i]].(Commutator[Commutator[Href,b],b]).vλ[[i]],{i,1,m}]/Zref];
trc2ref = 2+c2ref11;
c3ref11= Sum[Exp[-λ[[i]]/T]*(vλ[[i]].(Commutator[Commutator[Href,Commutator[Href,b],bd]).vλ[[i]],{i,1,m}]/Zref];
trq2ref = 2+c3ref11-(c2ref11^2-c2ref12^2);
Gref11[ω]=Sum[Sum[If[δ>0,(Exp[-λ[[i]]/T]-Exp[-λ[[j]]/T])*(vλ[[i]].b.vλ[[j]])*(vλ[[j]].bd.vλ[[i]])/(I+ω +λ[[i]]-λ[[j]]),0],{i,1,m},{j,1,m}]/Zref];
Gref12[ω]=Sum[Sum[If[δ>0,(Exp[-λ[[i]]/T]-Exp[-λ[[j]]/T])*(vλ[[i]].b.vλ[[j]])*(vλ[[j]].b.vλ[[i]])/(I+ω +λ[[i]]-λ[[j]]),0],{i,1,m},{j,1,m}]/Zref];
Gref10 =Sum[Sum[If[δ>0,(Exp[-λ[[i]]/T]-Exp[-λ[[j]]/T])*(vλ[[i]].b.vλ[[j]])*(vλ[[j]].bd.vλ[[i]])/(λ[[i]]-λ[[j]]),0],{i,1,m},{j,2,m}]/Zref
+ (-Sum[Exp[-λ[[i]]/T]*(vλ[[i]].b.vλ[[i]])*(vλ[[i]].bd.vλ[[i]]),{i,1,m}]/Zref+βref+βref)/T];
Gref120 =Sum[Sum[If[δ>0,(Exp[-λ[[i]]/T]-Exp[-λ[[j]]/T])*(vλ[[i]].b.vλ[[j]])*(vλ[[j]].b.vλ[[i]])/(λ[[i]]-λ[[j]]),0],{i,1,m},{j,1,m}]/Zref
+ (-Sum[Exp[-λ[[i]]/T]*(vλ[[i]].b.vλ[[i]])*(vλ[[i]].b.vλ[[i]]),{i,1,m}]/Zref+βref+βref)/T];
detGref0 = Abs[Gref10]^2-Abs[Gref120]^2;
IGref10= Gref10/detGref0;
IGref120= -Gref120/detGref0;
list1=Gref11[2*Pi+7*Range[mmax]];
βΔ = -0.5*(NIntegrate[Log[Det[-G[k1,k2,k3,0]]],{k1,0,2*Pi},{k2,0,2*Pi},{k3,0,2*Pi},Method->"LocalAdaptive"]/(2*Pi)^3
+Log[7^2]+c2tk/(2*7)-q2tk/(12*7^2)+2*Sum[NIntegrate[Log[Det[I+oz.G[k1,k2,k3,2*Pi+7*n]]],{k1,0,2*Pi},{k2,0,2*Pi},{k3,0,2*Pi}]/(2*Pi)^3
+Log[(2*Pi+7*n)^2]-q2tk/(I+2*Pi+7*n)^2,{n,1,mmax}]);
(* SELF-ENERGY FUNCTIONAL;
Γ = -Log[Zref] + (0.5*Conjugate[β].IG0[0,0,0,0].0)/T - (0.5*Conjugate[βref].IGref[0].βref)/T +βΔ-βAref; Γ]

```

THE SELF - ENERGY FUNCTIONAL 'ISFT' (ALTERNATIVE AND FASTER IMPLEMENTATION)

```

'ISFT2[T,μ,F,δ00,δ01,δ2,δ,ε,m,mmax]:=Module[{},
b=Table[Which[j==1,Sqrt[i],True,0],{i,1,m},{j,1,m}];
bd=Table[Which[i==j+1,Sqrt[j],True,0],{i,1,m},{j,1,m}];
Href=δ+bd.b.(bd.b-IdentityMatrix[m])/2 -μ+bd.b.F+(bd+b)+(δ00*(bd.b+bd.b)+δ01*(b.b+bd.bd))/2;
λ=Eigenvalues[Href];
vλ=Eigenvectors[Href];
Zref=Sum[Exp[-λ[[i]]/T],{i,1,m}];
βref= Sum[Exp[-λ[[i]]/T]*(vλ[[i]].b.vλ[[i]]),{i,1,m}]/Zref;
c2ref11= -Sum[Exp[-λ[[i]]/T]*(vλ[[i]].(Commutator[Commutator[Href,b],bd]).vλ[[i]],{i,1,m}]/Zref];
c2ref12= -Sum[Exp[-λ[[i]]/T]*(vλ[[i]].(Commutator[Commutator[Href,b],b]).vλ[[i]],{i,1,m}]/Zref];
trc2ref = 2+c2ref11;
c3ref11= Sum[Exp[-λ[[i]]/T]*(vλ[[i]].(Commutator[Commutator[Href,Commutator[Href,b],bd]).vλ[[i]],{i,1,m}]/Zref];
trq2ref = 2+c3ref11-(c2ref11^2-c2ref12^2);
Gref11[ω]=Sum[Sum[If[δ>0,(Exp[-λ[[i]]/T]-Exp[-λ[[j]]/T])*(vλ[[i]].b.vλ[[j]])*(vλ[[j]].bd.vλ[[i]])/(I+ω +λ[[i]]-λ[[j]]),0],{i,1,m},{j,1,m}]/Zref];
Gref12[ω]=Sum[Sum[If[δ>0,(Exp[-λ[[i]]/T]-Exp[-λ[[j]]/T])*(vλ[[i]].b.vλ[[j]])*(vλ[[j]].b.vλ[[i]])/(I+ω +λ[[i]]-λ[[j]]),0],{i,1,m},{j,1,m}]/Zref];
Gref10 =Sum[Sum[If[δ>0,(Exp[-λ[[i]]/T]-Exp[-λ[[j]]/T])*(vλ[[i]].b.vλ[[j]])*(vλ[[j]].bd.vλ[[i]])/(λ[[i]]-λ[[j]]),0],{i,1,m},{j,2,m}]/Zref
+ (-Sum[Exp[-λ[[i]]/T]*(vλ[[i]].b.vλ[[i]])*(vλ[[i]].bd.vλ[[i]]),{i,1,m}]/Zref+βref+βref)/T];
Gref120 =Sum[Sum[If[δ>0,(Exp[-λ[[i]]/T]-Exp[-λ[[j]]/T])*(vλ[[i]].b.vλ[[j]])*(vλ[[j]].b.vλ[[i]])/(λ[[i]]-λ[[j]]),0],{i,1,m},{j,1,m}]/Zref
+ (-Sum[Exp[-λ[[i]]/T]*(vλ[[i]].b.vλ[[i]])*(vλ[[i]].b.vλ[[i]]),{i,1,m}]/Zref+βref+βref)/T];
detGref0 = Abs[Gref10]^2-Abs[Gref120]^2;
IGref10= Gref10/detGref0;
IGref120= -Gref120/detGref0;
list1=Gref11[2*Pi+7*Range[mmax]];

```



```

list2=Gref12[2*Pi+T*Range[nmax]];
list={};
For[n=1,nmax,n++,
Gref1n=list1[[n]];
Gref12n=list2[[n]];
detGrefn= Abs[Gref1n]^2-Abs[Gref12n]^2;
IGref1n= Gref1n/detGrefn;
IGref12n= -Gref12n/detGrefn;
AppendTo[list,{Gref1n,Gref12n,detGrefn,IGref1n,IGref12n}];
s011=μ-Δ00+c2ref11;
s012=-Δ01-c2ref12;
trc2=2*(c2ref11-Δ00);
trq2=2*(c3ref11-c2ref11^2+c2ref12^2)+z^2+μ^2-2*μ*(μ-Δ00+c2ref11)+s011^2-s012^2;
βΔGref=0.5*(Log[Γ^2*detGref0]+trc2ref/(2*7)-trq2ref/(12*7^2)+2*Sum[Log[(2*Pi+T+n)^2*list[[n,3]]-trq2ref/(1+2*Pi+T+n)^2,(n,1,nmax)]];
βΔG=0.5*(NIntegrate[-Log[(1Gref10+Δ00-e^{k1,k2,k3})^2-(1Gref120+Δ01)^2],{k1,0,Π},{k2,0,Π},{k3,0,Π},Method->"LocalAdaptive"]/(Π)^3
+Log[Γ^2]+trc2/(2*7)-trq2/(12*7^2)+2*NIntegrate[Sum[-Log[Abs[list[[n,4]]+Δ00-e^{k1,k2,k3})^2-Abs[list[[n,5]]+Δ01]^2]+Log[(2*Pi+T+n)^2]-trq2/(1+2*Pi+T+n)^2,(n,1,nmax)},{k1,0,Π},{k2,0,Π},{k3,0,Π},Method->"LocalAdaptive"]/(Π)^3);
Γ=-Log[Zref]+((β-Gref*(μ-Δ00-Δ01))^2/(μ+z+3))/T-(βref^2*(μ-Δ00-Δ01))/T-βΔGref+βΔG;
Γ]

```

FINDING STATIONARY POINTS OF TSFT (ALGORITHM BASED ON NEWTON'S METHOD IN OPTIMIZATION)

```

f = -3.6; (* Initial guess for f *)
Δ00 = -1.5; (* Initial guess for Δ00 *)
Δ01 = 0.5; (* Initial guess for Δ01 *)
m = 11;
z = 6;
J = 1;
U = 20;
μ = 0.4*U;
T = 3.5;

nmax = 1000;
δ = 0.001; (* Infinitesimal increments used in derivatives *)
For[j=1,j<=10,j++,
xa = {f,Δ00,Δ01};
abc = Re[TSFT2[T,μ,f,Δ00,Δ01,3,U,z,m,nmax]];
ap0 = Re[TSFT2[T,μ,f+δ,Δ00,Δ01,3,U,z,m,nmax]];
am0 = Re[TSFT2[T,μ,f-δ,Δ00,Δ01,3,U,z,m,nmax]];
bp0 = Re[TSFT2[T,μ,f,Δ00+δ,Δ01,3,U,z,m,nmax]];
bm0 = Re[TSFT2[T,μ,f,Δ00-δ,Δ01,3,U,z,m,nmax]];
cp0 = Re[TSFT2[T,μ,f,Δ00,Δ01+δ,3,U,z,m,nmax]];
cm0 = Re[TSFT2[T,μ,f,Δ00,Δ01-δ,3,U,z,m,nmax]];
ap0bp0 = Re[TSFT2[T,μ,f+δ,Δ00+δ,Δ01,3,U,z,m,nmax]];
am0bm0 = Re[TSFT2[T,μ,f-δ,Δ00-δ,Δ01,3,U,z,m,nmax]];
ap0cp0 = Re[TSFT2[T,μ,f+δ,Δ00,Δ01+δ,3,U,z,m,nmax]];
am0cm0 = Re[TSFT2[T,μ,f-δ,Δ00,Δ01-δ,3,U,z,m,nmax]];
bp0cp0 = Re[TSFT2[T,μ,f,Δ00+δ,Δ01+δ,3,U,z,m,nmax]];
bm0cm0 = Re[TSFT2[T,μ,f,Δ00-δ,Δ01-δ,3,U,z,m,nmax]];
d1df = (ap0 - am0) / (2*δ);
d1dΔ00 = (bp0 - bm0) / (2*δ);
d1dΔ01 = (cp0 - cm0) / (2*δ);
d2fd2f = (ap0 - 2*abc+am0) / (δ^2);
d2fd2Δ00 = (bp0 - 2*abc+bm0) / (δ^2);
d2fd2Δ01 = (cp0 - 2*abc+cm0) / (δ^2);
d2fd00df = (ap0bp0-ap0-bp0+2*abc+am0bm0-am0-bm0) / (2*δ^2);
d2fd01df = (ap0cp0-ap0-cp0+2*abc+am0cm0-am0-cm0) / (2*δ^2);
d2fd01d00 = (bp0cp0-bp0-cp0+2*abc+bm0cm0-bm0-cm0) / (2*δ^2);
gradf = {d1df,d1dΔ00,d1dΔ01}; (* Gradient of TSFT *)
H = {{d2fd2f,d2fd00df,d2fd01df},{d2fd00df,d2fd200,d2fd01d00},{d2fd01df,d2fd01d00,d2fd201}}; (* Hessian of TSFT *)
xb = xa-1*Inverse[H].gradf; (* Fixed Point Iteration *)
If[Sqrt[Abs[(xa-xb).(xa-xb)]] > 0.000001,And[f<xb[[1]],Δ00<xb[[2]],Δ01<xb[[3]],Break[]];];
Print[padIt[T,{10,9}], " ",padIt[μ,{10,9}], " ",padIt[f,{10,9}], " ",padIt[Δ00,{10,9}], " ",padIt[Δ01,{10,9}], " ",j];

```

3.500000000 0.400000000 -3.566072041 -0.766474518 0.584067458 6

OBSERVABLES : DENSITY AND KINETIC ENERGY

```

Δ={Δ00,Δ01},{Conjugate[Δ01],Δ00};
F={f,Conjugate[f]};
b=Table[Which[j==1,Sqrt[i],True,0],{i,1,m},{j,1,m}];
bd=Table[Which[i==1,Sqrt[j],True,0],{i,1,m},{j,1,m}];
Href=U*bd.b.b/2-μ*bd.b+f*bd+Conjugate[f]*b+(Δ00*(bd.b+bd.b)+Conjugate[Δ01]*b.b+Δ01*bd.bd)/2;
λ=Eigenvalues[Href];
vλ=Eigenvectors[Href];
Zref=Sum[Exp[-λ[[i]]/T],{i,1,m}];
sref1=Sum[Exp[-λ[[i]]/T]*(vλ[[i]].b.vλ[[i]])],{i,1,m}]/Zref;
sref2=Sum[Exp[-λ[[i]]/T]*(vλ[[i]].bd.vλ[[i]])],{i,1,m}]/Zref;
sref={sref1,sref2};
Gref11[ω]=Sum[If[λ[[i]]>0,Exp[-λ[[i]]/T]-Exp[-λ[[i]]/T]*(vλ[[i]].b.vλ[[i]])+(vλ[[i]].b.vλ[[i]])*(vλ[[i]].bd.vλ[[i]])/(1+ω+λ[[i]]-λ[[i]]),0],{i,1,m},{j,1,m}]/(Zref)
+If[ω==0,-Sum[Exp[-λ[[i]]/T]*(vλ[[i]].b.vλ[[i]])+(vλ[[i]].bd.vλ[[i]])],{i,1,m}]/(T*Zref)+sref1+sref2/T,0];
Gref12[ω]=Sum[If[λ[[i]]>0,Exp[-λ[[i]]/T]-Exp[-λ[[i]]/T]*(vλ[[i]].bd.vλ[[i]])+(vλ[[i]].bd.vλ[[i]])*(vλ[[i]].b.vλ[[i]])/(1+ω+λ[[i]]-λ[[i]]),0],{i,1,m},{j,1,m}]/(Zref)
+If[ω==0,-Sum[Exp[-λ[[i]]/T]*(vλ[[i]].bd.vλ[[i]])+(vλ[[i]].b.vλ[[i]])],{i,1,m}]/(T*Zref)+sref2+sref1/T,0];
Gref21[ω]=Sum[If[λ[[i]]>0,Exp[-λ[[i]]/T]-Exp[-λ[[i]]/T]*(vλ[[i]].bd.vλ[[i]])+(vλ[[i]].bd.vλ[[i]])*(vλ[[i]].bd.vλ[[i]])/(1+ω+λ[[i]]-λ[[i]]),0],{i,1,m},{j,1,m}]/(Zref)
+If[ω==0,-Sum[Exp[-λ[[i]]/T]*(vλ[[i]].bd.vλ[[i]])+(vλ[[i]].bd.vλ[[i]])],{i,1,m}]/(T*Zref)+sref2+sref1/T,0];
Gref22[ω]=Sum[If[λ[[i]]>0,Exp[-λ[[i]]/T]-Exp[-λ[[i]]/T]*(vλ[[i]].bd.vλ[[i]])+(vλ[[i]].bd.vλ[[i]])*(vλ[[i]].b.vλ[[i]])/(1+ω+λ[[i]]-λ[[i]]),0],{i,1,m},{j,1,m}]/(Zref)
+If[ω==0,-Sum[Exp[-λ[[i]]/T]*(vλ[[i]].bd.vλ[[i]])+(vλ[[i]].bd.vλ[[i]])],{i,1,m}]/(T*Zref)+sref2+sref1/T,0];
Gref[ω]={{Gref11[ω],Gref12[ω]},{Gref21[ω],Gref22[ω]}};
IGref[ω]=Inverse[Gref[ω]];
IGref0[ω]=1*ω+μ*IdentityMatrix[2]-Δ;
Gref0[ω]=Inverse[IGref0[ω]];
X12ref=F-IGref0[0].sref;
Xref[ω]=IGref0[ω]-IGref[ω];
H COEFFICIENTS;
c1ref=oz;

```

```

c2ref11= -Sum[Exp[-λ[[i]]/T]*(vλ[[i]]*(Commutator[Commutator[Href,b],bd]).vλ[[i]]),(i,1,m)]/(Zref);
c2ref12= -Sum[Exp[-λ[[i]]/T]*(vλ[[i]]*(Commutator[Commutator[Href,b],b]).vλ[[i]]),(i,1,m)]/(Zref);
c2ref21= -Sum[Exp[-λ[[i]]/T]*(vλ[[i]]*(Commutator[Commutator[Href,bd],bd]).vλ[[i]]),(i,1,m)]/(Zref);
c2ref22= -Sum[Exp[-λ[[i]]/T]*(vλ[[i]]*(Commutator[Commutator[Href,bd],b]).vλ[[i]]),(i,1,m)]/(Zref);
c2ref={c2ref11,c2ref12},c2ref21,c2ref22};
c3ref11= Sum[Exp[-λ[[i]]/T]*(vλ[[i]]*(Commutator[Commutator[Href,Commutator[Href,b],bd]).vλ[[i]]),(i,1,m)]/(Zref);
c3ref12= Sum[Exp[-λ[[i]]/T]*(vλ[[i]]*(Commutator[Commutator[Href,Commutator[Href,b],b]).vλ[[i]]),(i,1,m)]/(Zref);
c3ref21= Sum[Exp[-λ[[i]]/T]*(vλ[[i]]*(Commutator[Commutator[Href,Commutator[Href,bd],bd]).vλ[[i]]),(i,1,m)]/(Zref);
c3ref22= Sum[Exp[-λ[[i]]/T]*(vλ[[i]]*(Commutator[Commutator[Href,Commutator[Href,bd],b]).vλ[[i]]),(i,1,m)]/(Zref);
c3ref={c3ref11,c3ref12},c3ref21,c3ref22};
q2ref=oz.c3ref - MatrixPower[oz.c2ref,2];
c2kaTr[c2ref];
q2k = Tr[q2ref];
s0=IdentityMatrix[2]-Δ +oz.c2ref.oz;
s1=oz.c3ref.oz-oz.c2ref.oz.c2ref.oz;
;; TRACE LOG;
βAref = -0.5*(Log[Det[-Gref[0]])+Log[T^2]+c2k/(2*T)-q2k/(12*T^2)+2*Sum[Log[Det[I+oz.Gref[2+Pi+T+n]] +Log[(2+Pi+T+n)^2]-q2k/(1+2+Pi+T+n)^2,{n,1,nmax}]]];
;; LATTICE SYSTEM;
IG0[h1_,h2_,h3_,ω_]:=I+ω+oz*(μ-(e[h1,h2,h3])*IdentityMatrix[2];
G0[h1_,h2_,h3_,ω_]:=Inverse[IG0[h1,h2,h3,ω]];
IG[h1_,h2_,h3_,ω_]:=IG0[h1,h2,h3,ω]-Eref[ω];
G[h1_,h2_,h3_,ω_]:=Inverse[IG[h1,h2,h3,ω]];
μ =-G0[0,0,0,0].112ref;
;; COEFFICIENTS;
c2t[h1_,h2_,h3_]:=oz*((e[h1,h2,h3]-μ)*IdentityMatrix[2]+s0).oz;
c3t[h1_,h2_,h3_]:=oz.s1.oz + MatrixPower[(oz*((e[h1,h2,h3]-μ)*IdentityMatrix[2]+s0)),2].oz;
q2t[h1_,h2_,h3_]:=oz.c3t[h1,h2,h3] - MatrixPower[oz.c2t[h1,h2,h3],2]/2;
c2tk=NIntegrate[Tr[c2t[k1,k2,k3]],{k1,0,2+Pi},{k2,0,2+Pi},{k3,0,2+Pi}]/(2+Pi)^3;
q2tk=NIntegrate[Tr[q2t[k1,k2,k3]],{k1,0,2+Pi},{k2,0,2+Pi},{k3,0,2+Pi}]/(2+Pi)^3;
pk[h1_,h2_,h3_]:=-(Tr[G[h1,h2,h3,0]]+2*Sum[Tr[G[h1,h2,h3,2+Pi+n*T]]-Tr[c2t[h1,h2,h3]]/(1+2+Pi+T+n)^2,{n,1,nmax}]+(1/T)*(1-Tr[c2t[h1,h2,h3]]/(12*T)))+T/2;
ρce=0.5*ρ; (* Condensate Density *)
ρ=NIntegrate[ρk[k1,k2,k3],{k1,0,Pi},{k2,0,Pi},{k3,0,Pi},Method->"LocalAdaptive"]/(Pi)^3+ρc; (* Total Number Density *)
Ekin=NIntegrate[e[k1,k2,k3]*ρk[k1,k2,k3],{k1,0,Pi},{k2,0,Pi},{k3,0,Pi},Method->"LocalAdaptive"]/(Pi)^3+e[0,0,0]*ρc; (* Kinetic Energy *)
Print[padIt[T,{10,9}],",",padIt[μ,U,{10,9}],",",padIt[E,{10,9}],",",padIt[Δ00,{10,9}],",",padIt[Δ01,{10,9}],",",padIt[ρ,{10,9}],",",padIt[Re[Ekin],{10,9}]];

```

```

3.500000000 0.400000000 -3.566072041 -0.766474518 0.584067458 1.024460704 -3.089783898

```

Appendix D

Equation of State and Pressure for the Harmonic Confinement

Considering the two dimensional setup discussed in Section 3.6, the total pressure P_{total} is evaluated by integrating the Gibbs-Duhem relation $dP = \rho d\mu + s dT$ at fixed temperature T over the lattice

$$P_{total} = \int_{-\infty}^{\mu_0} \rho d\mu = - \int_0^{\infty} \rho(r) \frac{d\mu}{dr} dr . \quad (\text{D.1})$$

For an isotropic harmonic trap in the xy plane, $\mu = \mu_0 - \frac{1}{2}m\omega^2 r^2$ and $\frac{d\mu}{dr} = -m\omega^2 r$; then Eq. (D.1) becomes

$$P_{total} = m\omega^2 \int_0^{\infty} \rho(r) r dr . \quad (\text{D.2})$$

The total number of particles N_{total} is obtained by integration of the local density $\rho(r)$ according to

$$N_{total} = 2\pi \int_0^{\infty} \rho(r) r dr . \quad (\text{D.3})$$

Comparing both Eqs. (D.2) and (D.3), we deduce the equation of state

$$P_{total} = \frac{m\omega^2}{2\pi} N_{total} , \quad (\text{D.4})$$

valid for 2D gases including an isotropic harmonic confinement [124, 125]. There is also another interesting observation concerning the value of the fixed total pressure. Since the density ρ is a derivative of the free energy Ω , see Eq. (3.34), we can write P_{total} as

$$\begin{aligned} P_{total} &= - \int_{-\infty}^{\mu_0} \frac{1}{V} \left(\frac{\partial \Omega}{\partial \mu} \right)_T d\mu \\ &= \frac{1}{V} [\Omega(\mu = -\infty) - \Omega(\mu_0)] . \end{aligned} \quad (\text{D.5})$$

Considering that $\Omega(\mu = -\infty) = 0$ and $-PV = \Omega$, the total pressure is equal to the local pressure at the center of the trap

$$P_{total} = P(\mu_0) = P(r = 0) , \quad (\text{D.6})$$

as Fig. ??(a) confirms.

Appendix E

Perturbation Theory

E.1 General Aspects

In this section, we explore the finite-temperature perturbation theory (PT) around the atomic limit in order to describe the normal phase [185, 186]. The non-local kinetic energy term is treated perturbatively by expanding the grand canonical free-energy and the Green's function in powers of the hopping amplitude. Therefore, we decompose the Bose-Hubbard Hamiltonian into

$$H = H^{(0)} + \mathcal{H} , \tag{E.1}$$

where the atomic limit is given by

$$H^{(0)} = \frac{U}{2} \sum_i n_i(n_i - 1) - \mu \sum_i n_i , \tag{E.2}$$

and the kinetic term follows as

$$\mathcal{H} = \sum_{i,j} J_{ij} b_i^\dagger b_j , \tag{E.3}$$

with the summation comprehending the whole lattice without restrictions and the hopping matrix element J_{ij} considered as a general term. In this framework, the

operators are represented in the Dirac interaction picture according to

$$O(\tau) = e^{\tau H^{(0)}} O e^{-\tau H^{(0)}} . \quad (\text{E.4})$$

The time evolution operator $\mathcal{U}(\tau, \tau_0)$ obeys the following Schrodinger's equation

$$\frac{d}{d\tau} \mathcal{U}(\tau, \tau_0) = -\mathcal{H}(\tau) \mathcal{U}(\tau, \tau_0) , \quad (\text{E.5})$$

with initial condition $\mathcal{U}(\tau_0, \tau_0) = 1$, whose formal solution is given by the Dyson's expansion

$$\begin{aligned} \mathcal{U}(\tau, \tau_0) &= \mathcal{T} \left[e^{-\int_{\tau_0}^{\tau} \mathcal{H}(\tau') d\tau'} \right] \\ &= \sum_{n=0}^{\infty} \frac{(-1)^n}{n!} \int_{\tau_0}^{\tau} d\tau_1 \int_{\tau_0}^{\tau} d\tau_2 \cdots \int_{\tau_0}^{\tau} d\tau_n \mathcal{T} [\mathcal{H}(\tau_1) \mathcal{H}(\tau_2) \cdots \mathcal{H}(\tau_n)] . \end{aligned} \quad (\text{E.6})$$

The definition of Eq. (E.3) into Eq. (E.6) yields an explicit expression of the imaginary time evolution operator

$$\begin{aligned} \mathcal{U}(\tau, \tau_0) &= \sum_{n=0}^{\infty} \frac{(-1)^n}{n!} \sum_{j'_1 \cdots j'_n, j_1 \cdots j_n} J_{j'_1 j_1} \cdots J_{j'_n j_n} \times \\ &\quad \times \int_{\tau_0}^{\tau} d\tau_1 \int_{\tau_0}^{\tau} d\tau_2 \cdots \int_{\tau_0}^{\tau} d\tau_n \mathcal{T} \left[b_{j'_1}^{\dagger}(\tau_1) b_{j_1}(\tau_1) \cdots b_{j'_n}^{\dagger}(\tau_n) b_{j_n}(\tau_n) \right] , \end{aligned} \quad (\text{E.7})$$

from which perturbative approximations can be established. Including finite-temperature effects (with $k_B T = 1/\beta$), the partition function $\mathcal{Z} = \text{Tr}[\mathcal{T} e^{-\mathcal{S}}]$ follows as a trace comprising the imaginary time-ordered exponential of the euclidean action \mathcal{S} [106–108], taking the form

$$\begin{aligned} \mathcal{Z} &= \text{Tr} \left\{ \mathcal{T} \left[e^{-\int_0^{\beta} H(\tau) d\tau} \right] \right\} \\ &= \text{Tr} \left\{ e^{-\beta H^{(0)}} \mathcal{T} \left[e^{-\int_0^{\beta} \mathcal{H}(\tau) d\tau} \right] \right\} \\ &= \text{Tr} \left\{ e^{-\beta H^{(0)}} \mathcal{U}(\beta, 0) \right\} . \end{aligned} \quad (\text{E.8})$$

If we introduce the atomic limit partition function $\mathcal{Z}^{(0)}$ into Eq. (E.8), we obtain

$$\begin{aligned}\mathcal{Z} &= \mathcal{Z}^{(0)} \frac{1}{\mathcal{Z}^{(0)}} \text{Tr} \left\{ e^{-\beta H^{(0)}} \mathcal{T} \left[e^{-\int_0^\beta \mathcal{H}(\tau) d\tau} \right] \right\} \\ &= \mathcal{Z}^{(0)} \left\langle \mathcal{T} \left[e^{-\int_0^\beta \mathcal{H}(\tau) d\tau} \right] \right\rangle_0 \\ &= \mathcal{Z}^{(0)} \langle \mathcal{U}(\beta, 0) \rangle_0 ,\end{aligned}\tag{E.9}$$

describing \mathcal{Z} in terms of thermal averages $\langle \dots \rangle_0$ taken with respect to the unperturbed Hamiltonian $H^{(0)}$. By setting $\tau_0 = 0$ and $\tau = \beta$, Eq. (E.7) yields

$$\begin{aligned}\langle \mathcal{U}(\beta, 0) \rangle_0 &= \sum_{n=0}^{\infty} \frac{(-1)^n}{n!} \sum_{j'_1 \dots j'_n, j_1 \dots j_n} J_{j'_1 j_1} \dots J_{j'_n j_n} \times \\ &\quad \times \int_0^\beta d\tau_1 \dots \int_0^\beta d\tau_n \left\langle \mathcal{T} \left[b_{j'_1}^\dagger(\tau_1) b_{j_1}(\tau_1) \dots b_{j'_n}^\dagger(\tau_n) b_{j_n}(\tau_n) \right] \right\rangle_0\end{aligned}\tag{E.10}$$

which provides an expansion of \mathcal{Z} in powers of the hopping matrix element J_{ij} and the creation/annihilation operators. The ensemble averages appearing can be identified as the n -particle Green' function taken with respect to the unperturbed system and evaluated at equal times $\tau_m = \tau'_m$

$$G_n^{(0)}(j'_1, \tau'_1, \dots, j'_n, \tau'_n | j_1, \tau_1, \dots, j_n, \tau_n) \equiv \left\langle \mathcal{T} \left[b_{j'_1}^\dagger(\tau'_1) b_{j_1}(\tau_1) \dots b_{j'_n}^\dagger(\tau'_n) b_{j_n}(\tau_n) \right] \right\rangle_0\tag{E.11}$$

In a more concise notation, we can group space and time variables producing

$$G_n^{(0)}(1', \dots, n' | 1, \dots, n) \equiv G_n^{(0)}(j'_1, \tau'_1, \dots, j'_n, \tau'_n | j_1, \tau_1, \dots, j_n, \tau_n) .\tag{E.12}$$

E.2 Moments and Cumulants

In order to determine the moments $G_n^{(0)}$, the standard Wick's theorem [107] cannot be applied because the unperturbed Hamiltonian $H^{(0)}$ is not quadratic in the bosonic operators. Therefore, the well-known formalism of perturbative techniques based on standard Feynman diagrams [108] derived from Wick's theorem are not suitable for our perturbative analysis. Nevertheless, it is possible to simplify the terms $G_n^{(0)}$ by

decomposing them into cumulants $C_n^{(0)}$. Indeed, as we address in the next paragraphs, the moments can be generally expressed as a summation over the cumulants considering all possible partitions of random variables.

The moments G of a set of random variables X_1, \dots, X_n are defined as the expectation value E

$$G(X_1, \dots, X_m) = E [X_1 \dots X_m] , \quad (\text{E.13})$$

regarding a general probability distribution. They are obtained through a moment generating function, or partition function, defined by the following expectation value

$$\mathcal{Z}(\mathbf{t}) = E [e^{\mathbf{t} \cdot \mathbf{X}}] = E [e^{\sum_i t_i X_i}] , \quad (\text{E.14})$$

where $\mathbf{t} = (t_1, \dots, t_n)$ and $\mathbf{X} = (X_1, \dots, X_n)$. Indeed, the moments are simply the coefficients of the power series expansion of the moment generating function, given by successive differentiation of \mathcal{Z} according to

$$G(X_1, \dots, X_m) = \left. \frac{\partial}{\partial t_m} \dots \frac{\partial}{\partial t_1} \mathcal{Z}(\mathbf{t}) \right|_{\mathbf{t}=0} . \quad (\text{E.15})$$

Analogously, the cumulants C can be obtained through a cumulant generating function

$$\mathcal{W}(\mathbf{t}) = \ln \mathcal{Z}(\mathbf{t}) = \ln E [e^{\sum_i t_i X_i}] , \quad (\text{E.16})$$

which is the logarithm of the moment generating function. Being the coefficients of the power series expansion of the generating function \mathcal{W} , they are obtained by successive differentiation as

$$C(X_1, \dots, X_m) = \left. \frac{\partial}{\partial t_m} \dots \frac{\partial}{\partial t_1} \mathcal{W}(\mathbf{t}) \right|_{\mathbf{t}=0} . \quad (\text{E.17})$$

From their respective definitions, these statistical quantities are closely related to each other. Indeed, it is possible to express the expectation value G [187] as a summation

of products of cumulants over all possible partitions π of the set $\{1, \dots, m\}$, yielding

$$G(X_1, \dots, X_m) = \sum_{\pi} \prod_{B \in \pi} C(X_i; i \in B). \quad (\text{E.18})$$

For example, the expectation value $G(X_1, X_2, X_3)$ is decomposed as

$$\begin{aligned} G(X_1, X_2, X_3) &= C(X_1, X_2, X_3) + C(X_1, X_2)C(X_3) + C(X_1, X_3)C(X_2) \\ &\quad + C(X_2, X_3)C(X_1) + C(X_1)C(X_2)C(X_3). \end{aligned}$$

Based on these previous observations and general remarks, the Green's functions taken with respect to the unperturbed system are derived directly from a moment generating functional

$$\mathcal{Z}^{(0)}[\mathbf{F}] = \left\langle \mathcal{T} e^{-\int_0^\beta d\tau \mathbf{F}_\alpha^\dagger(\tau) \mathbf{b}^\alpha(\tau)} \right\rangle_0 = \left\langle \mathcal{T} e^{-\sum_j \int_0^\beta d\tau [F_j^*(\tau) b_j(\tau) + F_j(\tau) b_j^\dagger(\tau)]} \right\rangle_0 \quad (\text{E.19})$$

of the introduced linear fields $F_j(\tau)$ and $F_j^*(\tau)$ in the Nambu notation. Successive functional differentiation yields the moments, or Green's functions, as follows

$$\mathbf{G}_n^{(0)}(j'_1, \tau'_1, \dots, j'_n, \tau'_n | j_1, \tau_1, \dots, j_n, \tau_n) = \frac{\delta}{\delta F_{j_n}^*(\tau_n)} \frac{\delta}{\delta F_{j'_n}(\tau'_n)} \cdots \frac{\delta}{\delta F_{j_1}^*(\tau_1)} \frac{\delta}{\delta F_{j'_1}(\tau'_1)} \mathcal{Z}^{(0)}[\mathbf{F}] \Bigg|_{\mathbf{F}=0}. \quad (\text{E.20})$$

The cumulant generating functional is obtained from the logarithm of the partition function

$$\begin{aligned} \mathcal{W}^{(0)}[\mathbf{F}] &= \ln \mathcal{Z}^{(0)}[\mathbf{F}] = \ln \left\langle \mathcal{T} e^{-\int_0^\beta d\tau \mathbf{F}_\alpha^\dagger(\tau) \mathbf{b}^\alpha(\tau)} \right\rangle_0 \\ &= \ln \left\langle \mathcal{T} e^{-\sum_j \int_0^\beta d\tau [F_j^*(\tau) b_j(\tau) + F_j(\tau) b_j^\dagger(\tau)]} \right\rangle_0, \end{aligned} \quad (\text{E.21})$$

with the cumulants $C_n^{(0)}$, or connected Green's functions, defined according to

$$C_n^{(0)}(j'_1, \tau'_1, \dots, j'_n, \tau'_n | j_1, \tau_1, \dots, j_n, \tau_n) = \frac{\delta}{\delta F_{j_n}^*(\tau_n)} \frac{\delta}{\delta F_{j'_n}(\tau'_n)} \cdots \frac{\delta}{\delta F_{j_1}^*(\tau_1)} \frac{\delta}{\delta F_{j'_1}(\tau'_1)} \mathcal{W}^{(0)}[\mathbf{F}] \Bigg|_{\mathbf{F}=0}. \quad (\text{E.22})$$

From them, we extract direct expressions for the cumulants in terms of the moments for each value of n :

$$\begin{aligned}
C_1^{(0)}(1'|1) &= \left. \frac{\delta^2 \mathcal{W}^{(0)}[\mathbf{F}]}{\delta F^*(1) \delta F(1')} \right|_{\mathbf{F}=0} \\
&= -\langle b(1) \rangle_0 \langle b^\dagger(1') \rangle_0 + \langle \mathcal{T} [b^\dagger(1') b(1)] \rangle_0 \\
&= \langle \mathcal{T} [b^\dagger(1') b(1)] \rangle_0 \\
&= G_1^{(0)}(1'|1), \tag{E.23}
\end{aligned}$$

$$\begin{aligned}
C_2^{(0)}(1', 2'|1, 2) &= \left. \frac{\delta^4 \mathcal{W}^{(0)}[\mathbf{F}]}{\delta F^*(2) \delta F(2') \delta F^*(1) \delta F(1')} \right|_{\mathbf{F}=0} \\
&= -6 \langle b(2) \rangle_0 \langle b^\dagger(2') \rangle_0 \langle b(1) \rangle_0 \langle b^\dagger(1') \rangle_0 + 2 \langle \mathcal{T} [b^\dagger(2') b(2)] \rangle_0 \langle b(1) \rangle_0 \langle b^\dagger(1') \rangle_0 \\
&\quad + 2 \langle b^\dagger(2') \rangle_0 \langle \mathcal{T} [b(1) b(2)] \rangle_0 \langle b^\dagger(1') \rangle_0 + 2 \langle b^\dagger(2') \rangle_0 \langle b(1) \rangle_0 \langle \mathcal{T} [b^\dagger(1') b(2)] \rangle_0 \\
&\quad + 2 \langle b(2) \rangle_0 \langle \mathcal{T} [b(1) b^\dagger(2')] \rangle_0 \langle b^\dagger(1') \rangle_0 - \langle \mathcal{T} [b(1) b^\dagger(2') b(2)] \rangle_0 \langle b^\dagger(1') \rangle_0 \\
&\quad - \langle \mathcal{T} [b(1) b^\dagger(2')] \rangle_0 \langle \mathcal{T} [b^\dagger(1') b(2)] \rangle_0 + 2 \langle b(2) \rangle_0 \langle b(1) \rangle_0 \langle \mathcal{T} [b^\dagger(1') b^\dagger(2')] \rangle_0 \\
&\quad - \langle \mathcal{T} [b(1) b(2)] \rangle_0 \langle \mathcal{T} [b^\dagger(1') b^\dagger(2')] \rangle_0 - \langle b(1) \rangle_0 \langle \mathcal{T} [b^\dagger(1') b^\dagger(2') b(2)] \rangle_0 \\
&\quad + 2 \langle b(2) \rangle_0 \langle b^\dagger(2') \rangle_0 \langle \mathcal{T} [b^\dagger(1') b(1)] \rangle_0 - \langle \mathcal{T} [b^\dagger(2') b(2)] \rangle_0 \langle \mathcal{T} [b^\dagger(1') b(1)] \rangle_0 \\
&\quad - \langle b^\dagger(2') \rangle_0 \langle \mathcal{T} [b^\dagger(1') b(1) b(2)] \rangle_0 - 2 \langle b(2) \rangle_0 \langle \mathcal{T} [b^\dagger(1') b(1) b^\dagger(2')] \rangle_0 \\
&\quad + \langle \mathcal{T} [b^\dagger(1') b(1) b^\dagger(2') b(2)] \rangle_0 \\
&= -\langle \mathcal{T} [b^\dagger(1') b(1)] \rangle_0 \langle \mathcal{T} [b^\dagger(2') b(2)] \rangle_0 - \langle \mathcal{T} [b^\dagger(2') b(1)] \rangle_0 \langle \mathcal{T} [b^\dagger(1') b(2)] \rangle_0 \\
&\quad + \langle \mathcal{T} [b^\dagger(1') b(1) b^\dagger(2') b(2)] \rangle_0 \\
&= G_2^{(0)}(1', 2'|1, 2) - C_1^{(0)}(1'|1) C_2^{(0)}(2'|2) - C_2^{(0)}(2'|1) C_1^{(0)}(1'|2), \tag{E.24}
\end{aligned}$$

and similarly for higher orders. In Eqs. (E.23) and (E.24) the averages containing an odd number of operators vanish identically since there is no symmetry breaking in the described normal phase. Such relations allows for expressing the moments in terms of cumulants as stated in Eq. (E.18), with the possible partitions encompassing the sets of indices with equal number of primed and unprimed variables. Therefore,

for $n = 1$, we trivially obtain from Eq. (E.23)

$$G_1^{(0)}(1'|1) = C_1^{(0)}(1'|1). \quad (\text{E.25})$$

For $n = 2$, there are two types of partitions: $C_2^{(0)}$ (1 term) and $C_1^{(0)} \otimes C_1^{(0)}$ (2 terms) producing according to Eq. (E.24)

$$\begin{aligned} G_2^{(0)}(1', 2'|1, 2) &= C_2^{(0)}(1', 2'|1, 2) + C_1^{(0)}(1'|1)C_1^{(0)}(2'|2) \\ &\quad + C_1^{(0)}(1'|2)C_1^{(0)}(2'|1). \end{aligned} \quad (\text{E.26})$$

For $n = 3$, there are three types of partitions: $C_3^{(0)}$ (1 term), $C_2^{(0)} \otimes C_1^{(0)}$ (9 terms), and $C_1^{(0)} \otimes C_1^{(0)} \otimes C_1^{(0)}$ (6 terms) yielding

$$\begin{aligned} G_3^{(0)}(1', 2', 3'|1, 2, 3) &= C_3^{(0)}(1', 2', 3'|1, 2, 3) + C_2^{(0)}(1', 2'|1, 2)C_1^{(0)}(3'|3) \\ &\quad + C_2^{(0)}(1', 3'|1, 2)C_1^{(0)}(2'|3) + C_2^{(0)}(2', 3'|1, 2)C_1^{(0)}(1'|3) \\ &\quad + C_2^{(0)}(1', 2'|1, 3)C_1^{(0)}(3'|2) + C_2^{(0)}(1', 3'|1, 3)C_1^{(0)}(2'|2) \\ &\quad + C_2^{(0)}(2', 3'|1, 3)C_1^{(0)}(1'|2) + C_2^{(0)}(1', 2'|2, 3)C_1^{(0)}(3'|1) \\ &\quad + C_2^{(0)}(1', 3'|2, 3)C_1^{(0)}(2'|1) + C_2^{(0)}(2', 3'|2, 3)C_1^{(0)}(1'|1) \\ &\quad + C_1^{(0)}(1'|1)C_1^{(0)}(2'|2)C_1^{(0)}(3'|3) + C_1^{(0)}(1'|1)C_1^{(0)}(3'|2)C_1^{(0)}(2'|3) \\ &\quad + C_1^{(0)}(3'|1)C_1^{(0)}(2'|2)C_1^{(0)}(1'|3) + C_1^{(0)}(2'|1)C_1^{(0)}(1'|2)C_1^{(0)}(3'|3) \\ &\quad + C_1^{(0)}(3'|1)C_1^{(0)}(1'|2)C_1^{(0)}(2'|3) + C_1^{(0)}(3'|2)C_1^{(0)}(2'|1)C_1^{(0)}(1'|3), \end{aligned} \quad (\text{E.27})$$

and similarly for higher order terms. The previous results also show that the number of terms appearing in the cumulant decomposition increases substantially with the order n . On the other hand, the cumulants present an useful property: they are local quantities. Since $H^{(0)}$ is a sum of local operators and $\ln(xy) = \ln(x) + \ln(y)$, the generating functional of Eq. (E.21) becomes a sum of local functionals. Therefore, the cumulants derived from it vanish unless all site variable in $(1', \dots, n'|1, \dots, n)$ are

equal, with

$$C_n^{(0)}(j'_1, \tau'_1, \dots, j'_n, \tau'_n | j_1, \tau_1, \dots, j_n, \tau_n) = C_{nj_1}^{(0)}(\tau'_1, \dots, \tau'_n | \tau_1, \dots, \tau_n) \prod_{\alpha\beta} \delta_{j'_\alpha j_\beta}. \quad (\text{E.28})$$

A direct consequence of this locality property is due to the form of the hopping Hamiltonian: cumulants containing at least one corresponding pair $\{\alpha', \alpha\}$ of unprimed and primed variables, like $C_1^{(0)}(1'|1)$, $C_2^{(0)}(1', 2'|1, 3)$ or $C_3^{(0)}(1', 2', 3'|3, 4, 5)$, don't contribute to the perturbative expansion. This happens because the sites j_α and j'_α appearing in

$$\mathcal{H} = \sum_{j'_\alpha j_\alpha} J_{j'_\alpha j_\alpha} b_{j'_\alpha}^\dagger b_{j_\alpha}$$

gives a zero contribution when $j'_\alpha = j_\alpha$ ($J_{j_\alpha j_\alpha} = 0$ as the hopping necessarily occurs between different sites). Hence, when evaluating the momentum decomposition we need to consider only the partitions containing primed variables different from the unprimed ones in the expansion of $\langle \mathcal{U}(\beta, 0) \rangle_0$.

Rule 0 : The partition function $\mathcal{Z} = \mathcal{Z}^{(0)} \langle \mathcal{U}(\beta, 0) \rangle_0$ is explicitly represented by the power series

$$\langle \mathcal{U}(\beta, 0) \rangle_0 = \sum_{n=0}^{\infty} \frac{(-1)^n}{n!} \sum_{j'_1 \dots j'_n, j_1 \dots j_n} J_{j'_1 j_1} \dots J_{j'_n j_n} \int_0^\beta d\tau_1 \dots \int_0^\beta d\tau_n \left\langle \mathcal{T} \left[b_{j'_1}^\dagger(\tau_1) b_{j_1}(\tau_1) \dots b_{j'_n}^\dagger(\tau_n) b_{j_n}(\tau_n) \right] \right\rangle_0,$$

(a) The moments, or Green's functions, can be decomposed into products of cumulants, considering all possible partitions containing an equal number of primed and unprimed variables because there is no global symmetry breaking.

(b) The locality of the cumulants associated with the occurrence of hopping processes between different sites imply the following simplification on the evaluation of $\langle \mathcal{U}(\beta, 0) \rangle_0$: only the partitions containing primed variables different from the unprimed ones give non zero contributions into the power series expansion.

E.3 Diagrammatic Expansion of the Partition Function

Regarding the explored properties of moments and cumulants, we develop a diagrammatic representation of the partition function $\mathcal{Z} = \mathcal{Z}^{(0)} \langle \mathcal{U}(\beta, 0) \rangle_0$. The basic ingredients are the local cumulants and the hopping matrix elements. We symbolize the n -particle cumulant $C_{nj_\alpha}^{(0)}$ at the lattice site j_α by a vertex with n entering and n leaving lines, labeled with imaginary time variables; for example, the lower-order cumulants read as

$$C_{1j_\alpha}^{(0)}(\tau_1|\tau_2) = \tau_1 \longrightarrow \bullet \longleftarrow \tau_2 = \left\langle \mathcal{T} \left[b_{j_\alpha}^\dagger(\tau_1) b_{j_\alpha}(\tau_2) \right] \right\rangle_0, \quad (\text{E.29})$$

$$C_{2j_\alpha}^{(0)}(\tau_1, \tau_3|\tau_2, \tau_4) = \begin{array}{c} \tau_1 \swarrow \quad \searrow \tau_2 \\ \bullet \\ \tau_3 \swarrow \quad \searrow \tau_4 \\ j_\alpha \end{array} = \left\langle \mathcal{T} \left[b_{j_\alpha}^\dagger(\tau_1) b_{j_\alpha}(\tau_2) b_{j_\alpha}^\dagger(\tau_3) b_{j_\alpha}(\tau_4) \right] \right\rangle_0 - C_{1j_\alpha}^{(0)}(\tau_1|\tau_2) C_{1j_\alpha}^{(0)}(\tau_3|\tau_4) - C_{1j_\alpha}^{(0)}(\tau_1|\tau_4) C_{1j_\alpha}^{(0)}(\tau_3|\tau_2). \quad (\text{E.30})$$

Also, a line connecting two vertices j_α and j_β represents the hopping matrix amplitude $J_{j_\alpha j_\beta}$ according to

$$J_{j_\alpha j_\beta} = j_\alpha \longrightarrow j_\beta. \quad (\text{E.31})$$

In the following, we explore how to combine these elements composing diagrams order by order. Considering the first-order term of $\langle \mathcal{U}(\beta, 0) \rangle_0$, Eq. (E.25) brings the relation

$$\begin{aligned} - \sum_{j'_1, j_1} J_{j'_1, j_1} \int_0^\beta d\tau_1 C_1^{(0)}(1'|1) &= - \sum_{j'_1, j_1} J_{j'_1, j_1} \int_0^\beta d\tau_1 \delta_{j'_1, j_1} C_{1j_1}^{(0)}(\tau_1|\tau_1) \\ &= - \sum_{j_1} J_{j_1, j_1} \int_0^\beta d\tau_1 C_{1j_1}^{(0)}(\tau_1|\tau_1) = 0. \end{aligned} \quad (\text{E.32})$$

which produces an identically zero contribution since $J_{j_1, j_1} = 0$, as stated by **Rule 0**.

For the second-order term, **Rule 0** again implies that the only non-zero contribution composing $\langle \mathcal{U}(\beta, 0) \rangle_0$ comes from the cumulants $C_1^{(0)}(2'|1)C_1^{(0)}(1'|2)$ of the kind $C_1^{(0)} \otimes C_1^{(0)}$ exhibited in Eq. (E.26):

$$\begin{aligned} & \sum_{j'_1 j'_2, j_1 j_2} J_{j'_1, j_1} J_{j'_2, j_2} \int_0^\beta d\tau_1 \int_0^\beta d\tau_2 C_1^{(0)}(2'|1)C_1^{(0)}(1'|2) = \\ & \sum_{j'_1 j'_2, j_1 j_2} J_{j'_1, j_1} J_{j'_2, j_2} \int_0^\beta d\tau_1 \int_0^\beta d\tau_2 \delta_{j'_2 j_1} C_{1j_1}^{(0)}(\tau_2|\tau_1) \delta_{j'_1 j_2} C_{1j_2}^{(0)}(\tau_1|\tau_2) = \\ & \sum_{j_1 j_2} J_{j_2, j_1} J_{j_1, j_2} \int_0^\beta d\tau_1 \int_0^\beta d\tau_2 C_{1j_1}^{(0)}(\tau_2|\tau_1) C_{1j_2}^{(0)}(\tau_1|\tau_2) \equiv D_{2a}. \end{aligned} \quad (\text{E.33})$$

Using the representations introduced in Eqs. (E.29) and (E.31), the defined term D_{2a} is symbolized by the following diagram

$$D_{2a} \equiv \begin{array}{c} \tau_1 \\ \bullet \leftarrow \bullet \\ \tau_2 \end{array} \begin{array}{c} j_1 \quad j_2 \\ \leftarrow \quad \rightarrow \end{array} = \sum_{j_1 j_2} J_{j_2, j_1} J_{j_1, j_2} \int_0^\beta d\tau_1 \int_0^\beta d\tau_2 C_{1j_1}^{(0)}(\tau_2|\tau_1) C_{1j_2}^{(0)}(\tau_1|\tau_2), \quad (\text{E.34})$$

where the two cumulants at the vertices j_1 and j_2 are linked by hopping lines J_{j_2, j_1} and J_{j_1, j_2} . Note that the complete second-order term is $w[D_{2a}] = \frac{1}{2}D_2$, including the factor $\frac{1}{2}$ from the exponential series of Eq. (E.10).

In the third-order terms, the non zero contributions comes from the partitions $C_1^{(0)} \otimes C_1^{(0)} \otimes C_1^{(0)}$, with two cyclic elements

$$C_1^{(0)}(3'|1)C_1^{(0)}(1'|2)C_1^{(0)}(2'|3) \text{ and } C_1^{(0)}(3'|2)C_1^{(0)}(2'|1)C_1^{(0)}(1'|3),$$

as stated by **Rule 0** and Eq. (E.27). Both of them yield the same result

$$\begin{aligned} & \sum_{j'_1 j'_2 j'_3, j_1 j_2 j_3} J_{j'_1, j_1} J_{j'_2, j_2} J_{j'_3, j_3} \int_0^\beta d\tau_1 \int_0^\beta d\tau_2 \int_0^\beta d\tau_3 C_1^{(0)}(3'|1)C_1^{(0)}(1'|2)C_1^{(0)}(2'|3) = \\ & \sum_{j'_1 j'_2 j'_3, j_1 j_2 j_3} J_{j'_1, j_1} J_{j'_2, j_2} J_{j'_3, j_3} \int_0^\beta d\tau_1 \int_0^\beta d\tau_2 \int_0^\beta d\tau_3 \delta_{j'_3 j_1} C_{1j_1}^{(0)}(\tau_3|\tau_1) \delta_{j'_1 j_2} C_{1j_2}^{(0)}(\tau_1|\tau_2) \delta_{j'_2 j_3} C_{1j_3}^{(0)}(\tau_2|\tau_3) = \end{aligned}$$

$$\sum_{j_1 j_2 j_3} J_{j_3 j_1} J_{j_1 j_2} J_{j_2 j_3} \int_0^\beta d\tau_1 \int_0^\beta d\tau_2 \int_0^\beta d\tau_3 C_{1j_1}^{(0)}(\tau_3|\tau_1) C_{1j_2}^{(0)}(\tau_1|\tau_2) C_{1j_3}^{(0)}(\tau_2|\tau_3) \equiv D_{3a}, \quad (\text{E.35})$$

with diagrammatic representation

$$D_{3a} \equiv \begin{array}{c} j_2 \\ \nearrow \tau_1 \quad \searrow \tau_2 \\ \bullet \quad \bullet \\ \nwarrow \tau_3 \quad \nearrow \tau_3 \\ j_1 \quad j_3 \end{array} = - \sum_{j_1 j_2 j_3} J_{j_3 j_1} J_{j_1 j_2} J_{j_2 j_3} \int_0^\beta d\tau_1 \int_0^\beta d\tau_2 \int_0^\beta d\tau_3 C_{1j_1}^{(0)}(\tau_3|\tau_1) C_{1j_2}^{(0)}(\tau_1|\tau_2) C_{1j_3}^{(0)}(\tau_2|\tau_3). \quad (\text{E.36})$$

Hence the complete third-order weight is $w[D_{3a}] = \frac{2}{3!} D_{3a} = \frac{1}{3} D_{3a}$, since there are two equivalent terms and the exponential expansion factor $\frac{1}{3!}$.

Regarding the fourth order, the partitions of the form $C_1^{(0)} \otimes C_1^{(0)} \otimes C_1^{(0)} \otimes C_1^{(0)}$ contribute with 6 cyclic elements and 3 disconnected ones. The cyclic ones are

$$\begin{aligned} & C_1^{(0)}(4'|1) C_1^{(0)}(1'|2) C_1^{(0)}(2'|3) C_1^{(0)}(3'|4), \quad C_1^{(0)}(4'|1) C_1^{(0)}(1'|3) C_1^{(0)}(3'|2) C_1^{(0)}(2'|4), \\ & C_1^{(0)}(4'|2) C_1^{(0)}(2'|1) C_1^{(0)}(1'|3) C_1^{(0)}(3'|4), \quad C_1^{(0)}(4'|2) C_1^{(0)}(2'|3) C_1^{(0)}(3'|1) C_1^{(0)}(1'|4), \\ & C_1^{(0)}(4'|3) C_1^{(0)}(3'|1) C_1^{(0)}(1'|2) C_1^{(0)}(2'|4), \quad C_1^{(0)}(4'|3) C_1^{(0)}(3'|2) C_1^{(0)}(2'|1) C_1^{(0)}(1'|4), \end{aligned}$$

yielding the same value

$$D_{4a} \equiv \begin{array}{c} \tau_2 \\ \bullet \quad \bullet \\ \leftarrow \tau_1 \quad \rightarrow \tau_3 \\ \bullet \quad \bullet \\ \tau_4 \end{array} \quad (\text{E.37})$$

$$= \sum_{j_1 j_2 j_3 j_4} J_{j_4 j_1} J_{j_1 j_2} J_{j_2 j_3} J_{j_3 j_4} \int_0^\beta d\tau_1 \int_0^\beta d\tau_2 \int_0^\beta d\tau_3 \int_0^\beta d\tau_4 C_{1j_1}^{(0)}(\tau_4|\tau_1) C_{1j_2}^{(0)}(\tau_1|\tau_2) C_{1j_3}^{(0)}(\tau_2|\tau_3) C_{1j_4}^{(0)}(\tau_3|\tau_4),$$

whose contribution is $w[D_{4a}] = \frac{6}{4!} D_{4a} = \frac{1}{4} D_{4a}$. The 3 disconnected elements are $C_1^{(0)}(4'|1) C_1^{(0)}(1'|4) C_1^{(0)}(2'|3) C_1^{(0)}(3'|2)$, $C_1^{(0)}(4'|2) C_1^{(0)}(2'|4) C_1^{(0)}(1'|3) C_1^{(0)}(3'|1)$ and $C_1^{(0)}(4'|3) C_1^{(0)}(3'|4) C_1^{(0)}(1'|2) C_1^{(0)}(2'|1)$, producing

$$D_{4b} \equiv \begin{array}{c} \tau_1 \\ \bullet \quad \bullet \\ \leftarrow \tau_4 \quad \rightarrow \tau_1 \\ \bullet \quad \bullet \\ \tau_2 \\ \bullet \quad \bullet \\ \leftarrow \tau_3 \quad \rightarrow \tau_2 \\ \bullet \quad \bullet \\ \tau_3 \end{array} \quad (\text{E.38})$$

$$= \sum_{j_1 j_4} J_{j_4 j_1} J_{j_1 j_4} \int_0^\beta d\tau_1 \int_0^\beta d\tau_4 C_{1j_1}^{(0)}(\tau_4|\tau_1) C_{1j_4}^{(0)}(\tau_1|\tau_4) \times \sum_{j_2 j_3} J_{j_3 j_2} J_{j_2 j_3} \int_0^\beta d\tau_2 \int_0^\beta d\tau_3 C_{1j_2}^{(0)}(\tau_3|\tau_2) C_{1j_3}^{(0)}(\tau_2|\tau_3),$$

with a complete weight equals to $w[D_{4b}] = \frac{3}{4!}D_{4b} = \frac{1}{8}D_{4b}$. Also, note that D_{4b} is essentially a product of two lower-order diagrams $D_{4b} = D_{2a} \times D_{2a}$, being disconnected. The partitions $C_2^{(0)} \otimes C_1^{(0)} \otimes C_1^{(0)}$ generate 12 terms:

$$\begin{aligned} & C_2^{(0)}(3', 4'|1, 2)C_1^{(0)}(1'|3)C_1^{(0)}(2'|4), C_2^{(0)}(3', 4'|1, 2)C_1^{(0)}(1'|4)C_1^{(0)}(2'|3), \\ & C_2^{(0)}(2', 4'|1, 3)C_1^{(0)}(1'|2)C_1^{(0)}(3'|4), C_2^{(0)}(2', 4'|1, 3)C_1^{(0)}(1'|4)C_1^{(0)}(3'|2), \\ & C_2^{(0)}(2', 3'|1, 4)C_1^{(0)}(1'|2)C_1^{(0)}(4'|3), C_2^{(0)}(2', 3'|1, 4)C_1^{(0)}(1'|3)C_1^{(0)}(4'|2), \\ & C_2^{(0)}(1', 4'|2, 3)C_1^{(0)}(2'|1)C_1^{(0)}(3'|4), C_2^{(0)}(1', 4'|2, 3)C_1^{(0)}(2'|4)C_1^{(0)}(3'|1), \\ & C_2^{(0)}(1', 3'|2, 4)C_1^{(0)}(2'|1)C_1^{(0)}(4'|3), C_2^{(0)}(1', 3'|2, 4)C_1^{(0)}(2'|3)C_1^{(0)}(4'|1). \end{aligned}$$

They result in

$$\begin{aligned} D_{4c} & \equiv \begin{array}{c} \tau_1 \qquad \tau_2 \\ \bullet \leftarrow \tau_4 \qquad \tau_3 \rightarrow \bullet \\ j_1 \qquad j_2 \qquad j_3 \end{array} \\ & = \sum_{j_1 j_2 j_3} J_{j_2 j_1} J_{j_1 j_2} J_{j_2 j_3} J_{j_3 j_2} \int_0^\beta d\tau_1 \int_0^\beta d\tau_2 \int_0^\beta d\tau_3 \int_0^\beta d\tau_4 C_{1j_1}^{(0)}(\tau_4|\tau_1) C_{2j_2}^{(0)}(\tau_1, \tau_3|\tau_2, \tau_4) C_{1j_3}^{(0)}(\tau_2|\tau_3), \end{aligned} \quad (\text{E.39})$$

with a total value of $w[D_{4c}] = \frac{12}{4!}D_{4c} = \frac{1}{2}D_{4c}$. The remaining contributions take the form from $C_2^{(0)} \otimes C_2^{(0)}$, with 3 terms: $C_2^{(0)}(3', 4'|1, 2)C_2^{(0)}(1', 2'|3, 4)$, $C_2^{(0)}(2', 4'|1, 3)C_2^{(0)}(1', 3'|2, 4)$ and $C_2^{(0)}(2', 3'|1, 4)C_2^{(0)}(1', 4'|2, 3)$

$$\begin{aligned} D_{4d} & \equiv \begin{array}{c} \tau_1 \\ \bullet \leftarrow \tau_2 \qquad \tau_3 \rightarrow \bullet \\ \tau_4 \\ j_1 \qquad j_2 \end{array} \\ & = \sum_{j_1 j_2} J_{j_2 j_1} J_{j_1 j_2} J_{j_2 j_1} J_{j_1 j_2} \int_0^\beta d\tau_1 \int_0^\beta d\tau_2 \int_0^\beta d\tau_3 \int_0^\beta d\tau_4 C_{2j_1}^{(0)}(\tau_3, \tau_4|\tau_1, \tau_2) C_{2j_2}^{(0)}(\tau_1, \tau_2|\tau_3, \tau_4), \end{aligned} \quad (\text{E.40})$$

accounting for $w[D_{4d}] = \frac{3}{4!}D_{4d} = \frac{1}{8}D_{4d}$. By collecting all the previously calculated diagrams, the average of the time-evolution operator reads as

$$\langle \mathcal{U}(\beta, 0) \rangle_0 = 1 + \frac{1}{2}D_{2a} + \frac{1}{3}D_{3a} + \frac{1}{4}D_{4a} + \frac{1}{8}D_{4b} + \frac{1}{2}D_{4c} + \frac{1}{8}D_{4d} + \mathcal{O}(J^5). \quad (\text{E.41})$$

As a consequence, the partition function until the fourth power of J is given by

$$\mathcal{Z} = \mathcal{Z}^{(0)} \left(1 + \frac{1}{2}D_{2a} + \frac{1}{3}D_{3a} + \frac{1}{4}D_{4a} + \frac{1}{8}D_{4b} + \frac{1}{2}D_{4c} + \frac{1}{8}D_{4d} + \mathcal{O}(J^5) \right), \quad (\text{E.42})$$

or in a symbolic form

$$\mathcal{Z} = \mathcal{Z}^{(0)} \left(1 + \frac{1}{2} \begin{array}{c} \bullet \quad \bullet \\ \curvearrowright \\ \bullet \quad \bullet \end{array} + \frac{1}{3} \begin{array}{c} \bullet \\ \diagdown \quad \diagup \\ \bullet \quad \bullet \\ \diagup \quad \diagdown \\ \bullet \quad \bullet \end{array} + \frac{1}{4} \begin{array}{c} \bullet \quad \bullet \\ \leftarrow \quad \rightarrow \\ \bullet \quad \bullet \\ \leftarrow \quad \rightarrow \\ \bullet \quad \bullet \end{array} \right. \\ \left. + \frac{1}{8} \begin{array}{c} \bullet \quad \bullet \\ \curvearrowright \\ \bullet \quad \bullet \\ \curvearrowright \\ \bullet \quad \bullet \end{array} + \frac{1}{2} \begin{array}{c} \bullet \quad \bullet \\ \curvearrowright \\ \bullet \quad \bullet \\ \curvearrowright \\ \bullet \quad \bullet \end{array} + \frac{1}{8} \begin{array}{c} \bullet \\ \curvearrowright \\ \bullet \\ \curvearrowright \\ \bullet \\ \curvearrowright \\ \bullet \end{array} + \mathcal{O}(J^5) \right). \quad (\text{E.43})$$

We summarize and extent our conclusions in a set of simple and direct rules:

Rule 1 - Diagrammatic Expansion of the Partition Function

Rule (a) : Draw all topologically inequivalent diagrams D with vertices connected by directed lines such that the number of lines entering each vertex equals the number of leaving ones.

Rule (b) : Label each vertex with a lattice vector and each line with an imaginary time variable.

Rule (c) : Each line connecting two vertices j_α and j_β yields a factor of $J_{j_\alpha j_\beta}$.

Rule (d) : Each vertex j_α with n entering lines and n leaving lines corresponds to a cumulant $C_{nj_\alpha}^{(0)}$.

Rule (e) : Determine the sign of each diagram: plus/minus for even/odd number of connected lines.

Rule (f) : Determine the multiplicity of each diagram.

Rule (g) : For each diagram, multiply the hopping matrix elements [**Rule (c)**] and the cumulants [**Rule (d)**], integrate the imaginary time variable from 0 to β , sum each lattice vector over the whole lattice; multiply the result by the sign [**Rule (e)**], the multiplicity [**Rule (f)**], and divide it by the corresponding Taylor expansion factor. After this, we obtain a quantity $w[D]$ referred as the weight of the diagram D .

Rule (h) : The partition function is given by the following sum over all possible diagrams constructed according to the **Rules (a)-(g)**:

$$\mathcal{Z} = \mathcal{Z}^{(0)} \langle \mathcal{U}(\beta, 0) \rangle_0 = \mathcal{Z}^{(0)} \left(1 + \sum_D w[D] \right). \quad (\text{E.44})$$

E.4 Diagrammatic Expansion of the free energy

The free energy is obtained directly from the logarithm of the partition function exposed in Eq. (E.44)

$$\Omega = -\frac{1}{\beta} \ln \mathcal{Z} = \Omega^{(0)} - \frac{1}{\beta} \ln \langle \mathcal{U}(\beta, 0) \rangle_0 = \Omega^{(0)} - k_B T \ln \left(1 + \sum_D w[D] \right) \quad (\text{E.45})$$

Note that \mathcal{Z} contains both connected and disconnected diagrams. Indeed, up to the fourth order there are five connected diagrams: D_{2a} , D_{3a} , D_{4a} , D_{4c} and D_{4d} ; D_{4b} is the only disconnected contribution. In the following, we show that the action of the logarithm function on \mathcal{Z} is to remove its disconnected diagrams. The Taylor expansion of $\ln(1 + \epsilon) = \epsilon - \frac{\epsilon^2}{2} + \dots$, with the identification $\epsilon = \sum_D w[D]$, yields

$$\begin{aligned} \ln \left(1 + \sum_D w[D] \right) &= \ln \left(1 + \frac{1}{2}D_{2a} + \frac{1}{3}D_{3a} + \frac{1}{4}D_{4a} + \frac{1}{8}D_{4b} + \frac{1}{2}D_{4c} + \frac{1}{8}D_{4d} + \mathcal{O}(J^5) \right) \\ &= \frac{1}{2}D_{2a} + \frac{1}{3}D_{3a} + \frac{1}{4}D_{4a} + \frac{1}{8}D_{4b} + \frac{1}{2}D_{4c} + \frac{1}{8}D_{4d} \\ &\quad - \frac{1}{2} \left(\frac{1}{2}D_{2a} \right) \times \left(\frac{1}{2}D_{2a} \right) + \mathcal{O}(J^5) \\ &= \frac{1}{2}D_{2a} + \frac{1}{3}D_{3a} + \frac{1}{4}D_{4a} + \frac{1}{2}D_{4c} + \frac{1}{8}D_{4d} + \mathcal{O}(J^5), \end{aligned} \quad (\text{E.46})$$

since $D_{4b} = D_{2a} \times D_{2a}$. Clearly, the diagrams appearing in $-\frac{\epsilon^2}{2}, \frac{\epsilon^3}{3}, \dots$ cancel all the disconnected terms in ϵ . This happens because a disconnected diagram is a product of connected parts. Therefore, the linked-cluster theorem [185] applies; the free energy

comprehends the sum over all the connected diagrams

$$\begin{aligned}\Omega &= \Omega^{(0)} - k_B T \sum'_D w[D] \\ &= \Omega^{(0)} - k_B T \left(\frac{1}{2} D_{2a} + \frac{1}{3} D_{3a} + \frac{1}{4} D_{4a} + \frac{1}{2} D_{4c} + \frac{1}{8} D_{4d} + \mathcal{O}(J^5) \right), \quad (\text{E.47})\end{aligned}$$

symbolized by the primed sum. Schematically, Ω reads as

$$\begin{aligned}\Omega &= \Omega^{(0)} - k_B T \left(\frac{1}{2} \begin{array}{c} \bullet \quad \bullet \\ \curvearrowright \\ \bullet \quad \bullet \end{array} + \frac{1}{3} \begin{array}{c} \bullet \\ \swarrow \quad \searrow \\ \bullet \quad \bullet \\ \swarrow \quad \searrow \\ \bullet \end{array} + \frac{1}{4} \begin{array}{c} \bullet \quad \bullet \\ \rightarrow \quad \rightarrow \\ \bullet \quad \bullet \\ \leftarrow \quad \leftarrow \\ \bullet \quad \bullet \end{array} \right. \\ &\quad \left. + \frac{1}{2} \begin{array}{c} \bullet \quad \bullet \quad \bullet \\ \curvearrowright \quad \curvearrowright \\ \bullet \quad \bullet \quad \bullet \end{array} + \frac{1}{8} \begin{array}{c} \bullet \quad \bullet \\ \curvearrowright \quad \curvearrowright \\ \bullet \quad \bullet \\ \curvearrowleft \quad \curvearrowleft \\ \bullet \quad \bullet \end{array} + \mathcal{O}(J^5) \right). \quad (\text{E.48})\end{aligned}$$

Another interesting observation regarding the cancellation of the disconnected diagrams is related to the extensive properties of the free energy. Since each connected diagram yields a factor of N_s , the disconnected components are at least of order N_s^2 ; hence the existence of a finite free energy in the thermodynamic limit imply the cancellation of such diagrams.

Rule 2 - Diagrammatic Expansion of the Free-Energy

Rule (a) : The system's free-energy Ω is given by the sum over all connected diagrams constructed according to the **Rule 1**:

$$\Omega = \Omega^{(0)} - k_B T \sum'_D w[D]. \quad (\text{E.49})$$

E.5 Diagrammatic Expansion of the Green's Function

The one-particle (or two-point) Green's function is defined by the thermal average of the following time-ordered product

$$G_{j_\alpha j'_\alpha}(\tau_\alpha, \tau'_\alpha) = - \left\langle \mathcal{T} \left[b_{j_\alpha}(\tau_\alpha) b_{j'_\alpha}^\dagger(\tau'_\alpha) \right] \right\rangle, \quad (\text{E.50})$$

which can be rewritten as

$$\begin{aligned} G_{j_\alpha j'_\alpha}(\tau_\alpha, \tau'_\alpha) &= -\frac{1}{\mathcal{Z}} \text{Tr} \left\{ \mathcal{T} \left[e^{-\int_0^\beta H(\tau) d\tau} b_{j_\alpha}(\tau_\alpha) b_{j'_\alpha}^\dagger(\tau'_\alpha) \right] \right\} \\ &= -\frac{\text{Tr} \left\{ e^{-\beta H(0)} \mathcal{T} \left[\mathcal{U}(\beta, 0) b_{j_\alpha}(\tau_\alpha) b_{j'_\alpha}^\dagger(\tau'_\alpha) \right] \right\}}{\mathcal{Z}^{(0)} \langle \mathcal{U}(\beta, 0) \rangle_0} \\ &= -\frac{\left\langle \mathcal{T} \left[\mathcal{U}(\beta, 0) b_{j_\alpha}(\tau_\alpha) b_{j'_\alpha}^\dagger(\tau'_\alpha) \right] \right\rangle_0}{\langle \mathcal{U}(\beta, 0) \rangle_0}. \end{aligned} \quad (\text{E.51})$$

Note that a diagrammatic development of the denominator $\langle \mathcal{U}(\beta, 0) \rangle_0$ was already studied in the Subsection E.3. The numerator presents a similar structure except that the variables α and α' are fixed, not integrated or summed. Indeed, such term can be expanded in the power series

$$\begin{aligned} \left\langle \mathcal{T} \left[\mathcal{U}(\beta, 0) b_{j_\alpha}(\tau_\alpha) b_{j'_\alpha}^\dagger(\tau'_\alpha) \right] \right\rangle_0 &= \sum_{n=0}^{\infty} \frac{(-1)^n}{n!} \sum_{j'_1 \dots j'_n; j_1 \dots j_n} J_{j'_1 j_1} \dots J_{j'_n j_n} \int_0^\beta d\tau_1 \dots \int_0^\beta d\tau_n \times \\ &\quad \left\langle \mathcal{T} \left[b_{j'_1}^\dagger(\tau_1) b_{j_1}(\tau_1) \dots b_{j'_n}^\dagger(\tau_n) b_{j_n}(\tau_n) b_{j'_\alpha}^\dagger(\tau'_\alpha) b_{j_\alpha}(\tau_\alpha) \right] \right\rangle_0, \end{aligned} \quad (\text{E.52})$$

where

$$\begin{aligned} \left\langle \mathcal{T} \left[b_{j'_1}^\dagger(\tau_1) b_{j_1}(\tau_1) \dots b_{j'_n}^\dagger(\tau_n) b_{j_n}(\tau_n) b_{j'_\alpha}^\dagger(\tau'_\alpha) b_{j_\alpha}(\tau_\alpha) \right] \right\rangle_0 &= \\ G_{n+1}^{(0)}(j'_1, \tau_1, \dots, j'_n, \tau_n, j'_\alpha, \tau'_\alpha | j_1, \tau_1, \dots, j_n, \tau_n, j_\alpha, \tau_\alpha) \end{aligned} \quad (\text{E.53})$$

is identified with the $n + 1$ -particle Green's function relative to the unperturbed system. The decomposition of this average into cumulants enables an analysis order by order, according to the ideas already exposed in Subsection E.2. The only additional remark is related to the variables α and α' , which may yield a non-zero contribution when present in the same set of a partition.

Considering the zeroth-order term, we have a local contribution for

$$\left\langle \mathcal{T} \left[\mathcal{U}(\beta, 0) b_{j_\alpha}(\tau_\alpha) b_{j'_\alpha}^\dagger(\tau'_\alpha) \right] \right\rangle_0$$

given by

$$\left\langle \mathcal{T} \left[b_{j'_\alpha}^\dagger(\tau'_\alpha) b_{j_\alpha}(\tau_\alpha) \right] \right\rangle_0 = \delta_{j'_\alpha j_\alpha} C_{1j_\alpha}^{(0)}(\tau'_\alpha | \tau_\alpha) \equiv D_{0a}(\alpha' | \alpha), \quad (\text{E.54})$$

and represented as the diagram

$$D_{0a}(\alpha' | \alpha) \equiv \tau'_\alpha \xrightarrow{j'_\alpha = j_\alpha} \tau_\alpha = \delta_{j'_\alpha j_\alpha} C_{1j_\alpha}^{(0)}(\tau'_\alpha | \tau_\alpha), \quad (\text{E.55})$$

with total weight $w[D_{0a}(\alpha' | \alpha)] = D_{0a}(\alpha' | \alpha)$.

Concerning the first-order term, the contribution $C_1^{(0)}(\alpha' | 1) C_1^{(0)}(1' | \alpha)$ of the form $C_1^{(0)} \otimes C_1^{(0)}$ provides

$$\begin{aligned} & - \sum_{j'_1, j_1} J_{j'_1 j_1} \int_0^\beta d\tau_1 C_1^{(0)}(\alpha' | 1) C_1^{(0)}(1' | \alpha) = \\ & - \sum_{j'_1, j_1} J_{j'_1 j_1} \int_0^\beta d\tau_1 \delta_{j'_\alpha j_1} C_{1j_1}^{(0)}(\tau'_\alpha | \tau_1) \delta_{j'_1 j_\alpha} C_{1j_\alpha}^{(0)}(\tau_1 | \tau_\alpha) = \\ & - J_{j_\alpha j'_\alpha} \int_0^\beta d\tau_1 C_{1j'_\alpha}^{(0)}(\tau'_\alpha | \tau_1) C_{1j_\alpha}^{(0)}(\tau_1 | \tau_\alpha) \equiv D_{1a}(\alpha' | \alpha), \quad (\text{E.56}) \end{aligned}$$

symbolized by the diagram

$$D_{1a}(\alpha' | \alpha) \equiv \tau'_\alpha \xrightarrow{j'_\alpha} \tau_1 \xrightarrow{j_\alpha} \tau_\alpha = - J_{j_\alpha j'_\alpha} \int_0^\beta d\tau_1 C_{1j'_\alpha}^{(0)}(\tau'_\alpha | \tau_1) C_{1j_\alpha}^{(0)}(\tau_1 | \tau_\alpha), \quad (\text{E.57})$$

with a total weight $w[D_{1a}(\alpha'|\alpha)] = D_{1a}(\alpha'|\alpha)$.

For the second-order elements, there are three types of diagrams. The partitions of the form $C_1^{(0)} \otimes C_1^{(0)} \otimes C_1^{(0)}$ contribute with two cyclic terms and one disconnected. The cyclic ones are $C_1^{(0)}(\alpha'|2)C_1^{(0)}(2'|1)C_1^{(0)}(1'|\alpha)$ and $C_1^{(0)}(\alpha'|1)C_1^{(0)}(1'|2)C_1^{(0)}(2'|\alpha)$ yielding

$$\begin{aligned}
& \sum_{j'_1 j'_2, j_1 j_2} J_{j'_1 j_1} J_{j'_2 j_2} \int_0^\beta d\tau_1 \int_0^\beta d\tau_2 C_1^{(0)}(\alpha'|2)C_1^{(0)}(2'|1)C_1^{(0)}(1'|\alpha) = \\
& \sum_{j'_1 j'_2, j_1 j_2} J_{j'_1 j_1} J_{j'_2 j_2} \int_0^\beta d\tau_1 \int_0^\beta d\tau_2 \delta_{j'_\alpha j_2} C_{1j_2}^{(0)}(\tau'_\alpha|\tau_2) \delta_{j'_2 j_1} C_{1j_1}^{(0)}(\tau_2|\tau_1) \delta_{j'_1 j_\alpha} C_{1j_\alpha}^{(0)}(\tau_1|\tau_\alpha) = \\
& \sum_{j_1} J_{j'_\alpha j_1} J_{j_1 j_\alpha} \int_0^\beta d\tau_1 \int_0^\beta d\tau_2 C_{1j'_\alpha}^{(0)}(\tau'_\alpha|\tau_2) C_{1j_1}^{(0)}(\tau_2|\tau_1) C_{1j_\alpha}^{(0)}(\tau_1|\tau_\alpha) \equiv D_{2a}(\alpha'|\alpha),
\end{aligned} \tag{E.58}$$

with a diagrammatic representation

$$D_{2a}(\alpha'|\alpha) \equiv \tau'_\alpha \xrightarrow{j'_\alpha} \begin{array}{c} \tau_1 \\ \bullet \\ \xrightarrow{j_1} \end{array} \begin{array}{c} \tau_2 \\ \bullet \\ \xrightarrow{j_\alpha} \end{array} \tau_\alpha = \sum_{j_1} J_{j'_\alpha j_1} J_{j_1 j_\alpha} \int_0^\beta d\tau_1 \int_0^\beta d\tau_2 C_{1j'_\alpha}^{(0)}(\tau'_\alpha|\tau_2) C_{1j_1}^{(0)}(\tau_2|\tau_1) C_{1j_\alpha}^{(0)}(\tau_1|\tau_\alpha), \tag{E.59}$$

and $w[D_{2a}(\alpha'|\alpha)] = \frac{2}{2!} D_{2a}(\alpha'|\alpha) = D_{2a}(\alpha'|\alpha)$ (taking into account the factor $\frac{1}{2!}$ from the power series of Eq. (E.51) and the mentioned multiplicity). The disconnected term is $C_1^{(0)}(\alpha'|\alpha)C_1^{(0)}(2'|1)C_1^{(0)}(1'|2)$. It generates

$$\begin{aligned}
& \sum_{j'_1 j'_2, j_1 j_2} J_{j'_1 j_1} J_{j'_2 j_2} \int_0^\beta d\tau_1 \int_0^\beta d\tau_2 C_1^{(0)}(\alpha'|\alpha)C_1^{(0)}(2'|1)C_1^{(0)}(1'|2) = \\
& \sum_{j'_1 j'_2, j_1 j_2} J_{j'_1 j_1} J_{j'_2 j_2} \int_0^\beta d\tau_1 \int_0^\beta d\tau_2 \delta_{j'_\alpha j_\alpha} C_{1j_\alpha}^{(0)}(\tau'_\alpha|\tau_\alpha) \delta_{j'_2 j_1} C_{1j_1}^{(0)}(\tau_2|\tau_1) \delta_{j'_1 j_2} C_{1j_2}^{(0)}(\tau_1|\tau_2) = \\
& \delta_{j'_\alpha j_\alpha} C_{1j_\alpha}^{(0)}(\tau'_\alpha|\tau_\alpha) \times \sum_{j_1 j_2} J_{j_2 j_1} J_{j_1 j_2} \int_0^\beta d\tau_1 \int_0^\beta d\tau_2 C_{1j_1}^{(0)}(\tau_2|\tau_1) C_{1j_2}^{(0)}(\tau_1|\tau_2) \equiv D_{2b}(\alpha'|\alpha),
\end{aligned} \tag{E.60}$$

where $D_{2b}(\alpha'|\alpha) = D_{0a}(\alpha'|\alpha) \times D_{2a}$ is a product of two diagrams $D_{0a}(\alpha'|\alpha)$ and D_{2a} (see Eqs. (E.55) and (E.34), respectively), given by

$$D_{2b}(\alpha'|\alpha) \equiv \begin{array}{c} \begin{array}{c} j_2 \\ \updownarrow \\ \tau_1 \quad \tau_2 \\ \downarrow \uparrow \\ j_1 \\ \leftarrow \quad \rightarrow \\ \tau'_\alpha \quad \tau_\alpha \\ \leftarrow \quad \rightarrow \\ j'_\alpha = j_\alpha \end{array} \end{array} = \delta_{j'_\alpha j_\alpha} C_{1j_\alpha}^{(0)}(\tau'_\alpha|\tau_\alpha) \times \sum_{j_1 j_2} J_{j_2 j_1} J_{j_1 j_2} \int_0^\beta d\tau_1 \int_0^\beta d\tau_2 C_{1j_1}^{(0)}(\tau_2|\tau_1) C_{1j_2}^{(0)}(\tau_1|\tau_2), \quad (\text{E.61})$$

and totalizing $w[D_{2b}(\alpha'|\alpha)] = \frac{1}{2}D_{2b}(\alpha'|\alpha)$. The remaining partitions are of the form $C_2^{(0)} \otimes C_1^{(0)}$: $C_2^{(0)}(\alpha', 2'|1, \alpha)C_1^{(0)}(1'|2)$ and $C_2^{(0)}(\alpha', 1'|2, \alpha)C_1^{(0)}(2'|1)$; they produce the same contribution

$$\begin{aligned} & \sum_{j'_1 j'_2, j_1 j_2} J_{j'_1 j'_1} J_{j'_2 j'_2} \int_0^\beta d\tau_1 \int_0^\beta d\tau_2 C_2^{(0)}(\alpha', 2'|1, \alpha) C_1^{(0)}(1'|2) = \\ & \sum_{j'_1 j'_2, j_1 j_2} J_{j'_1 j'_1} J_{j'_2 j'_2} \int_0^\beta d\tau_1 \int_0^\beta d\tau_2 \delta_{j'_\alpha j_\alpha} \delta_{j'_2 j_2} \delta_{j'_1 j_1} C_{2j_\alpha}^{(0)}(\tau'_\alpha, \tau_2|\tau_1, \tau_\alpha) \delta_{j'_1 j_2} C_{1j_2}^{(0)}(\tau_1|\tau_2) = \\ & \delta_{j'_\alpha j_\alpha} \sum_{j_2} J_{j'_\alpha j_2} J_{j_2 j_\alpha} \int_0^\beta d\tau_1 \int_0^\beta d\tau_2 C_{2j_\alpha}^{(0)}(\tau'_\alpha, \tau_2|\tau_1, \tau_\alpha) C_{1j_2}^{(0)}(\tau_1|\tau_2) \equiv D_{2c}(\alpha'|\alpha), \end{aligned} \quad (\text{E.62})$$

which is illustrated by

$$D_{2c}(\alpha'|\alpha) \equiv \begin{array}{c} \begin{array}{c} j_2 \\ \updownarrow \\ \tau_1 \quad \tau_2 \\ \downarrow \uparrow \\ j_1 \\ \leftarrow \quad \rightarrow \\ \tau'_\alpha \quad \tau_\alpha \\ \leftarrow \quad \rightarrow \\ j'_\alpha = j_\alpha \end{array} \end{array} = \delta_{j'_\alpha j_\alpha} \sum_{j_2} J_{j'_\alpha j_2} J_{j_2 j_\alpha} \int_0^\beta d\tau_1 \int_0^\beta d\tau_2 C_{2j_\alpha}^{(0)}(\tau'_\alpha, \tau_2|\tau_1, \tau_\alpha) C_{1j_2}^{(0)}(\tau_1|\tau_2), \quad (\text{E.63})$$

with weight $w[D_{2c}(\alpha'|\alpha)] = \frac{1}{2}D_{2c}(\alpha'|\alpha)$. Therefore, the average in the numerator up to second order is

$$\begin{aligned} & \left\langle \mathcal{T} \left[\mathcal{U}(\beta, 0) b_{j_\alpha}(\tau_\alpha) b_{j'_\alpha}^\dagger(\tau'_\alpha) \right] \right\rangle_0 = \\ & = D_{0a}(\alpha'|\alpha) + D_{1a}(\alpha'|\alpha) + D_{2a}(\alpha'|\alpha) + \frac{1}{2}D_{2b}(\alpha'|\alpha) + D_{2c}(\alpha'|\alpha) + \mathcal{O}(J^3) \\ & = D_{0a}(\alpha'|\alpha) + D_{1a}(\alpha'|\alpha) + D_{2a}(\alpha'|\alpha) + \frac{1}{2}D_{0a}(\alpha'|\alpha) \times D_{2a} + D_{2c}(\alpha'|\alpha) + \mathcal{O}(J^3). \end{aligned} \quad (\text{E.64})$$

The combination of the Eqs. (E.64) and (E.41), numerator and denominator respectively, into Eq. (E.51) produces the one-particle Green's function

$$\begin{aligned}
-G_{j_\alpha j'_\alpha}(\tau_\alpha, \tau'_\alpha) &= \frac{\langle \mathcal{T} [\mathcal{U}(\beta, 0) b_{j_\alpha}(\tau_\alpha) b_{j'_\alpha}^\dagger(\tau'_\alpha)] \rangle_0}{\langle \mathcal{U}(\beta, 0) \rangle_0} \\
&= \frac{D_{0a}(\alpha'|\alpha) + D_{1a}(\alpha'|\alpha) + D_{2a}(\alpha'|\alpha) + \frac{1}{2}D_{0a}(\alpha'|\alpha) \times D_{2a} + D_{2c}(\alpha'|\alpha) + \mathcal{O}(J^3)}{1 + \frac{1}{2}D_{2a} + \mathcal{O}(J^3)} \\
&= D_{0a}(\alpha'|\alpha) + D_{1a}(\alpha'|\alpha) + D_{2a}(\alpha'|\alpha) + \frac{1}{2}D_{0a}(\alpha'|\alpha) \times D_{2a} + D_{2c}(\alpha'|\alpha) \\
&\quad - \frac{1}{2}D_{0a}(\alpha'|\alpha) \times D_{2a} + \mathcal{O}(J^3) \\
&= D_{0a}(\alpha'|\alpha) + D_{1a}(\alpha'|\alpha) + D_{2a}(\alpha'|\alpha) + D_{2c}(\alpha'|\alpha) + \mathcal{O}(J^3), \tag{E.65}
\end{aligned}$$

where the disconnected term gets cancelled by the denominator contributions. The symbolic representation takes the form

$$-G_{j_\alpha j'_\alpha}(\tau_\alpha, \tau'_\alpha) = \begin{array}{c} \tau'_\alpha \\ \bullet \\ \xrightarrow{\quad} \bullet \xrightarrow{\quad} \tau_\alpha \\ j'_\alpha = j_\alpha \end{array} + \begin{array}{c} \tau'_\alpha \\ \bullet \\ \xrightarrow{\quad} \bullet \xrightarrow{\quad} \bullet \xrightarrow{\quad} \tau_\alpha \\ j'_\alpha \quad j_\alpha \end{array} + \begin{array}{c} \tau'_\alpha \\ \bullet \\ \xrightarrow{\quad} \bullet \xrightarrow{\quad} \bullet \xrightarrow{\quad} \bullet \xrightarrow{\quad} \tau_\alpha \\ j'_\alpha \quad j_\alpha \end{array} + \begin{array}{c} \tau'_\alpha \\ \bullet \\ \xrightarrow{\quad} \bullet \xrightarrow{\quad} \tau_\alpha \\ \updownarrow \\ j'_\alpha = j_\alpha \end{array} + \mathcal{O}(J^3).$$

These results are addressed by the following rules:

Rule 3 - Diagrammatic Expansion of the Green's Function

Rule (a) : Draw all topologically inequivalent connected diagrams $D(\alpha'|\alpha)$ with vertices linked by internal lines and two other external lines (one entering and one exiting a vertex) such that the number of lines entering each vertex equals the number of leaving ones.

Rule (b) : Label each line with an imaginary time variable and each vertex with a lattice vector. The entering and leaving external lines are labeled by τ'_α and τ_α , respectively; the corresponding vertices are identified by j'_α and j_α (external vertices may coincide).

Rule (c) : Same as (c)-(f) in **Rule 1**.

Rule (g) : Same as in **Rule 1**, except that now the external variables remain fixed.

Rule (h) : The two-point Green's function is obtained by the sum of the weights $w[D(\alpha'|\alpha)]$ of all the previously diagrams:

$$G_{j_\alpha j'_\alpha}(\tau_\alpha, \tau'_\alpha) = - \sum_D w[D(\alpha'|\alpha)] . \quad (\text{E.66})$$

E.6 Evaluation of the Free energy and Green's Function

In this section we provide an explicit evaluation of the free energy Ω and the one-particle Green's function G using the previously described perturbative scheme. Our calculations encompass the first non-zero corrections around the atomic limit. Following the paper specifications, we consider hypercubic lattices described by a coordination number z ; also, the hopping is chosen to be restricted to first neighbors, written as

$$J_{j_\alpha j_\beta} = -\delta_{d(j_\alpha j_\beta), 1} J , \quad (\text{E.67})$$

where $d(j_\alpha, j_\beta)$ is the distance between the sites j_α and j_β in terms of the lattice spacing. Since our system is homogeneous, we can also drop the site index appearing in the cumulants. Collecting these observations, the cumulants, which are the main ingredients of the perturbative expansion, can be directly evaluated. As an explicit example we calculate the first cumulant, defined by Eq. (E.29) as

$$\begin{aligned} C_1^{(0)}(\tau'|\tau) &= \langle \mathcal{T} [b^\dagger(\tau')b(\tau)] \rangle_0 \\ &= \theta(\tau - \tau') \langle b(\tau)b^\dagger(\tau') \rangle_0 + \theta(\tau' - \tau) \langle b^\dagger(\tau')b(\tau) \rangle_0 . \end{aligned} \quad (\text{E.68})$$

The thermal averages in Eq. (E.68) are performed with respect to $H^{(0)}$, which is a sum of local operators of the form $H_1^{(0)} = \frac{U}{2}b^\dagger b^\dagger b b - \mu b^\dagger b$. Considering their number operator eigenvectors $|n\rangle$ and eigenvalues $E_n = \frac{U}{2}n(n-1) - \mu n$, the thermal averages

read as

$$\begin{aligned}
\langle b(\tau)b^\dagger(\tau') \rangle_0 &= \left\langle e^{\tau H^{(0)}} b e^{-\tau H^{(0)}} e^{\tau' H^{(0)}} b^\dagger e^{-\tau' H^{(0)}} \right\rangle_0 \\
&= \frac{1}{\mathcal{Z}_1^{(0)}} \sum_{n=0}^{\infty} \langle n | e^{\tau H_1^{(0)}} b e^{-\tau H_1^{(0)}} e^{\tau' H_1^{(0)}} b^\dagger e^{-\tau' H_1^{(0)}} | n \rangle e^{-\beta E_n} \\
&= \frac{1}{\mathcal{Z}_1^{(0)}} \sum_{n=0}^{\infty} e^{\tau E_n} \sqrt{n+1} e^{-\tau E_{n+1}} e^{\tau' E_{n+1}} \sqrt{n+1} e^{-\tau' E_n} e^{-\beta E_n} \\
&= \frac{1}{\mathcal{Z}_1^{(0)}} \sum_{n=0}^{\infty} (n+1) e^{(\tau-\tau')(E_n-E_{n+1})} e^{-\beta E_n} \tag{E.69}
\end{aligned}$$

and

$$\begin{aligned}
\langle b^\dagger(\tau')b(\tau) \rangle_0 &= \left\langle e^{\tau' H^{(0)}} b^\dagger e^{-\tau' H^{(0)}} e^{\tau H^{(0)}} b e^{-\tau H^{(0)}} \right\rangle_0 \\
&= \frac{1}{\mathcal{Z}_1^{(0)}} \sum_{n=0}^{\infty} \langle n | e^{\tau' H_1^{(0)}} b^\dagger e^{-\tau' H_1^{(0)}} e^{\tau H_1^{(0)}} b e^{-\tau H_1^{(0)}} | n \rangle e^{-\beta E_n} \\
&= \frac{1}{\mathcal{Z}_1^{(0)}} \sum_{n=0}^{\infty} e^{\tau' E_n} \sqrt{n} e^{-\tau' E_{n-1}} e^{\tau E_{n-1}} \sqrt{n} e^{-\tau E_n} e^{-\beta E_n} \\
&= \frac{1}{\mathcal{Z}_1^{(0)}} \sum_{n=0}^{\infty} n e^{(\tau'-\tau)(E_n-E_{n-1})} e^{-\beta E_n} , \tag{E.70}
\end{aligned}$$

where

$$\mathcal{Z}_1^{(0)}(T, \mu) = \sum_{n=0}^{\infty} e^{-\beta E_n} \tag{E.71}$$

is the single-site partition function. Therefore, the substitution of Eqs. (E.69) and (E.70) into Eq. (E.68) yields

$$C_1^{(0)}(\tau'|\tau) = \frac{1}{\mathcal{Z}_1^{(0)}} \sum_{n=0}^{\infty} [\theta(\tau-\tau')(n+1)e^{(\tau-\tau')(E_n-E_{n+1})} + \theta(\tau'-\tau)ne^{(\tau'-\tau)(E_n-E_{n-1})}] e^{-\beta E_n} . \tag{E.72}$$

E.7 The Free Energy

According to Eqs. (E.47) and (E.48) the first non-zero correction to the free energy is of second order in the hopping amplitude, given simply by the diagram D_{2a} as follows

$$\Omega = \Omega^{(0)} - k_B T \left(\frac{1}{2} D_{2a} + \mathcal{O}(J^3) \right). \quad (\text{E.73})$$

Combining the homogeneity condition to the mentioned hopping choice, such diagram defined by Eq. (E.34) yields

$$D_{2a} = \sum_{j_1, j_2} J_{j_2, j_1} J_{j_1, j_2} \int_0^\beta d\tau_1 \int_0^\beta d\tau_2 C_{1j_1}^{(0)}(\tau_2 | \tau_1) C_{1j_2}^{(0)}(\tau_1 | \tau_2) \quad (\text{E.74})$$

$$\begin{aligned} &= \sum_{j_1, j_2} \delta_{d(j_1, j_2), 1} J^2 \int_0^\beta d\tau_1 \int_0^\beta d\tau_2 C_1^{(0)}(\tau_2 | \tau_1) C_1^{(0)}(\tau_1 | \tau_2) \\ &= N_s z J^2 \int_0^\beta d\tau_1 \int_0^\beta d\tau_2 C_1^{(0)}(\tau_2 | \tau_1) C_1^{(0)}(\tau_1 | \tau_2). \end{aligned} \quad (\text{E.75})$$

From the cumulant expression of Eq. (E.72), we derive

$$\begin{aligned} D_{2a} &= \frac{N_s z J^2}{[\mathcal{Z}_1^{(0)}]^2} \sum_{n, m=0}^{\infty} e^{-\beta(E_n + E_m)} \int_0^\beta d\tau_1 \int_0^\beta d\tau_2 [\theta(\tau_1 - \tau_2)(n+1)m e^{(\tau_1 - \tau_2)(E_n - E_{n+1} + E_m - E_{m-1})} \\ &\quad + \theta(\tau_2 - \tau_1)n(m+1)e^{(\tau_2 - \tau_1)(E_n - E_{n-1} + E_m - E_{m+1})}] . \end{aligned} \quad (\text{E.76})$$

Also, the exchanges $n \longleftrightarrow m$ and $\tau_1 \longleftrightarrow \tau_2$ in the second term simplify the previous result to

$$\begin{aligned} D_{2a} &= \frac{2N_s z J^2}{[\mathcal{Z}_1^{(0)}]^2} \sum_{n, m=0}^{\infty} e^{-\beta(E_n + E_m)} \int_0^\beta d\tau_1 \int_0^\beta d\tau_2 \theta(\tau_1 - \tau_2)(n+1)m e^{(\tau_1 - \tau_2)(E_n - E_{n+1} + E_m - E_{m-1})} \\ &= \frac{2N_s z J^2}{[\mathcal{Z}_1^{(0)}]^2} \sum_{n, m=0}^{\infty} e^{-\beta(E_n + E_m)} \int_0^\beta d\tau_1 \int_0^{\tau_1} d\tau_2 (n+1)m e^{(\tau_1 - \tau_2)(E_n - E_{n+1} + E_m - E_{m-1})} . \end{aligned} \quad (\text{E.77})$$

If $m \neq n + 1$ (or $E_n - E_{n+1} + E_m - E_{m-1} \neq 0$), integration over the imaginary-time variables provides

$$\begin{aligned}
& \int_0^\beta d\tau_1 \int_0^{\tau_1} d\tau_2 e^{(\tau_1 - \tau_2)(E_n - E_{n+1} + E_m - E_{m-1})} = \\
& = \int_0^\beta d\tau_1 \frac{1}{E_n - E_{n+1} + E_m - E_{m-1}} \left[e^{\tau_1(E_n - E_{n+1} + E_m - E_{m-1})} - 1 \right] \\
& = \frac{1}{E_n - E_{n+1} + E_m - E_{m-1}} \left[\frac{e^{\beta(E_n - E_{n+1} + E_m - E_{m-1})} - 1}{E_n - E_{n+1} + E_m - E_{m-1}} - \beta \right]. \quad (\text{E.78})
\end{aligned}$$

On the other hand, for $m = n + 1$ (or $E_n - E_{n+1} + E_m - E_{m-1} = 0$) we deduce

$$\int_0^\beta d\tau_1 \int_0^{\tau_1} d\tau_2 e^{(\tau_1 - \tau_2)(E_n - E_{n+1} + E_m - E_{m-1})} = \int_0^\beta d\tau_1 \int_0^{\tau_1} d\tau_2 1 = \int_0^\beta d\tau_1 \tau_1 = \frac{\beta^2}{2}. \quad (\text{E.79})$$

Including both Eqs. (E.78) and (E.79) into Eq. (E.77), the diagram D_{2a} can be written as

$$\begin{aligned}
D_{2a} & = \frac{2N_s z J^2}{\left[\mathcal{Z}_1^{(0)} \right]^2} \sum_{m \neq n+1} \frac{(n+1)m e^{-\beta(E_n + E_m)}}{E_n - E_{n+1} + E_m - E_{m-1}} \left[\frac{e^{\beta(E_n - E_{n+1} + E_m - E_{m-1})} - 1}{E_n - E_{n+1} + E_m - E_{m-1}} - \beta \right] \\
& + \frac{N_s z J^2 \beta^2}{\left[\mathcal{Z}_1^{(0)} \right]^2} \sum_n (n+1)^2 e^{-\beta(E_n + E_{n+1})}, \quad (\text{E.80})
\end{aligned}$$

where the first summation excludes the terms $m = n + 1$. Finally, the free energy of Eq. (E.73) becomes

$$\begin{aligned}
\Omega & = \Omega^{(0)} - \frac{N_s z J^2}{\beta \left[\mathcal{Z}_1^{(0)} \right]^2} \sum_{m \neq n+1} \frac{(n+1)m e^{-\beta(E_n + E_m)}}{E_n - E_{n+1} + E_m - E_{m-1}} \left[\frac{e^{\beta(E_n - E_{n+1} + E_m - E_{m-1})} - 1}{E_n - E_{n+1} + E_m - E_{m-1}} - \beta \right] \\
& - \frac{N_s z J^2 \beta}{2 \left[\mathcal{Z}_1^{(0)} \right]^2} \sum_n (n+1)^2 e^{-\beta(E_n + E_{n+1})} + \mathcal{O}(J^4). \quad (\text{E.81})
\end{aligned}$$

Note that the third-order term is identically zero since the hopping is restricted to first neighbors in a hypercubic lattice; therefore, the next non-zero correction is proportional to J^4 .

E.8 The Green's Function and the atom-atom Correlation Function

The one-particle Green's function of Eq. (E.65) up to the first order is obtained by the sum of two diagrams

$$G_{j_\alpha j'_\alpha}(\tau_\alpha, \tau'_\alpha) = D_{0a}(\alpha'|\alpha) + D_{1a}(\alpha'|\alpha) + \mathcal{O}(J^2). \quad (\text{E.82})$$

The zeroth-order contribution is purely local, as Eq. (E.55) reveals

$$\begin{aligned} D_{0a}(\alpha'|\alpha) &= \delta_{j'_\alpha j_\alpha} C_1^{(0)}(\tau'_\alpha|\tau_\alpha) \\ &= \delta_{j'_\alpha j_\alpha} \frac{1}{Z_1^{(0)}} \sum_{n=0}^{\infty} \left[\theta(\tau_\alpha - \tau'_\alpha)(n+1)e^{(\tau_\alpha - \tau'_\alpha)(E_n - E_{n+1})} \right. \\ &\quad \left. + \theta(\tau'_\alpha - \tau_\alpha)n e^{(\tau'_\alpha - \tau_\alpha)(E_n - E_{n-1})} \right] e^{-\beta E_n}. \end{aligned} \quad (\text{E.83})$$

The first-order term is determined by Eq. (E.57), related to a contribution of the first neighbors according to

$$\begin{aligned} D_{1a}(\alpha'|\alpha) &= J_{j_\alpha j'_\alpha} \int_0^\beta d\tau_1 C_{1j'_\alpha}^{(0)}(\tau'_\alpha|\tau_1) C_{1j_\alpha}^{(0)}(\tau_1|\tau_\alpha) \\ &= -\delta_{d(j_\alpha, j_\beta), 1} J \int_0^\beta d\tau_1 C_1^{(0)}(\tau'_\alpha|\tau_1) C_1^{(0)}(\tau_1|\tau_\alpha). \end{aligned} \quad (\text{E.84})$$

As the main text discusses, from the two-point Green's function we extract the atom-atom correlations $\mathcal{C}_{j'_\alpha j_\alpha} = -G_{j_\alpha j'_\alpha}(0, 0^+)$. If we consider j'_α and j_α first neighbors, then $\delta_{j'_\alpha j_\alpha} = 1$ and we symbolize the correlation under these circumstances simply as \mathcal{C} . Hence Eqs. (E.82)-(E.84) imply

$$\mathcal{C} = J \int_0^\beta d\tau_1 C_1^{(0)}(0^+|\tau_1) C_1^{(0)}(\tau_1|0) + \mathcal{O}(J^3) \quad (\text{E.85})$$

By carrying out the imaginary-time integral, the atom-atom correlation function between first neighbors reads as

$$\begin{aligned}
\mathcal{C} &= \frac{J}{[\mathcal{Z}_1^{(0)}]^2} \sum_{n,m} e^{-\beta(E_n+E_m)} \int_0^\beta d\tau_1 (n+1) m e^{\tau_1(E_n-E_{n+1}+E_m-E_{m-1})} + \mathcal{O}(J^3) \\
&= \frac{2J}{[\mathcal{Z}_1^{(0)}]^2} \sum_{m \neq n+1} \frac{(n+1) m e^{-\beta(E_n+E_m)}}{E_n - E_{n+1} + E_m - E_{m-1}} \left[\frac{e^{\beta(E_n-E_{n+1}+E_m-E_{m-1})} - 1}{E_n - E_{n+1} + E_m - E_{m-1}} - \beta \right] \\
&\quad + \frac{J\beta^2}{[\mathcal{Z}_1^{(0)}]^2} \sum_n (n+1)^2 e^{-\beta(E_n+E_{n+1})} + \mathcal{O}(J^3). \tag{E.86}
\end{aligned}$$

Appendix F

Decomposition of the Specific Heat, Spectral Functions and Correlations

F.1 Decomposition of the Specific Heat

In the following, we demonstrate the decomposition of the specific heat capacity shown in Eq. (4.9). We explore its extensive related function, the heat capacity C . In general terms, the heat capacity accounts for fluctuations in energy with respect to its mean value according to

$$C = -T \left(\frac{\partial^2 \Omega}{\partial T^2} \right) = \beta^2 (\langle E^2 \rangle - \langle E \rangle^2) . \quad (\text{F.1})$$

The fluctuations around the mean value $(\delta E)^2 = \langle E^2 \rangle - \langle E \rangle^2$ are explicitly determined by the averages

$$\langle E^2 \rangle = \frac{1}{\mathcal{Z}} \sum_n E_n^2 e^{-\beta E_n} \quad (\text{F.2})$$

and

$$\langle E \rangle^2 = \frac{1}{\mathcal{Z}^2} \sum_{n,m} E_n E_m e^{-\beta(E_n + E_m)} , \quad (\text{F.3})$$

where

$$\mathcal{Z} = \sum_n e^{-\beta E_n} \quad (\text{F.4})$$

is the partition function. Alternatively, it is possible to express Eq. (F.2) in the form

$$\begin{aligned} \langle E^2 \rangle &= \left(\frac{1}{\mathcal{Z}} \sum_n E_n^2 e^{-\beta E_n} \right) \times \left(\frac{1}{\mathcal{Z}} \sum_m e^{-\beta E_m} \right) \\ &= \frac{1}{\mathcal{Z}^2} \sum_{n,m} E_n^2 e^{-\beta(E_n+E_m)}, \end{aligned} \quad (\text{F.5})$$

which allows us to write the heat capacity according to

$$C = k_B \frac{\beta^2}{\mathcal{Z}^2} \sum_{n,m} (E_n^2 - E_n E_m) e^{-\beta(E_n+E_m)}. \quad (\text{F.6})$$

Since the terms $n = m$ are zero, we separate the sum into two parts

$$\begin{aligned} C &= k_B \frac{\beta^2}{\mathcal{Z}^2} \sum_{n < m} (E_n^2 - E_n E_m) e^{-\beta(E_n+E_m)} \\ &\quad + k_B \frac{\beta^2}{\mathcal{Z}^2} \sum_{n > m} (E_n^2 - E_n E_m) e^{-\beta(E_n+E_m)}. \end{aligned} \quad (\text{F.7})$$

By exchanging the labels $n \rightarrow m$ and $m \rightarrow n$ in the second term, we obtain

$$\begin{aligned} C &= k_B \frac{\beta^2}{\mathcal{Z}^2} \sum_{n < m} (E_n^2 - E_n E_m) e^{-\beta(E_n+E_m)} \\ &\quad + k_B \frac{\beta^2}{\mathcal{Z}^2} \sum_{m > n} (E_m^2 - E_m E_n) e^{-\beta(E_m+E_n)} \\ &= k_B \frac{\beta^2}{\mathcal{Z}^2} \sum_{n < m} (E_n^2 - E_n E_m + E_m^2 - E_m E_n) e^{-\beta(E_n+E_m)} \\ &= k_B \frac{\beta^2}{\mathcal{Z}^2} \sum_{n < m} (E_n - E_m)^2 e^{-\beta(E_n+E_m)}. \end{aligned} \quad (\text{F.8})$$

Such decomposition impels us to define a partial specific heat $c^{(n,m)}$, which describes the fluctuations between the energy levels m and n

$$C^{(n,m)} = k_B \frac{\beta^2}{\mathcal{Z}^2} (E_n - E_m)^2 e^{-\beta(E_n + E_m)}. \quad (\text{F.9})$$

Therefore, the heat capacity becomes simply the sum of the defined partial components

$$C = \sum_{n < m} C^{(n,m)}. \quad (\text{F.10})$$

This result enables us to analyze and filter which energy level transitions are relevant to the specific heat behavior.

F.2 Spectral Function in the Atomic Limit

For $J = 0$, the local one-particle Green's function in Matsubara space is given by

$$G^{(0)}(i\omega_n) = \frac{1}{\mathcal{Z}^{(0)}} \sum_{n,m} \frac{\langle n | b | m \rangle \langle m | b^\dagger | n \rangle}{i\omega_n + E_n - E_m} (e^{-\beta E_n} - e^{-\beta E_m}),$$

when expressed using the Lehmann representation [114]. For interpretation purposes, this can be decomposed into particle and hole excitation branches [164] according to

$$G^{(0)}(i\omega_n) = G_p^{(0)}(i\omega_n) + G_h^{(0)}(i\omega_n), \quad (\text{F.11})$$

where

$$G_p^{(0)}(i\omega_n) = \frac{1}{\mathcal{Z}^{(0)}} \sum_{n,m} \frac{\langle n | b | m \rangle \langle m | b^\dagger | n \rangle}{i\omega_n + E_n - E_m} e^{-\beta E_n} \quad (\text{F.12})$$

and

$$G_h^{(0)}(i\omega_n) = \frac{1}{\mathcal{Z}^{(0)}} \sum_{n,m} \frac{\langle m | b | n \rangle \langle n | b^\dagger | m \rangle}{i\omega_n + E_m - E_n} e^{-\beta E_n}. \quad (\text{F.13})$$

By analytical continuation, we determine the retarded Green's function $G_R^{(0)}(\omega) = G^{(0)}(\omega + i\eta)$, with $\eta \rightarrow 0^+$. Also, the definition of the local spectral function of Eq. (4.10) implies

$$\begin{aligned} A(\omega) &= -\frac{1}{\pi} \Im[G_R^{(0)}(\omega)] \\ &= \frac{1}{\mathcal{Z}^{(0)}} \sum_{n,m} \delta(\omega - \Delta E_{n \rightarrow m}) |\langle n|b|m\rangle|^2 e^{-\beta E_n} \\ &\quad - \frac{1}{\mathcal{Z}^{(0)}} \sum_{n,m} \delta(\omega - \Delta E_{n \rightarrow m}) |\langle m|b|n\rangle|^2 e^{-\beta E_n}, \end{aligned}$$

as a consequence of the limit

$$\lim_{\eta \rightarrow 0^+} \frac{1}{(\omega - \Delta E) + i\eta} = -\pi \delta(\omega - \Delta E). \quad (\text{F.14})$$

The explicit evaluation of the previous matrix elements yields

$$\begin{aligned} A^{(0)}(\omega) &= \frac{1}{\mathcal{Z}^{(0)}} \sum_n \delta(\omega - \Delta E_{n \rightarrow n+1}) (n+1) e^{-\beta E_n} \\ &\quad - \frac{1}{\mathcal{Z}^{(0)}} \sum_n \delta(\omega - \Delta E_{n-1 \rightarrow n}) n e^{-\beta E_n}, \end{aligned} \quad (\text{F.15})$$

which shows the atomic limit spectral function as a collection delta functions at the consecutive transitions $|n\rangle \rightarrow |n+1\rangle$. This analysis makes explicit that the negative sign contributions of A comes from the hole excitation branch.

F.3 Correlations and free energy

In Subsec. 4.2 we presented how the free energy can be obtained from the atom-atom correlation function according to Eq. (4.19). In order to demonstrate this relation, we parametrize the system's Hamiltonian in the form $H^{(\lambda)} = H^{(0)} + \lambda \mathcal{H}$ according to Eqs. (4.16) and (4.17), interpolating the atomic limit $H^{(0)}$ and the original Hamiltonian $H^{(\lambda)}$ as λ continuously varies between 0 and 1.

The corresponding partition function is given by the trace

$$\mathcal{Z}^{(\lambda)} = \text{Tr} \left[e^{-\beta H^{(\lambda)}} \right], \quad (\text{F.16})$$

from which we extract the free energy

$$\Omega^{(\lambda)} = -\frac{1}{\beta} \ln \mathcal{Z}^{(\lambda)}. \quad (\text{F.17})$$

The derivative of $\Omega^{(\lambda)}$ with respect to λ provides

$$\begin{aligned} \frac{d\Omega^{(\lambda)}}{d\lambda} &= -\frac{1}{\beta} \frac{\text{Tr} \left[(-\beta \mathcal{H}) e^{-\beta H^{(\lambda)}} \right]}{\text{Tr} \left[e^{-\beta H^{(\lambda)}} \right]} \\ &= \frac{\text{Tr} \left[\mathcal{H} e^{-\beta H^{(\lambda)}} \right]}{\text{Tr} \left[e^{-\beta H^{(\lambda)}} \right]} = \langle \mathcal{H} \rangle_{\lambda}. \end{aligned} \quad (\text{F.18})$$

On the other hand, the free energy variation follows immediately from the integration

$$\int_0^1 \frac{d\Omega^{(\lambda)}}{d\lambda} d\lambda = \Omega - \Omega^{(0)} = \Delta\Omega, \quad (\text{F.19})$$

because $\Omega^{(1)} = \Omega$. By using the results of Eq. (F.18) into Eq. (F.19), we get

$$\Delta\Omega = \int_0^1 \langle \mathcal{H} \rangle_{\lambda} d\lambda. \quad (\text{F.20})$$

Furthermore, the expression for the tunneling term \mathcal{H} of Eq. (??) yields

$$\begin{aligned} \Delta\Omega &= -J \sum_{\langle i,j \rangle} \int_0^1 \langle b_i^\dagger b_j \rangle_{\lambda} d\lambda \\ &= -J \sum_{\langle i,j \rangle} \int_0^1 \mathcal{C}_{ij}^{(\lambda)} d\lambda, \end{aligned} \quad (\text{F.21})$$

where

$$\mathcal{C}_{ij}^{(\lambda)} = \langle b_i^\dagger b_j \rangle_{\lambda} \quad (\text{F.22})$$

is the correlation function considering first neighbors i and j , evaluated through a thermal average at a hopping λJ . For a homogeneous system the summation over all first neighbors yields zN_s , simplifying Eq. (F.21) to

$$\Delta\Omega = -zJN_s \int_0^1 \mathcal{C}^{(\lambda)} d\lambda . \quad (\text{F.23})$$

Appendix G

Publications and Submissions

RESEARCH ARTICLE

Core-softened potentials, multiple liquid–liquid critical points, and density anomaly regions: An exact solution

Eduardo O. Rizzatti¹, Marco Aurélio A. Barbosa^{2,†}, Marcia C. Barbosa^{1,‡}

¹*Instituto de Física, Universidade Federal do Rio Grande do Sul, Porto Alegre-RS, Brazil*

²*Programa de Pós-Graduação em Ciência de Materiais, Universidade de Brasília, Planaltina-DF, Brazil*

Corresponding authors. E-mail: [†]aureliobarbosa@unb.br; [‡]marcia.barbosa@ufrgs.br

Received March 2, 2017; accepted July 27, 2017

The pressure versus temperature phase diagram of a system of particles interacting through a multiscale shoulder-like potential is exactly computed in one dimension. The N -shoulder potential exhibits N density anomaly regions in the phase diagram if the length scales can be connected by a convex curve. The result is analyzed in terms of the convexity of the Gibbs free energy.

Keywords density anomalies regions

PACS numbers 61.20.Gy, 65.20.-w

1 Introduction

The phase behavior of single-component systems considered as particles interacting via the so-called core-softened (CS) potential has received attention since the work of Hemmer and Stell [1]. These potentials exhibit a repulsive core with a softened region having a shoulder or a ramp [1–12]. These models are motivated by the desire to construct a simple two-body isotropic potential capable of describing the complicated features of systems interacting via isotropic potentials. This procedure generates models that are analytically and computationally tractable, and that one hopes are capable of retaining the qualitative features of real complex systems.

The physical motivation behind these studies is the recently acknowledged possibility that some single-component systems exhibit the coexistence of two different liquid phases [1, 2, 6]. This has opened a discussion about the relationship among the presence of two liquid phases, the existence of thermodynamic anomalies in the liquids, and the form of the potential. The case of water has probably been the most intensively studied. For instance, liquid water has a temperature at

which the density is maximum at constant pressure [13]. It was proposed some time ago that the temperature of maximum density (TMD) might be associated with a critical point at the terminus of a liquid–liquid phase transition [14]. This hypothesis has been supported by simulations [14, 15] and experiments [16, 17].

The natural question that follows is whether a CS potential with two length scales will have one region in the pressure versus temperature phase diagram in which the density is anomalous and a liquid–liquid phase transition is present, and one with three length scales will have two TMD lines. To address this question, in this paper, we present an exact solution of a system of particles interacting through a multi-length-scale potential. Our analysis, even though it is restricted to one dimension, shows that the TMD lines are associated with the presence of liquid–liquid critical points. The existence of both various TMD lines and critical points depends on the shape of the pair interaction potential. If the length scales can be connected by a convex curve, multiple TMDs are present; otherwise, they are absent.

The rest of the paper is structured as follows. In Section 2, the exact solution is presented and applied to the one-shoulder, two-shoulder, and multiple-shoulder potentials. In Section 3, the analytic solution is applied to the lattice version of the model. Conclusions are presented in Section 4.

*Special Topic: Water and Water Systems (Eds. F. Mallamace, R. Car, and Limei Xu).

2 Analytic solution

We consider a one-dimensional system composed of a set of identical classical particles of mass m that interact only with their nearest neighbors. As the problem is treated using classical mechanics, we can assign to the particles moving on this line the positions $\mathbf{q} = (q_1, \dots, q_N)$ and linear momenta $\mathbf{p} = (p_1, \dots, p_N)$. The time evolution is described by the Hamiltonian

$$\mathcal{H}(\mathbf{q}, \mathbf{p}) = \frac{\mathbf{p}^2}{2m} + U(\mathbf{q}), \quad (1)$$

where U is the total potential energy. In addition, we suppose that interaction occurs among adjacent pairs through a potential Φ that is translationally invariant; U is then expressed as

$$U(\mathbf{q}) = \sum_{i=1}^{N-1} \Phi(q_{i+1} - q_i), \quad (2)$$

where $\Phi(q_{i+1} - q_i)$ is the potential energy between two particles.

The pressure ensemble corresponds to a system in thermodynamic equilibrium with heat and volume reservoirs, which fix the temperature $\beta^{-1} = k_B T$ and pressure p . A simplified expression for the partition function J is given by [18, 19]

$$J(T, p, N) = \frac{1}{(\beta p)^2 \Lambda_0 \Lambda^N} \left(\int_0^\infty e^{-\beta[\Phi(r) + pr]} dr \right)^{N-1}, \quad (3)$$

where $\beta = 1/(k_B T)$, Λ_0 is a constant with dimensions of length, and Λ is the de Broglie thermal wavelength, namely,

$$\Lambda(T) = \left(\frac{h^2}{2\pi m k_B T} \right)^{1/2}. \quad (4)$$

In the thermodynamic limit, where $N \rightarrow \infty$, the Gibbs

free energy per particle is then expressed as

$$g(T, p) = -k_B T \lim_{N \rightarrow \infty} \frac{1}{N} \log J = -\frac{1}{\beta} \log \frac{1}{\Lambda} \left(\int_0^\infty e^{-\beta[\Phi(r) + pr]} dr \right). \quad (5)$$

From this fundamental equation follows the equation of state,

$$v(T, p) = \frac{\partial g(T, p)}{\partial p},$$

$$\rho(T, p) = \frac{1}{v(T, p)}, \quad (6)$$

allowing us to map the behavior of the isobaric thermal expansion coefficient given by

$$\alpha(T, p) = \frac{1}{v} \left(\frac{\partial v}{\partial T} \right)_p. \quad (7)$$

3 Continuous potentials

3.1 One-shoulder pair potential

We begin by analyzing the simplest two-length scale potential Φ :

$$\Phi(r) = \begin{cases} \infty, & r < \lambda_0 \\ V_0, & \lambda_0 \leq r < \lambda_1 \\ V_1, & \lambda_1 \leq r. \end{cases} \quad (8)$$

Figure 1(a) shows the interparticle potential energy, $\Phi^* = \Phi/V_0$, versus the distance between particles, $r^* = r/\lambda_0$, where $V_1 = 0$, $\lambda_0 < \lambda_1 < 2\lambda_0$, and $\lambda_1^* = \lambda_1/\lambda_0$. For these reduced units, the Gibbs free energy in Eq. (5)

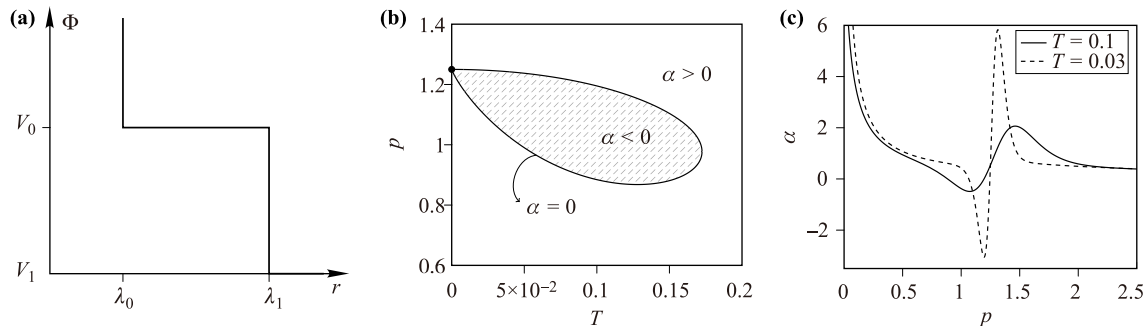


Fig. 1 (a) Pair potential $\Phi^* = \Phi/V_0$ versus $r^* = r/\lambda_0$, (b) pressure versus temperature, and (c) thermal expansion coefficient versus pressure for $\lambda_1^* = \lambda_1/\lambda_0$.

assumes the form

$$g^*(T, p) \equiv \frac{g(T, p)}{V_0} = -T^* \log \frac{T^*}{\Lambda^* p^*} \left[e^{-(1+p^*)/T^*} - e^{-(1+\lambda_1^* p^*)/T^*} + e^{-(V_1^* + \lambda_1^* p^*)/T^*} \right], \quad (9)$$

where the temperature, pressure, and thermal wavelength in reduced units are given by $T^* = k_B T / V_0$, $p^* = p \lambda_0 / V_0$, and $\Lambda^* = \Lambda / \lambda_0$, respectively, and the potential parameters are $\lambda_1^* = \lambda_1 / \lambda_0$ and $V_1^* = V_1 / V_0$.

The density versus temperature plot for a fixed pressure reveals the temperature at which the density is maximum. For different pressures, this maximum occurs at different temperatures, as illustrated in Fig. 1(b). The intuitive idea behind this is that competition between the two length scales in the potential generates a density maximum if both scales are accessible to the system [20–24]. The anomaly then manifests itself when the system passes from a less dense structure associated with the scale λ_1 to a more compact one associated with λ_0 when the temperature is increased at a fixed pressure. Furthermore, the response function α , shown in Fig. 1(c), not only changes sign, indicating the presence of a density anomaly region in the pressure versus temperature phase diagram, but also diverges as $T \rightarrow 0$, a behavior that is generally related to the presence of criticality [23].

One-dimensional systems with finite-range interactions, such as the model we are analyzing, obviously exhibit phase transitions only at $T = 0$. The temperature destroys any attempt at ordering. Indeed, Takahashi’s solution [18], which is illustrated in Eq. (3), does not violate this principle.

Let us analyze, therefore, the zero-temperature phase transitions in order to establish a relationship with the density anomaly regions. First, let us fix $p > 0$. The leading behavior of $g(T, p)$ depends essentially on the argument of its exponentials in Eq. (9). In this case, the condition $\lambda_1 > \lambda_0$ implies $V_0 + \lambda_0 p < V_0 + \lambda_1 p$ for every

$p > 0$; consequently,

$$\lim_{\beta \rightarrow \infty} g = - \lim_{\beta \rightarrow \infty} \frac{1}{\beta} \log \left[e^{-\beta(V_0 + \lambda_0 p)} + e^{-\beta(V_1 + \lambda_1 p)} \right]. \quad (10)$$

Hence, this limit is determined by the straight lines $\eta_0(p) = V_0 + \lambda_0 p$ and $\eta_1(p) = V_1 + \lambda_1 p$ of smallest value at a particular pressure p , as shown in Fig. 2(a). By defining their intersection as

$$p_{01} = \frac{V_0 - V_1}{\lambda_1 - \lambda_0}, \quad (11)$$

we can express $g = g(p)$ in this regime, as illustrated in Fig. 2(a), as

$$g(p) = \begin{cases} -\infty, & p = 0 \\ V_1 + \lambda_1 p, & 0 < p < p_{01} \\ V_0 + \lambda_0 p, & p_{01} < p. \end{cases} \quad (12)$$

In the ground state, $g(p)$, despite its well-defined concavity, as a function of p exhibits singularities at the origin ($p = 0$) and at $p = p_{01}$. At $p = p_{01}$, the system undergoes a discontinuous phase transition in which the high-density phase, $v = \lambda_0$, associated with the length scale λ_0 coexists with the low-density phase, $v = \lambda_1$, associated with λ_1 , according to Fig. 2(b). This suggests a mechanism for the density anomaly. Its origin should be related to the phase separation at $T = 0$. The system at zero temperature and p_{01} has two coexisting phases. As the temperature increases, the competition between these two phases give rise to the density anomaly.

We can extend this analysis and look for a connection between the interaction potential Φ and the thermodynamic anomaly. This can be approached through the expected value $\langle \Phi \rangle$, which is defined for equilibrium states as the probability measure of the pressure ensemble and expressed as

$$\langle \Phi \rangle = u - \frac{1}{2} k_B T. \quad (13)$$

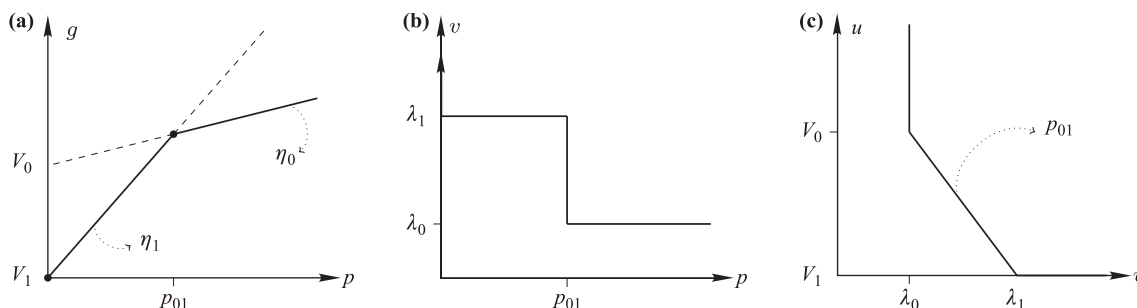


Fig. 2 (a) Gibbs free energy g as a function of the pressure p for $T = 0$ (solid line; the singularity at $p = 0$ was omitted); the coexistence pressure p_{01} is just the intersection of η_0 and η_1 . (b) Specific volume v versus p follows from the slopes of these lines. (c) Internal energy representation of the same system.

Hence, for $T \rightarrow 0$, the expected value of the potential coincides with the internal energy of the system. This result allows us to employ the internal energy representation $u = u(v)$ instead of the Gibbs representation. By performing the Legendre transformation¹⁾ between the conjugate variables $(v, -p)$, we obtain the energy

$$u(v) = \sup_p \{g(p) - pv\}. \quad (14)$$

Figure 2(c) shows the energy versus the pressure; as expected, the internal energy is a convex function of its argument, whereas its magnitude is the slope of the coexistence pressure p_{01} .

3.2 Two-shoulder pair potential

Next, we explore the possibility that there are two regions in the pressure versus temperature phase diagram where a density anomaly and criticality appear as the system interacts through a potential with three length scales. When another scale of interaction is added, the interaction potential Φ is given by

$$\Phi(r) = \begin{cases} \infty, & r < \lambda_0 \\ V_0, & \lambda_0 \leq r < \lambda_1 \\ V_1, & \lambda_1 \leq r < \lambda_2 \\ V_2, & \lambda_2 \leq r, \end{cases} \quad (15)$$

where $V_2 = 0$, and $\lambda_0 < \lambda_1 < \lambda_2 < 2\lambda_0$, as shown in Fig. 3.

Then, the Gibbs fundamental equation [Eq. (5)] of this system is expressed as

$$g(\beta, p) = -\frac{1}{\beta} \log \frac{1}{\Lambda \beta p} \left[e^{-\beta(V_0 + \lambda_0 p)} - e^{-\beta(V_0 + \lambda_1 p)} + e^{-\beta(V_1 + \lambda_1 p)} - e^{-\beta(V_1 + \lambda_2 p)} + e^{-\beta(V_2 + \lambda_2 p)} \right]. \quad (16)$$

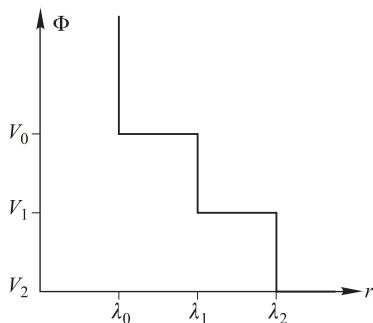


Fig. 3 Pair potential versus distance with three length scales.

¹⁾It is well defined because $\lim_{T \rightarrow 0} Ts(T, p) = 0$, where $s = s(T, p)$ is the entropy per particle.

It is reasonable to expect that the inclusion of a new scale of interaction allows for the occurrence of a new density anomaly region in the phase diagram. However, Fig. 4 shows that, depending on the choice of parameters, the system exhibits just one or two density anomaly regions in the pressure versus temperature phase diagram. The origin of this behavior can be understood if we analyze the ground-state phase transitions, which are precursors of density anomalies, as seen in the former section. First, take $p > 0$; then the zero-temperature Gibbs free energy is given by

$$\lim_{\beta \rightarrow \infty} g = - \lim_{\beta \rightarrow \infty} \frac{1}{\beta} \log \left[e^{-\beta(V_0 + \lambda_0 p)} + e^{-\beta(V_1 + \lambda_1 p)} + e^{-\beta(V_2 + \lambda_2 p)} \right]. \quad (17)$$

The zero-temperature Gibbs free energy is determined by the smallest value among the straight lines $\eta_0(p) = V_0 + \lambda_0 p$, $\eta_1(p) = V_1 + \lambda_1 p$, and $\eta_2(p) = V_2 + \lambda_2 p$ for a particular pressure p . If we define their intersections as

$$p_{01} = \frac{V_0 - V_1}{\lambda_1 - \lambda_0}, \quad p_{02} = \frac{V_0 - V_2}{\lambda_2 - \lambda_0},$$

and

$$p_{12} = \frac{V_1 - V_2}{\lambda_2 - \lambda_1}, \quad (18)$$

two possible scenarios arise: $p_{01} \leq p_{12}$ or $p_{01} > p_{12}$ (a consequence of the restrictions $\lambda_0 < \lambda_1 < \lambda_2$). It follows that $g = g(p)$ in this regime [see Figure 5(a) and 5(b)] assumes the form

$$g(p) = \begin{cases} -\infty, & p = 0 \\ V_2 + \lambda_2 p, & 0 < p < p_{02} \\ V_0 + \lambda_0 p, & p_{02} < p \end{cases} \quad (19)$$

if $p_{01} \leq p_{12}$, or the form

$$g(p) = \begin{cases} -\infty, & p = 0 \\ V_2 + \lambda_2 p, & 0 < p < p_{12} \\ V_1 + \lambda_1 p, & p_{12} < p < p_{01} \\ V_0 + \lambda_0 p, & p_{01} < p \end{cases} \quad (20)$$

if $p_{01} > p_{12}$. Therefore, the phase diagram shows only one density anomaly region in the pressure versus temperature phase diagram in the first case and two density anomaly regions in the second case.

To visualize the energetic conditions for the existence of one or two density anomaly regions in the pressure versus temperature phase diagram, the behavior of Φ at $T = 0$ is analyzed. Eq. (13) shows that at $T = 0$, $\Phi = u(v)$. Therefore, in Fig. 4(a), the slopes of the lines joining the points (λ_0, V_0) , (λ_1, V_1) , and (λ_2, V_2) are equal in magnitude to the coexistence pressures defined by Eq. (18). The condition $p_{01} > p_{12}$, illustrated

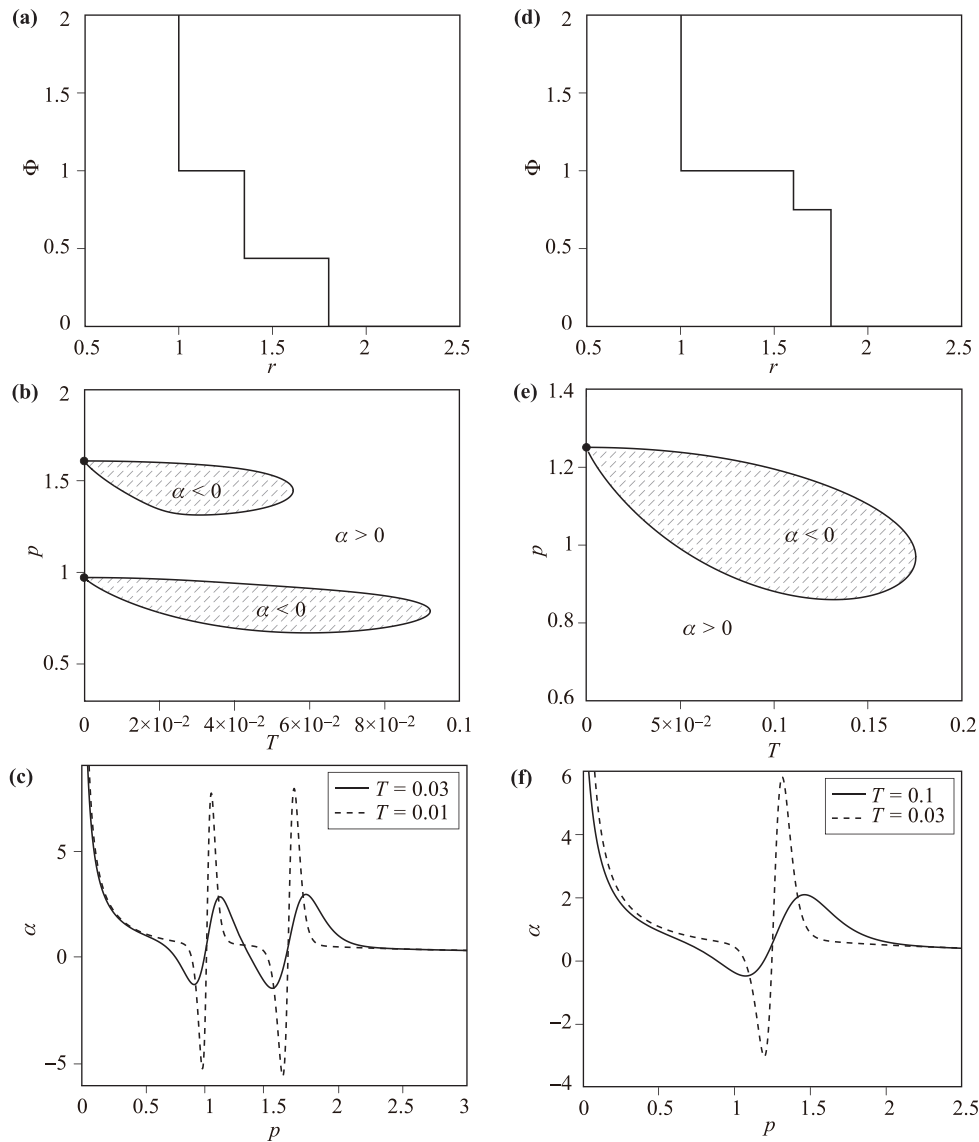


Fig. 4 Potential Φ versus r for $\lambda_2 = 1.8$, $\lambda_1 = 27/20$, $\lambda_0 = 1$, $V_1 = 7/16$, and $V_0 = 1$ (a) and $\lambda_2 = 1.8$, $\lambda_1 = 1.6$, $\lambda_0 = 1$, $V_1 = 0.75$, and $V_0 = 1$ (d). The corresponding phase diagrams exhibiting the density anomaly states are shown in (b) and (e), respectively. The divergence of the response function α at the critical pressures as the system approaches $T = 0$, as well as its sign change, are shown in (c) and (f), respectively.

in Fig. 4(b), permits all scales to be accessible inasmuch as it generates a convex u (phases of lower volume coexist at a pressure higher than phases of higher volume; translating this idea to our notation, stability requires $p_{01} > p_{12}$ for $\lambda_0 < \lambda_1 < \lambda_2$). Thus, the transitions 01 and 12 are allowed. Consequently, the thermal expansion coefficient shown in Fig. 4(c) exhibits two regions with divergence as $T \rightarrow 0$. On the other hand, if Φ versus distance behaves as shown in Fig. 4(d), $p_{01} \leq p_{12}$. The length scale, (λ_1, V_1) , becomes inaccessible because its location implies a nonconvex u as a function of the specific volume. The system then coexists only in phases 0 and 2, as illustrated in Fig. 4(e). In this case, the di-

vergence of the thermal expansion coefficient is similar to that in the system with two length scales, as shown in Fig. 4(f).

We can easily identify, for $T = 0$, whether the system has one or two density anomaly regions in the pressure versus temperature phase diagram by using the following geometric picture. First, we draw one straight line connecting (λ_0, V_0) and (λ_1, V_1) and another straight line connecting (λ_1, V_1) and (λ_2, V_2) in the potentials illustrated in Figs. 5(a) and (e). In Fig. 5(a), the two lines together form a convex curve, and two density anomaly regions are present, whereas in Fig. 5(e), a concave curve is present, and just one density anomaly region is present.

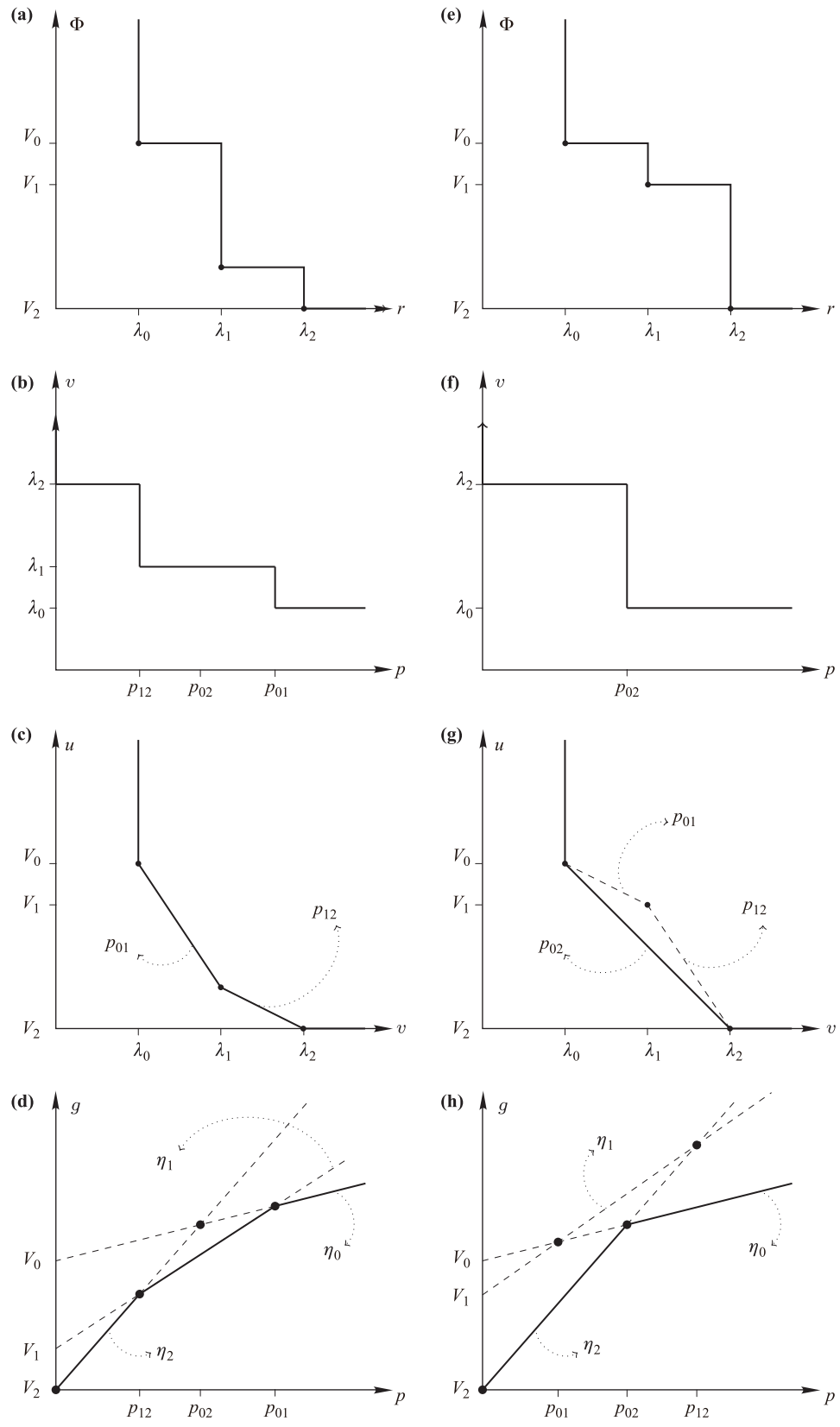


Fig. 5 Φ versus r for (a) $p_{01} \leq p_{12}$ and (e) $p_{01} > p_{12}$; v versus p for (b) $p_{01} \leq p_{12}$ and (f) $p_{01} > p_{12}$; u versus v for (c) $p_{01} \leq p_{12}$ and (g) $p_{01} > p_{12}$; and g versus p for (d) $p_{01} \leq p_{12}$ and (h) $p_{01} > p_{12}$.

The difference in the two cases is also reflected in the reduced volume versus pressure diagram, which shows three phases in Fig. 5(b) and two phases in Fig. 5(f). Consequently, the internal energy u versus v shows three stable densities in Fig. 5(c) and only two in Fig. 5(g). Finally, the free energy g as a function of p is a concave stable function with three densities in Fig. 5(d) and only two in Fig. 5(h).

Another way to visualize whether a pair potential leads to multiple density anomaly regions is to draw a line connecting (λ_0, V_0) and (λ_1, V_1) , another straight line connecting (λ_1, V_1) and (λ_2, V_2) , and a third line connecting (λ_0, V_0) and (λ_2, V_2) . If the first two lines lie above the third line, the system has two density anomaly regions.

This same argument will be generalized in the following section, where we will deal with the limit of N shoulders.

3.3 Infinite-shoulder pair potential

In this section, let us consider an extrapolation of the interaction potential Φ of the form

$$\Phi(r) = \begin{cases} \infty, & r < \lambda_0 \\ V_0, & \lambda_0 \leq r < \lambda_1 \\ \vdots & \\ V_i, & \lambda_i \leq r < \lambda_{i+1} \\ \vdots & \\ V_N, & \lambda_N \leq r < \lambda_{N+1}, \end{cases} \quad (21)$$

where $V_N = 0$, $\lambda_0 < \dots < \lambda_i < \dots < \lambda_N < 2\lambda_0$, and $\lambda_{N+1} \rightarrow \infty$. The Gibbs free energy g associated with this potential is

$$g(\beta, p) = -\frac{1}{\beta} \log \left[\frac{1}{\Lambda \beta p} \times \sum_{i=0}^N (e^{-\beta(V_i + \lambda_i p)} - e^{-\beta(V_i + \lambda_{i+1} p)}) \right]. \quad (22)$$

In the ground state, the free energy behaves as

$$\lim_{\beta \rightarrow \infty} g = - \lim_{\beta \rightarrow \infty} \frac{1}{\beta} \log \left[\sum_{i=0}^N e^{-\beta(V_i + \lambda_i p)} \right] \quad (23)$$

for $\lambda_i < \lambda_{i+1}$ and $0 \leq i \leq N$. If we define the straight lines

$$\eta_i(p) = V_i + \lambda_i p \quad (24)$$

for $0 \leq i \leq N$, the ground-state free energy becomes

$$g(p) = \inf_{0 \leq i \leq N} \eta_i(p) \quad (25)$$

for $p > 0$. The intersection of the $\eta_i(p)$ and $\eta_j(p)$

lines represents the possible coexistence pressures between phases i and j :

$$p_{ij} = \frac{V_i - V_j}{\lambda_j - \lambda_i}, \quad (26)$$

where $0 \leq i < j \leq N$.

For this multiscale system, the fundamental question is whether a scale (λ_k, V_k) determines a phase transition and consequently a density anomaly region. In other words, if there exists an interval I_k (on the domain of g) such that $p \in I_k$, this implies that $g(p) = V_k + \lambda_k p$. This happens only if $p_{ik} > p_{kj}$ for all i, j obeying $i < k < j$ (i.e., $\lambda_i < \lambda_k < \lambda_j$); $N+1$ phases and N density anomaly regions are present in the system.

Figure 6(a) shows the free energy versus pressure for a system with $N+1$ phases and N density anomaly regions, whereas Fig. 6(c) shows the free energy versus pressure for a system with N phases and $N - 1$ density anomaly regions. The internal energies of these two systems are shown in Figs. 6(b) and (d), respectively.

4 Lattice pair potentials

The previous section presented an analysis of one-dimensional systems interacting through shoulder pair potentials in continuous space. We found that the existence of many density anomaly regions in the pressure versus temperature phase diagram depends on the convexity of Φ . In this section, we test the generality of this result regarding the convexity of Φ for a lattice system. We consider a lattice gas model with a four-shoulder pair potential that is restricted to a lattice whose sites are regularly spaced by $l = l_0$, with $l_0 = 1$ (reduced units). A partition function similar to that derived in the previous section [Eq. (3)] but for a lattice system is given by $J(\beta, p, N)$:

$$J(\beta, p, N) = \left[\sum_r e^{-\beta \eta_r(p)} \right]^N, \quad (27)$$

where $\eta_r(p)$ was defined above.²⁾ It follows that an exact expression for g is simply

$$g = -\frac{1}{\beta} \ln \left[\sum_{r=1}^{\infty} e^{-\beta \eta_r(p)} \right], \quad (28)$$

which is identical to the low-temperature limit obtained for continuous models in Eq. (23). Thus, the restrictions obtained above for the scales (λ_k, u_k) on the continuous model can be applied to lattice models.

²⁾Note that $\eta_r(p)$ was previously interpreted as the microscopic enthalpy for a pair of successive particles in previous works, with $\eta_r(p) = h(r; p)$ [23, 25].

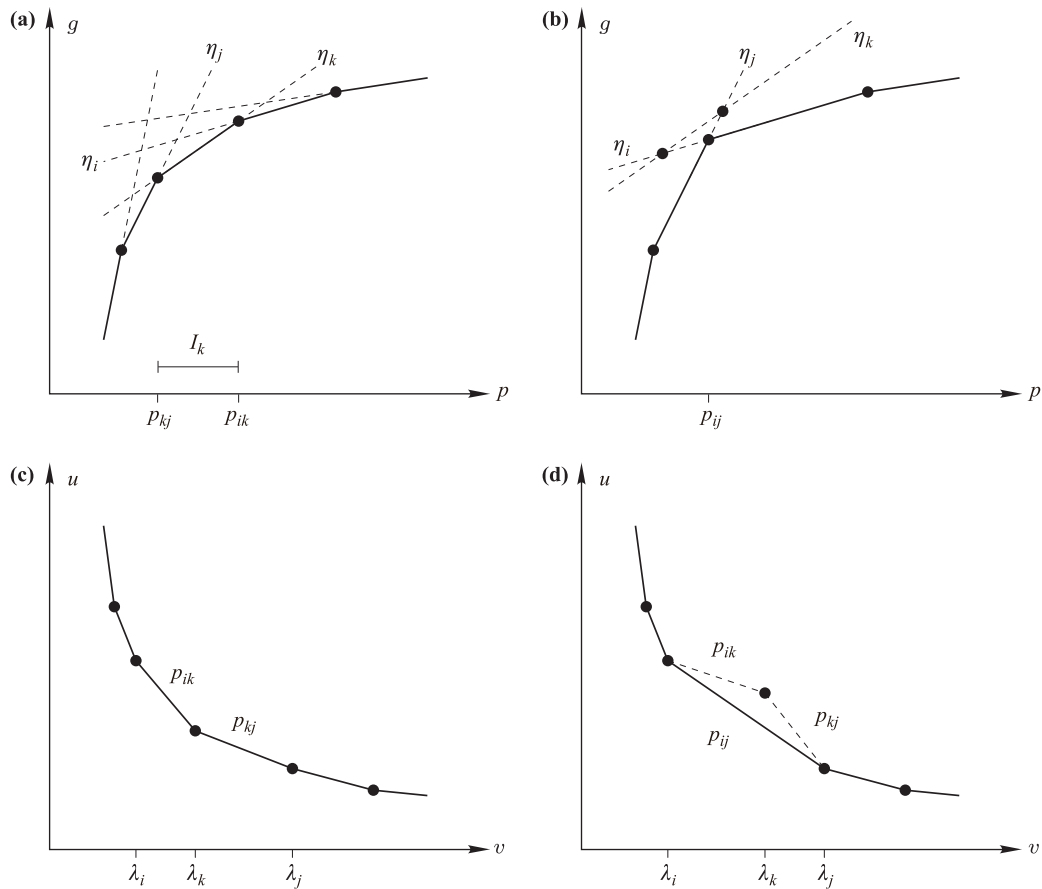


Fig. 6 Ground-state potentials $g = g(p)$ and $u = u(v)$ for the two scenarios described here.

As an application, we design a simple lattice gas model pair potential presenting five states in the ground state and four phase transitions between fluid phases.³⁾ The critical pressures are set to $p_{k,k+1} = 5 - k$, where the molecules in phase k are separated by k lattice sites. With this definition, the critical pressures are simply $\{p_{4,5} = 1, p_{3,4} = 2, p_{2,3} = 3, p_{1,2} = 4\}$, and a pair potential with this behavior can be found by starting with $u_5 = 0$ and recursively calculating u_k from Eq. (26). The resulting pair potential is shown in Fig. 7.

The pressure versus temperature phase diagram of the model is shown in Fig. 7, where ground-state phase transitions between different fluids are indicated by filled circles, at the expected pressures $p = 1, 2, 3, 4$, and a gas-liquid transition is indicated by a filled triangle at $p = 0$.

The TMD line is also shown in the upper right panel of Fig. 7. The TMD line emanates from each ground-state phase transition, creating four regions of negative thermal expansion coefficient, i.e., regions where the density anomalously increases with temperature at fixed pressure. Each TMD line reaches a maximum tempera-

ture and returns to a lower temperature, reaching the ground state at a pressure that is exactly between two critical points. The exact location for the endpoints of these TMD lines can be explained by the competing effects of contraction and expansion on the stable ground-state configuration (a similar calculation was described in Ref. [25]).

We finish discussing this example by investigating the behavior of thermal expansion as a function of pressure at fixed temperature. In the last panel of Fig. 7, α oscillates when crossing pressures near the critical value, indicating a relationship between phase transitions and density anomalies in one-dimensional systems. This result is consistent and was also found in other one-dimensional lattice models [24, 25], three-dimensional CS fluids [23], and the continuous one-dimensional systems investigated here.

5 Conclusions

In this paper, we obtained an exact solution for a family of one-dimensional potentials that are characterized by having N shoulders. The presence of one shoulder re-

³⁾For simplicity, neither the gas phase nor the liquid-gas phase transition are numbered.

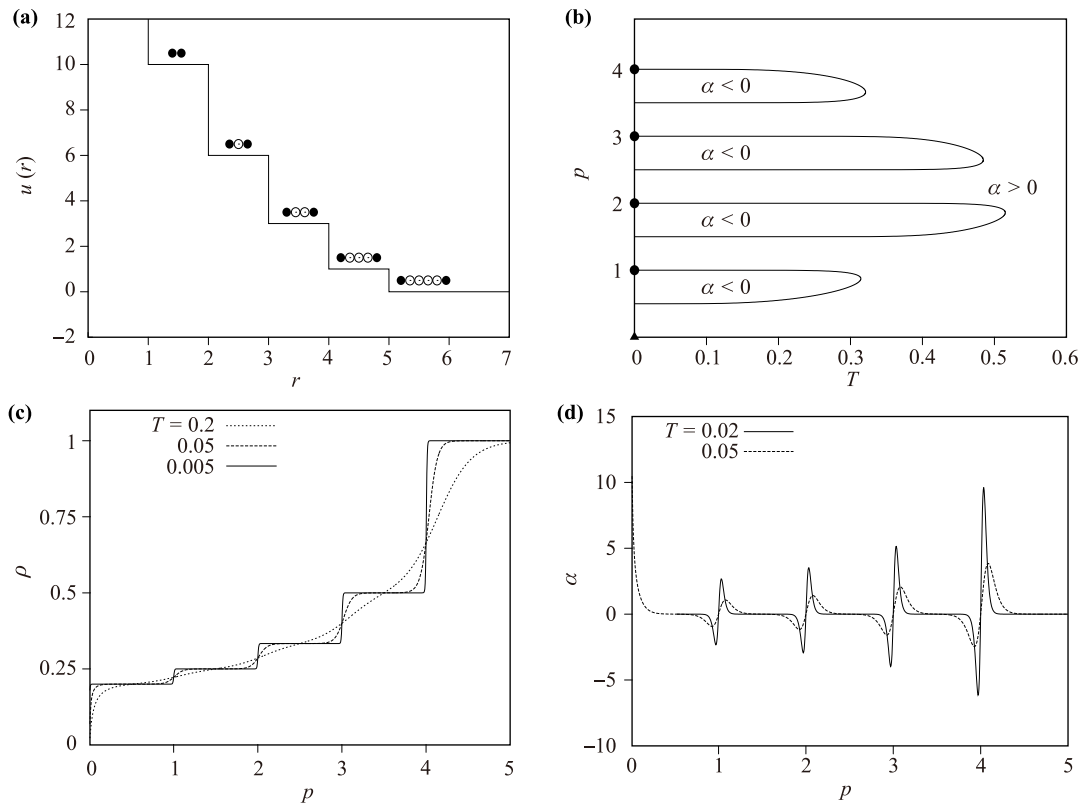


Fig. 7 (a) Pair potential exhibiting different phases, (b) pressure versus temperature phase diagram illustrating the TMD line, (c) density versus pressure for different temperatures, and (d) thermal expansion coefficient versus pressure for different temperatures.

sults in a density anomaly region in the pressure versus temperature phase diagram, and consequently, a zero-temperature liquid–liquid phase transition. The presence of two, three, \dots , N density anomaly regions for two, three, \dots , N shoulders occurs only if the pair potential forms a convex curve when the different length scales are connected.

The prediction in one dimension can be extrapolated to the three-dimensional case, and that for two shoulders results in the existence of two density anomaly regions and two liquid–liquid phase transitions [23].

References

1. P. C. Hemmer and G. Stell, Fluids with Several Phase Transitions, *Phys. Rev. Lett.* 24(23), 1284 (1970)
2. P. G. Debenedetti, V. S. Raghavan, and S. S. Borick, Spinodal curve of some supercooled liquids, *J. Chem. Phys.* 95(11), 4540 (1991)
3. S. Sastry, P. G. Debenedetti, F. Sciortino, and H. E. Stanley, Singularity-free interpretation of the thermodynamics of supercooled water, *Phys. Rev. E* 53(6), 6144 (1996)
4. C. J. Roberts and P. G. Debenedetti, Polyamorphism and density anomalies in network-forming fluids: Zeroth- and first-order approximations, *J. Chem. Phys.* 105(2), 658 (1996)
5. E. A. Jagla, Phase behavior of a system of particles with core collapse, *Phys. Rev. E* 58(2), 1478 (1998)
6. G. Franzese, G. Malescio, A. Skibinsky, S. V. Buldyrev, and H. E. Stanley, Generic mechanism for generating a liquid–liquid phase transition, *Nature* 409(6821), 692 (2001)
7. N. B. Wilding and J. E. Magee, Phase behavior and thermodynamic anomalies of core-softened fluids, *Phys. Rev. E* 66(3), 031509 (2002)
8. P. Camp, Structure and phase behavior of a two-dimensional system with core-softened and long-range repulsive interactions, *Phys. Rev. E* 68(6), 061506 (2003)
9. M. Pretti and C. Buzano, Thermodynamic anomalies in a lattice model of water, *J. Chem. Phys.* 121(23), 11856 (2004)
10. A. Balladares and M. C. Barbosa, Density anomaly in core-softened lattice gas, *J. Phys.: Condens. Matter* 16(49), 8811 (2004)

11. A. B. Oliveira and M. C. Barbosa, Density anomaly in a competing interactions lattice gas model, *J. Phys.: Condens. Matter* 17(3), 399 (2005)
12. Yu. D. Fomin, E. N. Tsiok, and V. N. Ryzhov, Complex phase behavior of the system of particles with smooth potential with repulsive shoulder and attractive well, *J. Chem. Phys.* 134(4), 044523 (2011)
13. G. S. Kell, Precise representation of volume properties of water at one atmosphere, *J. Chem. Eng. Data* 12(1), 66 (1967)
14. P. H. Poole, F. Sciortino, U. Essmann, and H. E. Stanley, Phase behaviour of metastable water, *Nature* 360(6402), 324 (1992)
15. J. C. Palmer, F. Martelli, Y. Liu, R. Car, A. Z. Panagiotopoulos, and P. G. Debenedetti, Metastable liquid-liquid transition in a molecular model of water, *Nature* 510(7505), 385 (2014)
16. A. Faraone, L. Liu, C. Y. Mou, C. W. Yen, and S. H. Chen, Fragile-to-strong liquid transition in deeply supercooled confined water, *J. Chem. Phys.* 121(22), 10843 (2004)
17. J. A. Sellberg, C. Huang, T. A. McQueen, N. D. Loh, H. Laksmono, et al., Ultrafast X-ray probing of water structure below the homogeneous ice nucleation temperature, *Nature* 510, 381 (2014)
18. H. Takahashi, *Mathematical Physics in One Dimension*, Academic Press, 1966, pp 25–34
19. G. Gallavotti, *Statistical Mechanics: A Short Treatise*, Berlin: Springer, 1999, pp 162–164
20. A. Barros de Oliveira, P. A. Netz, T. Colla, and M. C. Barbosa, Thermodynamic and dynamic anomalies for a three-dimensional isotropic core-softened potential, *J. Chem. Phys.* 124(8), 084505 (2006)
21. A. Barros de Oliveira, P. A. Netz, T. Colla, and M. C. Barbosa, Thermodynamic and dynamic anomalies for a three-dimensional isotropic core-softened potential, *J. Chem. Phys.* 124(8), 084505 (2006)
22. E. Barraz, Salcedo, and M. C. Barbosa, Thermodynamic, dynamic, and structural anomalies for shoulder-like potentials, *J. Chem. Phys.* 131(9), 094504 (2009)
23. M. A. A. Barbosa, E. Salcedo, and M. C. Barbosa, Multiple liquid-liquid critical points and density anomaly in core-softened potentials, *Phys. Rev. E* 87(3), 032303 (2013)
24. M. A. A. Barbosa, F. V. Barbosa, and F. A. Oliveira, Thermodynamic and dynamic anomalies in a one-dimensional lattice model of liquid water, *J. Chem. Phys.* 134(2), 024511 (2011)
25. F. B. V. da Silva, F. A. Oliveira, and M. A. A. Barbosa, Residual entropy and waterlike anomalies in the repulsive one dimensional lattice gas, *J. Chem. Phys.* 142(14), 144506 (2015)



Contents lists available at ScienceDirect

Physica A

journal homepage: www.elsevier.com/locate/physa

Waterlike anomalies in the Bose–Hubbard model

Eduardo Osório Rizzatti ^a, Márcio Sampaio Gomes Filho ^b, Mariana Malard ^c, Marco Aurélio A. Barbosa ^{c,*}^a Instituto de Física, Universidade Federal de do Rio Grande do Sul, Porto Alegre-RS, Brazil^b Instituto de Física, Universidade de Brasília, Brasília-DF, Brazil^c Programa de Pós-Graduação em Ciência de Materiais, Faculdade UnB Planaltina, Universidade de Brasília, Planaltina-DF, Brazil

HIGHLIGHTS

- Density anomalies are found in the atomic limit of the Bose–Hubbard model.
- In this limit the model presents an infinite number of ground state phase transitions between Mott-Insulator phases with commensurate occupation number.
- A temperature of maximum density (TMD) line emanate from each ground state transition.
- It is shown that residual entropies are connected to phase transitions and TMD lines.

ARTICLE INFO

Article history:

Received 29 August 2018

Received in revised form 29 November 2018

Available online 7 December 2018

Keywords:

Bose–Hubbard model

Density anomaly

Waterlike behavior

ABSTRACT

Although well-researched as a prototype Hamiltonian for strongly interacting quantum systems, the Bose–Hubbard model has not so far been explored as a fluid system with waterlike anomalies. In this work we show that this model supports, in the limit of a strongly localizing confining potential, density anomalies which can be traced back to ground state (zero-temperature) phase transitions between different Mott insulators.

© 2018 Elsevier B.V. All rights reserved.

1. Introduction

The Hubbard model [1,2] is of great interest in many areas of condensed matter physics and has been extensively investigated through a variety of methods for strongly interacting quantum systems [3,4]. In particular, the Bose–Hubbard model [5–9] regained attention since its realization with cold bosonic atoms trapped on optical lattices [10–13]. Indeed, such systems became a remarkable experimental arena for testing a myriad of theoretical concepts, playing the celebrated role of quantum simulators [14,15].

In parallel, water is relevant for many reasons including its abundance on Earth, its role on the chemistry of life and as a human resource [16,17]. It also possess particular physicochemical properties, including its high latent heat, diffusion and thermal response functions [16,18–24]. A striking property of water is the increase of density with temperature in the range from 0°C to 4°C, setting it apart from regular liquids [19]. In liquid water, the temperature of maximum density (TMD) decreases with pressure entering the metastable regime above 40 MPa [25,26], and is associated to a region with negative value of the thermal expansion coefficient. Water also presents anomalies in its structure which are connected to density and diffusion anomalies through the so-called hierarchy of anomalies [27–31].

* Corresponding author.

E-mail address: aureliobarbosa@unb.br (M.A.A. Barbosa).

Water and its anomalies were investigated by various models, from which we mention simplified lattice and core softened models. Among lattice models for water, it should be relevant to mention that waterlike anomalies were found for models of orientational bonding fluids in the triangular lattice, and on 3D simple cubic lattice, through a variety of techniques, varying from Bethe lattice [32], cluster variational method [33,34] and Monte Carlo simulations [35]. Core softened models were investigated using molecular dynamics simulations [36–38] and analytically through integral equations [39], being found that pair potentials with competing two scale can reproduce various anomalies including those on density, structure and diffusion.

According to the second critical point (SCP) hypothesis the high temperature thermodynamic and dynamic anomalous behavior of liquid water is attributed to the presence of a metastable liquid–liquid phase transition ending in a critical point [40,41]. The SCP hypothesis has been proposed from the observation of a liquid–liquid phase transition on computer simulations of the ST2 atomically detailed model of water [40], and was followed by extensive investigations on other models for water (see Ref. [22] for discussion). Similar transitions were also investigated in models for carbon [42], silicon [43], silica [44] and experimentally observed in phosphorus [45], triphenyl phosphite and n-butanol [46]. Although much debated in the literature [22,47], recent experiments with mixtures of water and glycerol [48] and measurements of correlations functions using time-resolved optical Kerr effect (OKE) of supercooled water [49] favor the SCP hypothesis.

The debate on the relation between water anomalies and phase transitions would be benefited if other experimental systems, such as quantum gases on optical lattices, could be shown to present anomalous behavior similar to liquid water, while associated with phase transitions. Such a comparison would be even more interesting if in certain regimes a limiting behavior could be approached, or extrapolated, in which a simple statistical mechanical description could be achieved. It is our opinion that the Bose–Hubbard model can be used for achieving this goal, since it can be “simulated” with quantum gases on optical lattices.

The purpose of this work is to investigate waterlike anomalous behavior on Bose–Hubbard model in the so-called “atomic limit” [1], where the hopping contribution to the Hamiltonian becomes vanishingly small. In this regime the Bose–Hubbard model turns into an analytically solvable toy model which, despite being simple, does present a rich waterlike phenomenology and, to our knowledge, is presented for the first time in this work. An study of waterlike behavior on the Bose–Hubbard Hamiltonian including hopping is outside the scope of this work and will be presented elsewhere. Our proposal is based on previous investigations which established a connection between ground state phase transitions (GSPT) and waterlike anomalies in the context of classical lattice and off-lattice models of fluids in one dimension [50–53].

This paper is organized as follows: the Bose–Hubbard model and its ground state in the atomic limit are analyzed in Section 2, the grand canonical partition function and relevant thermodynamic quantities are calculated in Section 3, with the detailed expressions for pressure and chemical potential left for the Appendix. Our results are discussed in Section 4 and the final remarks made in Section 5.

2. The Bose–Hubbard model and its grand canonical ground state

On its simplest realization, the Bose–Hubbard model consists of a lattice whose sites are empty or occupied by a certain number of particles and its hamiltonian presents terms for hopping ($J > 0$), chemical potential (μ), and the on site interaction disfavoring multiple occupation on the same site ($U > 0$). Creation and annihilation operators are defined as usual with symbols \hat{a}_i^\dagger and \hat{a}_i and the number operator on site i is $\hat{n}_i = \hat{a}_i^\dagger \hat{a}_i$. With these definitions this hamiltonian becomes [5]:

$$\hat{H} = - \sum_{\langle i,j \rangle} J \hat{a}_i^\dagger \hat{a}_j + \sum_i \frac{U}{2} \hat{n}_i (\hat{n}_i - 1) - \sum_i \mu \hat{n}_i, \quad (1)$$

where the first summation is performed over all pairs of nearest neighbor sites and the other two involve all sites in a system with size L .

Here we analyze the atomic limit by setting $J = 0$. With this choice, tunneling between different sites is forbidden and the superfluid phase, which is composed by particles in a delocalized state, does not exist but regions of waterlike anomalous density behavior can be observed in the regular fluid phase. In the context of quantum gases on optical traps this limit corresponds to a strong trapping field. Following this simplification the hamiltonian splits into single-site terms, \hat{H}_i , which are diagonalizable in the number operators vector space, $\hat{n}_i |n_i\rangle = n_i |n_i\rangle$. Hence, the energy eigenvalue of a single site with occupation $n_i = n$ becomes

$$\epsilon_n = \frac{U}{2} n(n - 1) - \mu n, \quad (2)$$

and, since lattice sites are *distinguishable*, quantum statistics end up identical to Boltzmann statistics [54].

We proceed by investigating the ground state. At $T = 0$ and a given μ , the grand canonical free energy $\Phi = V\phi$ (volume $V = v_0 L$, with v_0 defining the lattice cell volume) is simply the result of the minimization procedure $\phi(T = 0, \mu) = \min_n \epsilon_n$. Therefore, $\phi(T = 0, \mu) = \epsilon_n$ for n satisfying $(n - 1)U < \mu < nU$. This implies that GSPT occur whenever the chemical potential hits an integer value of the on site interaction, where a coexistence between successive occupation states n and $n + 1$, called Mott Insulators, takes place. This analysis yields the critical chemical potentials $\mu_n = nU$ and the corresponding critical pressures $P_n v_0 = n(n + 1) \frac{U}{2}$.

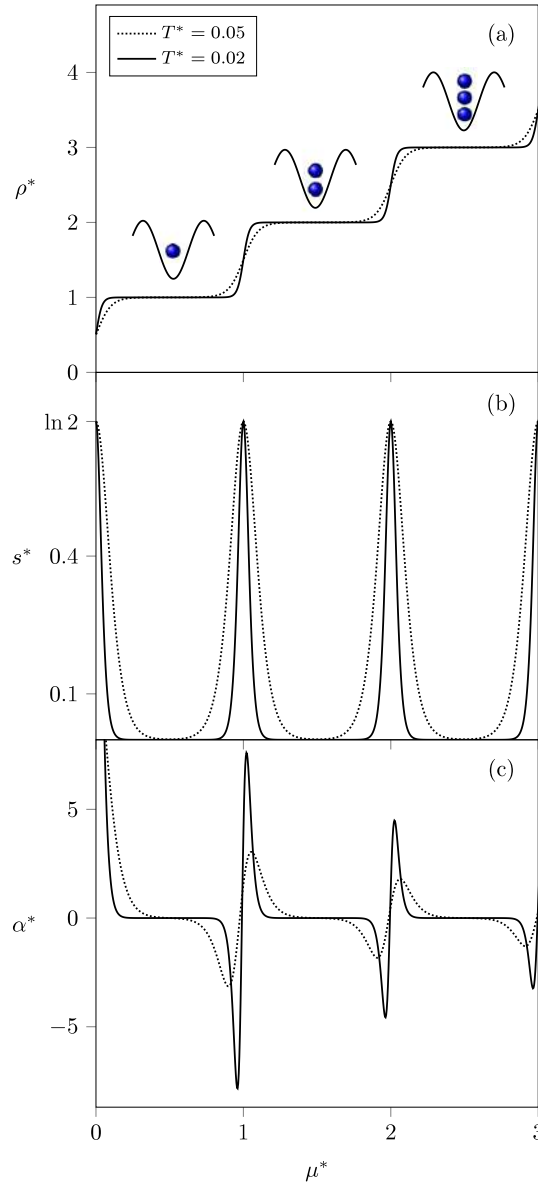


Fig. 1. (a) Density, (b) entropy, and (c) thermal expansion coefficient, as a function of the chemical potential at fixed temperatures.

Calculating densities in the GSPT at fixed chemical potential in the μVT ensemble is simple and requires assuming that states n and $n + 1$ are equal *a priori*. The result is $v_0 \rho_n = n + 1/2$, and will not be the same observed at fixed pressures in the NPT ensemble since the pressure is a non-differentiable function of μ at the GSPT. These numbers can be obtained exactly within a two states description, as will be explained in the [Appendix](#).

3. Thermodynamics

The grand canonical partition function of the system can be expressed as:

$$\Xi(T, V, \mu) = \left(\sum_{n=0}^{\infty} e^{-\beta \epsilon_n} \right)^L, \tag{3}$$

where $\beta = 1/k_B T$, with T being the temperature and k_B the Boltzmann constant. Considering that $\Xi = e^{-\beta \Phi}$ the fundamental relation for the grand thermodynamic potential Φ becomes:

$$\Phi(T, V, \mu) = -k_B T L \ln \left[\sum_{n=0}^{\infty} e^{-\beta \epsilon_n} \right]. \tag{4}$$

Pressure can be obtained using $\Phi = -PV$, and one can calculate density and entropy per site employing the standard expressions:

$$\rho(T, \mu) = \frac{N}{V} = -\frac{1}{V} \left(\frac{\partial \Phi}{\partial \mu} \right)_T, \quad (5)$$

and

$$s(T, \mu) = \frac{S}{V} = -\frac{1}{V} \left(\frac{\partial \Phi}{\partial T} \right)_\mu. \quad (6)$$

For the purpose of comparing our results with other works on the literature of the Bose–Hubbard model, it will be important to write the thermal expansion coefficient in terms of appropriate variables. Through a Jacobian transformation [55, p. 364] one obtains:

$$\begin{aligned} \alpha &= \frac{1}{V} \left(\frac{\partial V}{\partial T} \right)_{P,N} = -\frac{1}{\rho} \left(\frac{\partial \rho}{\partial T} \right)_P \\ &= \alpha_\mu + \frac{1}{\rho} \left(\frac{\partial \rho}{\partial \mu} \right)_T \frac{\left(\frac{\partial \Phi}{\partial T} \right)_\mu}{\left(\frac{\partial \Phi}{\partial \mu} \right)_T}, \end{aligned} \quad (7)$$

where α_μ was defined as:

$$\alpha_\mu(T, \mu) = -\frac{1}{\rho} \left(\frac{\partial \rho}{\partial T} \right)_\mu. \quad (8)$$

Expressions (5)–(8) will be calculated in the μVT ensemble and converted to the NPT ensemble whenever necessary.

4. Results and discussions

Before proceeding let us note that variables are reduced in terms of U , v_0 and k_B , as $T^* = k_B T/U$, $\mu^* = \mu/U$ and $P^* = P v_0/U$. Our analysis starts by comparing density, entropy and thermal expansion, α , as a function of chemical potential at fixed temperature (Fig. 1). Also note that α is the same used in the fluid literature and was calculated from (7). Fig. 1(a) shows that the density is highly sensitive to changes in the chemical potential around $\mu_n^* = n$, for integer n , and that this response becomes sharper at lower temperatures, approaching true phase transition discontinuities in the $T \rightarrow 0$ limit. This confirms that μ_n^* are indeed the critical values of the zero-temperature GSPT.

In Fig. 1(b) entropy is shown to develop maximum values exactly at the critical chemical potentials μ_n^* . As temperature decreases entropy goes to zero except at the transition points, where it becomes sharper and turn into a residual entropy in the limit $T \rightarrow 0$. Note that the maximum equals $s_n^* = \ln 2$, which is expected for a two state mixture. From the Maxwell relation

$$\left(\frac{\partial S}{\partial P} \right)_T = - \left(\frac{\partial V}{\partial T} \right)_P = -V\alpha, \quad (9)$$

it follows that α is negative (positive) whenever entropy increases (decreases) with pressure.¹ Thus, an entropy maximum introduces an oscillation in thermal expansion α , with its amplitude increasing as temperature is lowered according to Fig. 1(c). The oscillations evolve to a peculiar double divergence with $\alpha \rightarrow -\infty (+\infty)$ as $\mu \rightarrow \mu_n^- (\mu_n^+)$. Indeed, such mechanism establishes a quite general connection between GSPT, residual entropy and density anomaly. The multiple configurations remaining from each critical point produce a macroscopic zero point entropy. When temperature is raised, the possibility of the system accessing these states can induce an anomalous behavior depending on the chosen external fields.

Next we discuss the emergence of TMD lines on the phase diagram of the model. In Fig. 2 their *loci*, corresponding to $\alpha = 0$, are shown at pressures covering two regions where density increases with temperature ($\alpha < 0$). As in our previous studies [50,52], TMD lines are emanating from GSPT (filled circles) and draws a curve enclosing a region of the phase diagram starting and ending at $T = 0$. The endpoint of these lines can be obtained by analyzing enthalpy variations for adding or excluding a particle in the system. Even though we have chosen to show two TMD lines starting from transitions at $P_1^* = 1$ and 3, the model exhibits an infinite number of GSPT and also an infinite number of regions on the $P \times T$ phase diagram where $\alpha < 0$.

A more detailed view on the density behavior is presented in Fig. 3, where it is plotted against temperature at pressures slightly above, below and equal to the critical value $P_1^* = 1$. It is interesting to observe that density increases with temperature below P_1^* , reaching a maximum value and then decreasing again, while above P_1^* density decreases, as in a normal fluid. Exactly at P_1^* density reaches a fixed value at about the same temperature where the TMD line becomes

¹ The chemical potential monotonically increases with pressure.

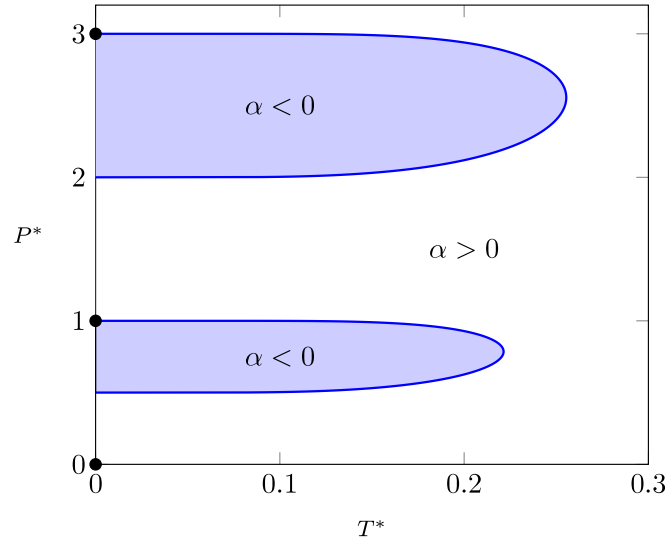


Fig. 2. Pressure vs. temperature phase diagram with GSPT marked with filled circles and continuous lines representing the TMD. The anomalous states are represented by the filled areas.

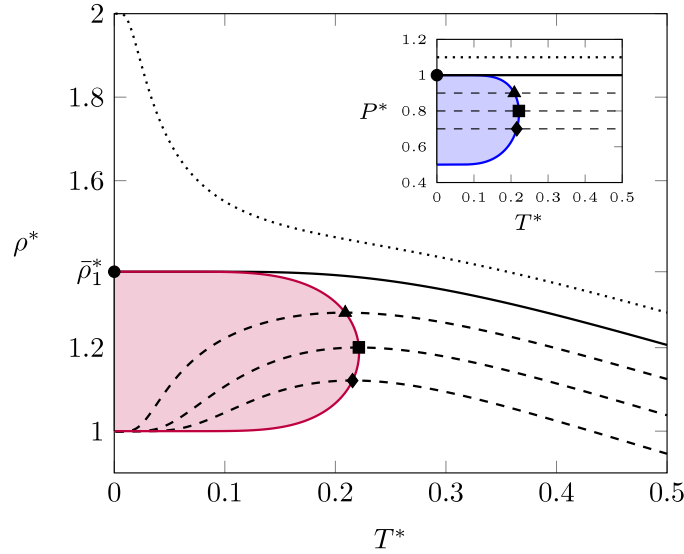


Fig. 3. Density as a function of temperature for fixed pressures. Density increases with temperature (filled region) and presents a maximum (filled symbols) for pressures slightly below (dashed lines) the critical pressure $P_1^* = 1$ (continuous black line). Density decreases monotonically with temperature for pressures above (dotted line) the critical value. The inset contains the $P \times T$ phase diagram featuring a TMD line and the pressures chosen.

horizontal in the $P \times T$ phase diagram (see the inset of Fig. 3). It is possible to calculate this value within a low temperature, two-states expansion (see Appendix), resulting in the polynomial:

$$(1 - 2\delta_n)^{n+1} = 2(1 + 2\delta_n)^n \tag{10}$$

where $\delta_n = \bar{\rho}_n^* - \rho_n^*$, with $\bar{\rho}_n^*$ ($\rho_n^* = n + 1/2$) being the critical density at fixed pressure (fixed chemical potential) for the n th transition. From this it is possible to find $\bar{\rho}_1^*$, the critical density at constant pressure for $n = 1$, as

$$\bar{\rho}_1^* = \frac{5 - \sqrt{5}}{2} \approx 1.381966. \tag{11}$$

Accordingly, the critical densities obtained from Eq. (10) are indeed relevant as they predict the maximum densities found along the TMD lines emanating from GSPT at critical pressures $P_n^* = n(n + 1)/2$.

Next, let us compare the low temperature aspects of α and α_μ by rewriting Eq. (7) as:

$$\rho(\alpha - \alpha_\mu) = \frac{s}{\rho} \left(\frac{\partial \rho}{\partial \mu} \right)_T.$$

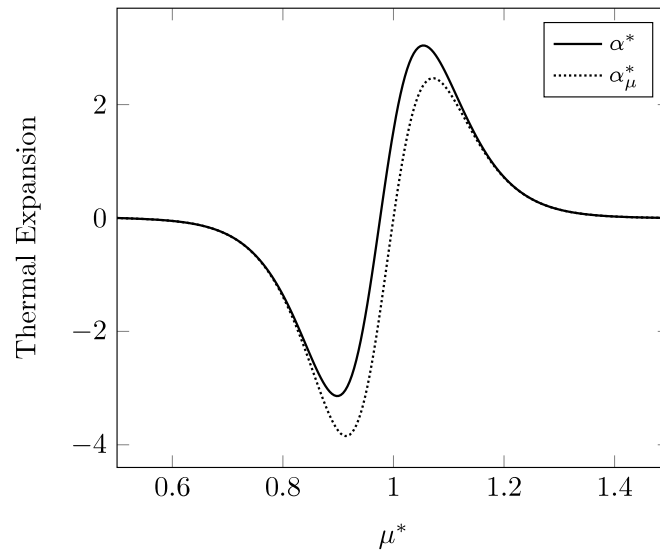


Fig. 4. Comparison between fixed pressure and fixed chemical potential thermal expansion coefficients, α^* and α_μ^* , as a function of chemical potential at temperature $T^* = 0.05$. At low temperature the behavior of both coefficients are similar (see text).

For sufficiently small temperatures, it follows from the r.h.s. of this expression that $\alpha \approx \alpha_\mu$ since $\lim_{T \rightarrow 0} s \rightarrow 0$, except at $\mu = \mu_n$. Consequently, α and α_μ are resembling functions at low temperatures, and $\alpha_\mu < 0$ can be used to infer a waterlike behavior in the *NPT* ensemble. As shown in Fig. 4, near the ground state phase transition between fluid phases with $n = 1$ and $n = 2$ particles (at $\mu_1^* = 1$), α_μ presents an oscillation similar to α , this being a signature of the proximity to the GSPT and waterlike behavior [52].

5. Conclusion

In this work waterlike volumetric anomalies were observed in the Bose–Hubbard model by considering the so-called atomic limit, where particle hopping across the lattice is strongly suppressed. In this case the model becomes analytically solvable since all lattice sites are disconnected and the hamiltonian becomes diagonal in the basis representing each site’s particle number. Ground state analysis captured transitions between Mott insulators with different fillings, *i.e.*, ground state phase transitions, with residual entropies taking place along each transition point.

The grand canonical partition function was calculated and density, entropy, and thermal expansion coefficient (at fixed pressure) were shown to behave anomalously in certain regions of the phase diagram. It was found that TMD lines were emerging from GSPT, being associated to residual entropy occurring on these transitions. These findings points towards a connection between phase transitions, residual entropies and density anomalies, and how these effects come together to produce an oscillatory thermal expansion coefficient, a hypothesis that was explored in previous works [50–53]. It was demonstrated that at low temperatures the thermal expansion coefficient α is approximately equal to α_μ , and that the oscillatory behavior can be observed in both. This fact should be helpful, as it allows to identify regions where waterlike anomalies are expected to happen in the *NPT* ensemble while looking at the behavior of α_μ in μVT ensemble at low temperatures.

The fact that the atomic limit of the Bose–Hubbard model presents waterlike behavior allows us to question whether the Bose–Hubbard model (with hopping term), and the real systems represented by this hamiltonian, can also present such phenomenology; what is the relation between the hopping term and temperature of maximum density, and how the emergence of the superfluid phase fits in the simplified scenario presented here. We advance that these questions have been investigated in the Bose–Hubbard model with small J/U using standard mean field approaches and more elaborate quantum statistical techniques (manuscript submitted).

Acknowledgments

We acknowledge useful discussions with Marcia Barbosa. This work has been supported by the Brazilian funding agencies FAPDF, CNPq and CAPES (Brazil).

Appendix. Two-states approximation and the critical densities

Near the GSPT between configurations with occupation numbers n and $n + 1$ the grand canonical free energy can be approximated by

$$\Phi \approx -\frac{1}{\beta} \ln \left(e^{-\beta\epsilon_n} + e^{-\beta\epsilon_{n+1}} \right)^L, \quad (\text{A.1})$$

from which we calculate pressure as

$$Pv_0 \approx -\frac{\epsilon_n + \epsilon_{n+1}}{2} + \frac{1}{\beta} \ln \left\{ 2 \cosh \left[\frac{\beta(\epsilon_n - \epsilon_{n+1})}{2} \right] \right\}. \quad (\text{A.2})$$

Now we define $\Delta P = P - P_n$ and $\Delta\mu = \mu - \mu_n$ to rewrite

$$\Delta Pv_0 = \left(n + \frac{1}{2} \right) \Delta\mu + \frac{1}{\beta} \ln \left[2 \cosh \left(\frac{\beta\Delta\mu}{2} \right) \right], \quad (\text{A.3})$$

and calculate

$$\rho v_0 = \left(n + \frac{1}{2} \right) + \tanh \left(\frac{\beta\Delta\mu}{2} \right). \quad (\text{A.4})$$

By inverting Eq. (A.4) it is possible to obtain

$$e^{\beta\Delta P^*} (1 - 2\delta_n)^{n+1} = 2(1 + 2\delta_n)^n, \quad (\text{A.5})$$

with $\delta_n = \bar{\rho}_n^* - \rho_n^*$ as defined above. At the critical pressure $\Delta P^* = 0$ and Eq. (10) is recovered. The case $n = 1$ leads to the second order polynomial


$$4\delta_1^2 - 8\delta_1 - 1 = 0, \quad (\text{A.6})$$

whose physically viable solution is $\delta_1 = (2 - \sqrt{5})/2$, resulting in $\bar{\rho}_1^* = (5 - \sqrt{5})/2$, as discussed in Section 4. The values of the critical densities for arbitrary n can be calculated numerically from Eq. (10). These solutions have the property $\lim_{n \rightarrow \infty} \delta_n = 0$, meaning that in this limit critical densities become identical when calculated at fixed μ and fixed P .

References

- [1] J. Hubbard, Electron correlations in narrow energy bands, Proc. R. Soc. Lond. Ser. A Math. Phys. Eng. Sci. 276 (1365) (1963) 238–257, <http://dx.doi.org/10.1098/rspa.1963.0204>.
- [2] M.C. Gutzwiller, Effect of correlation on the ferromagnetism of transition metals, Phys. Rev. Lett. 10 (5) (1963) 159–162, <http://dx.doi.org/10.1103/PhysRevLett.10.159>.
- [3] D. Jaksch, P. Zoller, The cold atom Hubbard toolbox, Ann. Physics 315 (1) (2005) 52–79, <http://dx.doi.org/10.1016/j.aop.2004.09.010>.
- [4] O. Dutta, M. Gajda, P. Hauke, M. Lewenstein, D.-S. Lühmann, B.A. Malomed, T. Sowiński, J. Zakrzewski, Non-standard Hubbard models in optical lattices: a review, Rep. Progr. Phys. 78 (6) (2015) 066001, <http://dx.doi.org/10.1088/0034-4885/78/6/066001>.
- [5] M.P.A. Fisher, P.B. Weichman, G. Grinstein, D.S. Fisher, Boson localization and the superfluid-insulator transition, Phys. Rev. B 40 (1) (1989) 546–570, <http://dx.doi.org/10.1103/PhysRevB.40.546>.
- [6] K. Sheshadri, H.R. Krishnamurthy, R. Pandit, T.V. Ramakrishnan, Superfluid and insulating phases in an interacting-Boson model: Mean-field theory and the RPA, Europhys. Lett. 22 (4) (1993) 257–263, <http://dx.doi.org/10.1209/0295-5075/22/4/004>.
- [7] J.K. Freericks, H. Monien, Phase diagram of the Bose-Hubbard Model, Europhys. Lett. 26 (7) (1994) 545–550, <http://dx.doi.org/10.1209/0295-5075/26/7/012>.
- [8] D. Jaksch, C. Bruder, J.J. Cirac, C.W. Gardiner, P. Zoller, Cold bosonic atoms in optical lattices, Phys. Rev. Lett. 81 (15) (1998) 3108–3111, <http://dx.doi.org/10.1103/PhysRevLett.81.3108>.
- [9] K.V. Krutitsky, Ultracold bosons with short-range interaction in regular optical lattices, Phys. Rep. 607 (2016) 1–101, <http://dx.doi.org/10.1016/j.physrep.2015.10.004>.
- [10] M. Greiner, O. Mandel, T. Esslinger, T.W. Hänsch, I. Bloch, Quantum phase transition from a superfluid to a Mott insulator in a gas of ultracold atoms, Nature 415 (6867) (2002) 39–44, <http://dx.doi.org/10.1038/415039a>.
- [11] I. Bloch, Quantum gases in optical lattices, Phys. World 17 (4) (2004) 25–29, <http://dx.doi.org/10.1088/2058-7058/17/4/32>.
- [12] I. Bloch, Ultracold quantum gases in optical lattices, Nat. Phys. 1 (1) (2005) 23–30, <http://dx.doi.org/10.1038/nphys138>.
- [13] P. Windpassinger, K. Sengstock, Engineering novel optical lattices, Rep. Progr. Phys. 76 (8) (2013) 086401, <http://dx.doi.org/10.1088/0034-4885/76/8/086401>.
- [14] M. Lewenstein, A. Sanpera, V. Ahufinger, B. Damski, A. Sen(De), U. Sen, Ultracold atomic gases in optical lattices: mimicking condensed matter physics and beyond, Adv. Phys. 56 (2) (2007) 243–379, <http://dx.doi.org/10.1080/00018730701223200>.
- [15] I. Bloch, J. Dalibard, S. Nascimbène, Quantum simulations with ultracold quantum gases, Nat. Phys. 8 (4) (2012) 267–276, <http://dx.doi.org/10.1038/nphys2259>.
- [16] E. Brini, C.J. Fennell, M. Fernandez-Serra, B. Hribar-Lee, M. Lukšič, K.A. Dill, How Water's Properties are encoded in its molecular structure and energies, Chem. Rev. 117 (19) (2017) 12385–12414, <http://dx.doi.org/10.1021/acs.chemrev.7b00259>.
- [17] F. Franks, Water: A Matrix of Life, Royal Society of Chemistry, Cambridge, 2000, <http://dx.doi.org/10.1039/9781847552341>.
- [18] P.G. Debenedetti, Supercooled and glassy water, J. Phys.: Condens. Matter 15 (2003) 1669.
- [19] D.S. Eisenberg, W. Kauzmann, The structure and properties of water, vol. 166, Oxford University Press, Oxford, 2005, p. 861.

- [20] D. Nayar, C. Chakravarty, Water and water-like liquids: relationships between structure, entropy and mobility, *Phys. Chem. Chem. Phys.* 15 (34) (2013) 14162–14177.
- [21] P. Netz, F. Starr, H. Stanley, M.C. Barbosa, Static and dynamic properties of stretched water, *J. Chem. Phys.* 115 (2001) 344.
- [22] P. Gallo, K. Amann-Winkel, C.A. Angell, M.A. Anisimov, F. Caupin, C. Chakravarty, E. Lascaris, T. Loerting, A.Z. Panagiotopoulos, J. Russo, J.A. Sellberg, H.E. Stanley, H. Tanaka, C. Vega, L. Xu, L.G.M. Pettersson, Water: A tale of two liquids, *Chem. Rev.* 116 (13) (2016) 7463–7500, <http://dx.doi.org/10.1021/acs.chemrev.5b00750>.
- [23] P.A. Netz, F.W. Starr, H.E. Stanley, M.C. Barbosa, Static and dynamic properties of stretched water, *J. Chem. Phys.* 115 (1) (2001) 344–348, <http://dx.doi.org/10.1063/1.1376424>.
- [24] P. Netz, F. Starr, M. Barbosa, H. Stanley, Translational and rotational diffusion in stretched water, *J. Molecular Liquids* 101 (1–3) (2002) 159–168, [http://dx.doi.org/10.1016/S0167-7322\(02\)00090-9](http://dx.doi.org/10.1016/S0167-7322(02)00090-9).
- [25] C.A. Angell, H. Kanno, Density maxima in high-pressure supercooled water and liquid silicon dioxide, *Science* 193 (4258) (1976) 1121–1122, <http://dx.doi.org/10.1126/science.193.4258.1121>.
- [26] D.R. Caldwell, The maximum density points of pure and saline water, *Deep-Sea Res.* 25 (2) (1978) 175–181, [http://dx.doi.org/10.1016/0146-6291\(78\)90005-X](http://dx.doi.org/10.1016/0146-6291(78)90005-X).
- [27] J.R. Errington, P.G. Debenedetti, Relationship between structural order and the anomalies of liquid water, *Nature* 409 (6818) (2001) 318–321, <http://dx.doi.org/10.1038/35053024>.
- [28] Y.D. Fomin, V.N. Ryzhov, B.A. Klumov, E.N. Tsiok, How to quantify structural anomalies in fluids?, *J. Chem. Phys.* 141 (3) (2014) 034508, <http://dx.doi.org/10.1063/1.4890211>.
- [29] N.V. Gribova, Y.D. Fomin, D. Frenkel, V.N. Ryzhov, Waterlike thermodynamic anomalies in a repulsive-shoulder potential system, *Phys. Rev. E* 79 (5) (2009) 051202, <http://dx.doi.org/10.1103/PhysRevE.79.051202>.
- [30] Y.D. Fomin, E.N. Tsiok, V.N. Ryzhov, Silicalike sequence of anomalies in core-softened systems, *Phys. Rev. E* 87 (4) (2013) 042122, <http://dx.doi.org/10.1103/PhysRevE.87.042122>.
- [31] Y.D. Fomin, E.N. Tsiok, V.N. Ryzhov, Inversion of sequence of diffusion and density anomalies in core-softened systems, *J. Chem. Phys.* 135 (23) (2011) 234502, <http://dx.doi.org/10.1063/1.3668313>.
- [32] M.A.A. Barbosa, V.B. Henriques, Frustration and anomalous behavior in the Bell-Lavis model of liquid water, *Phys. Rev. E* 77 (5) (2008) 051204, <http://dx.doi.org/10.1103/PhysRevE.77.051204>.
- [33] C. Buzano, E. De Stefanis, M. Pretti, Cluster-variation approximation for a network-forming lattice-fluid model, *J. Chem. Phys.* 129 (2) (2008) 024506, <http://dx.doi.org/10.1063/1.2919126>.
- [34] M. Pretti, C. Buzano, Thermodynamic anomalies in a lattice model of water, *J. Chem. Phys.* 121 (23) (2004) 11856–11866, <http://dx.doi.org/10.1063/1.1817924>.
- [35] V.B. Henriques, M.C. Barbosa, Liquid polymorphism and density anomaly in a lattice gas model, *Phys. Rev. E* 71 (3) (2005) 031504, <http://dx.doi.org/10.1103/PhysRevE.71.031504>.
- [36] A.B. de Oliveira, P.A. Netz, M.C. Barbosa, An ubiquitous mechanism for water-like anomalies, *Europhys. Lett.* 85 (3) (2009) 36001, <http://dx.doi.org/10.1209/0295-5075/85/36001>.
- [37] A.B. de Oliveira, P.A. Netz, T. Colla, M.C. Barbosa, Structural anomalies for a three dimensional isotropic core-softened potential, *J. Chem. Phys.* 125 (12) (2006) 124503, <http://dx.doi.org/10.1063/1.2357119>.
- [38] A. Barros de Oliveira, P.A. Netz, T. Colla, M.C. Barbosa, Thermodynamic and dynamic anomalies for a three-dimensional isotropic core-softened potential, *J. Chem. Phys.* 124 (8) (2006) 084505, <http://dx.doi.org/10.1063/1.2168458>.
- [39] E. Lomba, N.G. Almarza, C. Martín, C. McBride, Phase behavior of attractive and repulsive ramp fluids: Integral equation and computer simulation studies, *J. Chem. Phys.* 126 (24) (2007) 244510, <http://dx.doi.org/10.1063/1.2748043>.
- [40] P.H. Poole, F. Sciortino, U. Essmann, H.E. Stanley, Phase behaviour of metastable water, *Nature* 360 (6402) (1992) 324–328, <http://dx.doi.org/10.1038/360324a0>.
- [41] H.E. Stanley, P. Kumar, G. Franzese, L. Xu, Z. Yan, M.G. Mazza, S.V. Buldyrev, S.-H. Chen, F. Mallamace, Liquid polymorphism: Possible relation to the anomalous behaviour of water, *Eur. Phys. J. Spec. Top.* 161 (1) (2008) 1–17, <http://dx.doi.org/10.1140/epjst/e2008-00746-3>.
- [42] J.N. Glosli, F.H. Ree, Liquid-liquid phase transformation in carbon, *Phys. Rev. Lett.* 82 (23) (1999) 4659–4662, <http://dx.doi.org/10.1103/PhysRevLett.82.4659>.
- [43] S. Sastry, C. Austen Angell, Liquid-liquid phase transition in supercooled silicon, *Nature Mater.* 2 (11) (2003) 739–743, <http://dx.doi.org/10.1038/nmat994>.
- [44] I. Saika-Voivod, F. Sciortino, T. Grande, P. Poole, Simulated silica, *Phil. Trans. R. Soc. A* 363 (1827) (2005) 525–535, <http://dx.doi.org/10.1098/rsta.2004.1506>.
- [45] G. Monaco, S. Falconi, W. Crichton, M. Mezouar, Nature of the first-order phase transition in fluid phosphorus at high temperature and pressure, *Phys. Rev. Lett.* 90 (25) (2003) 255701, <http://dx.doi.org/10.1103/PhysRevLett.90.255701>.
- [46] R. Kurita, H. Tanaka, On the abundance and general nature of the liquid-liquid phase transition in molecular systems, *J. Phys.: Condens. Matter* 17 (27) (2005) L293–L302, <http://dx.doi.org/10.1088/0953-8984/17/27/L01>.
- [47] D.T. Limmer, D. Chandler, The putative liquid-liquid transition is a liquid-solid transition in atomistic models of water. II, *J. Chem. Phys.* 138 (21) (2013) 214504, <http://dx.doi.org/10.1063/1.4807479>.
- [48] K.-I. Murata, H. Tanaka, General nature of liquid-liquid transition in aqueous organic solutions, *Nature Commun.* 4 (1) (2013) 2844, <http://dx.doi.org/10.1038/ncomms3844>.
- [49] A. Taschin, P. Bartolini, R. Eramo, R. Righini, R. Torre, Evidence of two distinct local structures of water from ambient to supercooled conditions, *Nature Commun.* 4 (2013) 1–8, <http://dx.doi.org/10.1038/ncomms3401>.
- [50] M.A.A. Barbosa, F.V. Barbosa, F.A. Oliveira, Thermodynamic and dynamic anomalies in a one-dimensional lattice model of liquid water, *J. Chem. Phys.* 134 (2011) 24511.
- [51] M.A.A. Barbosa, E. Salcedo, M.C. Barbosa, Multiple liquid-liquid critical points and density anomaly in core-softened potentials, *Phys. Rev. E* 87 (3) (2013) 032303, <http://dx.doi.org/10.1103/PhysRevE.87.032303>.
- [52] F.B.V. da Silva, F.A. Oliveira, M.A.A. Barbosa, Residual entropy and waterlike anomalies in the repulsive one dimensional lattice gas, *J. Chem. Phys.* 142 (144506) (2015).
- [53] E.O. Rizzatti, M.A.A. Barbosa, M.C. Barbosa, Core-softened potentials, multiple liquid-liquid critical points, and density anomaly regions: An exact solution, *Front. Phys.* 13 (1) (2018) 136102, <http://dx.doi.org/10.1007/s11467-017-0725-3>.
- [54] R.E. Wilde, S. Singh, *Statistical Mechanics: Fundamentals and Modern Applications*, Wiley, 1997.
- [55] S.R. Salinas, *Introduction to Statistical Physics*, Springer-Verlag, New York, 2001.

Quantum density anomaly in optically trapped ultracold gasesEduardo O. Rizzatti ^{1,*} Marco Aurélio A. Barbosa,² and Marcia C. Barbosa¹¹*Instituto de Física, Universidade Federal do Rio Grande do Sul, Porto Alegre-RS, Brazil*²*Programa de Pós-Graduação em Ciência de Materiais, Universidade de Brasília, Planaltina-DF, Brazil*

(Received 26 April 2019; accepted 20 July 2020; published 22 September 2020)

Water, the substance of life, is known for its myriad of anomalous properties, whose origins are still the subject of intense debates. In order to provide a different insight into this problem, we show how its density anomaly can be reproduced using a quantum simulator. In particular, we demonstrate that the Bose-Hubbard model, a paradigm system in quantum mechanics, exhibits an increase in density with temperature at fixed pressure in the regular fluid regime and in the superfluid phase. We propose that the mechanism underlying the anomalies is related to zero-point entropies and ground-state phase transitions. A connection with the typical experimental scales and setups including confinement effects is also addressed. In this scenario, such finding opens a pathway for theoretical and experimental studies of waterlike anomalies in the area of ultracold quantum gases.

DOI: [10.1103/PhysRevA.102.033331](https://doi.org/10.1103/PhysRevA.102.033331)**I. INTRODUCTION**

The experimental realization of the Bose-Einstein condensation [1,2] inaugurated a new era in physics by merging different areas, from condensed matter [3,4] to quantum information [5,6]. This landmark provided grounds for new applications involving the manipulation of ultracold atoms, from which optical lattices, literal crystal arrays of light trapping neutral cold atoms [7,8], stand as a prominent one. Among these applications, systems known as quantum simulators [9,10] have attained great importance since they can be used to experimentally implement and simulate scenarios for a plethora of theoretical ideas [11,12]. Indeed, it is possible to engineer them in highly controllable ways in regards to parameters such as dimensionality, lattice structure, composition, and atomic interactions [13]. In a theoretical level, the Bose-Hubbard model can be considered as a true prototype system, currently used to investigate quantum phase transitions, quantum coherence, and quantum computation [14–16].

In this work we theoretically show that the density of bosons in optical lattices, described by the Bose-Hubbard model, anomalously increases with temperature at fixed pressure in both superfluid and normal fluid regimes. Such counterintuitive behavior, usually denominated as *density anomaly*, according to our analysis occurs at temperatures below 1.8 nK (superfluid) and 14.8 nK (normal fluid) for rubidium-87 atoms trapped in a simple cubic optical lattice. These anomalies are similar to those presented by liquid water between 0 and 4 °C at 1 atm [17,18] and are useful to test the concept that thermodynamic waterlike anomalies arise from the competition between two scales of interaction, associated with critical phenomena. In a quantum-mechanical context such anomaly has also been reported experimentally for liquid helium [19,20]. The advantage exhibited by the optical lattice environment is the possibility to control and tune the interactions between particles, enabling a clear analysis regarding possible physical mechanisms.

An explanation for the thermodynamic and dynamic anomalous behavior of liquid water has been disputed through different thermodynamic scenarios. In the second critical point (SCP) hypothesis, which is based on computer simulations of the ST2 atomically detailed model of water [21], followed by extensive investigations on other models for water [22], the apparent divergence of thermodynamic response functions in a metastable region is a consequence of a metastable liquid-liquid phase transition ending in a critical point [21,23]. Nevertheless, this behavior in the case of water was never observed experimentally. The liquid-liquid transitions were reported in models for carbon [24], silicon [25], and silica [26], and experimentally observed in phosphorus [27], triphenyl phosphite, and n-butanol [28]. More recently, experiments with mixtures of water and glycerol [29] and measurements of correlation functions using time-resolved optical Kerr effect (OKE) of supercooled water [30] favor the SCP hypothesis, despite debates in literature [22,31].

The suggested connection between thermodynamic anomalies and criticality in water is difficult to test experimentally since the system freezes before reaching the critical temperature. In addition, the complexity of the water structure makes it difficult to unveil the relation between the microscopic interactions, thermodynamic anomalies, and criticality. Due to its experimental manageability and for being numerically treatable, we propose using the Bose-Hubbard model as a platform to establish this connection. In such context, we explore simple cubic and square geometries, constructed by sets of orthogonal, counterpropagating laser beams of wavelength λ . The resultant standing waves determine the scenario for the interacting bosons, an optical potential of the form

$$V_L(\mathbf{r}) = V_0 \sum_{i=1}^d \sin^2\left(\frac{\pi x_i}{a}\right), \quad (1)$$

where $a = \lambda/2$ is the lattice spacing, V_0 is the depth of the optical potential, and d represents the dimensionality of our system with coordination number $z = 2d$. Our theoretical calculations are based on the bosonic self-energy functional

*eduardo.rizzatti@ufrgs.br

theory [32], which generates results numerically close to quantum Monte Carlo [33] and bosonic dynamical mean-field theory (BDMFT) techniques.

The paper is organized as follows. First, we introduce the model and its relevant parameters in Sec. II. The theoretical methods employed are explained in Sec. III, with greater details given in the Appendix. The density anomaly in simple cubic and square lattice geometries is discussed in Sec. IV and a mechanism involving residual entropies is proposed in Sec. V for the reported phenomenon. In Sec. VI, we discuss how the anomaly could be experimentally observed based on 2D *in situ* imaging of the atoms. Final considerations are addressed in Sec. VII.

II. BOSE-HUBBARD MODEL

The dynamics of itinerant bosons in a lattice occupying the lowest-energy band is governed by the Bose-Hubbard Hamiltonian [14,16]

$$H = -J \sum_{(i,j)} b_i^\dagger b_j + \frac{U}{2} \sum_i n_i(n_i - 1) - \mu \sum_i n_i, \quad (2)$$

where b_i^\dagger , b_i , and n_i designate the bosonic creation, annihilation, and number operators at site i , respectively; μ is the chemical potential.

The parameter U represents the (typically repulsive) interaction of bosons on the same lattice site. More precisely, it corresponds to the atom-atom s -wave scattering process, which can be regarded as an effective contact interaction of the form $U(\mathbf{r}) = g\delta(\mathbf{r})$, with a coupling constant $g = 4\pi\hbar^2 a_s/m$ depending on the s -wave scattering length a_s and mass m of the atoms. By employing the local Wannier states $w(\mathbf{r})$, the term U is expressed through the matrix element

$$U = g \int d\mathbf{r} |w(\mathbf{r})|^4. \quad (3)$$

On the other hand, the parameter J indicates the hopping amplitude, a kinetic term involving the probability of tunneling between first neighbor sites. Explicitly, it is quantified as the following overlapping integral over adjacent Wannier functions:

$$J = - \int d\mathbf{r} w(\mathbf{r} - \mathbf{r}_i) \left(-\hbar^2 \frac{\nabla^2}{2m} + V_L(\mathbf{r}) \right) w(\mathbf{r} - \mathbf{r}_j). \quad (4)$$

Therefore, the Bose-Hubbard model terms U and J can be related to the experimental parameters λ , a_s , and V_0 through Eqs. (3) and (4) [34], numerically calculating the band structure and obtaining the Wannier states [35,36]. These prescriptions allow us to express temperatures in kelvin units and the lattice depth in terms of the recoil energy $E_r = \hbar^2\pi^2/2ma^2$, according to the values of U and J chosen. It is thus possible to consider our theoretical results within the context of a specific optical trap implementation, from which we select a gas of rubidium-87 atoms in simple cubic [7,8] and square optical lattices [37,38].

III. METHODOLOGY

In order to map the thermodynamics of the bosons we employ a variational and nonperturbative self-consistent ap-

proach, the self-energy functional theory derived by Hügel *et al.* [32], inspired in the original works for fermions by Potthoff [39]. The formalism, which includes U(1) symmetry breaking and comprehends previous BDMFT approaches [40–43], is based on successive Legendre transformations of the free-energy functional Ω leading to a new functional Ω_{SE} of the self-energies. The approximation scheme to the many-body problem constricts the variational space: the self-energy domain is restricted to a subspace of self-energies of a simpler reference system. Then, the original problem is transformed into determining stationary solutions of this new functional in terms of the reference system's free propagators. This section is devoted to providing an overview of the method, following Refs. [32,44,45].

First, we write the Hamiltonian of Eq. (2) in a more concise and general form,

$$H = \frac{1}{2} \mathbf{b}_\alpha^\dagger \mathbf{t}_\beta^\alpha \mathbf{b}^\beta + \mathcal{V} + \mathbf{F}_\alpha^\dagger \mathbf{b}^\alpha, \quad (5)$$

including an explicit symmetry breaking field \mathbf{F} which couples to the bosonic operators. In this notation, we use the Einstein summation convention and the superindex α spans the site index i as well as the Nambu index ν . Explicitly, the bosonic operator reads as $\mathbf{b}_\alpha^\dagger \equiv \mathbf{b}_{i\nu}^\dagger = (b_i^\dagger, b_i)_\nu$, with commutation relations $[\mathbf{b}_\alpha, \mathbf{b}_\beta^\dagger] = (\mathbf{1} \otimes \sigma_z)_\beta^\alpha$. Also, we have the generalized hopping $\mathbf{t}_\beta^\alpha = \mathbf{t}_{j\nu}^{\alpha} = t_{ij} \otimes \mathbf{1}_{\eta\nu}$ and interaction of the form $\mathcal{V} = U_{\alpha\beta\gamma\delta} \mathbf{b}^\alpha \mathbf{b}^\beta \mathbf{b}^\gamma \mathbf{b}^\delta$.

Including finite-temperature effects (with $k_B T = 1/\beta$), the partition function $\mathcal{Z} = \text{Tr}[\mathcal{T} e^{-S}]$ follows as a trace comprising the imaginary time-ordered exponential of the action \mathcal{S} [46–48],

$$\begin{aligned} \mathcal{S}[\mathbf{F}, \mathbf{G}_0^{-1}] = & -\frac{1}{2} \int_0^\beta \int_0^\beta d\tau d\tau' \mathbf{b}^\dagger(\tau) \mathbf{G}_0^{-1}(\tau, \tau') \mathbf{b}(\tau') \\ & + \int_0^\beta d\tau \mathcal{V}[\mathbf{b}(\tau)] + \int_0^\beta d\tau \mathbf{F}^\dagger \mathbf{b}(\tau), \end{aligned} \quad (6)$$

written according to its explicit dependence on \mathbf{F} and the noninteracting Green's function \mathbf{G}_0 :

$$\mathbf{G}_0^{-1} = \delta(\tau - \tau') (-[\mathbf{1} \otimes \sigma_z] \partial_{\tau'} - \mathbf{t}). \quad (7)$$

From the partition function, averages can be defined as $\langle O(\tau) \rangle = \text{Tr}[\mathcal{T} e^{-S} O(\tau)]/\mathcal{Z}$. Also, its logarithm provides the free energy $\Omega[\mathbf{F}, \mathbf{G}_0^{-1}] = -\ln[\mathcal{Z}]/\beta$, which is a generating functional of the propagators: the condensate Green's function Φ ,

$$\beta \frac{\delta \Omega}{\delta \mathbf{F}^\dagger} = \langle \mathbf{b} \rangle \equiv \Phi, \quad (8)$$

and the connected interacting Green's function \mathbf{G} ,

$$2\beta \frac{\delta \Omega}{\delta \mathbf{G}_0^{-1}} = -\langle \mathbf{b}(\tau) \mathbf{b}^\dagger(\tau') \rangle \equiv \mathbf{G}(\tau, \tau') - \Phi \Phi^\dagger. \quad (9)$$

Further details regarding products and traces are addressed in Appendixes A and B.

Based on a Legendre transformation, the free-energy functional dependence can be exchanged from \mathbf{F} and \mathbf{G}_0^{-1} to the dressed propagators Φ and \mathbf{G} , leading to the Baym-Kadanoff

functional [49–52]

$$\beta\Omega_{\text{BK}}[\Phi, \mathbf{G}] = \mathbf{F}^\dagger \Phi - \frac{1}{2} \Phi^\dagger \mathbf{G}_0^{-1} \Phi + \frac{1}{2} \text{Tr} [\mathbf{G}_0^{-1} \mathbf{G}] + \frac{1}{2} \text{Tr} \ln[-\mathbf{G}^{-1}] + \Phi_{\text{LW}}[\Phi, \mathbf{G}]. \quad (10)$$

In Eq. (10), $\Phi_{\text{LW}}[\Phi, \mathbf{G}]$ is the Luttinger-Ward functional [53,54], a universal contribution which encompasses the complexity of the many-body system, containing all two-particle irreducible (2PI) diagrams [55,56]. At the physical solution, the functional $\Omega_{\text{BK}}[\Phi, \mathbf{G}]$ is stationary,

$$\frac{\delta\Omega_{\text{BK}}}{\delta\Phi^\dagger} = 0, \quad \frac{\delta\Omega_{\text{BK}}}{\delta\mathbf{G}} = 0, \quad (11)$$

and it is equal to the equilibrium free energy $\Omega_{\text{BK}} = \Omega$. The variations,

$$\beta \frac{\delta\Omega_{\text{BK}}}{\delta\Phi^\dagger} = \mathbf{F} - \mathbf{G}_0^{-1} \Phi + \frac{\delta\Phi_{\text{LW}}}{\delta\Phi^\dagger} \quad (12)$$

and

$$2\beta \frac{\delta\Omega_{\text{BK}}}{\delta\mathbf{G}} = \mathbf{G}_0^{-1} - \mathbf{G}^{-1} + 2 \frac{\delta\Phi_{\text{LW}}}{\delta\mathbf{G}}, \quad (13)$$

associated to the conditions of Eq. (11) lead to the following identification:

$$\Sigma_{1/2} = -\frac{\delta\Phi_{\text{LW}}}{\delta\Phi^\dagger}, \quad \Sigma = -2 \frac{\delta\Phi_{\text{LW}}}{\delta\mathbf{G}}, \quad (14)$$

where $\Sigma_{1/2}$ and Σ are the one- and two-point self-energies, respectively. Therefore, the propagators obey the Dyson equations

$$\mathbf{G}_0^{-1} \Phi = \mathbf{F} - \Sigma_{1/2} \quad (15)$$

and

$$\mathbf{G}^{-1} = \mathbf{G}_0^{-1} - \Sigma. \quad (16)$$

With another Legendre transform, the Baym-Kadanoff functional dependence can be exchanged from the one- and two-point propagators Φ and \mathbf{G} to their respective self-energies $\Sigma_{1/2}$ and Σ , yielding the self-energy functional

$$\beta\Omega_{\text{SE}}[\Sigma_{1/2}, \Sigma] = \frac{1}{2} (\mathbf{F} - \Sigma_{1/2})^\dagger \mathbf{G}_0 (\mathbf{F} - \Sigma_{1/2}) + \frac{1}{2} \text{Tr} \ln[-(\mathbf{G}_0^{-1} - \Sigma)] + \mathcal{F}[\Sigma_{1/2}, \Sigma]. \quad (17)$$

The universal functional $\mathcal{F}[\Sigma_{1/2}, \Sigma] = \Phi_{\text{LW}}[\Phi, \mathbf{G}] + \Sigma_{1/2}^\dagger \Phi + \frac{1}{2} \text{Tr}[\Sigma \mathbf{G}]$ is simply the Legendre transform of the Luttinger-Ward functional $\Phi_{\text{LW}}[\Phi, \mathbf{G}]$, with the following variations:

$$\frac{\delta\mathcal{F}}{\delta\Sigma_{1/2}^\dagger} = \Phi, \quad 2 \frac{\delta\mathcal{F}}{\delta\Sigma} = \mathbf{G}. \quad (18)$$

At the physical solution, Ω_{SE} is stationary and equal to the free energy $\Omega_{\text{SE}} = \Omega_{\text{BK}} = \Omega$ (as a result of Ω , Ω_{BK} , and Ω_{SE} being connected by successive Legendre transforms), yielding once again the Dyson equations

$$0 = \beta \frac{\delta\Omega_{\text{SE}}}{\delta\Sigma_{1/2}^\dagger} = -\mathbf{G}_0 (\mathbf{F} - \Sigma_{1/2}) + \Phi \quad (19)$$

and

$$0 = 2\beta \frac{\delta\Omega_{\text{SE}}}{\delta\Sigma} = -(\mathbf{G}_0^{-1} - \Sigma)^{-1} + \mathbf{G}. \quad (20)$$

The mentioned universality of the functional \mathcal{F} enables us to overcome its complexity with the introduction of an exactly solvable reference system (denoted by primed quantities) exhibiting the same symmetry and interactions as the original one. According to Eq. (17), the reference system's self-energy functional

$$\beta\Omega'_{\text{SE}}[\Sigma'_{1/2}, \Sigma'] = \frac{1}{2} (\mathbf{F}' - \Sigma'_{1/2})^\dagger \mathbf{G}'_0 (\mathbf{F}' - \Sigma'_{1/2}) + \frac{1}{2} \text{Tr} \ln[-(\mathbf{G}'_0^{-1} - \Sigma')] + \mathcal{F}'[\Sigma'_{1/2}, \Sigma'] \quad (21)$$

evaluated at the physical solutions $\Sigma_{1/2} = \Sigma'_{1/2}$ and $\Sigma = \Sigma'$ is equal to the reference system's free energy $\Omega'_{\text{SE}}[\Sigma'_{1/2}, \Sigma'] = \Omega'[\mathbf{F}', \mathbf{G}'_0^{-1}]$. Subtracting Eq. (21) from Eq. (17), Ω_{SE} evaluated at $\Sigma_{1/2} = \Sigma'_{1/2}$ and $\Sigma = \Sigma'$ becomes

$$\beta\Omega_{\text{SE}}[\Sigma'_{1/2}, \Sigma'] = \beta\Omega' + \frac{1}{2} (\mathbf{F} - \Sigma'_{1/2})^\dagger \mathbf{G}_0 (\mathbf{F} - \Sigma'_{1/2}) - \frac{1}{2} (\mathbf{F}' - \Sigma'_{1/2})^\dagger \mathbf{G}'_0 (\mathbf{F}' - \Sigma'_{1/2}) + \frac{1}{2} \text{Tr} \ln \left[\frac{\mathbf{G}_0^{-1} - \Sigma'}{\mathbf{G}'_0^{-1} - \Sigma'} \right]. \quad (22)$$

Therefore, the solution of the reference system provides a parametrization of the self-energies in terms of \mathbf{F}' and \mathbf{G}'_0^{-1} , which allows for the construction of the self-energy functional theory approximation Ω_{SFT} to the self-energy functional Ω_{SE} according to

$$\Omega_{\text{SFT}}[\mathbf{F}', \mathbf{G}'_0^{-1}] = \Omega_{\text{SE}}[\Sigma'_{1/2}[\mathbf{F}', \mathbf{G}'_0^{-1}], \Sigma'[\mathbf{F}', \mathbf{G}'_0^{-1}]]. \quad (23)$$

The approximation consists in constraining the variational principle to the subspace of self-energies of the reference system; this procedure applied to the variations of Eqs. (19) and (20) yields the Euler equations $\delta_{\mathbf{F}'} \Omega_{\text{SFT}} = 0$ and $\delta_{\mathbf{G}'_0^{-1}} \Omega_{\text{SFT}} = 0$.

In particular, we choose a local reference system, the SFA3 minimal construction [32], comprehending three variational parameters: the U(1) symmetry breaking linear field F' conjugated to the creation b^\dagger and annihilation b operators, the two fields Δ_{00} , coupled with the density $b^\dagger b$, and Δ_{01} , conjugated to pair creation $b^\dagger b^\dagger$ and pair annihilation bb operators. The Hamiltonian describing the bosonic state is given by

$$H'[\mathbf{F}', \Delta] = \frac{1}{2} \mathbf{b}^\dagger \Delta \mathbf{b} + \frac{U}{2} n(n-1) - \mu n + \mathbf{F}'^\dagger \mathbf{b}, \quad (24)$$

where $\mathbf{b} = (b, b^\dagger)$, $\mathbf{F}' = (F', F'^*)$, and $\Delta = \Delta_{00} \mathbf{1} + \Delta_{01} \sigma_x$.

Therefore, the states of thermodynamic equilibrium are determined by the stationary points of Ω_{SFT} , given by $\nabla \Omega_{\text{SFT}}[F, \Delta_{00}, \Delta_{01}] = 0$ (or $\delta_{\mathbf{F}'} \Omega_{\text{SFT}} = 0$ and $\delta_{\Delta} \Omega_{\text{SFT}} = 0$). The functional can be evaluated according to the following steps, which are completely developed throughout the Appendix sections. Given the parameters F' , Δ_{00} , and Δ_{01} , the Hamiltonian of Eq. (24) is determined. From Appendix C, the reference system's partition function and free energy are computed through Eqs. (C1) and (C2), followed by its one- and two-point propagators of Eqs. (C3) and (C5), and the self-energies according to the Dyson Eqs. (C7) and (C8). The next step is to calculate the lattice system's one- and two-point propagators by using Eqs. (D4) and (D3), respectively. These

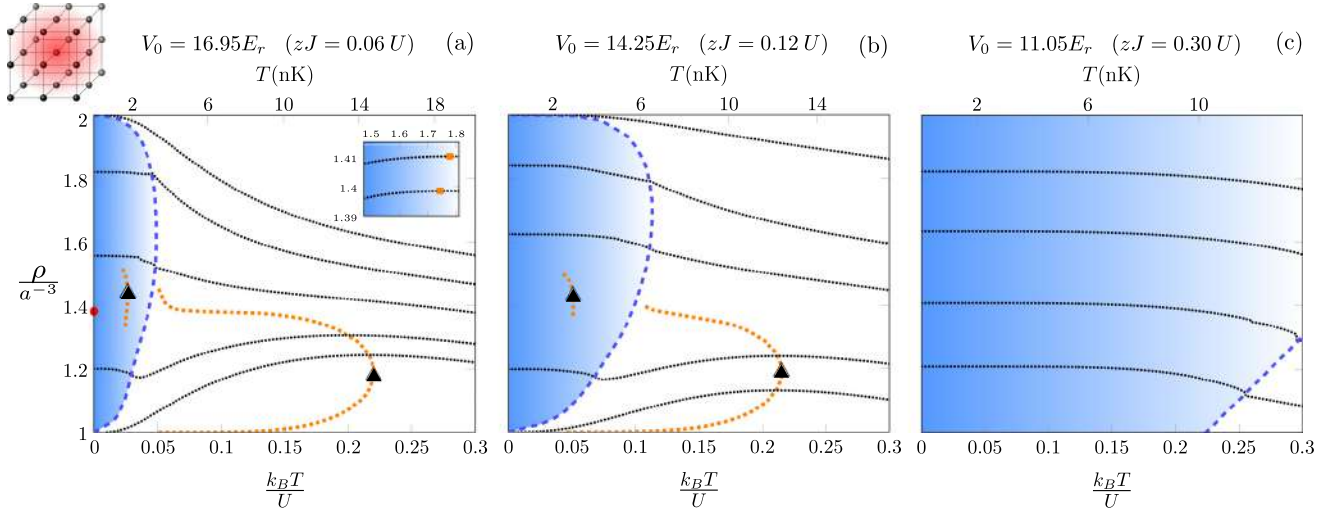


FIG. 1. Density ρ as a function of the reduced temperature $k_B T/U$ (bottom) and the temperature T in nanokelvin units (top) at fixed pressures for hopping amplitudes: (a) $zJ = 0.06U$, (b) $zJ = 0.12U$, and (c) $zJ = 0.30U$, considering a simple cubic lattice ($z = 6$). The superfluid phase is highlighted in blue, while the normal phase is portrayed in white. Blue dashed lines denote the boundaries between superfluid and normal phases, while orange dotted lines represent the TMD curves. In (a), the inset exhibits a zoom of isobaric curves in the superfluid phase, while the red point signals the atomic limit critical point at $T = 0$. The triangular points denote the maximum temperatures reached by each TMD curve.

products and the logarithmic trace $\text{Tr} \ln[\mathbf{G}'\mathbf{G}^{-1}]$ are determined following the prescriptions presented in Appendixes A and B, respectively. By collecting the required terms in Eq. (22), the desired self-energy functional is evaluated and its stationary points can be determined. The code employed in our calculations is available in the Supplemental Material [57].

IV. DENSITY ANOMALY

From the equilibrium free energy $\Omega = \Omega_{\text{SFT}}$ calculated previously, the density is given by

$$\rho = -\frac{1}{V} \left(\frac{\partial \Omega}{\partial \mu} \right)_T, \quad (25)$$

where $V = N_s a^d$ is the volume and N_s is the number of lattice sites. Its temperature dependence at fixed pressure P is determined by the isobaric thermal expansion coefficient

$$\alpha = -\frac{1}{\rho} \left(\frac{\partial \rho}{\partial T} \right)_P. \quad (26)$$

For $\alpha < 0$, density increases with temperature and a region of anomalous density behavior is identified by a temperature of maximum density (TMD) line defined as $\alpha = 0$. The pressure is fixed employing the Gibbs-Duhem relation $dP = \rho d\mu + s dT = 0$, where $s = -\frac{1}{V} \left(\frac{\partial \Omega}{\partial T} \right)_\mu$ is the entropy density and P is related to the grand-canonical potential according to $-PV = \Omega = \Omega_{\text{SFT}}$.

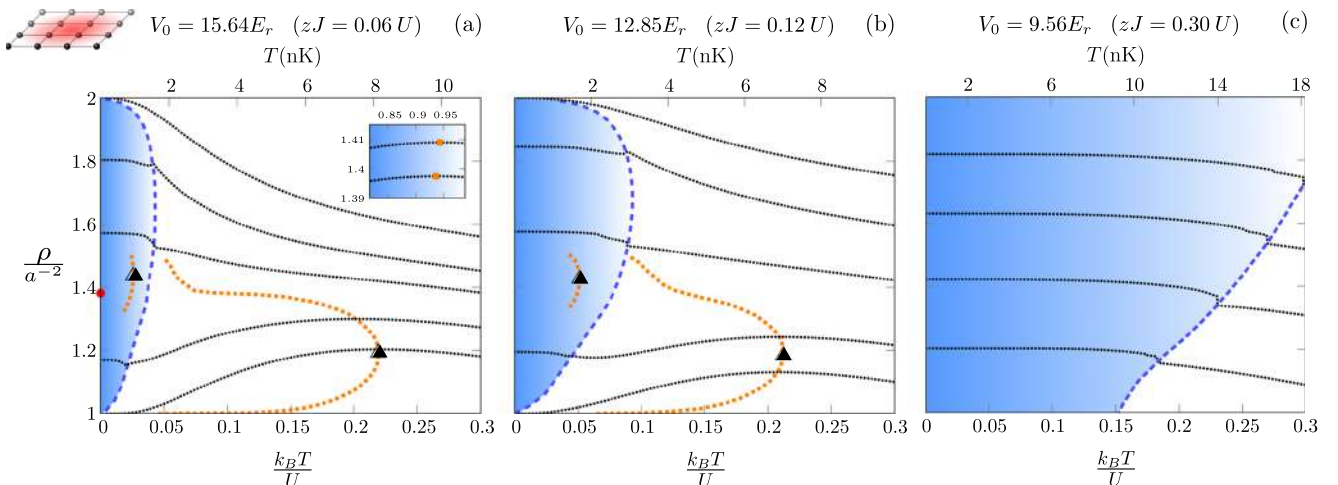


FIG. 2. Density ρ as a function of the reduced temperature $k_B T/U$ (bottom) and the temperature T in nanokelvin units (top) at fixed pressures for hopping amplitudes: (a) $zJ = 0.06U$, (b) $zJ = 0.12U$, and (c) $zJ = 0.30U$, considering a square lattice ($z = 4$).

TABLE I. Experimental parameters regarding potential depths V_0 , scattering length a_s , and laser wavelengths λ of optical lattices implemented using different alkali-metal elements, for the hopping amplitudes $zJ = 0.06U$ and $zJ = 0.12U$. The maximum temperatures in which density anomalies are observed in superfluid T_{SF} and normal phases T_{NA} (the highlighted triangular points in Fig. 1 and Fig. 2) are also addressed. In the 2D scenarios, the vertical confinement is achieved by an optical potential along the z axis. For rubidium-87 [38] the lattice depth is $V_{0,z} = 26E_r$, while the cesium-133 [58] atoms are confined in a Gaussian wave packet of width $a_z = 0.30 \mu\text{m}$.

Element	Geometry	λ (nm)	a_s (a_0)	$zJ = 0.06U$			$zJ = 0.12U$		
				V_0/E_r	T_{NA} (nK)	T_{SA} (nK)	V_0/E_r	T_{NA} (nK)	T_{SA} (nK)
^{23}Na [59]	Simple cubic ($z = 6$)	595	52	18.30	88.35	10.68	15.49	74.67	17.82
^{87}Rb [7]	Simple cubic ($z = 6$)	852	103	16.95	14.76	1.78	14.25	12.39	2.95
^{87}Rb [38]	Square ($z = 4$)	1064	103	15.64	8.13	0.95	12.85	7.00	1.69
^{133}Cs [58]	Square ($z = 4$)	1064	310	16.65	4.36	0.51	13.77	3.77	0.91

Considering a simple cubic lattice, with $z = 6$, Figs. 1(a)–1(c) illustrate the density ρ versus the reduced temperature $k_B T/U$ at fixed pressures (represented as black lines) for increasing hopping amplitudes: (a) $zJ = 0.06U$, (b) $zJ = 0.12U$, and (c) $zJ = 0.30U$. The corresponding potential depths, which decrease from (a) to (c), and temperature scales in nanokelvin units are calculated considering atoms of rubidium-87, with realistic values based on the experiments performed by Greiner *et al.* [7]. The superfluid to normal phase boundary is illustrated as a reentrant dashed blue line and the blue filled area represents the superfluid phase. Figures 1(a) and 1(b) show that at sufficient high values of V_0 (low values of zJ/U) there are two regions in which density presents a local maximum, with the TMD curves represented as orange dots: one at the normal phase [normal phase anomaly (NA)] and another at the superfluid phase [superfluid phase anomaly (SA)]. The maximum temperature values reached by the TMD curves are highlighted as triangular black points.

Figure 1(a) portrays a large area in the density versus temperature phase diagrams where the NA is present. However, as the hopping increases, according to Fig. 1(b), the anomaly occupies a smaller region in temperatures. In addition to the normal phase TMD, the superfluid phase also exhibits a density anomalous behavior illustrated in Fig. 1(a), with a few superfluid isobaric densities drawn in the inset. When the hopping becomes larger it dominates the free energy, leading the superfluid to occupy a bigger region in the phase diagram and suppressing both superfluid and normal anomalies, as presented in Fig. 1(c).

Analogously, Fig. 2 displays the two-dimensional results considering a square lattice geometry, with $z = 4$. For comparison reasons, we chose the same ratios zJ/U as shown in Fig. 1. The superfluid domain exhibits a small retraction when compared to the simple cubic case. In spite of this, the same general behavior is observed. Specifically, Fig. 2(a) presents the density anomaly in both phases; the anomaly is reduced for a larger hopping amplitude as illustrated in Fig. 2(b) and finally it vanishes completely as shown in Fig. 2(c). For this two-dimensional system, the respective potential depths and temperature scales in nanokelvin units are calculated also considering atoms of rubidium-87, with parameters according to the experiments performed by Sherson *et al.* [38].

Although the upper temperature scales and potential depths addressed in Figs. 1 and 2 refer to specific setups using

rubidium-87, they can be adapted to other elements. Indeed, we collect in Table I the temperatures, T_{SA} and T_{NA} , that must be achieved for experimentally detecting SA and NA not only for the previous cases of rubidium-87 but also for sodium-23 [59] (in a simple cubic lattice) and cesium-133 [58,60,61] (in a square lattice). These points are marked as the triangular symbols over the TMD curves.

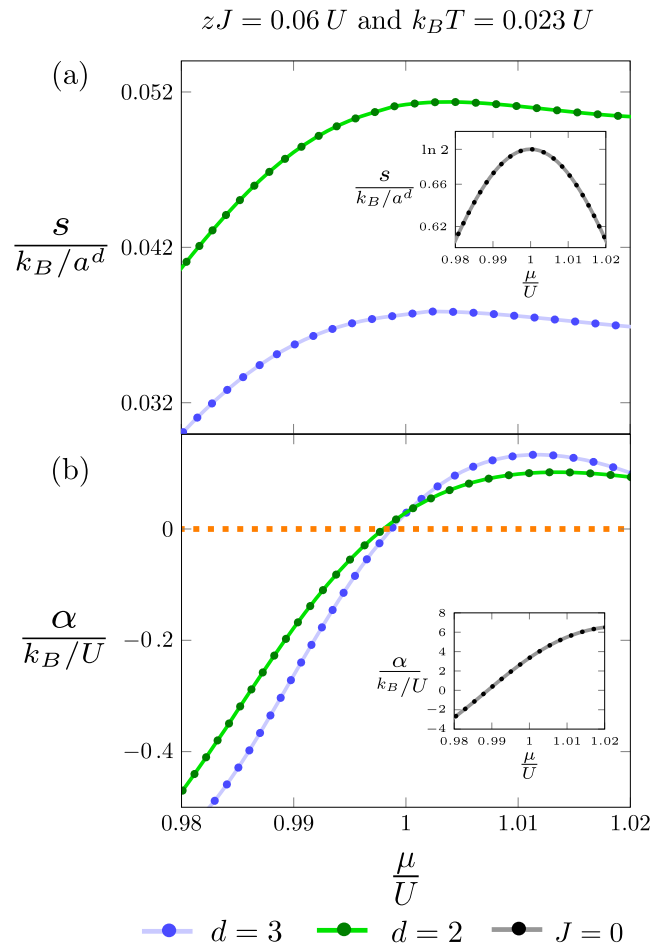


FIG. 3. Considering square ($d = 2$) and simple cubic ($d = 3$) lattices, the entropy (a) and thermal expansion coefficient (b) are exhibited as functions of the chemical potential μ for $zJ = 0.06U$ at $k_B T = 0.023U$ deep in the superfluid regime. The respective insets depict the atomic limit ($J = 0$) scenario.

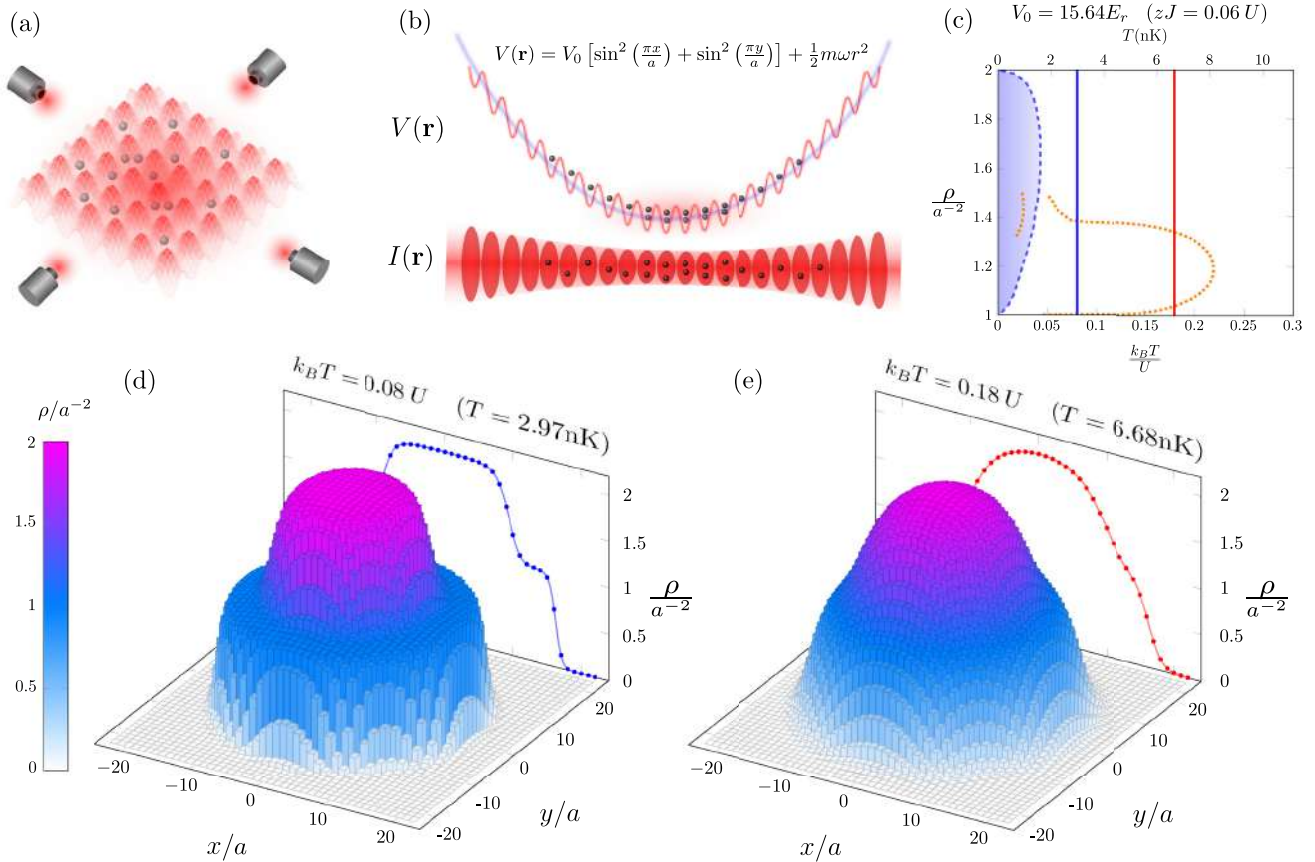


FIG. 4. Density distribution in the normal phase, considering harmonic confinement effects. (a) The two-dimensional configuration of a square optical lattice is created by counterpropagating red detuned laser beams. The additional harmonic effects are represented in (b), where the optical potential $V(\mathbf{r})$ and the intensity profile $I(\mathbf{r})$ are schematically shown. (c) The phase diagram ρ versus T for the configuration $V_0 = 15.64E_r$ ($zJ = 0.06U$) highlights two chosen temperatures $k_B T = 0.08U$ (blue) and $k_B T = 0.18U$ (red). Considering the LDA scenario, the density ρ is mapped in the xy plane for the respective temperatures in (d) and (e).

V. RESIDUAL ENTROPY MECHANISM

The density anomalies in the normal fluid can be traced back to the ground-state phase transitions between Mott insulators of successive occupation numbers [62]. This anomalous behavior, present even in the absence of hopping, arises from the competition between the chemical potential, which promotes the boson occupation in the lattice, with the on-site repulsion interaction U , which favors the boson removal. As the temperature increases, entropy first favors filling up the sites but, for high enough temperatures, entropy increases by removing particles from the system to increase the mobility of the particles left. This is a classical behavior similar to that of liquid water, where bonding and nonbonding structures compete: at lower temperatures density increases by disrupting hydrogen bonds, while at higher temperatures enhanced particles' velocities increase the available volume, decreasing density. The difference here is that this phase is not completely destroyed by the hopping, persisting for values of the J possible to be observed experimentally.

Indeed, the hopping brings another phenomenon not observed for $J = 0$: the SA, a quantum density anomaly. The physical origin of this behavior is also the competition between chemical potential and the repulsion U . But for the

SA the TMD line appears at lower temperatures and higher densities when compared with the NA, because in this case the hopping contributes to the temperature effects, favoring the movement and the spread of particle over the lattice.

Such competition of interaction scales can also be translated in terms of degeneracies and residual entropies. Inhibiting the hopping, a ground-state degeneracy, related to a phase transition in number occupation between Mott insulators, is settled whenever the chemical potential μ reaches an integer value of the interaction U . At such transition points, two states are equally accessible and this degeneracy accounts for an observed macroscopic residual entropy of $k_B \ln 2$ per site. For finite temperatures, these entropies develop into peaks near those points as the chemical potential is varied; see the inset of Fig. 3(a). By turning on the tunneling probability adiabatically the superfluid phase emerges exactly from Mott insulator transition points, mitigating residual entropies, since the previous degeneracy gets lifted. Thus, for a finite hopping transition, the mentioned entropy maxima remain deep in the superfluid phase but are less prominent, as shown in Fig. 3(a) for $zJ = 0.06U$ and $k_B T = 0.023U$. Formally, the entropy peaks mark a change in the behavior of density with temperature according to the Maxwell

relation

$$\left(\frac{\partial s}{\partial \mu}\right)_T = \left(\frac{\partial \rho}{\partial T}\right)_\mu = -\rho \alpha_\mu, \quad (27)$$

which results in the sign flip of thermal expansion in the superfluid phase illustrated in Fig. 3(b).

VI. 2D *IN SITU* OBSERVATION INCLUDING CONFINEMENT EFFECTS

On the basis of the recently developed *in situ* measurements of ultracold gases in optical lattices [63], we discuss a physical realization of the reported phenomenon considering rubidium-87 atoms disposed in a square lattice, as Fig. 4(a) depicts. These modern tools encompass high resolution absorption [58,61], fluorescence imaging [37,38], and even scanning electron microscopy [64], each technique with its specific applications. Considering the range of density and fluctuations presented here, our theoretical proposal appears better suited to the absorption imaging realized by Chin *et al.* [58,61], complementing the well-known time-of-flight methods which probe the system in momentum space. In such experimental framework, *in situ* density distributions $\rho(x, y)$ of 2D gases can be determined by performing absorption imaging perpendicular to the horizontal plane xy . This technique allows for mapping the occupation number at a single site resolution, providing direct access to density fluctuations, which is our ultimate goal in the analysis of the anomaly.

In our discussion, the confinement effects of the harmonic trapping field, represented in Fig. 4(b), are considered using a local density approximation (LDA). The harmonic confinement potential is given by $V_h(r) = \frac{1}{2}m\omega^2 r^2$, where $r = \sqrt{x^2 + y^2}$ is the radial distance from the center of the trap and the associated oscillation frequency ω is fixed at $\omega/2\pi = 60$ Hz, as typically chosen. Consequently, in the LDA framework the chemical potential across the lattice takes the form $\mu(r) = \mu_0 - V_h(r)$. The lattice depth is held at $V_0 = 15.64E_r$ ($zJ = 0.06U$), as already discussed in Fig. 2(a). Furthermore, the total number of particles is kept constant, $N_{\text{total}} = 1096$, as well as the total pressure, $P_{\text{total}} = 1.9765 U/a^2$. Under these described conditions, such quantities satisfy the equation of state [65,66]

$$P_{\text{total}} = \frac{m\omega^2}{2\pi} N_{\text{total}}, \quad (28)$$

as demonstrated in Appendix F. This simple relation implies that, if N_{total} is fixed, then P_{total} is naturally held constant. Given all these parameters, we restrict our analysis to the normal phase anomaly since the variations in density with temperature are more prominent.

Since we want to investigate how the density behaves when temperature is changed at fixed pressure, Figs. 4(d) and 4(e) exhibit the density ρ on each lattice site of the xy plane for temperatures $k_B T = 0.08U$ ($T = 2.97$ nK) and $k_B T = 0.18U$ ($T = 6.68$ nK), respectively. These two temperatures are also marked as blue and red straight lines in the phase diagram of Fig. 4(c), showing that only the normal phase is present. In

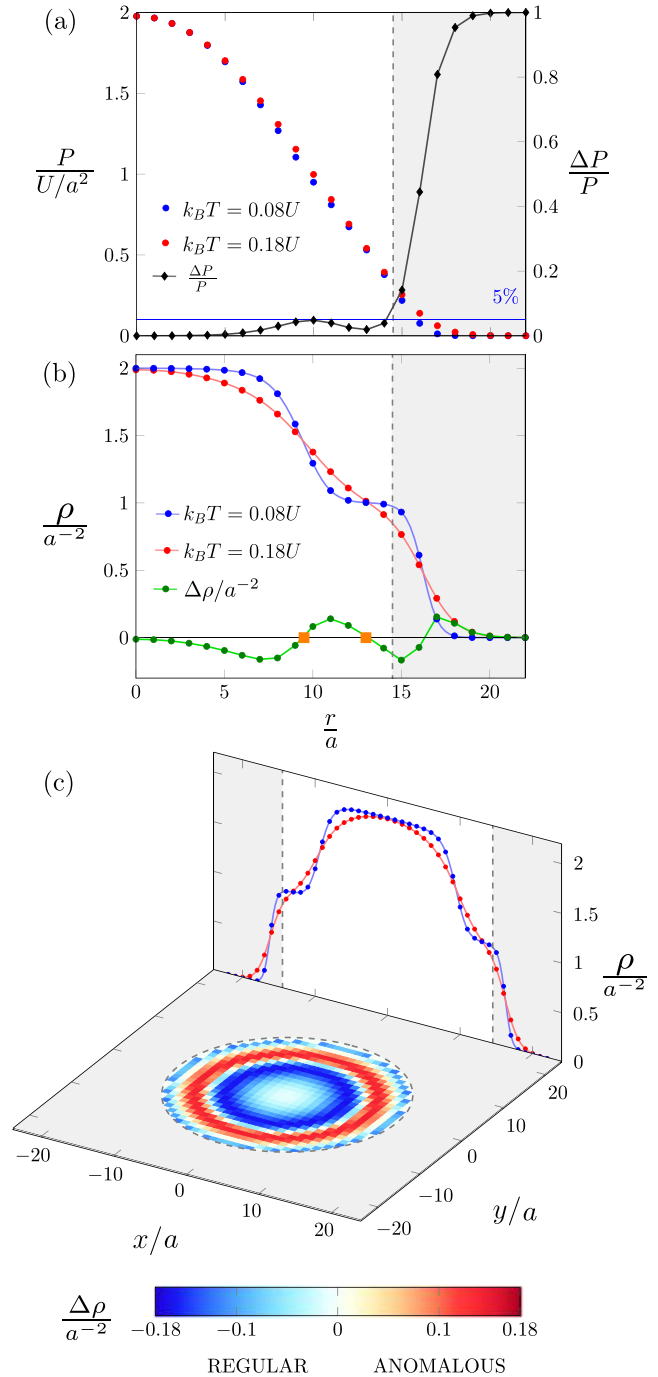


FIG. 5. Analysis of the setup presented in Fig. 4. Panel (a) shows the pressure P for two different temperatures ($k_B T = 0.08U$ and $k_B T = 0.18U$) and their relative differences $\Delta P/P$ as a function of the radial distance r . The gray area signals the distances where such pressure deviation becomes greater than 5%. (b) The density profiles for these temperatures are exhibited as functions of the distance r as well as their difference $\Delta\rho$, with the anomalous region ($9a < r < 14a$) delimited by two TMD points (orange squares). (c) $\Delta\rho$ is represented as a color map in the xy plane.

a qualitative perspective, we observed a melting of the steps as temperature is raised and a larger number fluctuations between the steps of integer density. Quantitatively, a closer look

at how the local pressure P varies across the radial direction is discussed in Fig. 5(a). Due to the finite deviation between such temperatures $k_B \Delta T = 0.1U$, there are differences in pressure ΔP compared to their respective values at each site which are less than 5% until $r = 14a$. Larger distances are filled in gray, comprehending an area where the relative variation $\Delta P/P$ grows towards the boundaries of the lattice. Hence the pressure is kept approximately constant at each site except inside the gray area, where $r > 14a$. Figure 5(b) shows the radial density profiles in greater detail, with their difference $\Delta \rho$ in green. This curve shows oscillations, taking on positive values. These positive values indicate the density anomaly and are limited by two TMD points, shown as orange square points. Finally, Fig. 5(c) summarizes our analysis where the difference in density $\Delta \rho$ is represented through a color map in the xy plane. The anomalous region $\Delta \rho > 0$ denotes an increase in density with temperature at fixed pressure, while the regular behavior corresponds to $\Delta \rho < 0$. As previously, the gray area excludes the regions where the local pressure does not remain fixed. Under these circumstances, we have shown a signature of the density anomaly in this 2D configuration, illustrated as the red circular ring of Fig. 5(c).

VII. CONCLUSION

We have predicted theoretically the occurrence of density anomaly in a quantum system considering parameters compatible with its experimental realization in optical lattices, within the framework described by the self-energy functional theory. It was also shown that the physical mechanism underlying normal density anomalies relies on the presence of a zero-point entropy in the atomic limit, marking phase transitions between Mott insulators with different occupation. The inclusion of the hopping amplitude (enabling the rise of a superfluid phase) lifts the ground-state degeneracy, generates correlations among different sites, and damps residual entropies and thermal expansion. Nevertheless, regions of anomalous density behavior can be found in a perturbative regime ($J \ll U$) corresponding to atomic recoil energy being much smaller than the intensities of the confining field $E_r \ll V_0$. For very intense confining fields waterlike anomalies are also found inside the superfluid regime, as was illustrated for the case of rubidium-87 in Figs. 1 and 2. Our proposition is that by understanding the competition between different physical mechanisms contributing to free energy, usually manifested through interactions between particles (but here including chemical potential and hopping), and the relation between residual entropy and ground-state phase transitions, it is possible to design and predict the phenomenology of density anomaly in systems other than liquid water, as illustrated here with optical lattices of rubidium-87, sodium-23, and cesium-133 atoms.

ACKNOWLEDGMENTS

We acknowledge the financial support of the Brazilian funding agencies FAPDF, CNPq, and CAPES.

APPENDIX A: TENSOR PRODUCTS

The product $\mathbf{V}^\alpha(\tau)$ of a second-order tensor $\mathbf{M}_\beta^\alpha(\tau, \tau')$ and a first-order tensor $\mathbf{F}^\alpha(\tau)$ comprises the sum over the superindex and integration in imaginary time according to

$$\mathbf{V}^\alpha(\tau) = \sum_\gamma \int_0^\beta d\tilde{\tau} \mathbf{M}_\gamma^\alpha(\tau, \tilde{\tau}) \mathbf{F}^\gamma(\tilde{\tau}). \quad (\text{A1})$$

Similarly, the product $\mathbf{M}_\beta^\alpha(\tau, \tau')$ of two second-order tensors $\mathbf{A}_\beta^\alpha(\tau, \tau')$ and $\mathbf{B}_\beta^\alpha(\tau, \tau')$ is defined by

$$\mathbf{M}_\beta^\alpha(\tau, \tau') = \sum_\gamma \int_0^\beta d\tilde{\tau} \mathbf{A}_\gamma^\alpha(\tau, \tilde{\tau}) \mathbf{B}_\beta^\gamma(\tilde{\tau}, \tau'). \quad (\text{A2})$$

As a consequence, a scalar $R = \mathbf{V}^\dagger \mathbf{M} \mathbf{F}$, given by the contraction of two first-order tensors $\mathbf{V}^\alpha(\tau)$ and $\mathbf{F}^\alpha(\tau)$ with a second-order tensor $\mathbf{M}_\beta^\alpha(\tau, \tau')$, can be expressed as

$$R = \sum_{\alpha\beta} \int_0^\beta \int_0^\beta d\tau d\tau' \mathbf{V}_\alpha^\dagger(\tau) \mathbf{M}_\beta^\alpha(\tau, \tau') \mathbf{F}^\beta(\tau'). \quad (\text{A3})$$

Also, time and space translation invariances imply $\mathbf{M}_\beta^\alpha(\tau - \tau') = \mathbf{M}_{\mathbf{r}_j, \nu}^{\mathbf{r}_i, \eta}(\tau - \tau') = \mathbf{M}_\nu^\eta(\mathbf{r}_i - \mathbf{r}_j, \tau - \tau')$. The connection between the imaginary time domain and the Matsubara frequency space (with $\omega_n = \frac{2\pi}{\beta} n$) is established through the Fourier relations

$$\mathbf{M}_\beta^\alpha(i\omega_n) = \int_0^\beta d\tau e^{i\omega_n \tau} \mathbf{M}_\beta^\alpha(\tau), \quad (\text{A4})$$

$$\mathbf{M}_\beta^\alpha(\tau) = \frac{1}{\beta} \sum_{n=-\infty}^{\infty} e^{-i\omega_n \tau} \mathbf{M}_\beta^\alpha(i\omega_n). \quad (\text{A5})$$

Analogously, real and momentum spaces are related by

$$\mathbf{M}_\nu^\eta(\mathbf{k}, \tau) = \sum_{\mathbf{r}} e^{-i\mathbf{k} \cdot \mathbf{r}} \mathbf{M}_\nu^\eta(\mathbf{r}, \tau), \quad (\text{A6})$$

$$\mathbf{M}_\nu^\eta(\mathbf{r}, \tau) = \frac{1}{N_s} \sum_{\mathbf{k}} e^{i\mathbf{k} \cdot \mathbf{r}} \mathbf{M}_\nu^\eta(\mathbf{k}, \tau). \quad (\text{A7})$$

Similar conclusions also hold for first-order tensors. Combining space and time translation invariances, in momentum and Matsubara frequency space the products exhibited by Eqs. (A1)–(A3) simplify to

$$\mathbf{V}^\eta = \sum_\nu \mathbf{M}_\nu^\eta(\mathbf{k} = \mathbf{0}, i\omega_0) \mathbf{F}^\nu, \quad (\text{A8})$$

$$\mathbf{M}_\nu^\eta(\mathbf{k}, i\omega_n) = \sum_\mu \mathbf{A}_\mu^\eta(\mathbf{k}, i\omega_n) \mathbf{B}_\nu^\mu(\mathbf{k}, i\omega_n), \quad (\text{A9})$$

$$R = \beta N_s \sum_{\eta\nu} \mathbf{V}_\eta^\dagger \mathbf{M}_\nu^\eta(\mathbf{k} = \mathbf{0}, i\omega_0) \mathbf{F}^\nu. \quad (\text{A10})$$

APPENDIX B: TRACES

1. General definitions

The traces presented in the functional formulations are defined as the complete contraction over superindices and a double integration in imaginary time according to

$$\text{Tr}[\mathbf{M}] = \sum_\gamma \int_0^\beta \int_0^\beta d\tau d\tau' \delta_\gamma(\tau - \tau') \mathbf{M}_\gamma^\gamma(\tau, \tau'), \quad (\text{B1})$$

where $\delta_\nu(\tau) = \delta_{\mathbf{r}_i, \nu}(\tau) = \delta(\tau - (-1)^\nu 0^-)$ with $\nu = 0, 1$. The delta function is introduced in order to impose normal ordering of the diagonal Nambu components of \mathbf{M} . Considering time and space translation invariances, the trace defined by Eq. (B1) becomes

$$\begin{aligned} \text{Tr}[\mathbf{M}] &= \beta N_s \sum_\nu \mathbf{M}_\nu^v[\mathbf{r}_i = \mathbf{0}, \tau = (-1)^\nu 0^-] \\ &= \sum_{\nu \mathbf{k} n} e^{i\omega_n(-1)^\nu 0^+} \mathbf{M}_\nu^v(\mathbf{k}, i\omega_n). \end{aligned} \quad (\text{B2})$$

The summation over Matsubara frequencies within the described limit can impose difficulties depending on the asymptotic behavior of \mathbf{M} . In order to improve the convergence properties of such sums, we analyze explicitly its high-frequency expansion in the following.

2. High-frequency expansion

We define the high-frequency expansion of

$$\mathbf{M}(\mathbf{k}, i\omega_n) = \mathcal{M}(\mathbf{k}, i\omega_n) + O((i\omega_n)^{-(N_h+1)}) \quad (\text{B3})$$

up to order N_h according to

$$\mathcal{M}(\mathbf{k}, i\omega_n) = \sum_{p=1}^{N_h} \mathbf{m}_p(\mathbf{k}) Q_p(i\omega_n), \quad (\text{B4})$$

where

$$Q_p(i\omega_n) = \begin{cases} \frac{1}{(i\omega_n)^p}, & \omega_n \neq 0, \\ 0, & \omega_n = 0. \end{cases} \quad (\text{B5})$$

By adding and subtracting the term $\text{Tr}[\mathcal{M}]$ in Eq. (B2), the corresponding trace can be expressed as

$$\begin{aligned} \text{Tr}[\mathbf{M}] &= \sum_{\nu \mathbf{k}} \left(\sum_n [\mathbf{M}(\mathbf{k}, i\omega_n) - \mathcal{M}(\mathbf{k}, i\omega_n)]_\nu^v \right. \\ &\quad \left. + \beta \mathcal{M}_\nu^v[\mathbf{k}, \tau = (-1)^\nu 0^-] \right), \end{aligned} \quad (\text{B6})$$

since the asymptotic behavior $[\mathbf{M} - \mathcal{M}]_\nu^v \sim (i\omega_n)^{-(N_h+1)}$ allows us to drop the exponent present in the trace definition. Considering a finite number N_ω of Matsubara frequencies and a high-frequency expansion of order N_h , the trace approximation reads as

$$\begin{aligned} \text{Tr}[\mathbf{M}] &\approx \sum_{\nu \mathbf{k}} \left(\mathbf{M}_\nu^v(\mathbf{k}, i\omega_0) \right. \\ &\quad \left. + \sum_{n=-N_\omega}^{N_\omega} \left[\mathbf{M}(\mathbf{k}, i\omega_n) - \sum_{p=1}^{N_h} \frac{\mathbf{m}_p(\mathbf{k})}{(i\omega_n)^p} \right]_\nu^v \right. \\ &\quad \left. + \beta \sum_{p=1}^{N_h} [\mathbf{m}_p(\mathbf{k})]_\nu^v Q_p[\mathbf{k}, \tau = (-1)^\nu 0^-] \right), \end{aligned} \quad (\text{B7})$$

where the primed sum excludes $\omega_n = 0$. The calculations presented in this paper employ $N_\omega = 1000$ with a second-order $N_h = 2$ tail expansion.

In order to compute the trace approximation of Eq. (B7), the functions $Q_p(\tau)$, Fourier transforms of $Q_p(i\omega_n)$, need to

be determined. The idea is to visualize them as sums of the residues [46] of a given complex function as follows:

$$Q_p(\tau) = \frac{1}{\beta} \sum_{n=-\infty}^{\infty} \frac{e^{-i\omega_n \tau}}{(i\omega_n)^p} = \sum_{n=-\infty}^{\infty} \text{Res} \left[\frac{e^{-\tau z}}{z^p} h(z), i\omega_n \right], \quad (\text{B8})$$

with $h(z) = (1 - e^{-\beta z})^{-1}$. The poles $z = i\omega_n$ are located along the imaginary axis; then, the residue theorem allows us to relate the result to a contour integral, comprehending the imaginary axis of the complex plane

$$\sum_{n=-\infty}^{\infty} \text{Res} \left[\frac{e^{-\tau z}}{z^p} h(z), i\omega_n \right] = \oint_C \frac{dz}{2\pi i} \frac{e^{-\tau z}}{z^p} h(z). \quad (\text{B9})$$

By deforming the original contour C into two semicircles of infinite radius this same integral becomes

$$\oint_{C'} \frac{dz}{2\pi i} \frac{e^{-\tau z}}{z^p} h(z) = 0, \quad (\text{B10})$$

once this new path C' encloses regions free of poles. By inserting Eq. (B10) into Eq. (B9) and comparing to Eq. (B8), $Q_p(\tau)$ is determined simply by $n = 0$

$$Q_p(\tau) = -\text{Res} \left[\frac{e^{-\tau z}}{z^p} h(z), 0 \right]. \quad (\text{B11})$$

The relevant pole $z = 0$ is of order $p + 1$; hence the corresponding residue is given by the formula

$$Q_p(\tau) = -\frac{1}{p!} \lim_{z \rightarrow 0} \left(\frac{d}{dz} \right)^p z e^{-\tau z} h(z), \quad (\text{B12})$$

with the following first-order terms:

$$Q_1(\tau) = (2\tau - \beta)/(2\beta), \quad (\text{B13})$$

$$Q_2(\tau) = (-6\tau^2 + 6\beta\tau - \beta^2)/(12\beta). \quad (\text{B14})$$

Since the functions $Q_p(\tau)$ are periodic on the interval $\tau \in (0, \beta)$, the respective zero time limits are

$$Q_1[\tau = (-1)^\nu 0^-] = (-1)^\nu / 2, \quad (\text{B15})$$

$$Q_2[\tau = (-1)^\nu 0^-] = -\beta/12. \quad (\text{B16})$$

3. Trace of logarithm

Besides the already mentioned ordinary traces, the self-energy functionals also contain traces regarding the logarithm of the Green's function \mathbf{G} . Actually, in order to guarantee the correct noninteracting limit, a regularization factor must be included. Therefore, we define the regularized Matsubara trace logarithm functional $\mathcal{L}[\mathbf{G}]$,

$$\mathcal{L}[\mathbf{G}] = \frac{1}{2} \text{Tr} \ln[-\mathbf{G}^{-1}] - \frac{1}{2} \text{Tr} \ln[-\mathbf{G}_r^{-1}], \quad (\text{B17})$$

with the regularization carried by the second-order tensor

$$\mathbf{G}_r(i\omega_n) = \begin{cases} -\beta \mathbf{1}, & \omega_n = 0, \\ \frac{\sigma_z}{i\omega_n}, & \omega_n \neq 0. \end{cases} \quad (\text{B18})$$

According to Eq. (B2), such trace is represented as

$$\mathcal{L}[\mathbf{G}] = -\frac{1}{2} \sum_{\nu \mathbf{k} n} e^{i\omega_n(-1)^\nu 0^+} \{ \ln[\mathbf{G}_r^{-1} \mathbf{G}(\mathbf{k}, i\omega_n)] \}_\nu^v,$$

and the approximation described by Eq. (B7) yields

$$\begin{aligned} \mathcal{L}[\mathbf{G}] \approx & -\frac{1}{2} \sum_{\mathbf{k}} \left(\ln[-\mathbf{G}(\mathbf{k}, i\omega_0)/\beta] \right)_v^v \\ & + \sum_{n=-N_\omega}^{N_\omega} \left[\ln[(\sigma_z i\omega_n) \mathbf{G}(\mathbf{k}, i\omega_n)] - \sum_{p=1}^{N_h} \frac{\mathbf{q}_p(\mathbf{k})}{(i\omega_n)^p} \right]_v^v \\ & + \beta \sum_{p=1}^{N_h} [\mathbf{q}_p(\mathbf{k})]_v^v \mathcal{Q}_p[\mathbf{k}, \tau = (-1)^v 0^-]. \end{aligned} \quad (\text{B19})$$

The terms $\mathbf{q}_p(\mathbf{k})$ are the coefficients from the high-frequency expansion of $\ln[(\sigma_z i\omega_n) \mathbf{G}(\mathbf{k}, i\omega_n)] = \sum_{p=1}^{\infty} \frac{\mathbf{q}_p(\mathbf{k})}{(i\omega_n)^p}$ given explicitly by

$$\mathbf{q}_1(\mathbf{k}) = \sigma_z \mathbf{c}_2(\mathbf{k}), \quad (\text{B20})$$

$$\mathbf{q}_2(\mathbf{k}) = \sigma_z \mathbf{c}_3(\mathbf{k}) - \frac{[\sigma_z \mathbf{c}_2(\mathbf{k})]^2}{2}, \quad (\text{B21})$$

until second order, where $\mathbf{c}_p(\mathbf{k})$ are the coefficients in the high-frequency expansion of the Green's function

$$\mathbf{G}(i\omega_n) = \sum_{p=1}^{\infty} \frac{\mathbf{c}_p(\mathbf{k})}{(i\omega_n)^p}. \quad (\text{B22})$$

Hence, using second-order tail corrections, the Matsubara trace logarithm exposed in Eq. (B19) reads as

$$\begin{aligned} \mathcal{L}[\mathbf{G}] \approx & -\frac{1}{2} \sum_{\mathbf{k}} \left(\ln[-\mathbf{G}(\mathbf{k}, i\omega_0)/\beta] + \frac{\beta}{2} \mathbf{c}_2(\mathbf{k}) - \frac{\beta^2}{12} \mathbf{q}_2(\mathbf{k}) \right. \\ & \left. + \sum_{n=-N_\omega}^{N_\omega} \left[\ln[(\sigma_z i\omega_n) \mathbf{G}(\mathbf{k}, i\omega_n)] - \frac{\mathbf{q}_2(\mathbf{k})}{(i\omega_n)^2} \right] \right)_v^v. \end{aligned} \quad (\text{B23})$$

APPENDIX C: REFERENCE SYSTEM

In the basis of local occupation number states, we generate matrix representations for the reference system Hamiltonian H' of Eq. (24) and the bosonic creation and annihilation operators b^\dagger and b . A cutoff $N_{\max} = 10$ bounding the occupation number from above is introduced. The diagonalization of the Hamiltonian H' provides its eigenvalues E_n and eigenvectors $|n\rangle$. Given these procedures, the partition function is written as

$$\mathcal{Z}' = \sum_n e^{-\beta E_n}, \quad (\text{C1})$$

from which we derive the reference system free energy

$$\Omega' = -\frac{1}{\beta} \ln[\mathcal{Z}']. \quad (\text{C2})$$

Regarding the propagators, the static expectation value of \mathbf{b} , defined in Eq. (8), is given by

$$\Phi' = \langle \mathbf{b} \rangle = \frac{1}{\mathcal{Z}'} \sum_n e^{-\beta E_n} \langle n | \mathbf{b} | n \rangle, \quad (\text{C3})$$

and the connected Green's function of Eq. (9)

$$\mathbf{G}'(\tau) = -\langle \mathbf{b}(\tau) \mathbf{b}^\dagger \rangle + \Phi' \Phi'^\dagger \quad (\text{C4})$$

expressed in the Matsubara frequency space yields

$$\begin{aligned} \mathbf{G}'(i\omega_n) = & \frac{1}{\mathcal{Z}'} \sum_{n,m} \frac{(e^{-\beta E_n} - e^{-\beta E_m})}{i\omega_n + E_n - E_m} \langle n | \mathbf{b} | m \rangle \langle m | \mathbf{b}^\dagger | n \rangle \\ & - \delta_{\omega_n, 0} \beta \frac{1}{\mathcal{Z}'} \sum_n e^{-\beta E_n} \langle n | \mathbf{b} | n \rangle \langle n | \mathbf{b}^\dagger | n \rangle \\ & + \delta_{\omega_n, 0} \beta \Phi' \Phi'^\dagger. \end{aligned} \quad (\text{C5})$$

The noninteracting Green's function is determined by setting $U = 0$ in Eq. (24),

$$\mathbf{G}'_0^{-1}(i\omega_n) = \sigma_z i\omega_n + \mathbf{1}\mu - \mathbf{\Delta}, \quad (\text{C6})$$

while the self-energies follow from the Dyson equations, Eqs. (19) and (20), as

$$\Sigma'_{1/2} = \mathbf{F}' - \mathbf{G}'_0^{-1}(i\omega_0) \Phi', \quad (\text{C7})$$

$$\Sigma'(i\omega_n) = \mathbf{G}'_0^{-1}(i\omega_n) - \mathbf{G}'^{-1}(i\omega_n). \quad (\text{C8})$$

APPENDIX D: LATTICE SYSTEM

Considering the lattice system, the noninteracting Green's function satisfies

$$\mathbf{G}_0^{-1}(\mathbf{k}, i\omega_n) = \sigma_z i\omega_n + \mathbf{1}(\mu - \epsilon_{\mathbf{k}}), \quad (\text{D1})$$

where $\epsilon_{\mathbf{k}}$ is the energy dispersion relation

$$\epsilon_{\mathbf{k}} = -2J \sum_{i=1}^d \cos(k_i a) \quad (\text{D2})$$

for a hypercubic lattice in d dimensions. Also, the interacting lattice Green's function follows from Eq. (20) as

$$\mathbf{G}^{-1}(\mathbf{k}, i\omega_n) = \mathbf{G}_0^{-1}(\mathbf{k}, i\omega_n) - \Sigma'(i\omega_n), \quad (\text{D3})$$

evaluated at the reference system self-energy Σ' . According to Eq. (19), the other Dyson equation implies

$$\Phi = -\mathbf{G}_0(i\omega_0) \Sigma'_{1/2}, \quad (\text{D4})$$

taking into account that $\mathbf{F} = \mathbf{0}$, since there is no symmetry breaking field on the complete lattice.

APPENDIX E: HIGH-FREQUENCY EXPANSION OF THE GREEN'S FUNCTION

To complete the evaluation of the trace log functional of Eq. (B23), the coefficients \mathbf{c}_p , regarding the tail expansion of the Green's function in Eq. (B22), remain to be determined for both reference and lattice systems.

1. Reference system

By expressing the Matsubara Green's function as a Fourier transform of the imaginary time Green's function, successive

integration by parts yields

$$\begin{aligned} \mathbf{G}'(i\omega_n) &= \int_0^\beta d\tau e^{i\omega_n\tau} \mathbf{G}'(\tau) \\ &= \sum_{p=0}^{\infty} (-1)^p \frac{\partial_\tau^p \mathbf{G}'(\beta^-) - \partial_\tau^p \mathbf{G}'(0^+)}{(i\omega_n)^{p+1}}. \end{aligned} \quad (\text{E1})$$

Therefore, the high-frequency expansion coefficients take the form

$$\mathbf{c}'_{p+1} = (-1)^p [\partial_\tau^p \mathbf{G}'(\beta^-) - \partial_\tau^p \mathbf{G}'(0^+)]. \quad (\text{E2})$$

From the definition of the Green's function as the time-ordered expectation value of Eq. (C4) and the equation of motion satisfied by $\mathbf{b}(\tau)$

$$\partial_\tau \mathbf{b}(\tau) = [H', \mathbf{b}(\tau)], \quad (\text{E3})$$

we extract the imaginary time derivative of $\mathbf{G}'(\tau)$:

$$\partial_\tau \mathbf{G}'(\tau) = -\langle [H', \mathbf{b}(\tau)] \mathbf{b}^\dagger \rangle. \quad (\text{E4})$$

By induction on Eq. (E3) and Eq. (E4), the derivative of order p reads as

$$\partial_\tau^p \mathbf{G}'(\tau) = -\langle [[H', \mathbf{b}(\tau)]^{(p)} \mathbf{b}^\dagger] \rangle, \quad (\text{E5})$$

with $[[H', \mathbf{b}(\tau)]^{(p)}] = [H, \dots, [H, [H, \mathbf{b}(\tau)]] \dots]$ the left side commutator of H' with $\mathbf{b}(\tau)$ applied p times. The evaluation of such derivatives at the imaginary times $\tau = 0^+$ and $\tau = \beta^-$ allows us to fix the time ordering

$$\partial_\tau^p \mathbf{G}'(0^+) = -\langle [[H', \mathbf{b}]]^{(p)} \mathbf{b}^\dagger \rangle, \quad (\text{E6})$$

$$\partial_\tau^p \mathbf{G}'(\beta^-) = -\langle \mathbf{b}^\dagger [[H', \mathbf{b}]]^{(p)} \rangle. \quad (\text{E7})$$

Inserting these results into Eq. (E2), the desired coefficients simplify to

$$\mathbf{c}'_{p+1} = (-1)^p \langle [[H', \mathbf{b}]]^{(p)} \mathbf{b}^\dagger \rangle. \quad (\text{E8})$$

Explicitly, the first-order terms are

$$\mathbf{c}'_1 = \langle [\mathbf{b}, \mathbf{b}^\dagger] \rangle = \sigma_z, \quad (\text{E9})$$

$$\mathbf{c}'_2 = -\langle [[H', \mathbf{b}], \mathbf{b}^\dagger] \rangle, \quad (\text{E10})$$

$$\mathbf{c}'_3 = \langle [[H', [H', \mathbf{b}]], \mathbf{b}^\dagger] \rangle. \quad (\text{E11})$$

2. Lattice system

According to Eqs. (D1) and (D3), the lattice Green's function $\mathbf{G}(\mathbf{k}, i\omega_n)$ presents a tail expansion of the form

$$\begin{aligned} \mathbf{G}(\mathbf{k}, i\omega_n) &= \frac{\sigma_z}{i\omega_n} + \frac{\sigma_z [\mathbf{I}(\epsilon_{\mathbf{k}} - \mu) + \mathbf{s}'_0] \sigma_z}{(i\omega_n)^2} \\ &+ \frac{\sigma_z \mathbf{s}'_1 \sigma_z + \{\sigma_z [\mathbf{I}(\epsilon_{\mathbf{k}} - \mu) + \mathbf{s}'_0]\}^2 \sigma_z}{(i\omega_n)^3} + O\left(\frac{1}{(i\omega_n)^4}\right), \end{aligned}$$

where \mathbf{s}'_p are the high-frequency expansion coefficients of the reference system's self-energy $\Sigma'(i\omega_n) = \sum_{p=1}^{\infty} \frac{\mathbf{s}'_p}{(i\omega_n)^p}$. Hence the first-order terms are

$$\mathbf{c}_1(\mathbf{k}) = \sigma_z, \quad (\text{E12})$$

$$\mathbf{c}_2(\mathbf{k}) = \sigma_z [\mathbf{I}(\epsilon_{\mathbf{k}} - \mu) + \mathbf{s}'_0] \sigma_z, \quad (\text{E13})$$

$$\mathbf{c}_3(\mathbf{k}) = \sigma_z \mathbf{s}'_1 \sigma_z + \{\sigma_z [\mathbf{I}(\epsilon_{\mathbf{k}} - \mu) + \mathbf{s}'_0]\}^2 \sigma_z. \quad (\text{E14})$$

To determine the coefficients \mathbf{s}'_p of the self-energy $\Sigma'(i\omega_n) = \mathbf{G}'_0^{-1}(i\omega_n) - \mathbf{G}'^{-1}(i\omega_n)$, we need to compute the inverse of \mathbf{G}' , given by

$$\begin{aligned} \mathbf{G}'^{-1}(i\omega_n) &= \left[\frac{\sigma_z}{i\omega_n} + \sum_{p=2}^{\infty} \frac{\mathbf{c}'_p}{(i\omega_n)^p} \right]^{-1} \\ &= \sigma_z i\omega_n - \sigma_z \mathbf{c}'_2 \sigma_z \\ &\quad + \frac{-\sigma_z \mathbf{c}'_3 \sigma_z + (\sigma_z \mathbf{c}'_2)^2 \sigma_z}{i\omega_n} + O\left(\frac{1}{(i\omega_n)^2}\right). \end{aligned}$$

Then, the previous result combined to Eq. (C6) implies

$$\begin{aligned} \Sigma'^{-1}(i\omega_n) &= \mathbf{G}'_0^{-1}(i\omega_n) - \mathbf{G}'^{-1}(i\omega_n) \\ &= \mathbf{1}\mu - \mathbf{\Delta} + \sigma_z \mathbf{c}'_2 \sigma_z \\ &\quad - \frac{-\sigma_z \mathbf{c}'_3 \sigma_z + (\sigma_z \mathbf{c}'_2)^2 \sigma_z}{i\omega_n} + O\left(\frac{1}{(i\omega_n)^2}\right). \end{aligned}$$

Consequently, the first-order coefficients of the self-energy tail expansion can be written as

$$\mathbf{s}'_0 = \mathbf{1}\mu - \mathbf{\Delta} + \sigma_z \mathbf{c}'_2 \sigma_z, \quad (\text{E15})$$

$$\mathbf{s}'_1 = \sigma_z \mathbf{c}'_3 \sigma_z - (\sigma_z \mathbf{c}'_2)^2 \sigma_z. \quad (\text{E16})$$

From these terms, the desired lattice Green's function coefficients are evaluated according to Eqs. (E12)–(E14).

APPENDIX F: EQUATION OF STATE AND PRESSURE

Considering the two-dimensional setup discussed in Sec. VI, the total pressure P_{total} is evaluated by integrating the Gibbs-Duhem relation $dP = \rho d\mu + s dT$ at fixed temperature T over the lattice

$$P_{\text{total}} = \int_{-\infty}^{\mu_0} \rho d\mu = - \int_0^{\infty} \rho(r) \frac{d\mu}{dr} dr. \quad (\text{F1})$$

For an isotropic harmonic trap in the xy plane, $\mu = \mu_0 - \frac{1}{2}m\omega^2 r^2$ and $\frac{d\mu}{dr} = -m\omega^2 r$; then Eq. (F1) becomes

$$P_{\text{total}} = m\omega^2 \int_0^{\infty} \rho(r) r dr. \quad (\text{F2})$$

The total number of particles N_{total} is obtained by integration of the local density $\rho(r)$ according to

$$N_{\text{total}} = 2\pi \int_0^{\infty} \rho(r) r dr. \quad (\text{F3})$$

Comparing both Eqs. (F2) and (F3), we deduce the equation of state,

$$P_{\text{total}} = \frac{m\omega^2}{2\pi} N_{\text{total}}, \quad (\text{F4})$$

valid for 2D gases including an isotropic harmonic confinement [65,66]. There is also another interesting observation concerning the value of the fixed total pressure. Since the density ρ is a derivative of the free energy Ω , see Eq. (25),

we can write P_{total} as

$$\begin{aligned} P_{\text{total}} &= - \int_{-\infty}^{\mu_0} \frac{1}{V} \left(\frac{\partial \Omega}{\partial \mu} \right)_T d\mu \\ &= \frac{1}{V} [\Omega(\mu = -\infty) - \Omega(\mu_0)]. \end{aligned} \quad (\text{F5})$$

Considering that $\Omega(\mu = -\infty) = 0$ and $-PV = \Omega$, the total pressure is equal to the local pressure at the center of the trap

$$P_{\text{total}} = P(\mu_0) = P(r = 0), \quad (\text{F6})$$

as Fig. 5(a) confirms.

-
- [1] M. H. Anderson, J. R. Ensher, M. R. Matthews, C. E. Wieman, and E. A. Cornell, *Science* **269**, 198 (1995).
- [2] K. B. Davis, M. O. Mewes, M. R. Andrews, N. J. van Druten, D. S. Durfee, D. M. Kurn, and W. Ketterle, *Phys. Rev. Lett.* **75**, 3969 (1995).
- [3] O. Dutta, M. Gajda, P. Hauke, M. Lewenstein, D.-S. Lühmann, B. A. Malomed, T. Sowiński, and J. Zakrzewski, *Rep. Prog. Phys.* **78**, 066001 (2015).
- [4] M. Lewenstein, A. Sanpera, V. Ahufinger, B. Damski, A. Sen(De), and U. Sen, *Adv. Phys.* **56**, 243 (2007).
- [5] D. Jaksch, H.-J. Briegel, J. I. Cirac, C. W. Gardiner, and P. Zoller, *Phys. Rev. Lett.* **82**, 1975 (1999).
- [6] J. I. Cirac and P. Zoller, *Phys. Today* **57**(3), 38 (2004).
- [7] M. Greiner, O. Mandel, T. Esslinger, T. W. Hänsch, and I. Bloch, *Nature (London)* **415**, 39 (2002).
- [8] I. Bloch, *Nat. Phys.* **1**, 23 (2005).
- [9] D. Jaksch and P. Zoller, *Ann. Phys. (NY)* **315**, 52 (2005).
- [10] W. Hofstetter and T. Qin, *J. Phys. B: At., Mol., Opt. Phys.* **51**, 082001 (2018).
- [11] E. J. Mueller, *Phys. Rev. A* **70**, 041603(R) (2004).
- [12] E. Kapit and E. Mueller, *Phys. Rev. A* **83**, 033625 (2011).
- [13] P. Windpassinger and K. Sengstock, *Rep. Prog. Phys.* **76**, 086401 (2013).
- [14] M. P. A. Fisher, P. B. Weichman, G. Grinstein, and D. S. Fisher, *Phys. Rev. B* **40**, 546 (1989).
- [15] D. Jaksch, C. Bruder, J. I. Cirac, C. W. Gardiner, and P. Zoller, *Phys. Rev. Lett.* **81**, 3108 (1998).
- [16] S. Sachdev, *Quantum Phase Transitions* (Cambridge University Press, Cambridge, UK, 2011).
- [17] G. S. Kell, *J. Chem. Eng. Data* **12**, 66 (1967).
- [18] P. G. Debenedetti, *J. Phys.: Condens. Matter* **15**, R1669(R) (2003).
- [19] R. J. Donnelly and C. F. Barenghi, *J. Phys. Chem. Ref. Data* **27**, 1217 (1998).
- [20] F. Caupin, S. Balibar, and H. J. Maris, *Phys. Rev. Lett.* **87**, 145302 (2001).
- [21] P. H. Poole, F. Sciortino, U. Essmann, and H. E. Stanley, *Nature (London)* **360**, 324 (1992).
- [22] P. Gallo, K. Amann-Winkel, C. A. Angell, M. A. Anisimov, F. Caupin, C. Chakravarty, E. Lascaris, T. Loerting, A. Z. Panagiotopoulos, J. Russo, J. A. Sellberg, H. E. Stanley, H. Tanaka, C. Vega, L. Xu, and L. G. M. Pettersson, *Chem. Rev.* **116**, 7463 (2016).
- [23] H. E. Stanley, P. Kumar, G. Franzese, L. Xu, Z. Yan, M. G. Mazza, S. V. Buldyrev, S.-H. Chen, and F. Mallamace, *Eur. Phys. J.: Spec. Top.* **161**, 1 (2008).
- [24] J. N. Glosli and F. H. Ree, *Phys. Rev. Lett.* **82**, 4659 (1999).
- [25] S. Sastry and C. Austen Angell, *Nat. Mater.* **2**, 739 (2003).
- [26] I. Saika-Voivod, F. Sciortino, T. Grande, and P. H. Poole, *Philos. Trans. R. Soc., A* **363**, 525 (2005).
- [27] G. Monaco, S. Falconi, W. A. Crichton, and M. Mezouar, *Phys. Rev. Lett.* **90**, 255701 (2003).
- [28] R. Kurita and H. Tanaka, *J. Phys.: Condens. Matter* **17**, L293 (2005).
- [29] K.-i. Murata and H. Tanaka, *Nat. Commun.* **4**, 2844 (2013).
- [30] A. Taschin, P. Bartolini, R. Eramo, R. Righini, and R. Torre, *Nat. Commun.* **4**, 2401 (2013).
- [31] D. T. Limmer and D. Chandler, *J. Chem. Phys.* **138**, 214504 (2013).
- [32] D. Hügel, P. Werner, L. Pollet, and H. U. R. Strand, *Phys. Rev. B* **94**, 195119 (2016).
- [33] L. Pollet, *Rep. Prog. Phys.* **75**, 094501 (2012).
- [34] I. Bloch, J. Dalibard, and W. Zwerger, *Rev. Mod. Phys.* **80**, 885 (2008).
- [35] W. Zwerger, *J. Opt. B: Quantum Semiclass. Opt.* **5**, S9 (2003).
- [36] P. B. Blakie and C. W. Clark, *J. Phys. B: At., Mol., Opt. Phys.* **37**, 1391 (2004).
- [37] W. S. Bakr, J. I. Gillen, A. Peng, S. Fölling, and M. Greiner, *Nature (London)* **462**, 74 (2009).
- [38] J. F. Sherson, C. Weitenberg, M. Endres, M. Cheneau, I. Bloch, and S. Kuhr, *Nature (London)* **467**, 68 (2010).
- [39] M. Potthoff, *Eur. Phys. J. B* **32**, 429 (2003).
- [40] K. Byczuk and D. Vollhardt, *Phys. Rev. B* **77**, 235106 (2008).
- [41] A. Hubener, M. Snoek, and W. Hofstetter, *Phys. Rev. B* **80**, 245109 (2009).
- [42] W.-J. Hu and N.-H. Tong, *Phys. Rev. B* **80**, 245110 (2009).
- [43] P. Anders, E. Gull, L. Pollet, M. Troyer, and P. Werner, *New J. Phys.* **13**, 075013 (2011).
- [44] E. Arrigoni, M. Knap, and W. von der Linden, *Phys. Rev. B* **84**, 014535 (2011).
- [45] D. Hügel, H. U. R. Strand, and L. Pollet, *Quantum Sci. Technol.* **3**, 034006 (2018).
- [46] A. L. Fetter and J. D. Walecka, *Quantum Theory of Many-Particle Systems* (Dover Publications, Mineola, NY, 1971), p. 250.
- [47] J. Negele and H. Orland, *Quantum Many-Particle Systems* (Perseus Books, New York, 1998), p. 237.
- [48] J. Zinn-Justin, *Path Integrals in Quantum Mechanics* (Oxford University Press, Oxford, 2004).
- [49] G. Baym and L. P. Kadanoff, *Phys. Rev.* **124**, 287 (1961).
- [50] G. Baym, *Phys. Rev.* **127**, 1391 (1962).
- [51] C. De Dominicis and P. C. Martin, *J. Math. Phys.* **5**, 14 (1964).
- [52] C. De Dominicis and P. C. Martin, *J. Math. Phys.* **5**, 31 (1964).
- [53] J. M. Luttinger and J. C. Ward, *Phys. Rev.* **118**, 1417 (1960).
- [54] G. Stefanucci and R. van Leeuwen, *Nonequilibrium Many-Body Theory of Quantum Systems* (Cambridge University Press, Cambridge, UK, 2013), p. 249.

- [55] J. Berges, S. Borsányi, U. Reinosa, and J. Serreau, *Ann. Phys. (NY)* **320**, 344 (2005).
- [56] J. F. Rentrop, V. Meden, and S. G. Jakobs, *Phys. Rev. B* **93**, 195160 (2016).
- [57] See Supplemental Material at <http://link.aps.org/supplemental/10.1103/PhysRevA.102.033331> for the numerical code regarding the implementation of the self-energy functional theory.
- [58] N. Gemelke, X. Zhang, C. L. Hung, and C. Chin, *Nature (London)* **460**, 995 (2009).
- [59] K. Xu, Y. Liu, J. R. Abo-Shaeer, T. Mukaiyama, J. K. Chin, D. E. Miller, W. Ketterle, K. M. Jones, and E. Tiesinga, *Phys. Rev. A* **72**, 043604 (2005).
- [60] C. Chin, R. Grimm, P. Julienne, and E. Tiesinga, *Rev. Mod. Phys.* **82**, 1225 (2010).
- [61] X. Zhang, C.-L. Hung, S.-K. Tung, and C. Chin, *Science* **335**, 1070 (2012).
- [62] E. O. Rizzatti, M. S. Gomes Filho, M. Malard, and M. A. A. Barbosa, *Physica A* **518**, 323 (2019).
- [63] I. Bloch, *Nat. Phys.* **14**, 1159 (2018).
- [64] T. Gericke, P. Würtz, D. Reitz, T. Langen, and H. Ott, *Nat. Phys.* **4**, 949 (2008).
- [65] S. Nascimbène, N. Navon, F. Chevy, and C. Salomon, *New J. Phys.* **12**, 103026 (2010).
- [66] T.-L. Ho and Q. Zhou, *Nat. Phys.* **6**, 131 (2010).

Double-peak specific heat anomaly and correlations in the Bose-Hubbard model

Eduardo O. Rizzatti,^{1,*} Marco Aurélio A. Barbosa,² and Marcia C. Barbosa¹

¹*Instituto de Física, Universidade Federal do Rio Grande do Sul, Porto Alegre-RS, Brazil*

²*Programa de Pós-Graduação em Ciência de Materiais, Universidade de Brasília, Planaltina-DF, Brazil*

Considering the thermodynamics of bosons in a lattice described by the Bose-Hubbard Hamiltonian, we report the occurrence of anomalous double peaks in their specific heat dependence on temperature. This feature, usually associated with a high geometrical frustration, can also be a consequence of a purely energetic competition. By employing self-energy functional calculations combined with finite-temperature perturbation theory, we propose a mechanism based on ground-state degeneracies expressed as residual entropies. A general decomposition of the specific heat regarding all possible transitions between the system's eigenvalues provides an insight into the nature of each maximum. Furthermore, we address how the model parameters modify the structure of these peaks based on its spectral properties and atom-atom correlation function.

Keywords: Bose-Hubbard Model, specific heat, residual entropy, correlation function.

I. INTRODUCTION

In the field of condensed matter physics, the specific heat is a valuable physical observable that provides general information regarding the energy spectrum of a system, a key to its microscopic details [1, 2]. It encodes information on the entropy, a useful thermodynamic quantity directly connected to such microscopic degrees of freedom, in general inaccessible by direct measurements. Among interesting anomalous properties, the appearance of a second peak in the specific heat at low temperatures, known as the Schottky-type anomaly, is experimentally and theoretically observed in several frustrated systems. Typical examples are the magnetic systems on geometrically frustrated lattices with kagome, triangular, or pyrochlore structures. Experimentally, the double-peak anomaly is measured in magnetic pyrochlore oxides [3], the canonical spin-ice materials $\text{Dy}_2\text{Ti}_2\text{O}_7$ [4–6] and $\text{Tb}_2\text{Ti}_2\text{O}_7$ [7], their mixtures $\text{Dy}_{2-x}\text{Tb}_x\text{Ti}_2\text{O}_7$ [8], lead-based pyrochlores [9], and spin glasses like $\text{R}_2\text{Mo}_2\text{O}_7$ ($\text{R}=\text{Y}, \text{Sm}, \text{or Gd}$) [10]. Other examples include heavy-fermion compounds [11, 12], bosonic superfluids in spin-dimer networks [13], CO_2N_2 plasma [14], lipid bilayers containing cholesterol [15], as well as mixtures of liquid crystal and nanoparticles [16]. In a theoretical framework, the anomaly was verified for spin models with antiferromagnetic Heisenberg interactions [17–22], Ising pyrochlore magnets using Monte Carlo simulations [23, 24], Ising models [25–28] in distinct geometries, and quantum ferrimagnets [29].

Since the entropy dependence on temperature determines the specific heat of a given system, this thermodynamic quantity is a relevant ingredient to the presented anomaly. Fundamentally, the geometrical frustration arises from a conflict between the interaction degrees of freedom and the underlying crystal geometry [30]. The described frustration leads to a macro-

scopic degeneracy computed as a ground-state finite entropy, the so-called residual entropy. Linus Pauling provided one of the first examples of geometrical frustration when describing the low-temperature ordering of protons in water ice I_h [31]. The many ways of satisfying the lowest-energy state which reconcile the crystal structure of ice with the known bond lengths were given by the Bernal-Fowler rules [32]. Based on their prescription, Pauling calculated the ground-state entropy per hydrogen atom of $(1/2)R \ln(3/2) \approx 1.68 \text{ J mol}^{-1}\text{K}^{-1}$. Interestingly, a similar physical mechanism is verified for the already mentioned highly frustrated pyrochlore magnets, constituting the named spin-ice materials [4, 33]. The particular ways these systems can fluctuate between such multiple ground-state configurations can be responsible not only for the anomalies addressed but also for the emergence of all sorts of novel behaviors in fluid and solid phases, including even an artificial edition of electromagnetism [34].

In this work, we report the occurrence of the double-peak specific heat anomaly in the Bose-Hubbard model based on theoretical calculations. The Bose-Hubbard model [35–37] is a paradigm system studied in quantum mechanics. Since its experimental realization in optical lattices [38], the ultracold atomic physics has been developing a myriad of experimental and theoretical tools currently used to investigate quantum phase transitions, quantum coherence, and quantum computation [39–41]. Also, a great advantage regarding the arena of optical lattices is the sharp experimental control over parameters such as dimensionality, lattice structure, composition, and atomic interactions [42–45]. More specifically, the high-definition *in situ* imaging acquired through absorption [46, 47] and fluorescence techniques [48, 49] enables a precise evaluation of the specific heat [50]. Here we present an alternative mechanism of frustration observed in this model, devoting some attention to the influence of correlations created by a finite tunneling amplitude. In the previously mentioned systems, the frustration essentially derives from the incompatibilities between geometry and interactions; in the Bose-Hubbard

* eduardo.rizzatti@ufrgs.br

model, the frustration is a consequence of the competition between lattice occupation and local interactions. The main ingredient, a ground-state residual entropy, is also present. Our methodology comprehends numerical tools for treating the many-body thermodynamics of the bosons: self-energy functional theory (SFT) calculations [51, 52] (closely related to BDMFT approaches) and finite-temperature perturbation theory (PT) [53, 54].

The paper is structured as follows. In Sec. II we describe the Bose-Hubbard model, its relevant parameters, and the methodologies employed in our numerical calculations. The double-peak structure of the specific heat is first discussed for the atomic limit in Sec. III. The emergence of residual entropies and a specific heat decomposition based on all possible transitions between the energy levels of the spectrum are also discussed. Section IV addresses the effects of a finite hopping amplitude, including the analysis of spectral and correlation functions. Our main findings and final considerations are summarized in Sec. V.

II. MODEL AND METHODS

In the Bose-Hubbard model [35–37], the itinerant bosons occupying the lowest-energy band in a lattice are described by the Hamiltonian

$$H = -J \sum_{\langle i,j \rangle} b_i^\dagger b_j + \frac{U}{2} \sum_i n_i(n_i - 1) - \mu \sum_i n_i, \quad (1)$$

where b_i^\dagger , b_i , n_i represent the bosonic creation, annihilation, and number operators at site i , respectively; μ is the chemical potential. The parameter U designates the on-site interaction (typically repulsive, taking positive values) and J accounts for the hopping amplitude, a kinetic term involving the probability of tunneling between first neighbor sites.

We explore simple cubic [38] and square lattice [46, 49] configurations, extensively studied in experiments throughout the last 20 years. The thermodynamic properties of the bosons are mapped through a variational and non-perturbative self-consistent approach, the self-energy functional theory derived by Hügel *et al.* [51, 52], based on the original works for fermions by Potthoff [55]. The formalism, which contemplates the $U(1)$ symmetry breaking and BDMFT approaches [56–60], relies on successive Legendre transformations of the free-energy functional Ω producing a new functional of the self-energies. In a general panorama, such approximation strategy constricts the self-energy domain to a subspace of self-energies regarding a simpler reference system. Consequently, the original problem is simplified into seeking stationary solutions of this new functional, which is exact, in terms of the reference system's free propagators. When appropriate, we also complement our results with finite-temperature perturbation theory around the atomic limit. Both methods are detailed in the Supplemental Material.

Given the equilibrium free energy Ω obtained from the previously cited techniques, the specific heat is explicitly given by

$$c_\mu = -\frac{T}{N_s} \left(\frac{\partial^2 \Omega}{\partial T^2} \right)_\mu = T \left(\frac{\partial s}{\partial T} \right)_\mu, \quad (2)$$

where T is the temperature and s is the thermodynamic entropy per site

$$s = -\frac{1}{N_s} \left(\frac{\partial \Omega}{\partial T} \right)_\mu, \quad (3)$$

considering N_s sites at a fixed chemical potential μ .

III. THE ATOMIC LIMIT ($J = 0$)

In the following, we show the double-peak structure of c_μ as a function of T , considering the atomic limit ($J = 0$). In the absence of the hopping amplitude, there is no superfluid phase and the bosons are found in a normal fluid state. The Hamiltonian described by Eq. (1) becomes

$$H^{(0)} = \frac{U}{2} \sum_i n_i(n_i - 1) - \mu \sum_i n_i, \quad (4)$$

a sum of single-site Hamiltonians $H_i^{(0)}$ which can be diagonalized by the number operators eigenvectors $|n_i\rangle$. Thus, the energy eigenvalue of a single site with occupation n is expressed by

$$E_n = \frac{U}{2} n(n - 1) - \mu n. \quad (5)$$

In this scenario, the grand-canonical partition function

$$\mathcal{Z}^{(0)}(T, \mu) = \text{Tr} \left[e^{-\beta H^{(0)}} \right] = \prod_{i=1}^{N_s} \mathcal{Z}_i^{(0)} = \left[\mathcal{Z}_1^{(0)} \right]^{N_s} \quad (6)$$

becomes simply a product of single-site partition functions

$$\mathcal{Z}_1^{(0)}(T, \mu) = \sum_{n=0}^{\infty} e^{-\beta E_n}, \quad (7)$$

where $\beta = 1/k_B T$ and k_B is the Boltzmann constant. The free-energy potential $\Omega^{(0)}$ follows directly from Eqs. (6) and (7) according to

$$\Omega^{(0)}(T, \mu) = -\frac{1}{\beta} \ln \mathcal{Z}^{(0)} = -\frac{N_s}{\beta} \ln \mathcal{Z}_1^{(0)}. \quad (8)$$

Fig. 1(a) portrays the specific heat c_μ as a function of the temperature T in a three-dimensional diagram including a wide range of chemical potential values (in different colors), with the loci of maxima represented as dotted and continuous black lines in the μT plane. At zero temperature, there are ground-state phase transitions (GSPT) between Mott insulators of successive occupation numbers whenever the chemical potential μ takes

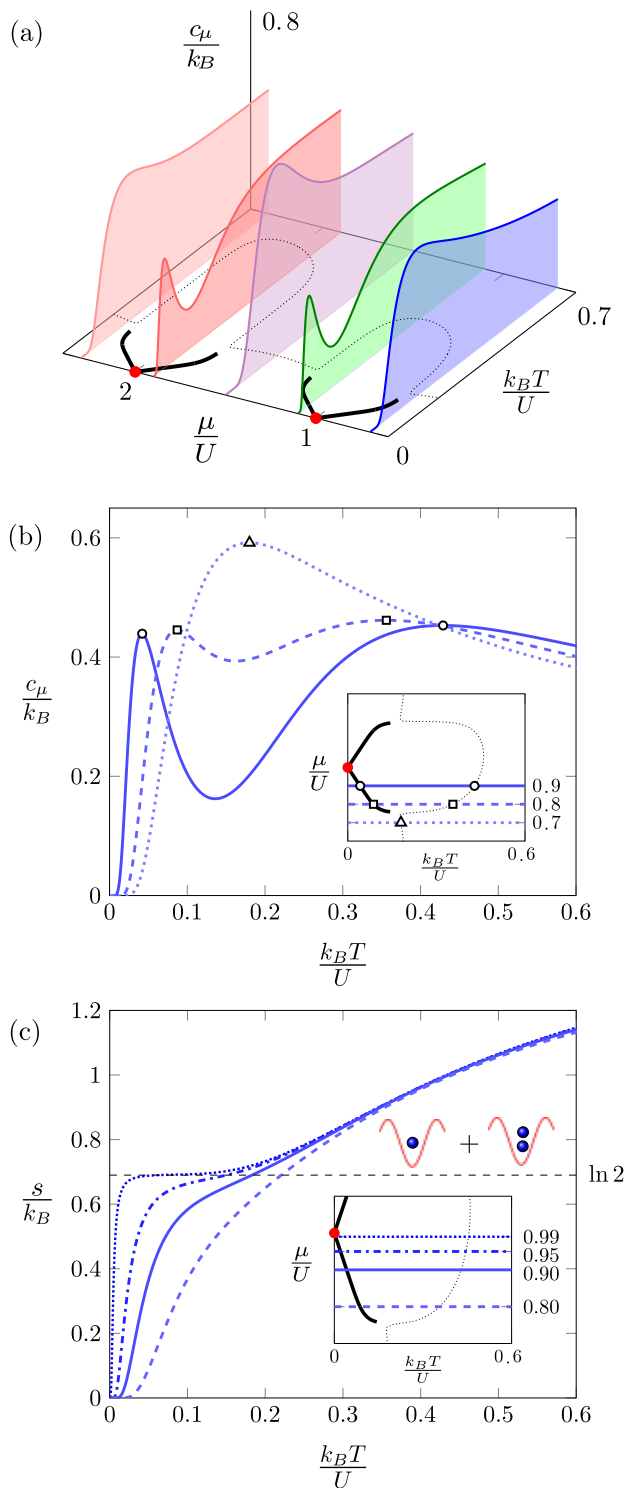


FIG. 1. Finite-temperature analysis of the specific heat and entropy in the atomic limit $J = 0$. (a) The 3D diagram portrays the specific heat c_μ as a function of the temperature T in a wide range of chemical potential values. The continuous and dotted black curves in the μT plane represent the loci of the maximum values attained by c_μ . Red dots denote ground-state phase transitions between Mott insulators. In (b) is shown a detailed vision on the temperature dependence of c_μ considering the values $\mu = 0.7U, 0.8U$ and $0.9U$, portrayed by the inset. Panel (c) contains the entropy per site s as temperature varies for $\mu = 0.8U, 0.9U, 0.95U$ and $0.99U$.

on integer values of the local interaction U [52, 61], shown as red dots. At higher temperatures, it is observed a maximum at any value of fixed μ , symbolized by dotted lines. However, as the chemical potential approaches integer values of the interaction, the specific heat develops another peak at low temperatures (the continuous black lines), which is connected to its corresponding GSPT. The low- and high-temperature maxima start to merge together as the chemical potential values move away from the integers values of U , finally coalescing in a single peak according to Fig. 1(b).

The entropy dependence on temperature illustrated in Fig. 1(c) suggests that the low-temperature maxima are related to a residual entropy per site of $k_B \ln 2$. This zero-point entropy is due to the degeneracy established at the GSPT between states with different occupations. As the chemical potential approaches the integer multiples of the local interaction, the entropy curves develop a sharp step towards the residual value $k_B \ln 2$ which induces a change in their concavities. This behavior leads to a Schottky-like peak at low temperatures close to the critical points.

A deeper understanding on the evolution of the reported double-peak structure can be attained by the following decomposition

$$c_\mu = \sum_{n < m} c_\mu^{(n,m)}, \quad (9)$$

demonstrated in Appendix A. The defined partial specific heat $c_\mu^{(n,m)}$ describes the fluctuations between the energy levels m and n according to

$$c_\mu^{(n,m)} = k_B \frac{\beta^2}{[\mathcal{Z}_1^{(0)}]^2} (E_n - E_m)^2 e^{-\beta(E_n + E_m)}. \quad (10)$$

Since the specific heat accounts for fluctuations in energy with respect to its mean value, the intuitive idea brought by this decomposition is to visualize the fluctuations in energy as a result of transitions between all possible energy levels. This outcome allows us to understand how these peaks behave and influence each other, isolating the relevance of each transition.

In Fig. 2 we present the specific heat as a function of temperature by continuous lines including four different values of chemical potential: (a) $\mu = 0.9U$, (b) $\mu = 1.1U$, (c) $\mu = 1.3U$ and (d) $\mu = 1.6U$. For each scenario, the most relevant partial contributions $c_\mu^{(n,m)}$ are addressed as the colored dotted lines, with the respective level transitions depicted accordingly. Figure 2(a) shows the $\mu = 0.9U$ case. The low-temperature peak appears due to the $|1\rangle \rightarrow |2\rangle$ transition. Other contributions add up to form the second maximum at a higher temperature; among them, the most relevant terms in this temperature range arise from the transitions $|1\rangle \rightarrow |0\rangle$ (red) and $|1\rangle \rightarrow |3\rangle$ (orange) which connect the states $|0\rangle$ and $|3\rangle$ to the ground state $|1\rangle$, respectively. In Fig. 2(b), for $\mu = 1.1U$, the ket $|2\rangle$ becomes the new

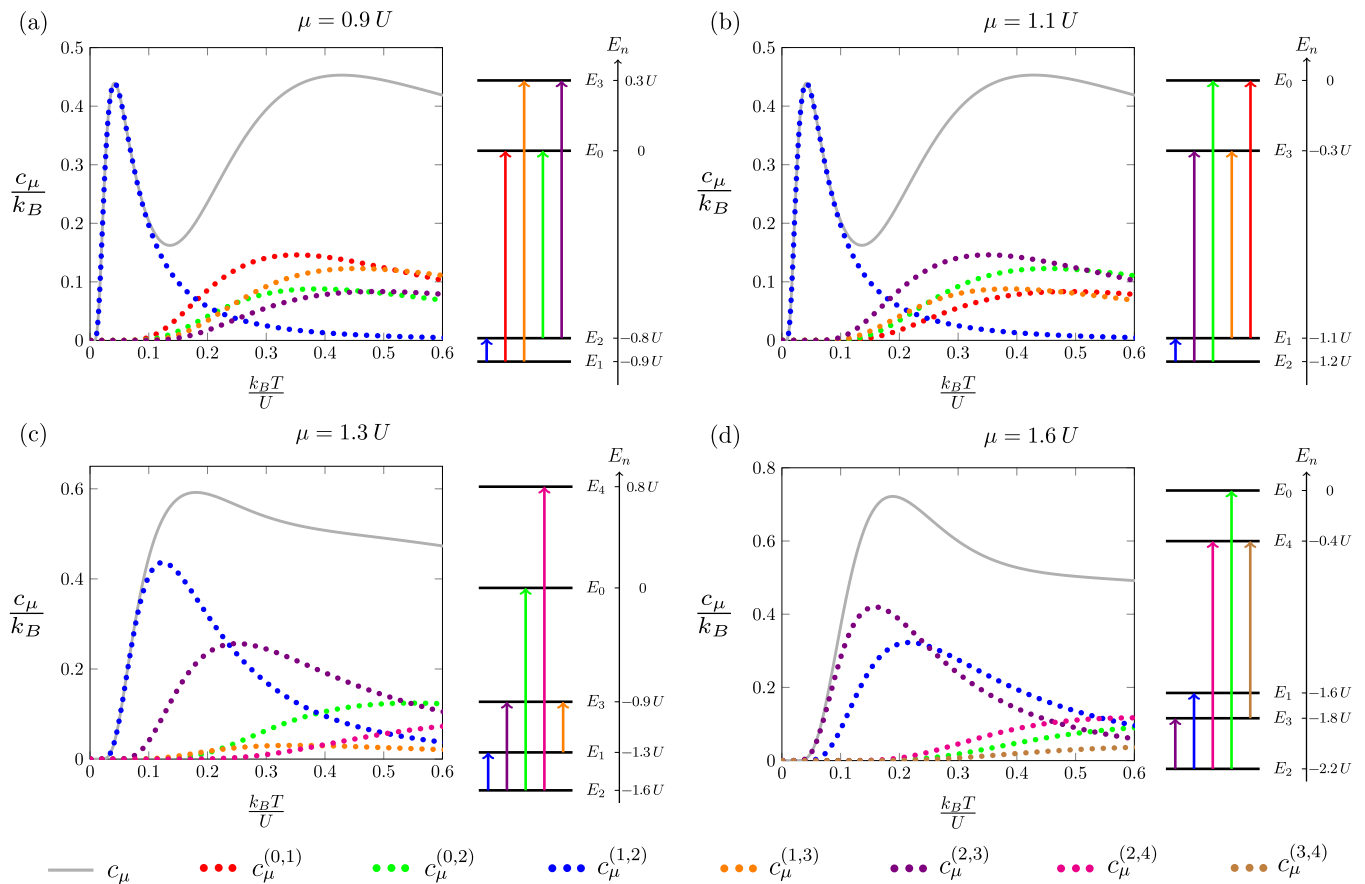


FIG. 2. The specific heat decomposition and its temperature behavior is exhibited considering four fixed values of chemical potential: (a) $\mu = 0.9U$, (b) $\mu = 1.1U$, (c) $\mu = 1.3U$ and (d) $\mu = 1.6U$. The dotted curves represent the contributions $c_\mu^{(n,m)}$ to the total specific heat c_μ , which is shown as the continuous curve. Each panel contains a diagram of energy levels assigning a different color to each transition $|n\rangle \rightarrow |m\rangle$ (with energies $E_n \rightarrow E_m$), referring to the respective term $c_\mu^{(n,m)}$.

ground state and the first peak persists due to the available transition $|2\rangle \rightarrow |1\rangle$. As a result of this new ground state, the contributions for the second maximum from $|2\rangle \rightarrow |0\rangle$ (green) and $|2\rangle \rightarrow |3\rangle$ (purple) become more prominent than the previous transitions $|1\rangle \rightarrow |0\rangle$ (red) and $|1\rangle \rightarrow |3\rangle$ (orange). In Fig. 2(c), where $\mu = 1.3U$, the transition $|2\rangle \rightarrow |3\rangle$ (purple) starts to gain relevance since the energy level E_3 approaches E_1 . As a consequence of these two competing contributions, the specific heat develops only one maximum. Figure 2(d), which displays $\mu = 1.6U$, finally shows E_3 becoming the first excited state, with $c^{(2,3)}$ the most relevant term at low temperatures. By increasing the chemical potential, another analogous cycle starts presenting the same fundamental mechanisms already explored.

IV. FINITE HOPPING ($J \neq 0$)

Including finite-hopping effects, the specific heat behavior with temperature for simple cubic and square lattices is illustrated in Figs. 3(a)-(d) and Figs. 3(e)-(h),

respectively. The observables were evaluated using the previously described SFT formalism. In this framework, we considered four values of tunneling: $J = 0.006U$, $J = 0.012U$, $J = 0.024U$ and $J = 0.042U$, at a fixed chemical potential $\mu = 0.9U$. Physically, such increasing tunneling amplitudes correspond to decreasing lattice potential depths, going from very deep lattices to shallower ones. The introduction of the kinetic term J gives rise to a superfluid phase which grows from the GSPT points [62]. The superfluid phase is represented in the blue area, with the superfluid to normal phase boundaries shown as dashed blue lines. The respective insets portray the μT phase diagrams.

First we analyze the three-dimensional case, exhibited in Figs. 3(a)-(d). Considering the chosen value $J = 0.006U$ in Fig. 3(a), the system is found in the normal phase and the two-peak structure of the specific heat remains present. For comparison reasons, we also indicate the corresponding atomic limit result as the gray continuous line. It is observed a clear reduction of the first peak when the hopping is slightly turned on; the second one, however, does not present relevant quantities

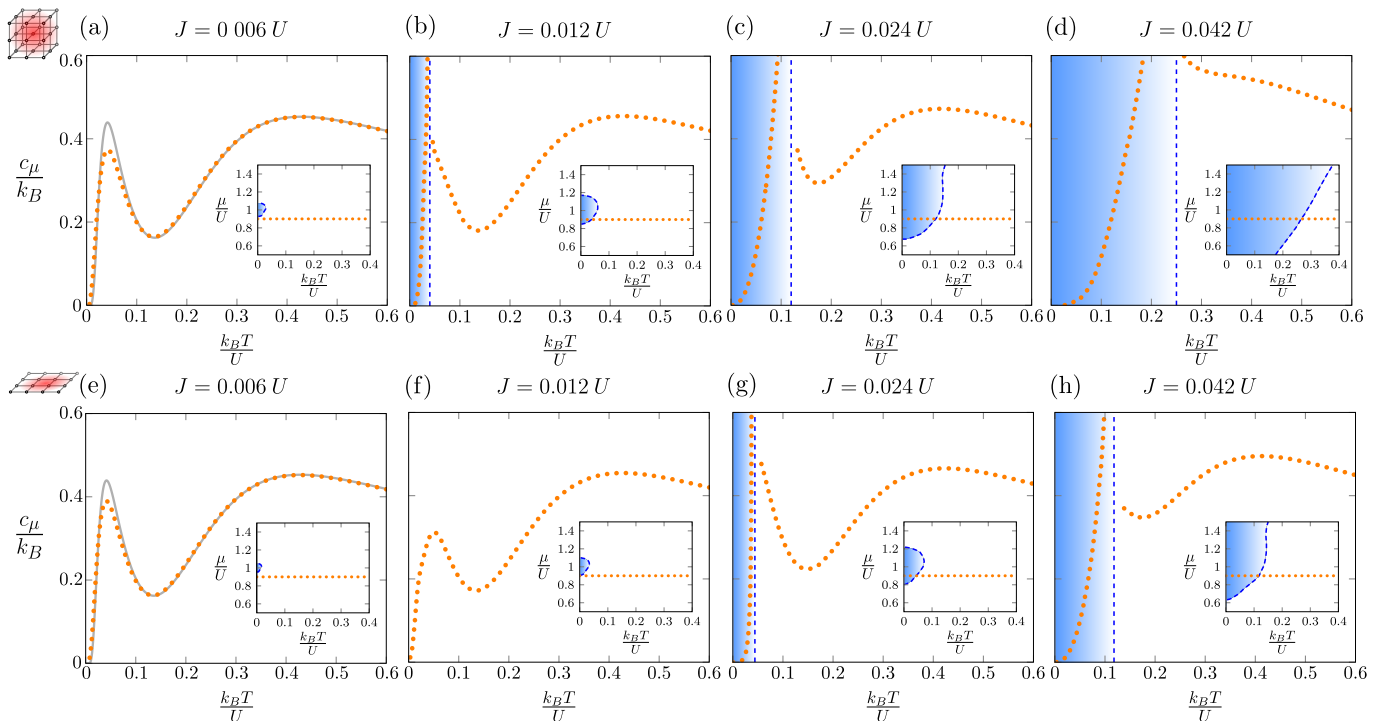


FIG. 3. The specific heat c_μ is shown as a function of the temperature T at constant $\mu = 0.9U$ for simple cubic (a)-(d) and square lattices (e)-(h) considering four different hopping amplitudes: (a) and (e) $J = 0.006U$ (the gray continuous lines are the corresponding atomic limits), (b) and (f) $J = 0.012U$, (c) and (g) $J = 0.024U$, (d) and (h) $J = 0.042U$. The superfluid domain is represented by the blue area, with the phase boundaries symbolized by the blue dashed lines. The insets exhibit the respective μT phase diagrams.

tive differences. Intuitively, as the low-temperature maximum derives from the energetic competition between two states, the introduction of the hopping breaks this degeneracy, mitigating its magnitude. A detailed analysis regarding such behavior is also developed in Subsecs. IV A and IV B, involving the analysis of spectral properties and correlation functions. By increasing the hopping to $J = 0.012U$, Fig. 3(b) shows the appearance of the superfluid phase. Inasmuch as response functions tend to grow in magnitude near continuous phase transitions, we detect an increasing of c_μ in the neighborhood of the phase transition. Consequently, the first peak turns into a critical divergence while the second one is still observed. Figure 3(c) portrays the $J = 0.024U$ scenario, where c_μ increases monotonically in the superfluid and the second maximum remains to be seen in the normal phase. For a larger hopping term $J = 0.042U$ in Fig. 3(d), the superfluid domain expands to an extent that the high-temperature peak disappears. Thus the two original maxima, born in the the atomic limit, are only verified in a perturbative regime.

Considering the same hopping values and $\mu = 0.9U$, Figs. 3(e)-(h) depict the specific heat dependence on temperature for the square lattice configuration. The superfluid domain for each tunneling amplitude is smaller when compared to the three-dimensional picture. Indeed, since there is a reduction on the number of available di-

rections for a particle to hop in a square lattice, the superfluid region shrinks. Therefore, it takes larger values of J to observe in a square lattice the same effects seen in a simple cubic one. For $J = 0.006U$, Fig. 3(e) shows two peaks in the normal phase, with the low-temperature one appearing reduced in comparison to the atomic limit (continuous line). Increasing J , Fig. 3(f) shows that such peak is diminished even further for $J = 0.012U$. Finally, Figs. 3(g) and 3(h) demonstrate that the rise of the superfluid phase starts to destroy the developed peaks.

In the next Subsections we analyze the two peaks of c_μ in the presence of hopping in greater detail. The $J = 0.006U$ case, which preserves such property in two and three dimensions, is explored inside the normal phase.

A. Spectral Functions

As spectral functions reveal how states occupy a given energy interval, they also provide useful information on the specific heat behavior. The spectral function $A(\mathbf{k}, \omega)$, a generalized density of states in frequency ω and momentum space \mathbf{k} , is defined by the imaginary part of the retarded Green's function [63] according to

$$A(\mathbf{k}, \omega) = -\frac{1}{\pi} \Im[G^R(\mathbf{k}, \omega)]. \quad (11)$$

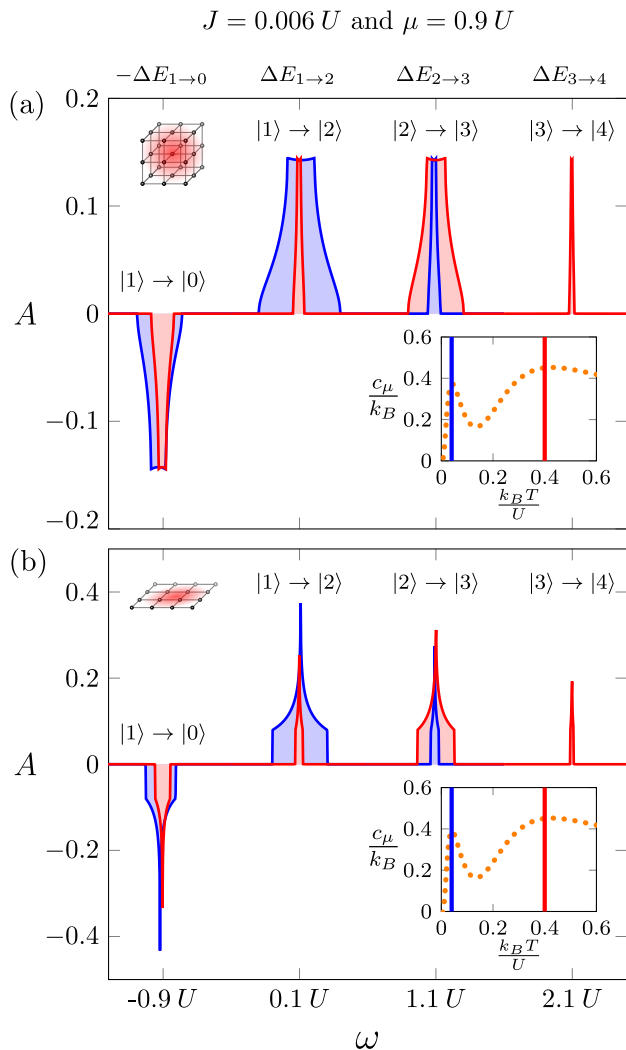


FIG. 4. The local spectral function A versus the real frequency ω at fixed $J = 0.006U$ and $\mu = 0.9U$, considering simple cubic (a) and square lattices (b). The two temperatures addressed $k_B T = 0.04U$ (blue) and $k_B T = 0.4U$ (red), located around each maximum of the specific heat, are marked in the inset panel. Above each resonance, the most significant transitions $|n\rangle \rightarrow |m\rangle$ are identified.

This follows from the Matsubara Green's function by analytic continuation, applying the prescription $i\omega_n \rightarrow \omega + i0^+$ where $\omega_n = 2\pi n/\beta$. Its integration over the momentum yields the local spectral function

$$A(\omega) = \frac{1}{N_s} \sum_{\mathbf{k}} A(\mathbf{k}, \omega). \quad (12)$$

Concerning other range of parameters, the spectral properties of the Bose-Hubbard were also discussed using SFT [51], as well as employing QMC and BDMFT methods [64, 65]. In Figs. 4(a) and 4(b), we show the behavior of A as ω is varied considering $\mu = 0.9U$ and $J = 0.006U$ in the SFT framework for simple cubic and square lattices, respectively. These are the same scenarios reported by Figs. 3(a) and 3(e). The temper-

atures addressed in our analysis, $k_B T = 0.04U$ (blue) and $k_B T = 0.4U$ (red), are located near each maximum of c_μ as the inset panel illustrates. The noticed resonances can be thought in terms of transitions between local occupation number states, which are eigenvectors of the zero-hopping Hamiltonian explored in Sec. III. As demonstrated in Appendix B, the local spectral function in the atomic limit reads as

$$A^{(0)}(\omega) = \frac{1}{Z^{(0)}} \sum_n \delta(\omega - \Delta E_{n \rightarrow n+1}) (n+1) e^{-\beta E_n} - \frac{1}{Z^{(0)}} \sum_n \delta(\omega - \Delta E_{n-1 \rightarrow n}) n e^{-\beta E_n}, \quad (13)$$

a collection of delta functions centered around the energy level transitions $\Delta E_{n \rightarrow m} = E_m - E_n$. With the perturbative inclusion of hopping, the relevant Hubbard bands emerge from such values, with a particular shape reflecting the dimensionality of each case.

Regarding the low-temperature regime (blue curve), there are contributions from only three transitions: singlon-holon $|1\rangle \rightarrow |0\rangle$, singlon-doublon $|1\rangle \rightarrow |2\rangle$ and doublon-triplon $|2\rangle \rightarrow |3\rangle$. Given its larger width, the most relevant of them is the portion $|1\rangle \rightarrow |2\rangle$, because the chosen μ value is close to the transition between states of occupation number 1 and 2. These states at low temperatures produce the Schottky peak as explained in the $J = 0$ scenario. Regarding the second maximum (red curve), other states of higher energy become available such as the transition triplon-quadruplon $|3\rangle \rightarrow |4\rangle$, while the transition singlon-doublon $|1\rangle \rightarrow |2\rangle$ are less probable to happen.

B. Correlations and the Double Peaks

As pointed out by Figs. 3(a) and 3(e), the first maximum appearing in the specific heat versus temperature plot presents a reduction when compared to the atomic limit. In Fig. 5, we supply a detailed view on this subject considering the simple cubic setup for deep lattices $J = 0.006U$ (the results in the square lattice are quantitatively similar) and three values of chemical potential: $\mu = 0.7U$ (purple), $\mu = 0.8U$ (green), and $\mu = 0.9U$ (orange). Colored dots symbolize SFT calculations while the respective continuous lines represent the perturbation theory until second order on J/U . Figure 5(a) exhibits c_μ as T varies in the described scenario, including the zero-hopping cases as continuous gray lines. We observe that the deviations from the $J = 0$ situation become more prominent as the chemical potential approaches $\mu = 1.0U$. Since the specific heat is essentially a second derivative of the free energy with respect to the temperature, Fig. 5(b) shows the difference $\Delta\Omega = \Omega - \Omega^{(0)}$ of the system's free energy Ω in the presence of hopping relative to its atomic limit $\Omega^{(0)}$. When $\mu = 0.7U$, the free energy is slightly reduced by the introduction of the tunneling term. However, for $\mu = 0.8U$ and $\mu = 0.9U$, important variations in a low-temperature regime are verified.

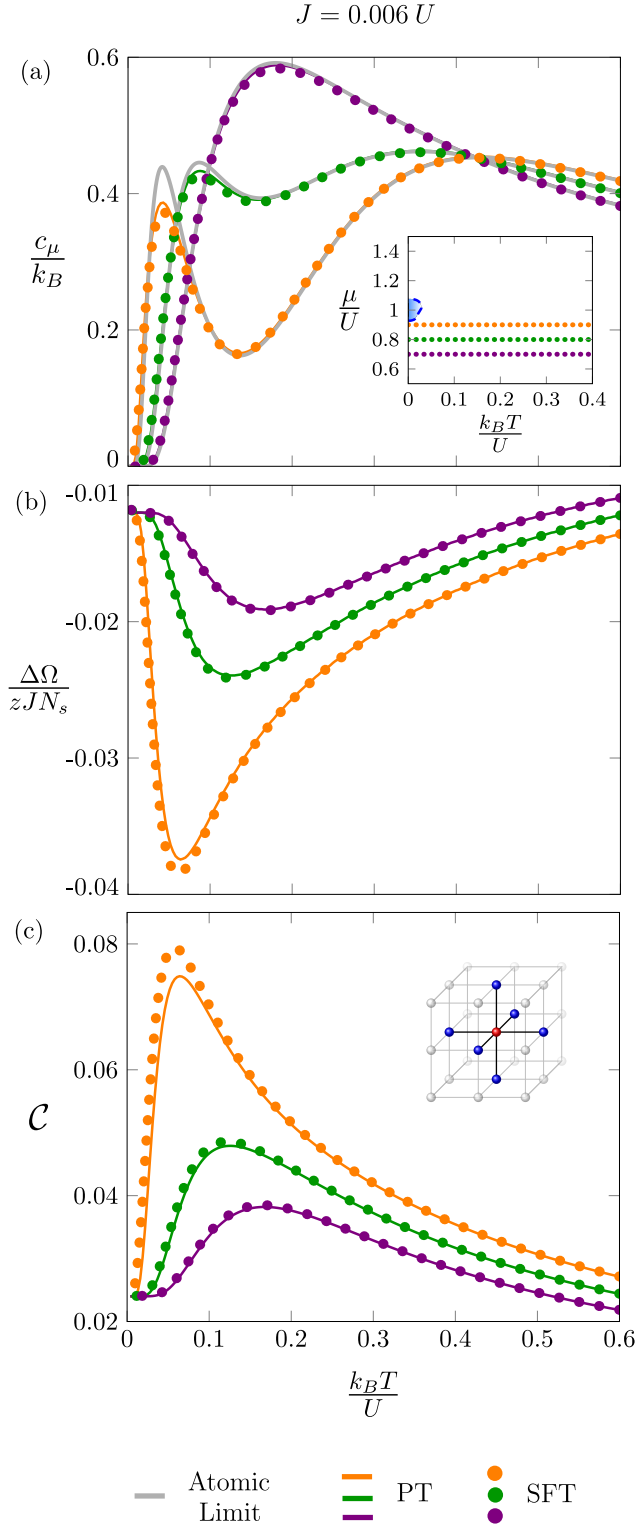


FIG. 5. The specific heat c_μ (a), free energy variation $\Delta\Omega$ (b) and atom-atom correlation \mathcal{C} (c) are shown as functions of temperature at $J = 0.006U$. As the inset phase diagram μT reveals, three values of chemical potential are considered: $\mu = 0.7U$ (purple), $\mu = 0.8U$ (green), and $\mu = 0.9U$ (orange). The dots represent SFT calculations while the respective colored continuous lines symbolize the PT results. The atomic limit of c_μ is shown as grey continuous curves in (a).

The prominent curvature $\Delta\Omega$ implies a relevant second derivative. This information gets translated into a contribution to c_μ , responsible for the magnitude reduction in the first maximum.

The question remaining is what physical mechanism generates such curvature in the free energy. Since the inclusion of the tunneling term induces correlations among particles located at different sites j' and j , we analyze the atom-atom correlation function [66, 67]

$$\mathcal{C}_{j'j} = \langle b_{j'}^\dagger b_j \rangle, \quad (14)$$

related to the imaginary-time Green's function

$$\mathcal{G}_{jj'}(\tau, \tau') = -\langle \mathcal{T}[b_j(\tau)b_{j'}^\dagger(\tau')] \rangle \quad (15)$$

through

$$\mathcal{C}_{j'j} = -G_{jj'}(0, 0^+). \quad (16)$$

Accordingly, these correlations can be indirectly probed as they are connected to the Fourier transform of the momentum distribution function

$$n(\mathbf{k}) = \frac{|w(\mathbf{k})|^2}{N_s} \sum_{j,j'} \mathcal{C}_{j'j} e^{-i\mathbf{k}(\mathbf{r}_{j'} - \mathbf{r}_j)}, \quad (17)$$

where $w(\mathbf{k})$ is the Fourier transform of the Wannier function. The quantity $n(\mathbf{k})$ is measured by the time-of-flight absorption experiments, in which the trapping field is turned off enabling the cloud of atoms to expand during a certain amount of time [68, 69]. More specifically, we focus our attention on the atom-atom correlation function between first neighbors (since the particles of the model are able to hop to first-neighbor sites), denoted simply as \mathcal{C} due to the system's homogeneity. In Fig. 5(c) we show \mathcal{C} as a function of the temperature, mirroring the parameters of Figs. 5(a) and 5(b). Similarly to the free energy corrections $\Delta\Omega$, the correlations become important as we increase the chemical potential towards the integer values of U , developing a sharp peak at low temperatures $k_B T \approx 0.1U$.

The impact of the correlations on the free energy can be examined in an analytical perspective. Indeed, it is possible to exactly determine the free energy from the atom-atom correlation function based on the introduction of a continuous coupling parameter, following Refs. [70, 71]. First, we parametrize the Hamiltonian of Eq. (1) in the form

$$H^{(\lambda)} = H^{(0)} + \lambda \mathcal{H}, \quad (18)$$

where $H^{(0)}$ corresponds to the atomic limit defined in Eq. (4) and \mathcal{H} is the kinetic term

$$\mathcal{H} = -J \sum_{\langle i,j \rangle} b_i^\dagger b_j. \quad (19)$$

Note that the value $\lambda = 0$ correspond to the atomic limit, while $\lambda = 1$ recovers the original model considered, with

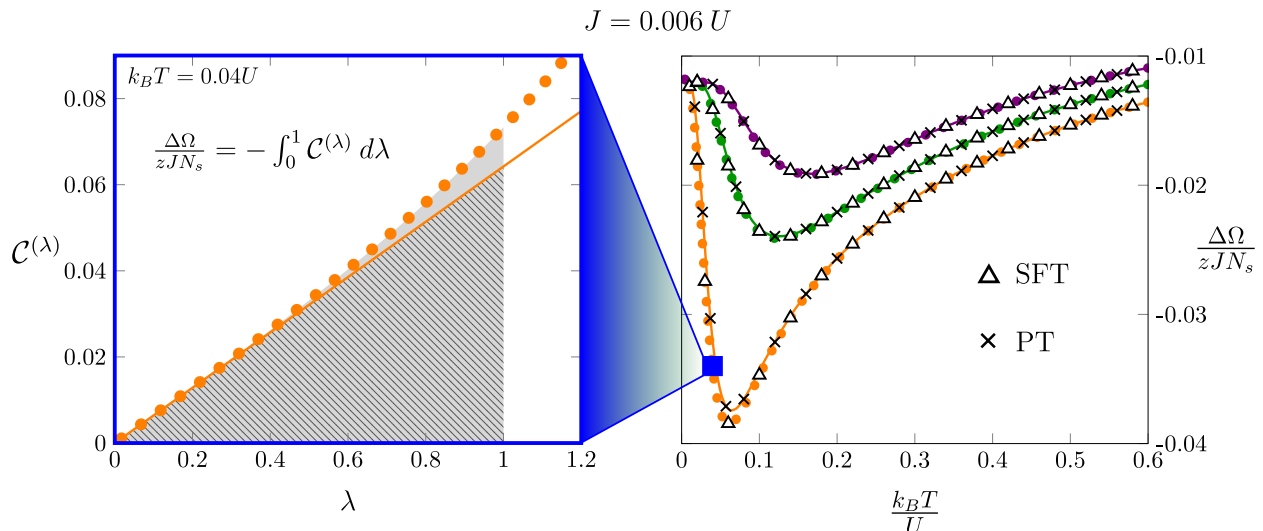


FIG. 6. In the right panel, $\Delta\Omega$ is plotted against temperature T showing the agreement between points (crosses and triangles) evaluated through Eq. (21) and the curves from Fig. 5(b). Crosses and triangles correspond to PT and SFT calculations, respectively. For $k_B T = 0.04U$ and $\mu = 0.9U$, the left panel illustrates how these points are determined by integration of the correlation function $\mathcal{C}(\lambda)$.

$H^{(1)} = H$. As demonstrated in Appendix C, the change in free energy caused by the hopping reads as

$$\Delta\Omega = \int_0^1 \langle \mathcal{H} \rangle_\lambda d\lambda, \quad (20)$$

considering thermal averages $\langle \dots \rangle_\lambda$ taken with respect to the Hamiltonian of Eq. (18). The definitions from Eqs. (19) and (14) substituted into Eq. (20) lead to the exact expression

$$\Delta\Omega = -zJN_s \int_0^1 \mathcal{C}(\lambda) d\lambda. \quad (21)$$

The term $\mathcal{C}(\lambda) = \langle b_j^\dagger b_{j'} \rangle_\lambda$ is simply the atom-atom correlation function between first neighbors j and j' , thermally averaged at a hopping value λJ . This expression associates the theoretical free energy to the atom-atom correlation, an indirect measurable quantity, by a process of charging up the tunneling amplitude until the desired value. Through Fig. 6, we verify the agreement between both sides of Eq. (21) considering SFT and perturbative methods. In particular, perturbation theory up to second order yields the direct relation

$$\Delta\Omega = -\frac{zJN_s}{2} \mathcal{C} + \mathcal{O}(J^4). \quad (22)$$

Therefore, the low-temperature correlations, which grow near integers multiples of the interaction, cause an important curvature change in the free energy, whose impact is revealed in the reduction of the first maximum of the specific heat.

V. CONCLUSIONS

We studied in detail the specific heat dependence on temperature of bosons described by the Bose-Hubbard model, considering simple cubic and square lattice geometries. Our theoretical analysis comprehended numerical methods, including the self-energy functional theory (a non-perturbative and self-consistent approach, suitable for the description of both normal and superfluid phases) complemented by finite-temperature perturbation theory around the atomic limit. Our results revealed an anomalous double-peak behavior of the specific heat capacity as temperature is varied, connected to a residual entropy established in the atomic limit. Indeed, for $J = 0$, the anomaly is present for values of μ near ground-state phase transitions between Mott insulators of successive occupation number. In this regime, such ground-state macroscopic degeneracy is originated from the energetic competition between the local interaction U and the chemical potential μ . While the local interaction is repulsive and tends to decrease the occupation of a single site, the chemical potential acts in the opposite direction, favoring occupation. Specifically, when μ takes on integer values of the on-site repulsion (which is exactly the energy required to add another particle at a given site), the system becomes frustrated energetically. This energetic frustration gets translated into an additional low-temperature maximum of c_μ as a function of T . In this framework, we also demonstrated a general decomposition of the specific heat, based on all possible transitions realizable between the energy eigenvalues of the system's spectrum. This result enabled us to identify the relevant energy level transitions and how the noted peaks evolve as the chemical potential is varied.

For finite hopping amplitudes, the superfluid phase tends to destroy the reported maxima. Indeed, the double-peak structure is only observed inside the normal phase and in a perturbative regime, corresponding to very deep optical lattices. Additionally, the low-temperature maximum presents a reduced magnitude when compared to zero-hopping scenario. This can be explained by the effects of correlations created between first neighbors (enabled by the hopping), producing a prominent change in the free energy's curvature. Such connection was established by an exact and general result relating the free energy change to the building up of correlations as the tunneling amplitude is turned on. Spectral functions were also used to illustrate the relevant excitations dominant at each maximum.

VI. ACKNOWLEDGMENTS

We acknowledge the financial support of the Brazilian funding agencies FAPDF, CNPq and CAPES.

Appendix A: Decomposition of the Specific Heat

In order to demonstrate Eq. (10), we explore the heat capacity C , its extensive related function. In general terms, the heat capacity accounts for fluctuations in energy with respect to its mean value according to

$$C = -T \left(\frac{\partial^2 \Omega}{\partial T^2} \right) = k_B \beta^2 (\langle E^2 \rangle - \langle E \rangle^2). \quad (\text{A1})$$

The fluctuations around the mean value $(\delta E)^2 = \langle E^2 \rangle - \langle E \rangle^2$ are explicitly determined by the averages

$$\langle E^2 \rangle = \frac{1}{\mathcal{Z}} \sum_n E_n^2 e^{-\beta E_n} \quad (\text{A2})$$

and

$$\langle E \rangle^2 = \frac{1}{\mathcal{Z}^2} \sum_{n,m} E_n E_m e^{-\beta(E_n + E_m)}, \quad (\text{A3})$$

where

$$\mathcal{Z} = \sum_n e^{-\beta E_n} \quad (\text{A4})$$

is the partition function. Alternatively, it is possible to express Eq. (A2) in the form

$$\begin{aligned} \langle E^2 \rangle &= \left(\frac{1}{\mathcal{Z}} \sum_n E_n^2 e^{-\beta E_n} \right) \times \left(\frac{1}{\mathcal{Z}} \sum_m e^{-\beta E_m} \right) \\ &= \frac{1}{\mathcal{Z}^2} \sum_{n,m} E_n^2 e^{-\beta(E_n + E_m)}, \end{aligned} \quad (\text{A5})$$

which allows us to write the heat capacity according to

$$C = k_B \frac{\beta^2}{\mathcal{Z}^2} \sum_{n,m} (E_n^2 - E_n E_m) e^{-\beta(E_n + E_m)}. \quad (\text{A6})$$

Since the terms $n = m$ are zero, we separate the sum into two parts

$$\begin{aligned} C &= k_B \frac{\beta^2}{\mathcal{Z}^2} \sum_{n < m} (E_n^2 - E_n E_m) e^{-\beta(E_n + E_m)} \\ &\quad + k_B \frac{\beta^2}{\mathcal{Z}^2} \sum_{n > m} (E_n^2 - E_n E_m) e^{-\beta(E_n + E_m)}. \end{aligned} \quad (\text{A7})$$

By exchanging the labels $n \rightarrow m$ and $m \rightarrow n$ in the second term, we obtain

$$\begin{aligned} C &= k_B \frac{\beta^2}{\mathcal{Z}^2} \sum_{n < m} (E_n^2 - E_n E_m) e^{-\beta(E_n + E_m)} \\ &\quad + k_B \frac{\beta^2}{\mathcal{Z}^2} \sum_{m > n} (E_m^2 - E_m E_n) e^{-\beta(E_m + E_n)} \\ &= k_B \frac{\beta^2}{\mathcal{Z}^2} \sum_{n < m} (E_n^2 - E_n E_m + E_m^2 - E_m E_n) e^{-\beta(E_n + E_m)} \\ &= k_B \frac{\beta^2}{\mathcal{Z}^2} \sum_{n < m} (E_n - E_m)^2 e^{-\beta(E_n + E_m)}. \end{aligned} \quad (\text{A8})$$

Such decomposition impels the definition of the partial specific heat $c^{(n,m)}$, describing the fluctuations between the energy levels m and n

$$C^{(n,m)} = k_B \frac{\beta^2}{\mathcal{Z}^2} (E_n - E_m)^2 e^{-\beta(E_n + E_m)}. \quad (\text{A9})$$

Therefore, the heat capacity becomes simply the sum of the defined partial components

$$C = \sum_{n < m} C^{(n,m)}. \quad (\text{A10})$$

This result enables us to analyze and filter the relevance of each energy level transitions.

Appendix B: Spectral Function in the Atomic Limit

For $J = 0$, the local one-particle Green's function in Matsubara space is given by

$$G^{(0)}(i\omega_n) = \frac{1}{\mathcal{Z}^{(0)}} \sum_{n,m} \frac{\langle n|b|m\rangle \langle m|b^\dagger|n\rangle}{i\omega_n + E_n - E_m} (e^{-\beta E_n} - e^{-\beta E_m}),$$

when expressed using the Lehmann representation [63]. For interpretation purposes, it is decomposed into particle and hole excitation branches [65] according to

$$G^{(0)}(i\omega_n) = G_p^{(0)}(i\omega_n) + G_h^{(0)}(i\omega_n), \quad (\text{B1})$$

where

$$G_p^{(0)}(i\omega_n) = \frac{1}{\mathcal{Z}^{(0)}} \sum_{n,m} \frac{\langle n|b|m\rangle \langle m|b^\dagger|n\rangle}{i\omega_n + E_n - E_m} e^{-\beta E_n} \quad (\text{B2})$$

and

$$G_h^{(0)}(i\omega_n) = \frac{1}{\mathcal{Z}^{(0)}} \sum_{n,m} \frac{\langle m|b|n\rangle \langle n|b^\dagger|m\rangle}{i\omega_n + E_m - E_n} e^{-\beta E_n}. \quad (\text{B3})$$

By analytical continuation, we determine the retarded Green's function $G_R^{(0)}(\omega) = G^{(0)}(\omega + i\eta)$, with $\eta \rightarrow 0^+$. Also, the definition of the local spectral function of Eq. (11) implies

$$\begin{aligned} A(\omega) &= -\frac{1}{\pi} \Im[G_R^{(0)}(\omega)] \\ &= \frac{1}{\mathcal{Z}^{(0)}} \sum_{n,m} \delta(\omega - \Delta E_{n \rightarrow m}) |\langle n|b|m\rangle|^2 e^{-\beta E_n} \\ &\quad - \frac{1}{\mathcal{Z}^{(0)}} \sum_{n,m} \delta(\omega - \Delta E_{n \rightarrow m}) |\langle m|b|n\rangle|^2 e^{-\beta E_n}, \end{aligned}$$

as a consequence of the limit

$$\lim_{\eta \rightarrow 0^+} \frac{1}{(\omega - \Delta E) + i\eta} = -\pi \delta(\omega - \Delta E). \quad (\text{B4})$$

The explicit evaluation of the previous matrix elements yields

$$\begin{aligned} A^{(0)}(\omega) &= \frac{1}{\mathcal{Z}^{(0)}} \sum_n \delta(\omega - \Delta E_{n \rightarrow n+1}) (n+1) e^{-\beta E_n} \\ &\quad - \frac{1}{\mathcal{Z}^{(0)}} \sum_n \delta(\omega - \Delta E_{n-1 \rightarrow n}) n e^{-\beta E_n}, \quad (\text{B5}) \end{aligned}$$

which shows the atomic limit spectral function as a collection delta functions at the consecutive transitions $|n\rangle \rightarrow |n+1\rangle$. This analysis makes explicit that the negative sign contributions of A comes from the hole excitation branch.

Appendix C: Correlations and free energy

In Subsec. IV B we presented how the free energy is obtained from the atom-atom correlation function according to Eq. (21). To demonstrate this relation, we parametrize the system's Hamiltonian in the form $H^{(\lambda)} = H^{(0)} + \lambda \mathcal{H}$ according to Eqs. (18) and (19), interpolating the atomic limit $H^{(0)}$ and the original Hamiltonian $H^{(1)}$ as λ continuously varies between 0 and 1.

The corresponding partition function is given by the

trace

$$\mathcal{Z}^{(\lambda)} = \text{Tr} \left[e^{-\beta H^{(\lambda)}} \right], \quad (\text{C1})$$

from which we extract the free energy

$$\Omega^{(\lambda)} = -\frac{1}{\beta} \ln \mathcal{Z}^{(\lambda)}. \quad (\text{C2})$$

The derivative of $\Omega^{(\lambda)}$ with respect to λ provides

$$\begin{aligned} \frac{d\Omega^{(\lambda)}}{d\lambda} &= -\frac{1}{\beta} \frac{\text{Tr} \left[(-\beta \mathcal{H}) e^{-\beta H^{(\lambda)}} \right]}{\text{Tr} \left[e^{-\beta H^{(\lambda)}} \right]} \\ &= \frac{\text{Tr} \left[\mathcal{H} e^{-\beta H^{(\lambda)}} \right]}{\text{Tr} \left[e^{-\beta H^{(\lambda)}} \right]} = \langle \mathcal{H} \rangle_\lambda. \quad (\text{C3}) \end{aligned}$$

On the other hand, the free energy variation follows immediately from the integration

$$\int_0^1 \frac{d\Omega^{(\lambda)}}{d\lambda} d\lambda = \Omega - \Omega^{(0)} = \Delta\Omega, \quad (\text{C4})$$

because $\Omega^{(1)} = \Omega$. By using the results of Eq. (C3) into Eq. (C4), we get

$$\Delta\Omega = \int_0^1 \langle \mathcal{H} \rangle_\lambda d\lambda. \quad (\text{C5})$$

Furthermore, the expression for the tunneling term \mathcal{H} of Eq. (19) yields

$$\begin{aligned} \Delta\Omega &= -J \sum_{\langle i,j \rangle} \int_0^1 \langle b_i^\dagger b_j \rangle_\lambda d\lambda \\ &= -J \sum_{\langle i,j \rangle} \int_0^1 \mathcal{C}_{ij}^{(\lambda)} d\lambda, \quad (\text{C6}) \end{aligned}$$

where

$$\mathcal{C}_{ij}^{(\lambda)} = \langle b_i^\dagger b_j \rangle_\lambda \quad (\text{C7})$$

is the correlation function considering first neighbors i and j , evaluated through a thermal average at a hopping λJ . For a homogeneous system the summation over all first neighbors yields zN_s , simplifying Eq. (C6) to

$$\Delta\Omega = -zJN_s \int_0^1 \mathcal{C}^{(\lambda)} d\lambda. \quad (\text{C8})$$

-
- [1] E. S. R. Gopal, *Specific Heats at Low Temperatures* (Springer US, Boston, MA, 1966).
[2] M. d. Souza, R. Paupitz, A. Seridonio, and R. E. Lagos, *Brazilian Journal of Physics* **46**, 206 (2016).
[3] J. S. Gardner, M. J. P. Gingras, and J. E. Greedan, *Reviews of Modern Physics* **82**, 53 (2010).
[4] A. P. Ramirez, A. Hayashi, R. J. Cava, R. Siddharthan, and B. S. Shastry, *Nature* **399**, 333 (1999).

- [5] K. Matsuhira, Z. Hiroi, T. Tayama, S. Takagi, and T. Sakakibara, *Journal of Physics: Condensed Matter* **14**, L559 (2002).
[6] Z. Hiroi, K. Matsuhira, S. Takagi, T. Tayama, and T. Sakakibara, *Journal of the Physical Society of Japan* **72**, 411 (2003).
[7] N. Hamaguchi, T. Matsushita, N. Wada, Y. Yasui, and M. Sato, *Physical Review B* **69**, 132413 (2004).

- [8] X. Ke, D. V. West, R. J. Cava, and P. Schiffer, *Physical Review B* **80**, 144426 (2009).
- [9] A. M. Hallas, A. M. Arevalo-Lopez, A. Z. Sharma, T. Munsie, J. P. Attfield, C. R. Wiebe, and G. M. Luke, *Physical Review B* **91**, 104417 (2015).
- [10] N. P. Raju, E. Gmelin, and R. K. Kremer, *Physical Review B* **46**, 5405 (1992).
- [11] R. Yamanaka, K. Matsubayashi, Y. Saiga, T. Kawae, and Y. Uwatoko, *Journal of Physics: Conference Series* **391**, 012078 (2012).
- [12] S. Lucas, K. Grube, C.-L. Huang, A. Sakai, S. Wunderlich, E. L. Green, J. Wosnitza, V. Fritsch, P. Gegenwart, O. Stockert, and H. v. Löhneysen, *Physical Review Letters* **118**, 107204 (2017).
- [13] J. Brambleby, P. A. Goddard, J. Singleton, M. Jaime, T. Lancaster, L. Huang, J. Wosnitza, C. V. Topping, K. E. Carreiro, H. E. Tran, Z. E. Manson, and J. L. Manson, *Physical Review B* **95**, 024404 (2017).
- [14] L. Zhong, X. Wang, M. Rong, and Y. Cressault, *The European Physical Journal D* **70**, 233 (2016).
- [15] J. Ipsen, O. Mouritsen, and M. Zuckermann, *Biophysical Journal* **56**, 661 (1989).
- [16] D. Jesenek, S. Kralj, G. Cordoyiannis, and Z. Kutnjak, *Molecular Crystals and Liquid Crystals* **546**, 3/[1473] (2011).
- [17] V. Elser, *Physical Review Letters* **62**, 2405 (1989).
- [18] J. B. Parkinson and J. Timonen, *Journal of Physics: Condensed Matter* **12**, 8669 (2000).
- [19] A. V. Syromyatnikov and S. V. Maleyev, *Journal of Experimental and Theoretical Physics Letters* **79**, 221 (2004).
- [20] N. P. Konstantinidis, *Physical Review B* **72**, 064453 (2005).
- [21] D. V. Efremov and R. A. Klemm, *Physical Review B* **74**, 064408 (2006).
- [22] A. Hucht, S. Sahoo, S. Sil, and P. Entel, *Physical Review B* **84**, 104438 (2011).
- [23] M. J. Harris, S. T. Bramwell, P. C. W. Holdsworth, and J. D. M. Champion, *Physical Review Letters* **81**, 4496 (1998).
- [24] R. G. Melko, B. C. den Hertog, and M. J. P. Gingras, *Physical Review Letters* **87**, 067203 (2001).
- [25] R. Mejdani and A. Lambros, *physica status solidi (b)* **196**, 433 (1996).
- [26] K. Karlová, J. Strečka, and T. Madaras, *Physica B: Condensed Matter* **488**, 49 (2016).
- [27] E. Jurčišinová and M. Jurčišin, *Journal of Magnetism and Magnetic Materials* **451**, 137 (2018).
- [28] E. Jurčišinová and M. Jurčišin, *Physical Review E* **97**, 052129 (2018).
- [29] T. Nakanishi and S. Yamamoto, *Physical Review B* **65**, 214418 (2002).
- [30] R. Moessner and A. P. Ramirez, *Physics Today* **59**, 24 (2006).
- [31] L. Pauling, *Journal of the American Chemical Society* **57**, 2680 (1935).
- [32] J. D. Bernal and R. H. Fowler, *The Journal of Chemical Physics* **1**, 515 (1933).
- [33] W. F. Giauque and J. W. Stout, *Journal of the American Chemical Society* **58**, 1144 (1936).
- [34] L. Balents, *Nature* **464**, 199 (2010).
- [35] M. P. A. Fisher, P. B. Weichman, G. Grinstein, and D. S. Fisher, *Physical Review B* **40**, 546 (1989).
- [36] D. Jaksch, C. Bruder, J. I. Cirac, C. W. Gardiner, and P. Zoller, *Physical Review Letters* **81**, 3108 (1998).
- [37] K. V. Krutitsky, *Physics Reports* **607**, 1 (2016).
- [38] M. Greiner, O. Mandel, T. Esslinger, T. W. Hänsch, and I. Bloch, *Nature* **415**, 39 (2002).
- [39] D. Jaksch, H.-J. Briegel, J. I. Cirac, C. W. Gardiner, and P. Zoller, *Physical Review Letters* **82**, 1975 (1999).
- [40] H.-J. Briegel, T. Calarco, D. Jaksch, J. I. Cirac, and P. Zoller, *Journal of Modern Optics* **47**, 415 (2000).
- [41] S. Sachdev, *Quantum Phase Transitions* (Cambridge University Press, Cambridge, 2011).
- [42] P. Windpassinger and K. Sengstock, *Reports on Progress in Physics* **76**, 086401 (2013).
- [43] M. Lewenstein, A. Sanpera, V. Ahufinger, B. Damski, A. Sen(De), and U. Sen, *Advances in Physics* **56**, 243 (2007).
- [44] W. Hofstetter, *Philosophical Magazine* **86**, 1891 (2006).
- [45] O. Dutta, M. Gajda, P. Hauke, M. Lewenstein, D.-S. Lühmann, B. A. Malomed, T. Sowiński, and J. Zakrzewski, *Reports on Progress in Physics* **78**, 066001 (2015).
- [46] N. Gemelke, X. Zhang, C. L. Hung, and C. Chin, *Nature* **460**, 995 (2009).
- [47] X. Zhang, C.-L. Hung, S.-K. Tung, and C. Chin, *Science* **335**, 1070 (2012).
- [48] W. S. Bakr, J. I. Gillen, A. Peng, S. Fölling, and M. Greiner, *Nature* **462**, 74 (2009).
- [49] J. F. Sherson, C. Weitenberg, M. Endres, M. Cheneau, I. Bloch, and S. Kuhr, *Nature* **467**, 68 (2010).
- [50] B. Yang, Y.-Y. Chen, Y.-G. Zheng, H. Sun, H.-N. Dai, X.-W. Guan, Z.-S. Yuan, and J.-W. Pan, *Physical Review Letters* **119**, 165701 (2017).
- [51] D. Hügel, P. Werner, L. Pollet, and H. U. R. Strand, *Physical Review B* **94**, 195119 (2016).
- [52] E. O. Rizzatti, M. A. A. Barbosa, and M. C. Barbosa, *Physical Review A* **102**, 033331 (2020).
- [53] W. Metzner, *Physical Review B* **43**, 8549 (1991).
- [54] B. Bradlyn, F. E. A. dos Santos, and A. Pelster, *Physical Review A* **79**, 013615 (2009).
- [55] M. Potthoff, *The European Physical Journal B - Condensed Matter* **32**, 429 (2003).
- [56] K. Byczuk and D. Vollhardt, *Physical Review B* **77**, 235106 (2008).
- [57] A. Hubener, M. Snoek, and W. Hofstetter, *Physical Review B* **80**, 245109 (2009).
- [58] W.-J. Hu and N.-H. Tong, *Physical Review B* **80**, 245110 (2009).
- [59] P. Anders, E. Gull, L. Pollet, M. Troyer, and P. Werner, *New Journal of Physics* **13**, 075013 (2011).
- [60] M. Snoek and W. Hofstetter (2013) pp. 355–365.
- [61] E. O. Rizzatti, M. S. Gomes Filho, M. Malard, and M. A. A. Barbosa, *Physica A: Statistical Mechanics and its Applications* **518**, 323 (2019).
- [62] J. K. Freericks and H. Monien, *Europhysics Letters (EPL)* **26**, 545 (1994).
- [63] G. Stefanucci and R. van Leeuwen, *Nonequilibrium Many-Body Theory of Quantum Systems* (Cambridge University Press, Cambridge, 2013) p. 249.
- [64] J. Panas, A. Kauch, J. Kuneš, D. Vollhardt, and K. Byczuk, *Physical Review B* **92**, 045102 (2015).
- [65] H. U. R. Strand, M. Eckstein, and P. Werner, *Physical Review A* **92**, 063602 (2015).
- [66] J. K. Freericks, H. R. Krishnamurthy, Y. Kato, N. Kawashima, and N. Trivedi, *Physical Review A* **79**,

- 053631 (2009).
- [67] N. Teichmann, D. Hinrichs, M. Holthaus, and A. Eckardt, *Physical Review B* **79**, 224515 (2009).
- [68] F. Gerbier, A. Widera, S. Fölling, O. Mandel, T. Gericke, and I. Bloch, *Physical Review Letters* **95**, 050404 (2005).
- [69] A. Hoffmann and A. Pelster, *Physical Review A* **79**, 053623 (2009).
- [70] A. L. Fetter and J. D. Walecka, *Quantum Theory of Many-Particle Systems* (Dover Publications, 1971) p. 250.
- [71] J. Negele and H. Orland, *Quantum Many-particle Systems* (Perseus Books, 1998) p. 237.

Geometric Aspects of Thermodynamics and Legendre Transformations

Eduardo O. Rizzatti^{1,*} and Marcia C. Barbosa¹

¹*Instituto de Física, Universidade Federal do Rio Grande do Sul, Porto Alegre-RS, Brazil*

In this paper we show the geometrical realization of the Legendre transformation as an extremum principle, connecting it to the foundations of the equilibrium Thermodynamics. In this formulation, the equation of state can be regarded as a path in the Gibbs manifold, which arises naturally as a test of thermodynamic stability. Particularly, we explore how these transformations codify a test for thermodynamic stability locally with response functions, and globally with the well known Maxwell construction.

Keywords: Thermodynamics. Legendre Transformation. Geometry. Gibbs Space.

I. INTRODUCTION

In this paper we explore the physical content regarding the Gibbs space geometry, its direct and natural relation to Legendre transformations and stability conditions about the equilibrium states.

Thermodynamics present in modern applications. Concerning the classical aspects of its logical construction (formulation), two schemes stand out: the thermodynamics of Clausius and Kelvin, with axiomatic foundations formulated by Carathéodory; and the Gibbs approach, with precise postulational basis given by Tisza. In the Gibbs theory, the attention

Thermodynamic systems or subsystems are treated as spatially disjoint volume elements, whose states are determined by a set of extensive quantities (variables proportional to the overall scale of the system) like energy/entropy, volume and number of particles. In this framework, the complete information about each subsystem is contained in the so-called fundamental equation, formulated in entropy/energy representations. The phase space spanned by these extensive variables is designated as *Gibbs space* and it plays an important role in the mathematical development of the theory. When the flux of such parameters between subsystems is allowed through the manipulation of appropriate walls, thermodynamic processes are said to occur. The new equilibrium state achieved is postulated to be the one which maximizes/minimizes the total entropy/energy restricted to manifold of the constrained variables. The essence of the theory relies on an extremum principle, just as seen in different context of physics. The application of the variational principle to the system coupled to reservoirs of extensive quantities leads naturally to the Legendre transformations. The procedure generates equations of states as solutions and also provide a test for the thermodynamic stability for local and global fluctuations about the obtained equilibrium states. Here we focus on the physical interpretation of some properties and elements regarding the geometry of the Gibbs space and Legendre transformations. Particularly, how these transformations

naturally codify a test for thermodynamic stability with the compliance coefficients (or response functions) and the well known Maxwell construction.

The paper is structured as follows. In Sec. , we provide the basic thermodynamic definitions and postulates based on the works of Tisza [1, 2], concerning the notation and the entropy maximum principle. Section discusses the Legendre transformations, considering them as extremization procedures, treated geometrically in the Gibbs space with Lagrangre multipliers. The local stability about equilibrium states is addressed in , and it physically inserted in the context of the Legendre transformations. Indeed, diagonalization of a quadratic form, a curvature from of the Gibbs manifold, with coordinates systems a diagonal coefficients deduced from fluctuations enabled by Legendre transformations in a physical process of interaction with reservoirs. Section discusses the stability in a global panorama, containing a natural reformulation of the Maxwell construction. Our final remarks and conclusions are exposed in Sec.

II. BASIC DEFINITIONS AND THE VARIATIONAL PRINCIPLE

We consider a composite thermodynamic system $\tilde{\sigma}$, constituted by a collection of simple subsystems $\{\sigma^{(\alpha)}\}$. Its equilibrium states are parametrized by a set of coordinates comprising $m + 1$ extensive variables $\mathbf{X}^{(\alpha)} = (X_1^{(\alpha)}, \dots, X_{m+1}^{(\alpha)})$, which can encompass energy/entropy, volume, and number of particles. The subsystem's boundaries may be permeable or not to the flux of such quantities, according to the appropriate collection of thermodynamic walls. The set of parameters $\{\mathbf{X}^{(\alpha)}\}$ specifies the state of the composite system; each quantity is considered additive over its subsystems, as well as conserved if the total system is isolated. Hence, the composite system variables satisfy

$$\tilde{\mathbf{X}} = \sum_{\alpha} \mathbf{X}^{(\alpha)}, \quad (1)$$

summed over all the subsystems. The referred thermodynamic walls constitute the internal constraints for the composite system, represented by relations $\omega_i(\{\mathbf{X}^{(\alpha)}\}) =$

* eduardo.rizzatti@ufrgs.br

0. For simplicity, we symbolize this set of equations by ω . These relations determine a new set of free variables usually called virtual states: states that are consistent with the imposed constraints. In this sense, virtual processes or displacements correspond to variations from one virtual state to another.

Based on these definitions, the classical thermodynamics is essentially developed from a variational principle, as usually seen in other areas of physics. In the present context, this idea is constructed by assigning to each subsystem an entropy function (also called fundamental equation or thermodynamic potential) $\Psi^{(\alpha)} = \Psi^{(\alpha)}(\mathbf{X}^{(\alpha)})$, first-order homogeneous, continuous, with piecewise continuous higher-order derivatives. The total entropy $\tilde{\Psi}$ of the composite system is introduced as an additive function over its components

$$\tilde{\Psi}(\{\mathbf{X}^{(\alpha)}\}) = \sum_{\alpha} \Psi^{(\alpha)}(\mathbf{X}^{(\alpha)}). \quad (2)$$

since the interactions among them are considered short ranged. The occurrence of thermodynamic processes, defined as the transfer of extensive quantities between the subsystems, is mediated by the modification of internal constraints, symbolized by the transformation $\omega \mapsto \theta$. In such scenario, the extremal principle is structured as follows: the new state of equilibrium achieved $\{\mathbf{X}_0^{(\alpha)}\}$ is such that it maximizes the total entropy restricted to the manifold of new internal constraints. In other terms, from all possible states obeying the restrictions $\theta_i(\{\mathbf{X}^{(\alpha)}\}) = 0$, the state of thermodynamic equilibrium $\{\mathbf{X}_0^{(\alpha)}\}$ corresponds to the largest value of total entropy:

$$\tilde{\Psi}(\{\mathbf{X}_0^{(\alpha)}\}) = \max \left\{ \sum_{\alpha} \Psi^{(\alpha)}(\mathbf{X}^{(\alpha)}) \right\}. \quad (3)$$

Therefore, the description of a thermodynamic system relies not only on defining its subsystems, through the corresponding fundamental equations, but also on the identification of its internal constraints.

The entropy maximum principle can be reformulated in terms of the internal energy $\Phi^{(\alpha)}$, represented by one of the variables $X_1^{(\alpha)}, \dots, X_{m+1}^{(\alpha)}$. The postulate of Eq. (3) becomes equivalent to the minimization of the total internal energy

$$\tilde{\Phi}(\{\mathbf{X}_0^{(\alpha)}\}) = \min \left\{ \sum_{\alpha} \Phi^{(\alpha)}(\mathbf{X}^{(\alpha)}) \right\}, \quad (4)$$

respecting the analogous constraints. The inversion of Eq. (2) is allowed locally since the derivative $\frac{\partial \Psi^{(\alpha)}}{\partial \Phi^{(\alpha)}} = \frac{1}{T^{(\alpha)}}$ is the inverse temperature, a quantity regarded as positive. These representations correspond to different physical configurations and setups. In the entropy scheme, the total system is considered in isolation with constant total energy while the entropy is permitted to vary. The energy scheme allows for fluctuations in energy at fixed total entropy by the coupling of an external

working source.

First we analyze the variational principle in a local perspective, studying infinitesimal virtual displacements around the equilibrium state. For a local extremum, the condition

$$\delta \tilde{\Phi} = 0 \quad (5)$$

implies the equality of the thermodynamic potential's first derivatives

$$P_j^{(\alpha)} = \frac{\partial \Phi^{(\alpha)}}{\partial X_j^{(\alpha)}}, \quad (6)$$

with

$$P_j^{(\alpha)} = P_j^{(\beta)} \quad (7)$$

for all $j = 1, \dots, m$ and α, β coupled through the exchange of X_j . These intensive quantities are named as the fields $P_j^{(\alpha)}$ conjugated to $X_j^{(\alpha)}$ and they act like passive generalized forces induced by the corresponding permeable walls. The relations brought by Eqs. (6) determine the so-called equations of state in a local scope. The entropic representation receives the notation

$$H_j^{(\alpha)} = \frac{\partial \Psi^{(\alpha)}}{\partial X_j^{(\alpha)}}. \quad (8)$$

The fundamental equation lacks direct physical appeal, sometimes distant from the experimental reality. Indeed, the connection between the formalism and the laboratory environment is established more properly by the already mentioned equations of state. As discussed in the Sec. III, they are naturally generated by Legendre transformations, arising from an adaptation of the extremum principle considering interactions between the system and proper reservoirs. In spite of being an extensively discussed subject, its possible to connect the Legendre transformations and the geometry of the Gibbs space through an unified view encompassing the obtaining of equations of state, and the analysis of local and global stability criteria.

III. LEGENDRE TRANSFORMATIONS

The Legendre transformations are commonly associated to the convex envelope or supporting hyperplanes of sufficient regular functions [3, 4], connected to the duality between points and lines [5]. Indeed, they preserve the information content of the original function by relating an element of the Gibbs manifold to its respective tangent space as illustrated in Fig. 1(a). This association is actually a consequence of the ideas brought by the extremal principle, subjecting it to adequate constraints. To explore this latent meaning in a geometrical perspective, we generalize the mental experiment from the previous section.

We consider a composite system $\tilde{\sigma}$ constituted by the

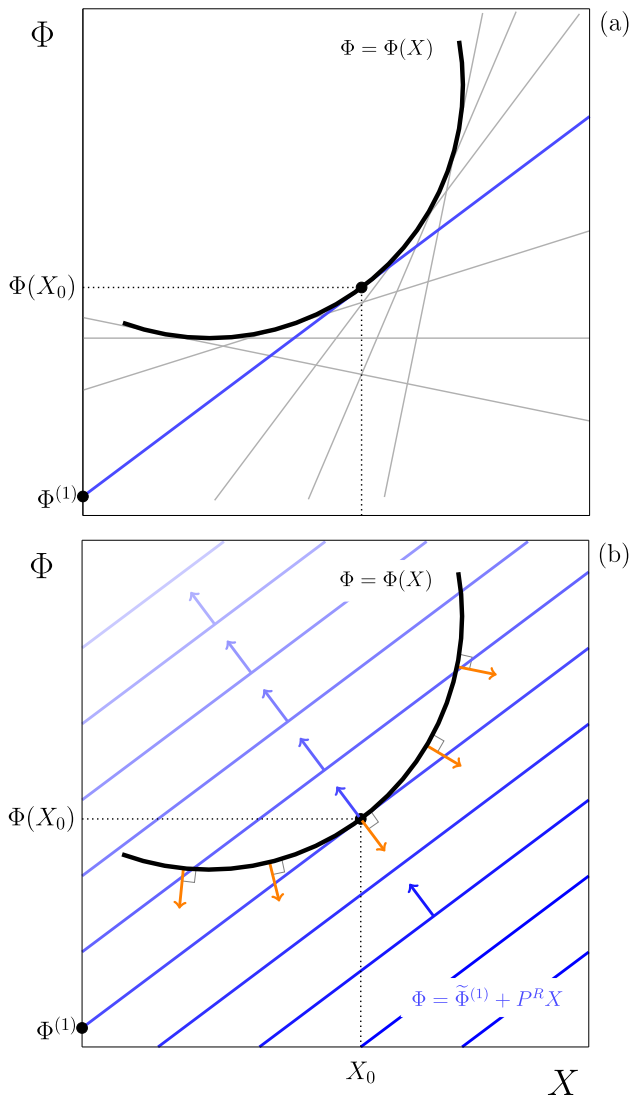


FIG. 1. Panel (a) depicts the fundamental equation as a function of the extensive variable X , with some of its tangent lines. Their intercepts with the Φ axis determine the Legendre transform $\Phi^{(1)}$. An equivalent construction is shown in (b), considering the intrinsic variational character of the discussed problem. The contour curves of $\tilde{\Phi}^{(1)} = \Phi - P^R X$ are shown as the blue lines with constant slope P^R , concerning the reservoir σ^R . This function is explicitly minimized subjected to the constraint $\Phi = \Phi(X)$, regarding the system σ originally studied. Arrows symbolize the gradient vectors of the corresponding curves. At the extremum solution X_0 , the gradient vectors become parallel, with $P^R = P$. The minimum value reached by the intercepts is $\Phi^{(1)} = \Phi^{(1)}(P^R)$, the Legendre transform of Φ at the value P^R . The extremization procedure yields also the equation of state $X_0 = X_0(P^R)$.

studied system σ and a reservoir σ^R . The later is characterized by the intensive parameter P^R conjugated to the extensive variable X . Both system are allowed to exchange X through a corresponding permeable wall. The

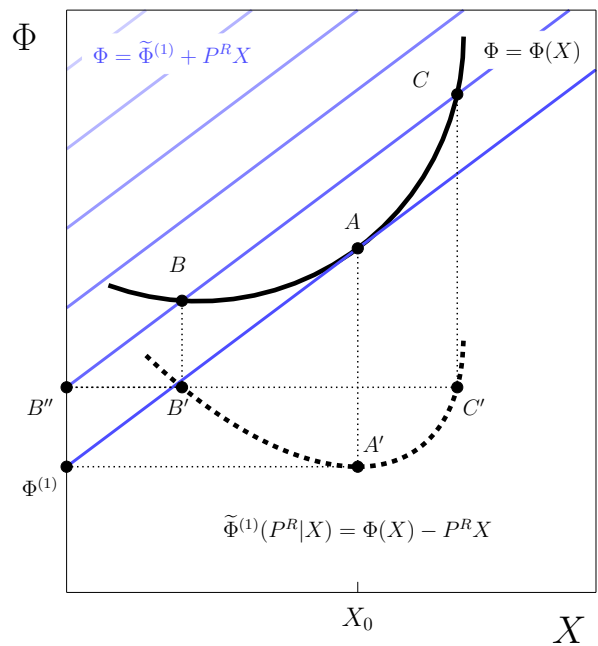


FIG. 2. The geometrical construction of the potential $\tilde{\Phi}^{(1)}(P^R|X) = \Phi(X) - P^R X$, involved in the reformulation of the extremal principle. The points A , B and C correspond to the intersection of $\Phi = \Phi(X)$ and the level curves $\Phi = \tilde{\Phi}^{(1)} + P^R X$. The intercepts A' , B' and C' projected into the X axis yields A' , B'' and C'' , composing the function $\tilde{\Phi}^{(1)}(P^R|X)$ (dotted curve). Its minimum value is the Legendre transform $\Phi^{(1)}$ of Φ at fixed P^R .

total energy is additive over its subsystems with

$$\tilde{\Phi}(X, X^R) = \Phi(X) + \Phi^R(X^R). \quad (9)$$

As Eq. (4) postulates, the equilibrium state (X_0, X_0^R) reached by the transfer of X is such that $\tilde{\Phi}(X_0, X_0^R) \leq \tilde{\Phi}(X, X^R)$, for any state (X, X^R) satisfying the imposed constraint

$$\tilde{X} = X + X^R, \quad (10)$$

with \tilde{X} constant. This implies that the deviation from equilibrium

$$\Delta\tilde{\Phi} \equiv \tilde{\Phi}(X, X^R) - \tilde{\Phi}(X_0, X_0^R) \geq 0 \quad (11)$$

must be positive-definite. We decompose this variation through Eq. (9), following the contribution of the two subsystems

$$\Delta\tilde{\Phi} = \Delta\Phi + \Delta\Phi^R. \quad (12)$$

According to Eq. (10), the fluxes of the analysed quantities vary in the opposite sense

$$\Delta X^R = -\Delta X \quad (13)$$

in order to ensure the conservation of \tilde{X} . The choice of a reservoir σ^R mediating the interactions with σ provides a

particularly simple variation for the total thermodynamic potential. Since the higher order derivatives of P^R are negligible for a reservoir, $\Delta\Phi^R$ becomes simply

$$\Delta\Phi^R = P^R\Delta X^R. \quad (14)$$

Indeed, using Eqs. (13) and (14), we rewrite Eq. (12) as

$$\begin{aligned} \Delta\tilde{\Phi} &= \Delta\Phi - P^R\Delta X \\ &= \Delta(\Phi - P^RX), \end{aligned} \quad (15)$$

since P^R is fixed. The energy minimum postulate brought by Eq. (11) and the deviation expressed in Eq. (15) imply that the equilibrium state achieved minimizes the function

$$\tilde{\Phi}^{(1)}(P^R|X) \equiv \Phi(X) - P^RX. \quad (16)$$

Consequently, the Legendre transform $\Phi^{(1)}(P^R)$ is defined by the solution of the variational procedure

$$\begin{aligned} \Phi^{(1)}(P^R) &= \min_X \{\Phi(X) - P^RX\} \\ &= \min_X \tilde{\Phi}^{(1)}(P^R|X) \\ &= \tilde{\Phi}^{(1)}(P^R|X_0), \end{aligned} \quad (17)$$

for each value of P^R as the reservoirs are varied. The solution obtained develops into an equation of state, with

$$X_0 = X_0(P^R). \quad (18)$$

These steps reformulate the extremal principle, allowing for fluctuations in the studied system. They reveal the essential ingredient composing the Legendre transformations: the maintenance of the variational principle adapted to a set of new constraints.

As typically done under these circumstances, the optimization problem in the presence of constraints is treated employing Lagrange multipliers, as Fig. 1(b) depicts. In the $X\Phi$ plane, the minimization of $\tilde{\Phi}^{(1)}(P^R|X)$ is equivalent to finding the minimum value of the function

$$\tilde{\Phi}^{(1)}(P^R|X) = \Phi - P^RX, \quad (19)$$

for a constant value of P^R and restricted to the manifold

$$\Phi = \Phi(X). \quad (20)$$

The level curves of $\tilde{\Phi}^{(1)}$ correspond to a family of lines with slope P^R ; their values constitute the intercepts of the Φ axis ($X = 0$). By defining the function $h(\Phi, X) = \Phi(X) - \Phi$, which is identically zero, the solution to the posed problem satisfies

$$\nabla\tilde{\Phi}^{(1)} = \lambda\nabla h, \quad (21)$$

corresponding to the equilibrium state X_0 . Geometrically, this codifies the parallelism of the gradient vectors regarding the considered curves. In other terms, the minimum value assumed by the intercepts of the refereed lines, restricted to $\Phi = \Phi(X)$, occurs for the line tangent

to the system's fundamental relation curve. Precisely, the components of Eq. (21) yield

$$\frac{\partial\tilde{\Phi}^{(1)}}{\partial\Phi} = \lambda\frac{\partial h}{\partial\Phi} \iff \lambda = -1, \quad (22)$$

and

$$\frac{\partial\tilde{\Phi}^{(1)}}{\partial X} = \lambda\frac{\partial h}{\partial X} \iff -P^R = \lambda\frac{\partial\Phi}{\partial X}, \quad (23)$$

whose combination provides

$$P^R = \frac{\partial\Phi}{\partial X}. \quad (24)$$

This relation brings up the equilibrium condition

$$P = P^R, \quad (25)$$

corroborating the equivalence between the tangent planes construction and the extremal principle adapted to the interaction with the reservoir.

Going further in our analysis, Fig. (2) details the geometrical construction of the function $\tilde{\Phi}^{(1)}(P^R|X)$, which is set to be minimized. As an example, the points A , B and C signal the crossing of the fundamental equation $\Phi = \Phi(X)$ and the family of parallel lines $\Phi = \tilde{\Phi}^{(1)} + P^RX$. The intercepts of these lines with the Φ axis correspond to the values of $\tilde{\Phi}^{(1)}$, designated by A' , B' , and C' . These points projected into their respective X values determine A'' , B'' , and C'' , which compose the function $\tilde{\Phi}^{(1)}(P^R|X)$ illustrated as the dotted curve. Indeed, the lengths of the segments AA'' , BB'' , and CC'' are equal to P^RX ; when the $\Phi(X)$ values (the points A , B , and C) are subtracted by P^RX (the length of AA'' , BB'' , and CC''), we obtain $\tilde{\Phi}^{(1)}(P^R|X)$. This affine construction naturally produces the Legendre transform as the extremal solution to the posed variational procedure, yielding an equation of state. The fluctuations of the variable X between the system and the reservoir are such that they minimize this new function, combining elements from the system and the reservoir.

To generalize our discussion in the multivariable case, we define the successive Legendre transform of order k by

$$\Phi^{(k)}(P_k) = \min_{X_k} \tilde{\Phi}^{(k)}(P_k|X_k), \quad (26)$$

following the extremization of

$$\tilde{\Phi}^{(k)}(P_k|X_k) \equiv \Phi^{(k-1)}(X_k) - P_kX_k. \quad (27)$$

Its solution, the equation of state

$$X_{k,0} = X_{k,0}(P_k), \quad (28)$$

is such that

$$\Phi^{(k)}(P_k) = \tilde{\Phi}^{(k)}(P_k|X_{k,0}). \quad (29)$$

Only the dependence on the transformed parameters is addressed; the complete notation reads as $\Phi^{(k)} = \Phi^{(k)}(P_1, \dots, P_k, X_{k+1}, \dots, X_{m+1})$.

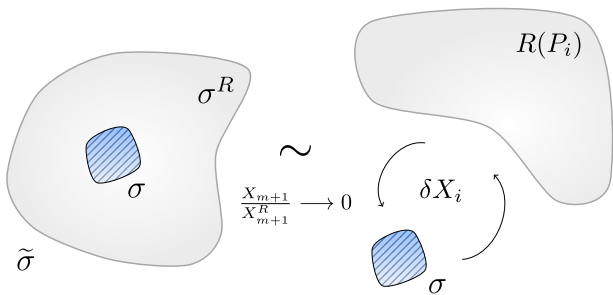


FIG. 3. Schematic representation of a thermodynamic system $\tilde{\sigma}$ and the mental experiment which enables the analysis of the fluxes δX_i , obeying the originally imposed constraints. In the left hand side, we highlight a subsystem σ , with a fixed scale parameter X_{m+1} . The right hand portion presents the limit $\frac{X_{m+1}}{X_{m+1}^R} \rightarrow 0$ leading to a replica of the studied system interacting with reservoirs $R(P_i)$ of extensive quantities X_i .

IV. THERMODYNAMIC STABILITY

The variational procedure can be employed not only to obtain the equilibrium state \mathbf{X}_0 of a homogeneous system $\tilde{\sigma}$ but also to probe its thermodynamic stability. In order to do so, we analyze the system's response to global or local fluctuations starting from the attained equilibrium state. (define global and local variations).

A. Local Stability

The presented formulation imposes an inherent obstacle: the fluctuations from the equilibrium value as a test to the stability must not violate the originally imposed constraints. We overcome this difficulty by highlighting a subsystem σ , with a fictitious boundary with the complementary subsystem σ^R . In analogy to the set theory, we write the described decomposition in the form $\tilde{\sigma} = \sigma \cup \sigma^R$. Such procedure enables the analysis of fluctuations about an equilibrium state obeying the system's constraints. If we assign to each subsystem its fundamental equation, the total energy becomes

$$\tilde{\Phi}(\mathbf{X}, \mathbf{X}^R) = \Phi(\mathbf{X}) + \Phi^R(\mathbf{X}^R), \quad (30)$$

with the enclosure relations

$$\tilde{\mathbf{X}} = \mathbf{X} + \mathbf{X}^R. \quad (31)$$

The subsystem σ can be regarded as a re-scaled replica of the original one due to its homogeneity.

We submit σ to a virtual process about the equilibrium state $(\mathbf{X}_0, \mathbf{X}_0^R)$. The minimum energy postulate states that $\Delta \tilde{\Phi} \equiv \tilde{\Phi}(\mathbf{X}, \mathbf{X}^R) - \tilde{\Phi}(\mathbf{X}_0, \mathbf{X}_0^R) \geq 0$, for any $(\mathbf{X}, \mathbf{X}^R)$ compatible with the constraints of Eq. (31). In terms of a Taylor expansion about $(\mathbf{X}_0, \mathbf{X}_0^R)$, this variation of the total energy corresponds to

$$\begin{aligned} \Delta \tilde{\Phi} &= \Delta \Phi + \Delta \Phi^R \\ &= (\delta \Phi + \delta^2 \Phi + \dots) + (\delta \Phi^R + \delta^2 \Phi^R + \dots). \end{aligned} \quad (32)$$

In a local neighborhood of the equilibrium state, the thermodynamic potential satisfies $\delta \tilde{\Phi} = \delta \Phi + \delta \Phi^R = 0$, according to Eq. (5). Hence, the remaining higher order terms provide

$$\Delta \tilde{\Phi} = (\delta^2 \Phi + \delta^3 \Phi + \dots) + (\delta^2 \Phi^R + \delta^3 \Phi^R + \dots). \quad (33)$$

Additionally, we can fix a scale parameter from the set of variables describing the system. Usually the number of particles or volume in a simple fluid; here we designate this variable as X_{m+1} . By employing the extensive property of the thermodynamic potential, we define the following generalized densities for σ

$$\phi = \frac{\Phi}{X_{m+1}} \quad \text{and} \quad x_i = \frac{X_i}{X_{m+1}}, \quad (34)$$

and the subsystem σ^R

$$\phi^R = \frac{\Phi^R}{X_{m+1}^R} \quad \text{and} \quad x_i^R = \frac{X_i^R}{X_{m+1}^R}, \quad (35)$$

considering $i = 1, \dots, m$. As both subsystems are complementary parts of the total system, the homogeneity condition brings the equation

$$\frac{\partial^2 \phi}{\partial x_i \partial x_j} = \frac{\partial^2 \phi^R}{\partial x_i^R \partial x_j^R}, \quad (36)$$

which readily yields

$$\frac{\partial^2 \Phi^R}{\partial X_i^R \partial X_j^R} = \frac{X_{m+1}}{X_{m+1}^R} \frac{\partial^2 \Phi}{\partial X_i \partial X_j}. \quad (37)$$

Since \tilde{X}_i is fixed, the restrictions from Eq. (31) imply

$$\delta \tilde{X}_i = -\delta X_i^R, \quad (38)$$

for all $i = 1, \dots, m$. The combination of Eqs. (37) and (38) relates the second order variations for σ^R and σ to the scale factor previously chosen according to

$$\delta^2 \Phi^R = \frac{X_{m+1}}{X_{m+1}^R} \delta^2 \Phi. \quad (39)$$

Similarly, the higher order variations also obey analogous relations

$$\delta^k \Phi^R = (-1)^k \left(\frac{X_{m+1}}{X_{m+1}^R} \right)^{k-1} \delta^k \Phi. \quad (40)$$

Note that $k = 1$ recovers the condition regarding a local extremum, from which we extract the equality between the intensive fields or generalized forces. In the limit

$$\frac{X_{m+1}}{X_{m+1}^R} \rightarrow 0, \quad (41)$$

the complementary system σ^R can be regarded as a reservoir if compared to the selected subsystem σ , which plays the role of a replica in reduced scale of the total system $\tilde{\sigma}$. This mental experiment is represented schematically in Fig. 3.

Considering the described scenario, the variation of the thermodynamic potential given in Eq. (33) simplifies to

$$\Delta\tilde{\Phi} \rightarrow \delta^2\Phi + \delta^3\Phi + \dots \quad (42)$$

Therefore, the sign of the quadratic form $\delta^2\Phi$ determines the thermodynamic stability in a local scope. Explicitly, the second variation $\delta^2\phi = \delta^2\phi(\mathbf{x}_0; \mathbf{x})$ of $\phi = \phi(x_1, \dots, x_m)$ is expressed by

$$\delta^2\phi = \frac{1}{2} \sum_{i=1}^m \sum_{j=1}^m \phi_{ij} \delta x_i \delta x_j, \quad (43)$$

a second order degree polynomial in m variables whose coefficients ϕ_{ij}

$$\phi_{ij} = \frac{\partial^2 \phi}{\partial x_i \partial x_j}(\mathbf{x}_0) \quad (44)$$

are elements of the hessian matrix of ϕ evaluated at the equilibrium state \mathbf{x}_0 . In matrix notation, Eq. (43) becomes

$$\delta^2\phi = \frac{1}{2} \delta \mathbf{x}^T Q \delta \mathbf{x}, \quad (45)$$

where $Q = Q(\mathbf{x}_0)$ is the Hessian matrix of ϕ calculated at \mathbf{x}_0 :

$$Q = \begin{bmatrix} \phi_{11} & \phi_{12} & \dots & \phi_{1m} \\ \phi_{21} & \phi_{22} & \dots & \phi_{2m} \\ \vdots & \vdots & \ddots & \vdots \\ \phi_{m1} & \phi_{m2} & \dots & \phi_{mm} \end{bmatrix}. \quad (46)$$

We seek a diagonal representation for this bilinear form in order to clarify the conditions determining its positivity. Indeed, every symmetric quadratic form admits a diagonal representation through a linear transformation [6]. Precisely, it is possible to conceive an appropriate change of basis $L : \delta \mathbf{x} \mapsto \delta \mathbf{y}$ given by

$$\delta \mathbf{y} = L \delta \mathbf{x}, \quad (47)$$

such that the quadratic form is diagonal

$$\delta^2\phi = \frac{1}{2} \sum_{i=1}^m \lambda_i \delta y_i^2. \quad (48)$$

In a matrix notation, Eq. (48) assumes the form

$$\delta^2\phi = \frac{1}{2} \delta \mathbf{y}^T \Lambda \delta \mathbf{y}, \quad (49)$$

with Λ the diagonal matrix

$$\Lambda = \begin{bmatrix} \lambda_1 & 0 & \dots & 0 \\ 0 & \lambda_2 & \dots & 0 \\ \vdots & \vdots & \ddots & \vdots \\ 0 & 0 & \dots & \lambda_m \end{bmatrix}. \quad (50)$$

Therefore, both transformation are connected by a conjugation relation

$$Q = L^T \Lambda L. \quad (51)$$

Consequently, our stability analysis relies on determining the sign of the coefficients $\{\lambda_i\}$. In general, the referred coordinate transformation is not unique [7]. Nevertheless, the number of positive, negative and null terms among the supra-cited coefficients is always the same. This statement is known as the Sylvester's law of inertia [8], whose name alludes to an intrinsic property of the quadratic form which resists the mentioned change of basis. In a geometrical scope, the dimensions of the maximal subspaces in which the quadratic form is positive or negatively defined are invariant under these circumstances.

Regarding the non uniqueness associated to Q , we seek the transformation carrying physical meaning in the explored context. For example, we can diagonalize the Hessian form through an orthogonal transformation. In the linear algebra scenario, the spectral theorem attests that every symmetric matrix is diagonalizable by an orthogonal transformation, which preserves the euclidean metric. However, such procedure does not exhibit any physical information and meaning for the manifold defined by the fundamental equation in the Gibbs space. On the other hand, the orthogonal transformation finds applications in the context of vibrations and stability of structures, once the physical space is naturally endowed with the euclidean metric. Alternatively, we show in the following that a deeper connection with the thermodynamic structure presented is established when the diagonalization is carried by completing squares, also known as the Lagrange method.

1. Diagonalization for a non-singular quadratic form

We treat initially a non-degenerate quadratic form, with $\det(Q) \neq 0$. For $\phi_{11} \neq 0$, we separate the terms containing δx_1 , completing the square according to

$$\delta^2\phi = \frac{1}{2} \left\{ \phi_{11} \left(\delta x_1 + \sum_{j=2}^m \frac{\phi_{1j}}{\phi_{11}} \delta x_j \right)^2 + \sum_{i,j=2}^m \left(\phi_{ij} - \frac{\phi_{1i} \phi_{1j}}{\phi_{11}} \right) \delta x_i \delta x_j \right\}. \quad (52)$$

Two new parameters naturally arise from this procedure: the coordinate system

$$\delta y_1 = \delta x_1 + \sum_{j=2}^m \frac{\phi_{1j}}{\phi_{11}} \delta x_j, \quad (53)$$

as well as the set of coefficients

$$\phi_{ij}^{(1)} = \phi_{ij} - \frac{\phi_{1i} \phi_{1j}}{\phi_{11}}, \quad (54)$$

for $i, j = 2, \dots, m$. Including these definitions, Eq. (52) becomes

$$\begin{aligned} \delta^2 \phi &= \frac{1}{2} \left\{ \phi_{11} \delta y_1^2 + \sum_{i,j=2}^m \phi_{ij}^{(1)} \delta x_i \delta x_j \right\} \\ &= \frac{1}{2} \phi_{11} \delta y_1^2 + \delta^2 \phi^{(1)}, \end{aligned} \quad (55)$$

where the remaining sum was redefined as

$$\delta^2 \phi^{(1)} = \sum_{i,j=2}^m \phi_{ij}^{(1)} \delta x_i \delta x_j. \quad (56)$$

As deduced in Eq. (55), the reduction process generates the first element in the diagonal representation, given simply by

$$\lambda_1 = \phi_{11} = \frac{\partial^2 \phi}{\partial x_1^2}. \quad (57)$$

The coefficients $\phi_{ij}^{(1)}$ defined through Eq. (54) receive this label because they are second derivatives of the Legendre transform $\phi^{(1)} = \phi^{(1)}(P_1, x_2, \dots, x_m)$ of ϕ with respect to x_1 ,

$$\phi_{ij}^{(1)} = \left(\frac{\partial^2 \phi^{(1)}}{\partial x_i \partial x_j} \right)_{P_1}, \quad (58)$$

evaluated in terms of the natural variables P_1, x_2, \dots, x_m . Also, from the change of coordinates carried by the Legendre transformation, the new coordinate δy_1 addressed in Eq. (53) can be expressed as

$$\delta y_1 = \delta x_1 - \sum_{j=2}^m \left(\frac{\partial x_1}{\partial x_j} \right)_{P_1} \delta x_j. \quad (59)$$

Both identifications shown in Eqs. (58) and (59) are demonstrated in Appendix A.

Note that we are in the same position when we started the diagonalization process. Therefore, it is possible to develop the next steps by induction. For $\phi_{22}^{(1)} \neq 0$, we obtain the new basis

$$\delta y_2 = \delta x_2 - \sum_{j=3}^m \left(\frac{\partial x_2}{\partial x_j} \right)_{P_1, P_2} \delta x_j, \quad (60)$$

and the coefficients

$$\phi_{ij}^{(2)} = \phi_{ij}^{(1)} - \frac{\phi_{2i}^{(1)} \phi_{2j}^{(1)}}{\phi_{22}^{(1)}}. \quad (61)$$

The next diagonal element is

$$\lambda_2 = \phi_{22}^{(1)} = \left(\frac{\partial^2 \phi^{(1)}}{\partial x_2^2} \right)_{P_1}, \quad (62)$$

and the second order variation from Eq. (55) transforms into

$$\delta^2 \phi = \frac{1}{2} \phi_{11} \delta y_1^2 + \frac{1}{2} \phi_{22}^{(1)} \delta y_2^2 + \delta^2 \phi^{(2)}. \quad (63)$$

In such non-singular case, the complete process provides the following diagonal terms

$$\lambda_k = \phi_{kk}^{(k-1)} = \left(\frac{\partial^2 \phi^{(k-1)}}{\partial x_k^2} \right)_{P_1, \dots, P_{k-1}}, \quad (64)$$

obtained through the change of basis

$$\delta y_k = \delta x_k - \sum_{j=k+1}^m \left(\frac{\partial x_k}{\partial x_j} \right)_{P_1, \dots, P_k} \delta x_j, \quad (65)$$

for $k = 1, \dots, m-1$ and

$$\delta y_m = \delta x_m. \quad (66)$$

In a matrix language, the transformation L which diagonalizes Q into Λ is given by

$$L = \begin{bmatrix} 1 - \left(\frac{\partial x_1}{\partial x_2} \right)_{P_1} & \cdots & - \left(\frac{\partial x_1}{\partial x_m} \right)_{P_1} \\ 0 & 1 & \cdots & - \left(\frac{\partial x_2}{\partial x_m} \right)_{P_1, P_2} \\ \vdots & \vdots & \ddots & \vdots \\ 0 & 0 & \cdots & 1 \end{bmatrix}. \quad (67)$$

The exposed diagonalization procedure presents a clear physical interpretation based on the presented decomposition for the total system $\tilde{\sigma}$. The artificial partition involves its re-scaled copy σ coupled to the complementary part σ^R , regarded as a reservoir of extensive quantities. This mental construction allows for testing the stability of an equilibrium state through fluctuations which are naturally implemented by Legendre transformations due to their intrinsic variational character. We begin our analysis with the variable x_1 . By enabling fluctuations δx_1 with the remaining variables x_2, \dots, x_m fixed, the extremal principle

$$\Delta \tilde{\phi} > 0 \quad (68)$$

transforms into

$$\Delta \tilde{\phi}^{(1)} = \Delta(\phi - P_1 x_1) > 0, \quad (69)$$

following. The local stability with respect to the induced variation requires that the function $\tilde{\phi}^{(1)}$ presents a local minimum at the studied equilibrium state. Precisely, the second fundamental form must be positive definite

$$\delta^2 \tilde{\phi}^{(1)} = \delta^2 \phi = \frac{\partial^2 \phi}{\partial x_1^2} (\delta x_1)^2 > 0, \quad (70)$$

yielding the first diagonal element

$$\lambda_1 = \frac{\partial^2 \phi}{\partial x_1^2} = \frac{\partial P_1}{\partial x_1} > 0. \quad (71)$$

This condition permits the local realization of the Legendre transformation involving the conjugate variables x_1 and P_1 . We derive the equation of state

$$x_1 = x_1(P_1, x_2, \dots, x_m) \quad (72)$$

as a solution of the extremization problem. Since its infinitesimal deviation $(\delta x_1)_{P_1}$ of x_1 at fixed P_1 is

$$(\delta x_1)_{P_1} = \left(\frac{\partial x_1}{\partial x_2} \right)_{P_1} \delta x_2 + \cdots + \left(\frac{\partial x_1}{\partial x_m} \right)_{P_1} \delta x_m, \quad (73)$$

the choice $\delta x_1 = (\delta x_1)_{P_1}$ implies $\delta y_1 = 0$, according to Eq. (59). This means that, once we perform the Legendre transformation, the analysis of sign regarding the direction δx_1 gets completed. Such procedure verifies automatically the local stability for the corresponding variations. After this, our attention turns towards the fluxes of the variable x_2 conjugated to P_2 . The corresponding successive Legendre transformation of $\phi^{(1)}$ satisfies the condition

$$\Delta \tilde{\phi}^{(2)} = \Delta(\phi^{(1)} - P_2 x_2) > 0, \quad (74)$$

which locally produces

$$\delta^2 \tilde{\phi}^{(2)} = \delta^2 \phi^{(1)} = \left(\frac{\partial^2 \phi^{(1)}}{\partial x_2^2} \right)_{P_1} (\delta x_2)^2 > 0, \quad (75)$$

where the quantities x_3, \dots, x_m are kept constant. Consequently, we deduce the second diagonal element

$$\lambda_2 = \left(\frac{\partial^2 \phi^{(1)}}{\partial x_2^2} \right)_{P_1} = \left(\frac{\partial P_2}{\partial x_2} \right)_{P_1} > 0. \quad (76)$$

The equation of state derived from the new extremal principle

$$x_2 = x_2(P_1, P_2, x_3, \dots, x_m) \quad (77)$$

exhibits the local variation

$$(\delta x_1)_{P_1, P_2} = \left(\frac{\partial x_2}{\partial x_3} \right)_{P_1, P_2} \delta x_3 + \cdots + \left(\frac{\partial x_2}{\partial x_m} \right)_{P_1, P_2} \delta x_m \quad (78)$$

at fixed P_1 and P_2 . The new basis, show in , assumes the form $\delta y_2 = \delta x_2 - (\delta x_1)_{P_1, P_2}$. For infinitesimal deviations determined by the path describing the obtained equation of state, with $\delta x_2 = (\delta x_1)_{P_1, P_2}$, the new basis yields. The diagonalization procedure can be carried out inductively providing the same conclusions. The path or directions in the Gibbs space which test the local stability of a given state are brought by the Legendre transforms through the change of coordinates L . Therefore the algebraic and physical level by the natural structure of Thermodynamics equilibrium.

From the positivity of the quadratic form in the energy representation, we extract the Le Chatelier principle

$$\frac{\partial P_k}{\partial x_k} > \left(\frac{\partial P_k}{\partial x_k} \right)_{P_1} > \cdots > \left(\frac{\partial P_k}{\partial x_k} \right)_{P_1, \dots, P_{k-1}} > 0, \quad (79)$$

where the displacement δx_k corresponds to a gradient of the generalized force δP_k . Such response is larger if the extensive quantities are kept fixed, and progressively smaller if the flux is allowed at fixed fields. Similarly, the local stability requires negative diagonal elements in the entropy representation.

As an example, consider a binary mixture described by a fundamental equation $U = U(S, V, N_1, N_2)$, involving the internal energy as a function of the entropy, volume, and number of particles N_i . From the total number of particles $N = N_1 + N_2$, we define the generalized densities

$$u = \frac{U}{N}, \quad s = \frac{S}{N}, \quad v = \frac{V}{N} \quad \text{and} \quad x = \frac{N_1}{N}. \quad (80)$$

The diagonalization of the quadratic form $\delta^2 u$ represented by

$$Q = \begin{bmatrix} \frac{\partial^2 u}{\partial s^2} & \frac{\partial^2 u}{\partial s \partial v} & \frac{\partial^2 u}{\partial s \partial x} \\ \frac{\partial^2 u}{\partial v \partial s} & \frac{\partial^2 u}{\partial v^2} & \frac{\partial^2 u}{\partial v \partial x} \\ \frac{\partial^2 u}{\partial x \partial s} & \frac{\partial^2 u}{\partial x \partial v} & \frac{\partial^2 u}{\partial x^2} \end{bmatrix} \quad (81)$$

provides the stability criteria

$$\lambda_1 = \frac{\partial^2 u}{\partial s^2} > 0, \quad (82)$$

$$\lambda_2 = \left(\frac{\partial^2 f}{\partial v^2} \right)_T > 0, \quad (83)$$

$$\lambda_3 = \left(\frac{\partial^2 g}{\partial x^2} \right)_{T, P} > 0, \quad (84)$$

according to . Indeed, these diagonal elements encompass appropriate curvature conditions over the internal energy $u = u(s, v, x)$ and its successive Legendre transforms: the Helmholtz free energy $f = f(t, v, x)$ and Gibbs free energy $g = g(T, P, x)$.

2. Diagonalization for a singular quadratic form

The so called critical points are commonly considered as the boundary between stable and unstable states. In the explored context, the critical manifold can be defined by the semi definite character of the previously analyzed quadratic form. This condition is achieved whenever one of its diagonal elements, say λ_r , becomes zero; this readily implies $\det Q = 0$. Since the order of the variables is not unique, we choose r with the least value as possible. We discern two possibilities: $r = m$ and $r < m$. In the case $r = m$, with

$$\lambda_m = \phi_{mm}^{(m-1)} = 0, \quad (85)$$

the diagonalization procedure is concluded without problems. This is the most usual scenario. Since the quadratic form can assume the value zero, a positive free-energy variation is guaranteed locally if

$$\frac{\partial^3 \phi^{(m-1)}}{\partial x_m^3} = 0 \quad (86)$$

and

$$\frac{\partial^4 \phi^{(m-1)}}{\partial x_m^4} > 0. \quad (87)$$

For the remaining case (responsible for the critical azeotropy in binary mixtures), the diagonalization is interrupted when we arrive at the variable x_r according to

$$\delta^2\phi = \frac{1}{2} \sum_{i=1}^{r-1} \lambda_i \delta y_i^2 + \delta^2\phi^{(r-1)}, \quad (88)$$

with

$$\delta^2\phi^{(r-1)} = \sum_{i,j=r}^m \phi_{ij}^{(r-1)} \delta x_i \delta x_j. \quad (89)$$

Considering

$$\lambda_r = \phi_{rr}^{(r-1)} = 0, \quad (90)$$

the quadratic form of Eq. (89) is semi-definite if

$$\phi_{rj}^{(r-1)} = 0, \quad (91)$$

for $j = r + 1, \dots, m$. Indeed, by choosing the displacements

$$\delta y_i = 0 \quad (92)$$

for $1 \leq i \leq r - 1$, as well as

$$\delta x_j = 0 \quad (93)$$

for $r + 1 \leq j \leq m$, the quadratic form

$$\delta^2\phi = \phi_{rk}^{(r-1)} \delta x_r \delta x_k + \phi_{kk}^{(r-1)} \delta x_k^2 \quad (94)$$

can take on positive and negative values according to the arbitrated values of δx_r and δx_k . Then, we continue the diagonalization process keeping fixed the coordinate x_r , without submitting it to the Legendre transformation. Consequently, there is a decoupling between the sets of variables $\{x_1, \dots, x_{r-1}\}$ and $\{x_{r+1}, \dots, x_m\}$. Collecting the previous results, the critical points are determined by the following conditions

$$\lambda_r = \frac{\partial^3 \phi^{(r-1)}}{\partial x_r^2} = 0, \quad \lambda_j > 0 \quad (j \neq r) \quad (95)$$

$$\frac{\partial^3 \phi^{(r-1)}}{\partial x_r^3} = 0, \quad \frac{\partial^4 \phi^{(r-1)}}{\partial x_r^4} > 0 \quad (96)$$

$$\frac{\partial^2 \phi^{(r-1)}}{\partial x_j \partial x_r} = 0, \quad (j = r + 1, \dots, m). \quad (97)$$

B. Global Stability and the Maxwell Construction

We extend our stability analysis to global variations, including the emergence of several local minimum states. The general idea is already contained in the extremal principle of Eq. which can be extended to its Legendre transformations according to . We highlight the following possibilities: locally

$$\delta^2 \tilde{\Phi}^{(k)} > 0 \quad (98)$$

$$\delta^2 \tilde{\Phi}^{(k)} = 0 \quad (99)$$

$$\delta^2 \tilde{\Phi}^{(k)} < 0, \quad (100)$$

and globally

$$\Delta \tilde{\Phi}^{(k)} \geq 0, \quad (101)$$

for $k = 1, \dots, m$. The equilibrium is stable if the conditions of Eqs. (99) and (101) are satisfied; in the critical case, the local quadratic approximation for the thermodynamic potential becomes degenerated as stated by Eq. (100). Also, if Eq. (99) is fulfilled with violation of Eq. (101) for a certain displacement, such equilibrium state is designated as metastable. The equilibrium state is unstable if Eq. (100) is verified by some local displacement.

We explore these definitions by studying fluctuations of the quantity X (from a fundamental relation $\Phi = \Phi(X)$) obtained via interaction with reservoirs $R(P)$ through Legendre transformations. Figure illustrates this procedure based on the described method of Lagrange multipliers, addressing three values of the conjugated field $P_\alpha > P_\beta > P_\gamma$. The respective thermodynamic potentials and families of lines of slope as functions of X are portrayed by Figs. ; the construction of the corresponding potentials $\tilde{\Phi}^{(1)}$ is exhibited in Figs. ; finally, Fig. depicts the equations of state resultant from the extremization procedure and locally symbolized by $\frac{\partial \Phi}{\partial X}$. In Figs., the case $P = P_\alpha$ points out the emergence of a local solution X_0^* to the extremization problem, besides the global minimum X_0 . The colored area in Fig. corresponds to the energetic barrier separating these equilibrium states. Precisely, this is verified because the highlighted region corresponds to the variation as follows

$$\begin{aligned} \int_{X_0}^{X_0^*} \left(P - \frac{\partial \Phi}{\partial X} \right) dX &= P(X_0 - X_0^*) - [\Phi(X_0) - \Phi(X_0^*)] \\ &= [\Phi(X_0^*) - PX_0^*] - [\Phi(X_0) - PX_0] \\ &= \Delta \tilde{\Phi}^{(1)}. \end{aligned} \quad (102)$$

For $P = P_\beta$, we observe a new metastable phase, the solution X_0' . The free energy available to reach the local maximum from this metastable state is not enough to accomplish the same process starting from the global minimum, since $\Delta \tilde{\Phi}''^{(1)} > \Delta \tilde{\Phi}'^{(1)}$. These variations are also represented by the areas in Fig . When $P = P_\gamma$, two global minima occur, X_0' and X_0'' . Thus, the previous variations become equal, with $\Delta \tilde{\Phi}''^{(1)} = \Delta \tilde{\Phi}'^{(1)}$. This is equivalent to the Maxwell Cconstruction. Indeed, the Maxwell construction is an artifice recovering a fundamental idea: the stable equilibrium states must be determined by the extremization of a thermodynamical potential. The variational procedure directly determines the equations of state, not the simple attribution

$$P \rightarrow \frac{\partial \Phi}{\partial X}, \quad (103)$$

which actually generates an imprecise equation of state that must be corrected by a Maxwell construction. The equilibrium points obtained in Fig are described in Fig..

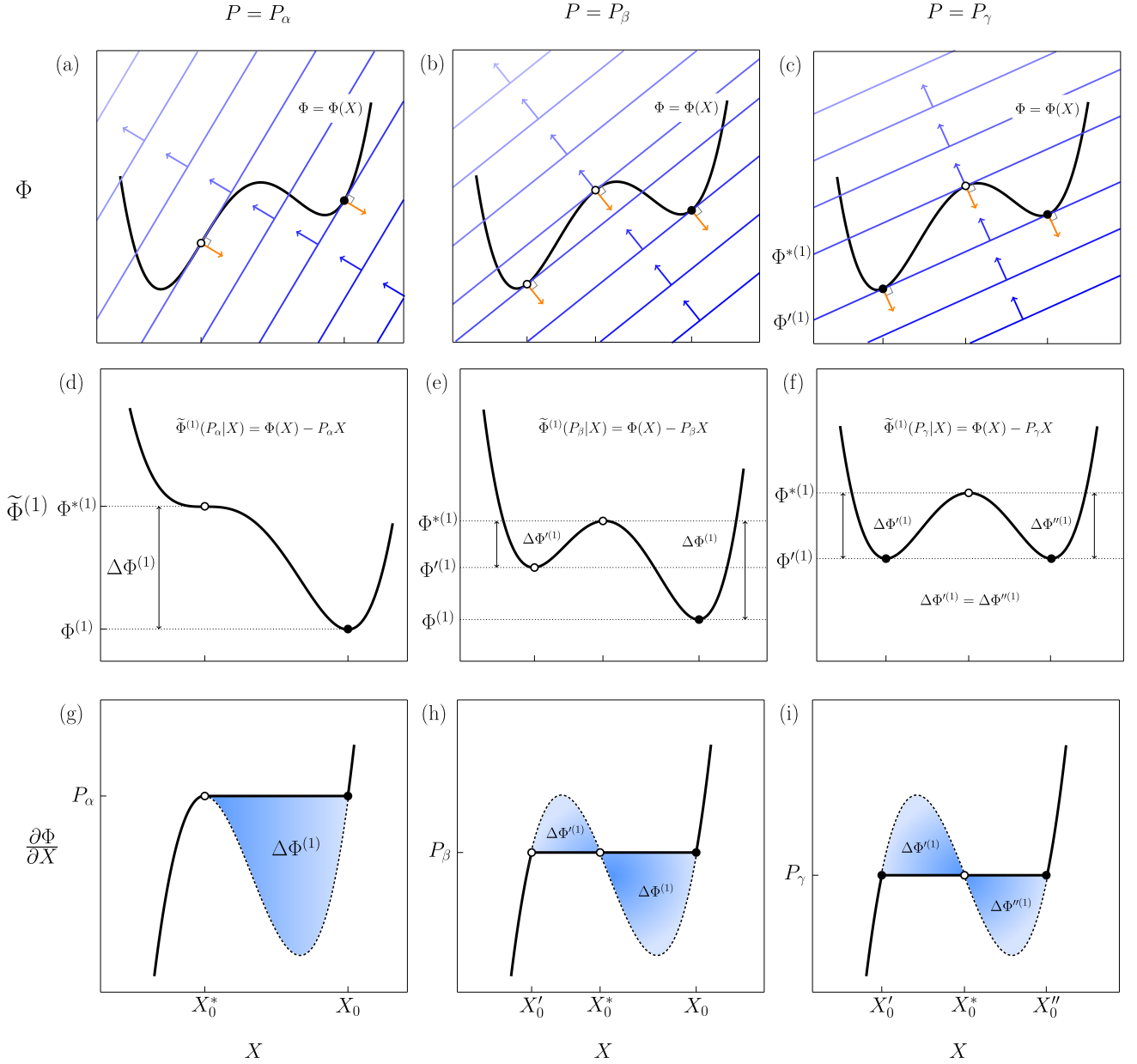


FIG. 4. The Legendre transformation and the Maxwell Construction, considering three different values of the fixed field P .

The stable presenting. Hence the adequate equation of state comes from the minimization of the potential

$$\Phi^{(1)} = \min_X \{\Phi(X) + PX\} \quad (104)$$

providing the correct solution $X_0 = X_0(P)$, with $\Phi^{(1)}(P) = \tilde{\Phi}^{(1)}(P|X_0)$.

V. CONCLUSION

VI. ACKNOWLEDGMENTS

We acknowledge the financial support of the Brazilian funding agencies CNPq and CAPES.

Appendix A: Change of variables and Legendre transformations

Our analysis begin with the case $k = 1$, exploring the intrinsic change of variables carried by the studied transformations. In order to check the relation for the new coordinates δy_1 and the coefficients $\phi_{ij}^{(1)}$, we consider the equation of state

$$x_1 = x_1(P_1, x_2, \dots, x_m) \quad (A1)$$

generated by the Legendre transformation $\phi^{(1)}$ of the thermodynamic potential ϕ with respect to x_1 . This solution establishes a relation of the form

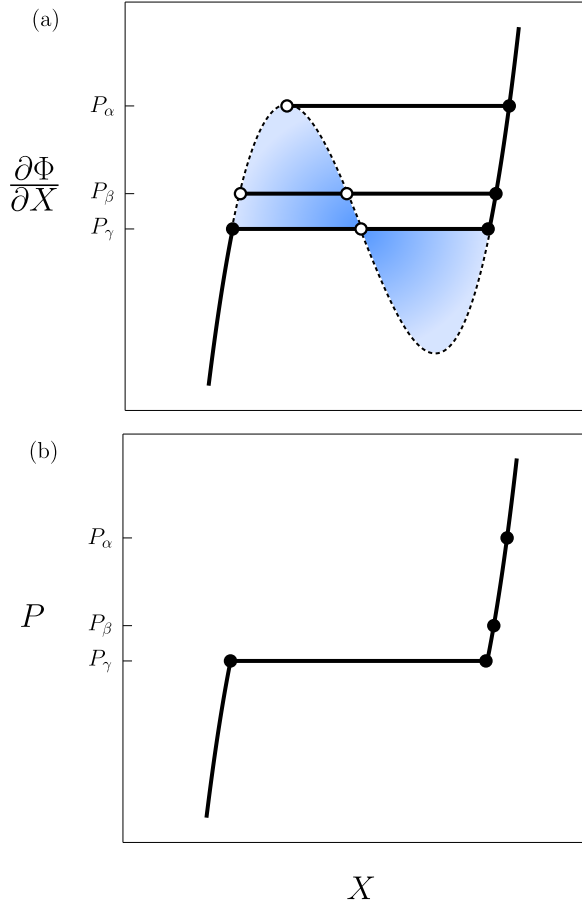


FIG. 5. The equation of state, obtained as the solution of the extremization procedure

$\eta(P_1, x_1, x_2, \dots, x_m) = 0$, whose implicit definition

$$\eta(P_1, x_1(P_1, x_2, \dots, x_m), x_2, \dots, x_m) = 0 \quad (\text{A2})$$

yields the derivative

$$\frac{\partial \eta}{\partial x_i} + \frac{\partial \eta}{\partial x_1} \left(\frac{\partial x_1}{\partial x_i} \right)_{P_1} = 0, \quad (\text{A3})$$

through the chain rule. Therefore, we achieve the expression

$$\left(\frac{\partial x_1}{\partial x_i} \right)_{P_1} = - \frac{\partial \eta}{\partial x_i} / \frac{\partial \eta}{\partial x_1}, \quad (\text{A4})$$

a consequence of the known implicit function theorem. If we choose

$$\eta = P_1(x_1, x_2, \dots, x_m) - P_1, \quad (\text{A5})$$

derived from the local inversion of Eq. (A1) or $P_1 = \frac{\partial \phi}{\partial x_1}$, the result provided by Eq. (A4) becomes

$$\begin{aligned} \left(\frac{\partial x_1}{\partial x_i} \right)_{P_1} &= - \frac{\partial P_1}{\partial x_i} / \frac{\partial P_1}{\partial x_1} \\ &= - \frac{\partial^2 \phi}{\partial x_i \partial x_1} / \frac{\partial^2 \phi}{\partial x_1^2} = \frac{\phi_{1i}}{\phi_{11}}, \end{aligned} \quad (\text{A6})$$

for $i = 2, \dots, m$ as well as the condition $\phi_{11} \neq 0$. Here we considered the compact notation introduced in Eq. (58). Consequently, by employing Eq. (A6), the new basis described in Eq. (??) becomes

$$\begin{aligned} \delta y_1 &= \delta x_1 + \sum_{i=2}^m \frac{\phi_{1i}}{\phi_{11}} \delta x_i \\ &= \delta x_1 - \sum_{i=2}^m \left(\frac{\partial x_1}{\partial x_i} \right)_{P_1} \delta x_i, \end{aligned} \quad (\text{A7})$$

as stated by Eq. (59).

Similarly, we analyze a generic function of the form $\xi = \xi(P_1, x_2, \dots, x_m)$. Its dependence on the variables P_1, x_2, \dots, x_m is implicitly described by the equation of state Eq. (A1) according to

$$\xi(P_1, x_2, \dots, x_m) = \xi(x_1(P_1, x_2, \dots, x_m), x_2, \dots, x_m),$$

The chain rule for its derivative provides

$$\left(\frac{\partial \xi}{\partial x_i} \right)_{P_1} = \frac{\partial \xi}{\partial x_i} + \frac{\partial \xi}{\partial x_1} \left(\frac{\partial x_1}{\partial x_i} \right)_{P_1}. \quad (\text{A8})$$

Based on the choice $\xi = \frac{\partial \phi^{(1)}}{\partial x_j}$, Eqs. (A6) and (A8) imply

$$\left(\frac{\partial^2 \phi^{(1)}}{\partial x_i \partial x_j} \right)_{P_1} = \frac{\partial^2 \phi}{\partial x_i \partial x_j} - \frac{\partial^2 \phi}{\partial x_1 \partial x_j} \frac{\partial^2 \phi}{\partial x_i \partial x_1} / \frac{\partial^2 \phi}{\partial x_1^2}$$

which, in a compact notation, is equivalent to

$$\phi_{ij}^{(1)} = \phi_{ij} - \frac{\phi_{1i} \phi_{1j}}{\phi_{11}}. \quad (\text{A9})$$

with $i, j = 2, \dots, m$. Hence the coefficients defined in Eq. (54) are the second derivatives with respect to the appropriate Legendre transformation of the fundamental equation. The $k > 1$ scenario follows in a straightforward manner by induction on k .

- [1] L. Tisza, *Annals of Physics* **13**, 1 (1961).
 [2] L. Tisza, *Generalized Thermodynamics* (M.I.T. Press, 1977).
 [3] R. Courant and D. Hilbert, *Methods of Mathematical Physics Vol II* (Wiley Interscience, 1966).

- [4] R. T. Rockafellar, *Convex Analysis* (Princeton University Press, 1970).
 [5] R. K. P. Zia, E. F. Redish, and S. R. McKay, *American Journal of Physics* **77**, 614 (2009).

- [6] M. Bocher, *Introduction to Higher Algebra* (Dover Publications, 2004).
- [7] M. Morse and S. Cairns, *Critical Point Theory in Global Analysis and Differential Topology* (Academic Press, 1969).
- [8] J. Sylvester, *The London, Edinburgh, and Dublin Philosophical Magazine and Journal of Science* **4**, 138 (1852).

Bibliography

- [1] Emiliano Brini, Christopher J. Fennell, Marivi Fernandez-Serra, Barbara Hribar-Lee, Miha Lukšič, and Ken A. Dill. How Water’s Properties Are Encoded in Its Molecular Structure and Energies. *Chemical Reviews*, 117(19):12385–12414, 10 2017.
- [2] Felix Franks. *Water: A Matrix of Life*. Royal Society of Chemistry, Cambridge, 2000.
- [3] Thérèse Encrenaz. Water in the Solar System. *Annual Review of Astronomy and Astrophysics*, 46(1):57–87, 9 2008.
- [4] Jestin Baby Mandumpal. *A Journey Through Water: A Scientific Exploration of The Most Anomalous Liquid on Earth*. Bentham Science Publishers, 2017.
- [5] Philip Ball. Water — an enduring mystery. *Nature*, 452(7185):291–292, 3 2008.
- [6] Martin Chaplin. *Water Structure and Science*.
- [7] G. S. Kell. Precise representation of volume properties of water at one atmosphere. *Journal of Chemical & Engineering Data*, 12(1):66–69, 1 1967.
- [8] Pablo G Debenedetti. Supercooled and glassy water. *J. Phys.: Cond. Matter*, 15:1669, 2003.
- [9] Paola Gallo, Katrin Amann-Winkel, Charles Austen Angell, Mikhail Alexeevich Anisimov, Frédéric Caupin, Charusita Chakravarty, Erik Lascaris, Thomas Lorting, Athanassios Zois Panagiotopoulos, John Russo, Jonas Alexander Sellberg, Harry Eugene Stanley, Hajime Tanaka, Carlos Vega, Limei Xu, and Lars

- Gunnar Moody Pettersson. Water: A Tale of Two Liquids. *Chemical Reviews*, 116(13):7463–7500, 7 2016.
- [10] Jeffrey R. Errington and Pablo G. Debenedetti. Relationship between structural order and the anomalies of liquid water. *Nature*, 409(6818):318–321, 1 2001.
- [11] Divya Nayar and Charusita Chakravarty. Water and water-like liquids: relationships between structure, entropy and mobility. *Physical Chemistry Chemical Physics*, 15(34):14162–14177, 2013.
- [12] Yu. D. Fomin, V. N. Ryzhov, B. A. Klumov, and E. N. Tsiok. How to quantify structural anomalies in fluids? *The Journal of Chemical Physics*, 141(3):034508, 7 2014.
- [13] N. V. Gribova, Yu. D. Fomin, Daan Frenkel, and V. N. Ryzhov. Waterlike thermodynamic anomalies in a repulsive-shoulder potential system. *Physical Review E*, 79(5):051202, 5 2009.
- [14] Philip H. Handle, Thomas Loerting, and Francesco Sciortino. Supercooled and glassy water: Metastable liquid(s), amorphous solid(s), and a no-man’s land. *Proceedings of the National Academy of Sciences*, 114(51):13336–13344, 12 2017.
- [15] J. A. Sellberg, C. Huang, T. A. McQueen, N. D. Loh, H. Laksmono, D. Schlesinger, R. G. Sierra, D. Nordlund, C. Y. Hampton, D. Starodub, D. P. DePonte, M. Beye, C. Chen, A. V. Martin, A. Barty, K. T. Wikfeldt, T. M. Weiss, C. Caronna, J. Feldkamp, L. B. Skinner, M. M. Seibert, M. Messerschmidt, G. J. Williams, S. Boutet, L. G. M. Pettersson, M. J. Bogan, and A. Nilsson. Ultrafast X-ray probing of water structure below the homogeneous ice nucleation temperature. *Nature*, 510(7505):381–384, 6 2014.
- [16] C. A. Angell and H. Kanno. Density Maxima in High-Pressure Supercooled Water and Liquid Silicon Dioxide. *Science*, 193(4258):1121–1122, 9 1976.
- [17] O. Mishima, L. D. Calvert, and E. Whalley. ‘Melting ice’ I at 77 K and 10 kbar: a new method of making amorphous solids. *Nature*, 310(5976):393–395, 8 1984.

- [18] O. Mishima, L. D. Calvert, and E. Whalley. An apparently first-order transition between two amorphous phases of ice induced by pressure. *Nature*, 314(6006):76–78, 3 1985.
- [19] Pablo G. Debenedetti. *Metastable Liquids Concepts and Principles*. 1997.
- [20] Peter H Poole, Francesco Sciortino, Ulrich Essmann, and H Eugene Stanley. Phase behaviour of metastable water. *Nature*, 360(6402):324–328, 11 1992.
- [21] H Eugene Stanley, P Kumar, G Franzese, Limei Xu, Z. Yan, M G Mazza, S V Buldyrev, S.-H. Chen, and F Mallamace. Liquid polyamorphism: Possible relation to the anomalous behaviour of water. *The European Physical Journal Special Topics*, 161(1):1–17, 7 2008.
- [22] James N Glosli and Francis H Ree. Liquid-Liquid Phase Transformation in Carbon. *Physical Review Letters*, 82(23):4659–4662, 6 1999.
- [23] Srikanth Sastry and C. Austen Angell. Liquid–liquid phase transition in super-cooled silicon. *Nature Materials*, 2(11):739–743, 11 2003.
- [24] I Saika-Voivod, F Sciortino, T Grande, and P H Poole. Simulated silica. *Philosophical Transactions of the Royal Society A: Mathematical, Physical and Engineering Sciences*, 363(1827):525–535, 2 2005.
- [25] G. Monaco, S Falconi, W A Crichton, and M Mezouar. Nature of the First-Order Phase Transition in Fluid Phosphorus at High Temperature and Pressure. *Physical Review Letters*, 90(25):255701, 6 2003.
- [26] Rei Kurita and Hajime Tanaka. On the abundance and general nature of the liquid–liquid phase transition in molecular systems. *Journal of Physics: Condensed Matter*, 17(27):L293–L302, 7 2005.
- [27] Ken-Ichiro Murata and Hajime Tanaka. General nature of liquid–liquid transition in aqueous organic solutions. *Nature Communications*, 4(1):2844, 12 2013.

- [28] A. Taschin, P. Bartolini, R. Eramo, R. Righini, and R. Torre. Evidence of two distinct local structures of water from ambient to supercooled conditions. *Nature Communications*, 4:1–8, 2013.
- [29] David T. Limmer and David Chandler. The putative liquid-liquid transition is a liquid-solid transition in atomistic models of water. II. *The Journal of Chemical Physics*, 138(21):214504, 6 2013.
- [30] Paola Gallo and H. Eugene Stanley. Supercooled water reveals its secrets. *Science*, 358(6370):1543–1544, 12 2017.
- [31] ZhaoRu Sun, Gang Sun, YiXuan Chen, and LiMei Xu. Liquid-liquid phase transition in water. *Science China Physics, Mechanics & Astronomy*, 57(5):810–818, 5 2014.
- [32] Marco Aurélio A Barbosa and Vera B Henriques. Frustration and anomalous behavior in the Bell-Lavis model of liquid water. *Phys. Rev. E*, 77:51204, 2008.
- [33] C. Buzano, E. De Stefanis, and M. Pretti. Cluster-variation approximation for a network-forming lattice-fluid model. *The Journal of Chemical Physics*, 129(2):024506, 7 2008.
- [34] Vera B. Henriques and Marcia C. Barbosa. Liquid polymorphism and density anomaly in a lattice gas model. *Physical Review E*, 71(3):031504, 3 2005.
- [35] A. B. de Oliveira, P. A. Netz, and M. C. Barbosa. An ubiquitous mechanism for water-like anomalies. *EPL (Europhysics Letters)*, 85(3):36001, 2 2009.
- [36] Alan Barros de Oliveira, Paulo A. Netz, Thiago Colla, and Marcia C. Barbosa. Structural anomalies for a three dimensional isotropic core-softened potential. *The Journal of Chemical Physics*, 125(12):124503, 9 2006.
- [37] Alan Barros de Oliveira, Paulo A. Netz, Thiago Colla, and Marcia C. Barbosa. Thermodynamic and dynamic anomalies for a three-dimensional isotropic core-softened potential. *The Journal of Chemical Physics*, 124(8):084505, 2 2006.

- [38] E. Lomba, N. G. Almarza, C. Martín, and C. McBride. Phase behavior of attractive and repulsive ramp fluids: Integral equation and computer simulation studies. *The Journal of Chemical Physics*, 126(24):244510, 6 2007.
- [39] Richard P. Feynman. Simulating physics with computers. *International Journal of Theoretical Physics*, 21(6-7):467–488, 6 1982.
- [40] S. Lloyd. Universal Quantum Simulators. *Science*, 273(5278):1073–1078, 8 1996.
- [41] Markus Greiner, Olaf Mandel, Tilman Esslinger, Theodor W. Hänsch, and Immanuel Bloch. Quantum phase transition from a superfluid to a Mott insulator in a gas of ultracold atoms. *Nature*, 415(6867):39–44, 1 2002.
- [42] M. H. Anderson, J. R. Ensher, M. R. Matthews, C. E. Wieman, and E. A. Cornell. Observation of Bose-Einstein Condensation in a Dilute Atomic Vapor. *Science*, 269(5221):198–201, 7 1995.
- [43] K. B. Davis, M. O. Mewes, M. R. Andrews, N. J. van Druten, D. S. Durfee, D. M. Kurn, and W. Ketterle. Bose-Einstein Condensation in a Gas of Sodium Atoms. *Physical Review Letters*, 75(22):3969–3973, 11 1995.
- [44] C. C. Bradley, C. A. Sackett, J. J. Tollett, and R. G. Hulet. Evidence of Bose-Einstein Condensation in an Atomic Gas with Attractive Interactions. *Physical Review Letters*, 75(9):1687–1690, 8 1995.
- [45] T.W. Hänsch and A.L. Schawlow. Cooling of gases by laser radiation. *Optics Communications*, 13(1):68–69, 1 1975.
- [46] Wolfgang Ketterle and N.J. Van Druten. Evaporative Cooling of Trapped Atoms. pages 181–236. 1996.
- [47] Immanuel Bloch and Markus Greiner. Exploring Quantum Matter with Ultracold Atoms in Optical Lattices. pages 1–47. 2005.
- [48] Patrick Windpassinger and Klaus Sengstock. Engineering novel optical lattices. *Reports on Progress in Physics*, 76(8):086401, 8 2013.

- [49] W. Hofstetter. Ultracold atoms in optical lattices: tunable quantum many-body systems. *Philosophical Magazine*, 86(13-14):1891–1906, 5 2006.
- [50] W Hofstetter and T Qin. Quantum simulation of strongly correlated condensed matter systems. *Journal of Physics B: Atomic, Molecular and Optical Physics*, 51(8):082001, 4 2018.
- [51] Leticia Tarruell and Laurent Sanchez-Palencia. Quantum simulation of the Hubbard model with ultracold fermions in optical lattices. *Comptes Rendus Physique*, 19(6):365–393, 9 2018.
- [52] Geoff Brumfiel. Simulation: Quantum leaps. *Nature*, 491(7424):322–324, 11 2012.
- [53] I. Buluta and F. Nori. Quantum Simulators. *Science*, 326(5949):108–111, 10 2009.
- [54] Immanuel Bloch. Ultracold quantum gases in optical lattices. *Nature Physics*, 1(1):23–30, 10 2005.
- [55] Immanuel Bloch, Jean Dalibard, and Sylvain Nascimbène. Quantum simulations with ultracold quantum gases. *Nature Physics*, 8(4):267–276, 4 2012.
- [56] Harold J. Metcalf and Peter van der Straten. *Laser Cooling and Trapping*. Graduate Texts in Contemporary Physics. Springer New York, New York, NY, 1999.
- [57] Curtis C. Bradley and Randall G. Hulet. Laser Cooling and Trapping of Neutral Atoms. pages 129–144. 1996.
- [58] Harold J. Metcalf and Peter van der Straten. Laser Cooling and Trapping of Neutral Atoms. In *The Optics Encyclopedia*. Wiley-VCH Verlag GmbH & Co. KGaA, Weinheim, Germany, 7 2007.

- [59] M. SIU LI V.S. BAGNATO, JARBAS C. CASTRO and S.C. ZILIO. Cooling and Trapping Neutral Atoms with Radiative Forces. *Revista Brasileira de Física*, 18(3):411–433, 198.
- [60] Carl E. Wieman, David E. Pritchard, and David J. Wineland. Atom cooling, trapping, and quantum manipulation. *Reviews of Modern Physics*, 71(2):S253–S262, 3 1999.
- [61] Craig Savage. Introduction to Light Forces, Atom Cooling, and Atom Trapping. *Australian Journal of Physics*, 49(4):745, 1996.
- [62] Claude Cohen-Tannoudji and Jean Dalibard. Manipulating atoms with photons. In Gordon Fraser, editor, *The New Physics*, pages 145–170. Cambridge University Press, Cambridge.
- [63] D. J. Wineland and H. Dehmelt. Proposed 1014 $\Delta\nu < \nu$ Laser Fluorescence Spectroscopy on Tl⁺ Mono-Ion Oscillator III. *Bulletin of the American Physical Society*. 20: 637, 1975.
- [64] P. D. Lett, W. D. Phillips, S. L. Rolston, C. E. Tanner, R. N. Watts, and C. I. Westbrook. Optical molasses. *Journal of the Optical Society of America B*, 6(11):2084, 11 1989.
- [65] Jérôme Estève. Trapped by nanostructures. *Nature Nanotechnology*, 8(5):317–318, 5 2013.
- [66] C. J. Pethick and H. Smith. *Bose–Einstein Condensation in Dilute Gases*. Cambridge University Press, Cambridge, 2008.
- [67] William D. Phillips. Nobel Lecture: Laser cooling and trapping of neutral atoms. *Reviews of Modern Physics*, 70(3):721–741, 7 1998.
- [68] Harald F. Hess. Evaporative cooling of magnetically trapped and compressed spin-polarized hydrogen. *Physical Review B*, 34(5):3476–3479, 9 1986.
- [69] <https://sites.ualberta.ca/~ljleblan/>.

- [70] T. Bergeman, Gidon Erez, and Harold J. Metcalf. Magnetostatic trapping fields for neutral atoms. *Physical Review A*, 35(4):1535–1546, 2 1987.
- [71] Alan L. Migdall, John V. Prodan, William D. Phillips, Thomas H. Bergeman, and Harold J. Metcalf. First Observation of Magnetically Trapped Neutral Atoms. *Physical Review Letters*, 54(24):2596–2599, 6 1985.
- [72] E. L. Raab, M. Prentiss, Alex Cable, Steven Chu, and D. E. Pritchard. Trapping of Neutral Sodium Atoms with Radiation Pressure. *Physical Review Letters*, 59(23):2631–2634, 12 1987.
- [73] V. S. Bagnato, G. P. Lafyatis, A. G. Martin, E. L. Raab, R. N. Ahmad-Bitar, and D. E. Pritchard. Continuous Stopping and Trapping of Neutral Atoms. *Physical Review Letters*, 58(21):2194–2197, 5 1987.
- [74] A. Ashkin. Trapping of Atoms by Resonance Radiation Pressure. *Physical Review Letters*, 40(12):729–732, 3 1978.
- [75] Steven Chu, J. E. Bjorkholm, A. Ashkin, and A. Cable. Experimental Observation of Optically Trapped Atoms. *Physical Review Letters*, 57(3):314–317, 7 1986.
- [76] Rudolf Grimm, Matthias Weidemüller, and Yurii B. Ovchinnikov. Optical Dipole Traps for Neutral Atoms. pages 95–170. 2000.
- [77] Claude Cohen-Tannoudji, Jacques Dupont-Roc, and Gilbert Grynberg. *Atom—Photon Interactions*. Wiley, 4 1998.
- [78] J. Dalibard and C. Cohen-Tannoudji. Dressed-atom approach to atomic motion in laser light: the dipole force revisited. *Journal of the Optical Society of America B*, 2(11):1707, 11 1985.
- [79] H. A. Gersch and G. C. Knollman. Quantum Cell Model for Bosons. *Physical Review*, 129(2):959–967, 1 1963.

- [80] Matthew P. A. Fisher, Peter B. Weichman, G. Grinstein, and Daniel S. Fisher. Boson localization and the superfluid-insulator transition. *Physical Review B*, 40(1):546–570, 7 1989.
- [81] D. Jaksch, C. Bruder, J. I. Cirac, C. W. Gardiner, and P. Zoller. Cold Bosonic Atoms in Optical Lattices. *Physical Review Letters*, 81(15):3108–3111, 10 1998.
- [82] Immanuel Bloch, Jean Dalibard, and Wilhelm Zwerger. Many-body physics with ultracold gases. *Reviews of Modern Physics*, 80(3):885–964, 7 2008.
- [83] Wilhelm Zwerger. Mott Hubbard transition of cold atoms in optical lattices. *Journal of Optics B: Quantum and Semiclassical Optics*, 5(2):S9–S16, 4 2003.
- [84] P Blair Blakie and Charles W Clark. Wannier states and bose–hubbard parameters for 2d optical lattices. *Journal of Physics B: Atomic, Molecular and Optical Physics*, 37(7):1391–1404, March 2004.
- [85] Waseem S. Bakr, Jonathon I. Gillen, Amy Peng, Simon Fölling, and Markus Greiner. A quantum gas microscope for detecting single atoms in a Hubbard-regime optical lattice. *Nature*, 462(7269):74–77, 11 2009.
- [86] Jacob F. Sherson, Christof Weitenberg, Manuel Endres, Marc Cheneau, Immanuel Bloch, and Stefan Kuhr. Single-atom-resolved fluorescence imaging of an atomic Mott insulator. *Nature*, 467(7311):68–72, 9 2010.
- [87] Subir Sachdev. *Quantum Phase Transitions*. Cambridge University Press, Cambridge, 2011.
- [88] Richard E. Wilde and Surjit Singh. *Statistical Mechanics: Fundamentals and Modern Applications*. Wiley, 1997.
- [89] Silvio R A Salinas. *Introduction to statistical physics*. Springer-Verlag, New York, 2001.

- [90] Fernando Barbosa V da Silva, Fernando Albuquerque Oliveira, and Marco Aurélio A Barbosa. Residual entropy and waterlike anomalies in the repulsive one dimensional lattice gas. *J. Chem. Phys.*, 142(144506), 2015.
- [91] Marco Aurélio A Barbosa, Fernando V Barbosa, and Fernando A Oliveira. Thermodynamic and dynamic anomalies in a one-dimensional lattice model of liquid water. *J. Chem. Phys.*, 134:24511, 2011.
- [92] Maciej Lewenstein, Anna Sanpera, Veronica Ahufinger, Bogdan Damski, Aditi Sen(De), and Ujjwal Sen. Ultracold atomic gases in optical lattices: mimicking condensed matter physics and beyond. *Advances in Physics*, 56(2):243–379, 3 2007.
- [93] K Sheshadri, H. R Krishnamurthy, R Pandit, and T. V Ramakrishnan. Superfluid and Insulating Phases in an Interacting-Boson Model: Mean-Field Theory and the RPA. *Europhysics Letters (EPL)*, 22(4):257–263, 5 1993.
- [94] P. Buonsante and A. Vezzani. Phase diagram for ultracold bosons in optical lattices and superlattices. *Physical Review A*, 70(3):033608, 9 2004.
- [95] Dario Hügel and Lode Pollet. Thermodynamics of the Bose-Hubbard model in a Bogoliubov+U theory. *Physical Review B*, 91(22):224510, 6 2015.
- [96] B. Capogrosso-Sansone, N. V. Prokof'ev, and B. V. Svistunov. Phase diagram and thermodynamics of the three-dimensional Bose-Hubbard model. *Physical Review B*, 75(13):134302, 4 2007.
- [97] Wen-Jun Hu and Ning-Hua Tong. Dynamical mean-field theory for the Bose-Hubbard model. *Physical Review B*, 80(24):245110, 12 2009.
- [98] Peter Anders, Emanuel Gull, Lode Pollet, Matthias Troyer, and Philipp Werner. Dynamical mean-field theory for bosons. *New Journal of Physics*, 13(7):075013, 7 2011.

- [99] Dario Hugel, Philipp Werner, Lode Pollet, and Hugo U. R. Strand. Bosonic self-energy functional theory. *Physical Review B*, 94(19):195119, 11 2016.
- [100] M. Potthoff. Self-energy-functional approach to systems of correlated electrons. *The European Physical Journal B - Condensed Matter*, 32(4):429–436, 4 2003.
- [101] Krzysztof Byczuk and Dieter Vollhardt. Correlated bosons on a lattice: Dynamical mean-field theory for Bose-Einstein condensed and normal phases. *Physical Review B*, 77(23):235106, 6 2008.
- [102] A. Hubener, M. Snoek, and W. Hofstetter. Magnetic phases of two-component ultracold bosons in an optical lattice. *Physical Review B*, 80(24):245109, 12 2009.
- [103] Michiel Snoek and Walter Hofstetter. Bosonic Dynamical Mean-Field Theory. pages 355–365. 4 2013.
- [104] Enrico Arrigoni, Michael Knap, and Wolfgang von der Linden. Extended self-energy functional approach for strongly correlated lattice bosons in the superfluid phase. *Physical Review B*, 84(1):014535, 7 2011.
- [105] Dario Hugel, Hugo U R Strand, and Lode Pollet. Self-energy functional theory with symmetry breaking for disordered lattice bosons. *Quantum Science and Technology*, 3(3):034006, 7 2018.
- [106] Alexander L. Fetter and John D. Walecka. *Quantum Theory of Many-Particle Systems*. Dover Publications, 1971.
- [107] John Negele and Henri Orland. *Quantum Many-particle Systems*. Perseus Books, 1998.
- [108] Jean Zinn-Justin. *Path Integrals in Quantum Mechanics*. Oxford University Press, 11 2004.
- [109] Gordon Baym and Leo P. Kadanoff. Conservation Laws and Correlation Functions. *Physical Review*, 124(2):287–299, 10 1961.

- [110] Gordon Baym. Self-Consistent Approximations in Many-Body Systems. *Physical Review*, 127(4):1391–1401, 8 1962.
- [111] Cyrano De Dominicis and Paul C. Martin. Stationary Entropy Principle and Renormalization in Normal and Superfluid Systems. I. Algebraic Formulation. *Journal of Mathematical Physics*, 5(1):14–30, 1 1964.
- [112] Cyrano De Dominicis and Paul C. Martin. Stationary Entropy Principle and Renormalization in Normal and Superfluid Systems. II. Diagrammatic Formulation. *Journal of Mathematical Physics*, 5(1):31–59, 1 1964.
- [113] J. M. Luttinger and J. C. Ward. Ground-State Energy of a Many-Fermion System. II. *Physical Review*, 118(5):1417–1427, 6 1960.
- [114] Gianluca Stefanucci and Robert van Leeuwen. *Nonequilibrium Many-Body Theory of Quantum Systems*. Cambridge University Press, Cambridge, 2013.
- [115] J. Berges, Sz. Borsányi, U. Reinosa, and J. Serreau. Nonperturbative renormalization for 2PI effective action techniques. *Annals of Physics*, 320(2):344–398, 12 2005.
- [116] J. F. Rentrop, V. Meden, and S. G. Jakobs. Renormalization group flow of the Luttinger-Ward functional: Conserving approximations and application to the Anderson impurity model. *Physical Review B*, 93(19):195160, 5 2016.
- [117] Nathan Gemelke, Xibo Zhang, Chen Lung Hung, and Cheng Chin. In situ observation of incompressible Mott-insulating domains in ultracold atomic gases. *Nature*, 460(7258):995–998, 2009.
- [118] K. Xu, Y. Liu, J. R. Abo-Shaeer, T. Mukaiyama, J. K. Chin, D. E. Miller, W. Ketterle, Kevin M. Jones, and Eite Tiesinga. Sodium bose-einstein condensates in an optical lattice. *Physical Review A*, 72(4), October 2005.
- [119] Cheng Chin, Rudolf Grimm, Paul Julienne, and Eite Tiesinga. Feshbach resonances in ultracold gases. *Reviews of Modern Physics*, 82(2):1225–1286, April 2010.

- [120] X. Zhang, C.-L. Hung, S.-K. Tung, and C. Chin. Observation of Quantum Criticality with Ultracold Atoms in Optical Lattices. *Science*, 335(6072):1070–1072, 3 2012.
- [121] Eduardo Osório Rizzatti, Márcio Sampaio Gomes Filho, Mariana Malard, and Marco Aurélio A. Barbosa. Waterlike anomalies in the Bose–Hubbard model. *Physica A: Statistical Mechanics and its Applications*, 518:323–330, 3 2019.
- [122] Immanuel Bloch. Quantum simulations come of age. *Nature Physics*, 14(12):1159–1161, 12 2018.
- [123] Tatjana Gericke, Peter Würtz, Daniel Reitz, Tim Langen, and Herwig Ott. High-resolution scanning electron microscopy of an ultracold quantum gas. *Nature Physics*, 4(12):949–953, October 2008.
- [124] Sylvain Nascimbène, Nir Navon, Frédéric Chevy, and Christophe Salomon. The equation of state of ultracold Bose and Fermi gases: a few examples. *New Journal of Physics*, 12(10):103026, 10 2010.
- [125] Tin-Lun Ho and Qi Zhou. Obtaining the phase diagram and thermodynamic quantities of bulk systems from the densities of trapped gases. *Nature Physics*, 6(2):131–134, 2 2010.
- [126] E. S. R. Gopal. *Specific Heats at Low Temperatures*. Springer US, Boston, MA, 1966.
- [127] Mariano de Souza, Ricardo Paupitz, Antonio Seridonio, and Roberto E. Lagos. Specific Heat Anomalies in Solids Described by a Multilevel Model. *Brazilian Journal of Physics*, 46(2):206–212, 4 2016.
- [128] Jason S. Gardner, Michel J. P. Gingras, and John E. Greedan. Magnetic pyrochlore oxides. *Reviews of Modern Physics*, 82(1):53–107, 1 2010.
- [129] A. P. Ramirez, A. Hayashi, R. J. Cava, R. Siddharthan, and B. S. Shastry. Zero-point entropy in ‘spin ice’. *Nature*, 399(6734):333–335, 5 1999.

- [130] K Matsuhira, Z Hiroi, T Tayama, S Takagi, and T Sakakibara. A new macroscopically degenerate ground state in the spin ice compound Dy₂Ti₂O₇ under a magnetic field. *Journal of Physics: Condensed Matter*, 14(29):L559–L565, 7 2002.
- [131] Zenji Hiroi, Kazuyuki Matsuhira, Seishi Takagi, Takashi Tayama, and Toshio Sakakibara. Specific Heat of Kagomé Ice in the Pyrochlore Oxide Dy₂Ti₂O₇. *Journal of the Physical Society of Japan*, 72(2):411–418, 2 2003.
- [132] Nobuko Hamaguchi, Taku Matsushita, Nobuo Wada, Yukio Yasui, and Masatoshi Sato. Low-temperature phases of the pyrochlore compound Tb₂Ti₂O₇. *Physical Review B*, 69(13):132413, 4 2004.
- [133] X. Ke, D. V. West, R. J. Cava, and P. Schiffer. Magnetothermal study of the hybrid frustrated magnet Dy_{2-x}Tb_xTi₂O₇. *Physical Review B*, 80(14):144426, 10 2009.
- [134] A. M. Hallas, A. M. Arevalo-Lopez, A. Z. Sharma, T. Munsie, J. P. Attfield, C. R. Wiebe, and G. M. Luke. Magnetic frustration in lead pyrochlores. *Physical Review B*, 91(10):104417, 3 2015.
- [135] N. P. Raju, E. Gmelin, and R. K. Kremer. Magnetic-susceptibility and specific-heat studies of spin-glass-like ordering in the pyrochlore compounds R₂Mo₂O₇ (R = Y, Sm, or Gd). *Physical Review B*, 46(9):5405–5411, 9 1992.
- [136] R Yamanaka, K Matsubayashi, Y Saiga, T Kawae, and Y Uwatoko. Heat Capacity Measurement of Heavy Fermion YbCo₂Zn₂₀ under Magnetic Field. *Journal of Physics: Conference Series*, 391:012078, 12 2012.
- [137] S. Lucas, K. Grube, C.-L. Huang, A. Sakai, S. Wunderlich, E. L. Green, J. Wosnitza, V. Fritsch, P. Gegenwart, O. Stockert, and H. v. Löhneysen. Entropy Evolution in the Magnetic Phases of Partially Frustrated CePdAl. *Physical Review Letters*, 118(10):107204, 3 2017.

- [138] J. Brambleby, P. A. Goddard, J. Singleton, M. Jaime, T. Lancaster, L. Huang, J. Wosnitza, C. V. Topping, K. E. Carreiro, H. E. Tran, Z. E. Manson, and J. L. Manson. Adiabatic physics of an exchange-coupled spin-dimer system: Magnetocaloric effect, zero-point fluctuations, and possible two-dimensional universal behavior. *Physical Review B*, 95(2):024404, 1 2017.
- [139] Linlin Zhong, Xiaohua Wang, Mingzhe Rong, and Yann Cressault. Effects of copper vapour on thermophysical properties of CO₂-N₂ plasma. *The European Physical Journal D*, 70(11):233, 11 2016.
- [140] J.H. Ipsen, O.G. Mouritsen, and M.J. Zuckermann. Theory of thermal anomalies in the specific heat of lipid bilayers containing cholesterol. *Biophysical Journal*, 56(4):661–667, 10 1989.
- [141] D. Jesenek, S. Kralj, G. Cordoyiannis, and Z. Kutnjak. Double Peak Specific Heat Capacity Anomaly in Mixtures of Liquid Crystals and Nanoparticles. *Molecular Crystals and Liquid Crystals*, 546(1):3/[1473]–10/[1480], 6 2011.
- [142] Veit Elser. Nuclear antiferromagnetism in a registered ³He solid. *Physical Review Letters*, 62(20):2405–2408, 5 1989.
- [143] J B Parkinson and J Timonen. Small clusters with Heisenberg antiferromagnetic exchange. *Journal of Physics: Condensed Matter*, 12(40):8669–8682, 10 2000.
- [144] A. V. Syromyatnikov and S. V. Maleyev. Double-peak specific heat feature in frustrated antiferromagnetic clusters. *Journal of Experimental and Theoretical Physics Letters*, 79(5):221–225, 3 2004.
- [145] N. P. Konstantinidis. Antiferromagnetic Heisenberg model on clusters with icosahedral symmetry. *Physical Review B*, 72(6):064453, 8 2005.
- [146] Dmitri V. Efremov and Richard A. Klemm. Spin anisotropy effects in dimer single molecule magnets. *Physical Review B*, 74(6):064408, 8 2006.

- [147] Alfred Hucht, Sanjubala Sahoo, Shreekantha Sil, and Peter Entel. Effect of anisotropy on small magnetic clusters. *Physical Review B*, 84(10):104438, 9 2011.
- [148] M. J. Harris, S. T. Bramwell, P. C. W. Holdsworth, and J. D. M. Champion. Liquid-Gas Critical Behavior in a Frustrated Pyrochlore Ferromagnet. *Physical Review Letters*, 81(20):4496–4499, 11 1998.
- [149] Roger G. Melko, Byron C. den Hertog, and Michel J. P. Gingras. Long-Range Order at Low Temperatures in Dipolar Spin Ice. *Physical Review Letters*, 87(6):067203, 7 2001.
- [150] R. Mejdani and A. Lambros. Ladder ising spin configurations. I. Heat capacity. *physica status solidi (b)*, 196(2):433–441, 8 1996.
- [151] Katarína Karľová, Jozef Strečka, and Tomáš Madaras. The Schottky-type specific heat as an indicator of relative degeneracy between ground and first-excited states: The case study of regular Ising polyhedra. *Physica B: Condensed Matter*, 488:49–56, 5 2016.
- [152] E. Jurčišínová and M. Jurčišín. Highly macroscopically degenerated single-point ground states as source of specific heat capacity anomalies in magnetic frustrated systems. *Journal of Magnetism and Magnetic Materials*, 451:137–142, 4 2018.
- [153] E. Jurčišínová and M. Jurčišín. Multipeak low-temperature behavior of specific heat capacity in frustrated magnetic systems: An exact theoretical analysis. *Physical Review E*, 97(5):052129, 5 2018.
- [154] Takashi Nakanishi and Shoji Yamamoto. Intrinsic double-peak structure of the specific heat in low-dimensional quantum ferrimagnets. *Physical Review B*, 65(21):214418, 5 2002.
- [155] Roderich Moessner and Arthur P. Ramirez. Geometrical frustration. *Physics Today*, 59(2):24–29, 2 2006.

- [156] Linus Pauling. The Structure and Entropy of Ice and of Other Crystals with Some Randomness of Atomic Arrangement. *Journal of the American Chemical Society*, 57(12):2680–2684, 12 1935.
- [157] J. D. Bernal and R. H. Fowler. A Theory of Water and Ionic Solution, with Particular Reference to Hydrogen and Hydroxyl Ions. *The Journal of Chemical Physics*, 1(8):515–548, 8 1933.
- [158] W. F. Giauque and J. W. Stout. The Entropy of Water and the Third Law of Thermodynamics. The Heat Capacity of Ice from 15 to 273°K. *Journal of the American Chemical Society*, 58(7):1144–1150, 7 1936.
- [159] Leon Balents. Spin liquids in frustrated magnets. *Nature*, 464(7286):199–208, 3 2010.
- [160] Eduardo O. Rizzatti, Marco Aurélio A. Barbosa, and Marcia C. Barbosa. Core-softened potentials, multiple liquid–liquid critical points, and density anomaly regions: An exact solution. *Frontiers of Physics*, 13(1):136102, 2 2018.
- [161] Eduardo O. Rizzatti, Marco Aurélio A. Barbosa, and Marcia C. Barbosa. Quantum density anomaly in optically trapped ultracold gases. *Physical Review A*, 102(3):033331, 9 2020.
- [162] J. K. Freericks and H. Monien. Phase diagram of the Bose-Hubbard Model. *Europhysics Letters (EPL)*, 26(7):545–550, 6 1994.
- [163] Jaromir Panas, Anna Kauch, Jan Kuneš, Dieter Vollhardt, and Krzysztof Byczuk. Numerical calculation of spectral functions of the Bose-Hubbard model using bosonic dynamical mean-field theory. *Physical Review B*, 92(4):045102, 7 2015.
- [164] Hugo U. R. Strand, Martin Eckstein, and Philipp Werner. Beyond the Hubbard bands in strongly correlated lattice bosons. *Physical Review A*, 92(6):063602, 12 2015.

- [165] J. K. Freericks, H. R. Krishnamurthy, Yasuyuki Kato, Naoki Kawashima, and Nandini Trivedi. Strong-coupling expansion for the momentum distribution of the Bose-Hubbard model with benchmarking against exact numerical results. *Physical Review A*, 79(5):053631, 5 2009.
- [166] Niklas Teichmann, Dennis Hinrichs, Martin Holthaus, and André Eckardt. Process-chain approach to the Bose-Hubbard model: Ground-state properties and phase diagram. *Physical Review B*, 79(22):224515, 6 2009.
- [167] Fabrice Gerbier, Artur Widera, Simon Fölling, Olaf Mandel, Tatjana Gericke, and Immanuel Bloch. Phase Coherence of an Atomic Mott Insulator. *Physical Review Letters*, 95(5):050404, 7 2005.
- [168] Alexander Hoffmann and Axel Pelster. Visibility of cold atomic gases in optical lattices for finite temperatures. *Physical Review A*, 79(5):053623, 5 2009.
- [169] Laszlo Tisza. The thermodynamics of phase equilibrium. *Annals of Physics*, 13(1):1–92, 4 1961.
- [170] L. Tisza. *Generalized Thermodynamics*. M.I.T. Press, 1977.
- [171] R. Courant and D. Hilbert. *Methods of Mathematical Physics Vol II*. Wiley Interscience, 1966.
- [172] Ralph Tyrell Rockafellar. *Convex Analysis*. Princeton University Press, 1970.
- [173] R. K. P. Zia, Edward F. Redish, and Susan R. McKay. Making sense of the Legendre transform. *American Journal of Physics*, 77(7):614–622, 7 2009.
- [174] Maxime Bocher. *Introduction to Higher Algebra*. Dover Publications, 2004.
- [175] Marston Morse and Stewart Cairns. *Critical Point Theory in Global Analysis and Differential Topology*. Academic Press, 1969.
- [176] J.J. Sylvester. XIX. A demonstration of the theorem that every homogeneous quadratic polynomial is reducible by real orthogonal substitutions to the form

- of a sum of positive and negative squares. *The London, Edinburgh, and Dublin Philosophical Magazine and Journal of Science*, 4(23):138–142, 8 1852.
- [177] Natalie Wolchover. Universal Quantum Phenomenon Found in Strange Metals, 2018.
- [178] John Negele and Henri Orland. *Quantum Many-particle Systems*. Perseus Books, 1998.
- [179] V. J. Emery and S. A. Kivelson. Superconductivity in Bad Metals. *Physical Review Letters*, 74(16):3253–3256, 4 1995.
- [180] J. G. Bednorz and K. A. Muller. Possible high T_c superconductivity in the Ba-La-Cu-O system. *Zeitschrift für Physik B Condensed Matter*, 64(2):189–193, 6 1986.
- [181] A. Schilling, M. Cantoni, J. D. Guo, and H. R. Ott. Superconductivity above 130 K in the Hg–Ba–Ca–Cu–O system. *Nature*, 363(6424):56–58, 5 1993.
- [182] Peter T. Brown, Debayan Mitra, Elmer Guardado-Sanchez, Reza Nourafkan, Alexis Reymbaut, Charles-David Hébert, Simon Bergeron, A.-M. S. Tremblay, Jure Kokalj, David A. Huse, Peter Schauß, and Waseem S. Bakr. Bad metallic transport in a cold atom Fermi-Hubbard system. *Science*, 363(6425):379–382, 1 2019.
- [183] Jean-Philippe Brantut. Transport with strong interactions. *Science*, 363(6425):344–345, 1 2019.
- [184] J. Hubbard. Electron Correlations in Narrow Energy Bands. *Proceedings of the Royal Society A: Mathematical, Physical and Engineering Sciences*, 276(1365):238–257, 11 1963.
- [185] Walter Metzner. Linked-cluster expansion around the atomic limit of the Hubbard model. *Physical Review B*, 43(10):8549–8563, 4 1991.

-
- [186] Barry Bradlyn, Francisco Ednilson A. dos Santos, and Axel Pelster. Effective action approach for quantum phase transitions in bosonic lattices. *Physical Review A*, 79(1):013615, 1 2009.
- [187] Peter McCullagh. *Tensor Methods in Statistics*. Chapman and Hall/CRC, 1 2018.